

IN THE UNITED STATES PATENT AND TRADEMARK OFFICE

In re Patent Application of Date: May 15, 2008
Applicants: Bednorz et al. Docket: YO987-074BZ
Serial No.: 08/479,810 Group Art Unit: 1751
Filed: June 7, 1995 Examiner: M. Kopec
For: NEW SUPERCONDUCTIVE COMPOUNDS HAVING HIGH TRANSITION
TEMPERATURE, METHODS FOR THEIR USE AND PREPARATION
Commissioner for Patents
United States Patent and Trademark Office
P.O. Box 1450
Alexandria, VA 22313-1450

**APPEAL BRIEF
PART IX**

CFR 37 § 41.37(c) (1) (ix)

SECTION 1

VOLUME 4

Part 3

BRIEF ATTACHMENTS F TO O

Respectfully submitted,

/Daniel P Morris/
Dr. Daniel P. Morris, Esq.
Reg. No. 32,053
(914) 945-3217

IBM CORPORATION
Intellectual Property Law Dept.
P.O. Box 218
Yorktown Heights, New York 10598

BRIEF ATTACHMENT F

IN THE UNITED STATES PATENT AND TRADEMARK OFFICE

In re Patent Application of

Applicants: Bednorz et al.

Serial No.: 08/479,810

Filed: June 7, 1995

For: **NEW SUPERCONDUCTIVE COMPOUNDS HAVING HIGH TRANSITION
TEMPERATURE, METHODS FOR THEIR USE AND PREPARATION**

Date: March 1, 2005

Docket: YO987-074BZ

Group Art Unit: 1751

Examiner: M. Kopec

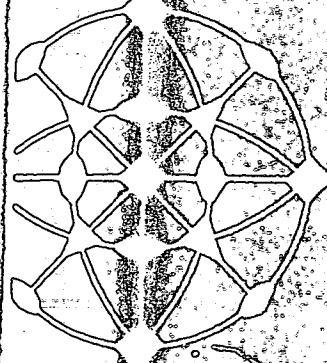
Commissioner for Patents
P.O. Box 1450
Alexandria, VA 22313-1450

FIRST SUPPLEMENTAL AMENDMENT

Sir:

In response to the Office Action dated July 28, 2004, please consider the following:

ATTACHMENT F

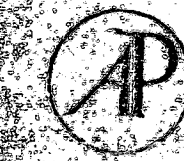


Journal of Solid State Chemistry

ACADEMIC PRESS

New York and London

A Subsidiary of Harcourt Brace Jovanovich Publishers



Oxygen Defect K_2NiF_4 -Type Oxides: The Compounds $La_{2-x}Sr_xCuO_{4-x/2+\delta}$

NINH NGUYEN, JACQUES CHOISNET,¹ MARYVONNE HERVIEU,
 AND BERNARD RAVEAU

*Laboratoire de Cristallographie et Chimie du Solide, L.A. 251, ISMRA,
 Université de Caen, 14032 Caen Cedex, France*

Received December 29, 1980; in final form February 18, 1981

Oxygen defect K_2NiF_4 -type oxides $La_{2-x}Sr_xCuO_{4-x/2+\delta}$ have been synthesized for a wide composition range: $0 \leq x \leq 1.34$. From the X-ray and electron diffraction study three domains have been characterized: orthorhombic compounds with La_2CuO_4 structure for $0 \leq x < 0.10$, tetragonal oxides similar to $LaSrCuO_4$ for $0.10 \leq x < 1$ and several superstructures derived from the tetragonal cell ($a = n \cdot a_{LaSrCuO_4}$ with $n = 3, 4, 4.5, 5, 6$) for $1 \leq x \leq 1.34$. The compounds corresponding to $0 < x < 1$ differ from the other oxides in that they are characterized by the presence of copper with two oxidation states: +2 and +3. A model structure for $La_{0.8}Sr_{1.2}Cu\lambda O_{3.4}$, in which copper has only the +2 oxidation state, and for which the actual cell is tetragonal— $a = 18.80 \text{ \AA}$ and $c = 12.94 \text{ \AA}$ —has been established. The particular structural evolution of these compounds is discussed in terms of a competition between the capability of Cu(II) to be oxidized to Cu(III) and the ordering of oxygen vacancies.

Introduction

A lot of oxides, with the A_2MO_4 formula, characterized by the intergrowth of perovskite- and sodium chloride-type layers are known at the present time. Contrary to the perovskite oxides, no oxygen defect has been observed for this structural series to our knowledge. Copper, due to its ability to take different coordinations smaller than six, is a potential candidate which could form such anion defect compounds. However the only isostructural copper compounds which have been synthesized, La_2CuO_4 (1, 2) and $SrLaCuO_4$ (3) are stoichiometric. Nevertheless, the recent results concerning the oxides $La_{2-x}A_{1+x}O_{6-x/2}$ ($A = Ca, Sr$) (4), whose

structure is strongly related to that of $Sr_3Ti_2O_7$ (5) suggest the possibility of oxygen defect for A_2CuO_4 compounds. Thus, the present work deals with the oxides $La_{2-x}Sr_xCuO_{4-x/2+\delta}$, for which the replacement of lanthanum by strontium leads to the formation of oxygen vacancies, involving order phenomena.

Experimental

For the synthesis of the compounds of the system $La_2CuO_4-Sr_2CuO_3$, $SrCO_3$, CuO and La_2O_3 were mixed according to the following ratios: $(2 - x)/2La_2O_3/x SrCO_3/1 CuO$. All these reactions were made in a platinum crucible in air. The synthesis of the compounds with high purity strongly depends on the temperature for a fixed pressure. The mixtures were thus first heated for 5 hr at $900^\circ C$, and then at tem-

¹ Author to whom reprint requests should be addressed.

peratures ranging 12 hr.

The oxidation s oxygen defect, was the compounds by reactions were foll try using a Setara

The crystallogr a published by two com ray diffractometry with a Philips goni fraction using an scope.

Results

Study of the System The Compounds $La_{2-x}Sr_xCuO_{4-x/2+\delta}$

According to the scribed, K_2NiF_4 -t spanding to the $La_{2-x}Sr_xCu^{II}O_{4-x/2}$ large composition r microthermogravir ides under hydro that a part of Cu(I)

Range	x
I	0
	0.08
II	0.25
	0.33 _a
	0.50
	0.66 _a
	0.88 _a
III	1.00 ^a
	1.28 ^a
	1.34 ^a
	1.20

^a The "a" parameters composition are given in

peratures ranging from 1000 to 1200°C for 12 hr.

The oxidation state of copper, i.e., the oxygen defect, was determined by reducing the compounds by hydrogen: the reduction reactions were followed by thermogravimetry using a Setaram microbalance.

The crystallographic data were established by two complementary methods: X-ray diffractometry using $CuK\alpha$ radiation with a Philips goniometer and electron diffraction using an EM 200 Philips microscope.

Results

Study of the System La_2CuO_4 - Sr_2CuO_3 : The Compounds $La_{2-x}Sr_xCuO_{4-x/2+\delta}$

According to the methods previously described, K_2NiF_4 -type compounds corresponding to the nominal composition $La_{2-x}Sr_xCu^{II}O_{4-x/2}$ were synthesized in a large composition range: $0 \leq x \leq 1.34$. The microthermogravimetric study of these oxides under hydrogen showed, however, that a part of Cu(II) had been oxidized to

Cu(III), leading to the formula $La_{2-x}Sr_xCuO_{4-x/2+\delta}$ with $0 \leq \delta < 0.12$. For $x > 1.34$ a mixture of the K_2NiF_4 -type phase and Sr_2CuO_3 (6) was observed.

The crystallographic data of different compositions are summarized in Table I. The study of the X-ray patterns showed a continuous evolution of the structure and allowed to characterize three composition ranges which were studied by electron diffraction.

(I) $0 \leq x < 0.10$. The X-ray patterns very similar to that of La_2CuO_4 (1) were indexed in an orthorhombic cell with:

$$\begin{aligned} a_1 &= 2a_p \sin \beta/2 = a_{La_2CuO_4}, \\ b_1 &= 2a_p \cos \beta/2 = b_{La_2CuO_4}, \\ c_1 &\approx c_{La_2CuO_4}, \end{aligned}$$

where a_p is the parameter of the perovskite cubic cell, and β defines the monoclinic distortion of the cell.

From the conditions limiting possible reflections— $hkl : h+k, l+h, k+l = 2n$ —three space groups are possible: $Fmmm$, $Fmm2$, and $F222$.

TABLE I
CRYSTALLOGRAPHIC DATA OF $La_{2-x}Sr_xCuO_{4-x/2+\delta}$ COMPOUNDS

Range	x	δ	Composition	a (Å)	b (Å)	c (Å)	Heating temperature (°C)
I	0	0	La_2CuO_4	5.366(2)	5.402(2)	13.149(4)	1100
	0.08	0.030(1)	$La_{1.92}Sr_{0.08}CuO_{3.99}$	5.351(1)	5.368(2)	13.200(5)	1000
II	0.25	0.060(4)	$La_{1.75}Sr_{0.25}CuO_{3.935}$	3.775(2)		13.247(5)	1000
	0.33 ₃	0.119(4)	$La_{1.66}Sr_{0.33}CuO_{3.85}$	3.776(1)		13.250(2)	1100
	0.50	0.100(4)	$La_{1.50}Sr_{0.50}CuO_{3.65}$	3.773(1)		13.204(3)	1160
	0.66 ₆	0.092(4)	$La_{1.33}Sr_{0.66}CuO_{3.75}$	3.775(1)		13.150(4)	1170
	0.88 ₀	0.088(4)	$La_{1.12}Sr_{0.88}CuO_{3.64}$	3.773(1)		13.073(5)	1170
III	1.00 ^a	0.0	$LaSrCuO_{3.50}$	3.767(1)		13.002(3)	1200
	1.28 ^a	0.0	$La_{0.72}Sr_{1.28}CuO_{3.38}$	3.761(2)		12.922(9)	1200
	1.34 ^a	0.0	$La_{0.66}Sr_{1.34}CuO_{3.33}$	3.759(3)		12.907(9)	1200
	1.20	0.0	$La_{0.50}Sr_{1.20}CuO_{3.40}$	18.803(7)		12.941(7)	1200

^a The "a" parameters of these compounds (range III) are those of the tetragonal subcell; n values for every composition are given in Table II.

(II) $0.10 \leq x < 1$. The symmetry is tetragonal like that of LaSrCuO_4 (3); the cell parameters are related to the latter and to I in the following manner:

$$a_{\text{II}} \approx a_1 / 2^{1/2} \approx a_p \approx a_{\text{LaSrCuO}_4},$$

$$c_{\text{II}} \approx c_1 \approx c_{\text{LaSrCuO}_4}.$$

The reflection conditions are those of $\text{LaSrCuO}_4 - hkl : h + k + l = 2n$ —involving the space groups: $I4/mmm$, $I4/m$, $I422$ and $I\bar{4}2m$.

(III) $1 \leq x \leq 1.34$. The X-ray diffractograms are characterized by the existence of a system of strong peaks, which was already observed for the compounds (II), involving at least the existence of a tetragonal subcell of the same type. However, for all these patterns, weak peaks were always observed which could not be indexed in this cell. An electron diffraction study was thus undertaken: about 50 crystals were examined for each value of x given in Table II. Several types of crystals were isolated:

—Small number of crystals, about 10%, were characterized by a tetragonal cell similar to that of LaSrCuO_4 :

$$a_{\text{III}} \approx a_{\text{II}} \approx a_p \approx a_{\text{LaSrCuO}_4},$$

$$c_{\text{III}} \approx c_{\text{II}} \approx c_1 \approx c_{\text{LaSrCuO}_4}.$$

—Most of the crystals, i.e., about 90%, presented, in addition to the fundamental reflections previously described, superstructure reflections with a variable inten-

sity. The electron diffraction patterns allowed us to find the following relations for the actual tetragonal cell for a composition x :

$$a_{\text{III}}^T = na_{\text{III}} \sim na_{\text{II}},$$

$$c_{\text{III}}^T = c_{\text{III}} \# c_{\text{II}} \approx c_1.$$

For a same composition x , several sorts of superstructures were generally observed, characterized either by integral n values ($n = 4, 5$, or 6) or nonintegral values of n (n ranging from 4.5 to 5.6), as shown for several compositions in Table II. Figure 1 shows, as an example, the electron diffraction patterns of the (001) planes for $\text{La}_{2/3}\text{Sr}_{4/3}\text{CuO}_{3.33}$. From Table II it can be seen that a pure term, characterized by a superstructure with an integral value of n ($n = 5$), is only obtained for $x = 1.20$. It has thus been attempted to elaborate a structural model for this phase.

A Structural Model for $\text{La}_{0.8}\text{Sr}_{1.2}\text{CuO}_{3.4}$

The actual cell of this compound is tetragonal: $a = 18.804 \text{ \AA}$ and $c = 12.94 \text{ \AA}$ ($Z = 50$). The conditions limiting possible reflections are the same as those of the subcell ($a = 3.760$, $c = 12.94 \text{ \AA}$; $Z = 2$), leading to the space groups $I4/mmm$, $I4/m$, $I422$, and $I\bar{4}2m$. The intensity calculations were first made in the K_2NiF_4 type cell, with the most symmetric space group $I4/mmm$. For these calculations, reflections corresponding only to the subcell were used. Copper atoms were placed on $2(a)$, lanthanum and strontium atoms were statistically distributed on $4e$, and oxygen atoms and anionic vacancies were statistically distributed over two sorts of sites $4e$ (O_1) and $4c$ (O_{II}). After refinement of the atomic parameters the discrepancy factor could not be lowered below $R = 0.104$. The possibility of an order of the oxygen atoms and vacancies over the O_1 and O_{II} sites was thus considered. The occupancy factors of both sites

TABLE II
 n VALUES OBSERVED BY ELECTRON DIFFRACTION FOR COMPOUNDS OF RANGE III

Composition	x	n
$\text{LaSrCuO}_{3.5}$	1.00	1; 4.5
$\text{La}_{0.88}\text{Sr}_{1.12}\text{CuO}_{3.44}$	1.12	1; 4.5; 5
$\text{La}_{0.80}\text{Sr}_{1.20}\text{CuO}_{3.40}$	1.20	5
$\text{La}_{0.72}\text{Sr}_{1.28}\text{CuO}_{3.36}$	1.28	1; 4.6; 5; 5.3; 5.4
$\text{La}_{0.66}\text{Sr}_{1.34}\text{CuO}_{3.33}$	1.34	1; 4; 5; 5.6; 6

FIG. 1. Electron dif
(d) 6.

were refined successively and the best (Table IV) was obtain

TAB
 $\text{La}_{0.80}\text{Sr}_{1.20}\text{O}_{3.40}$: ATOM PC

	Sites	x	y
La	4(e)	0	0
Sr	4(e)	0	0
Cu	2(a)	0	0
O_1	4(e)	0	0
O_{II}	4(c)	0	0.5

^a $a = 3.760 \text{ \AA}$; $c = 12.94$

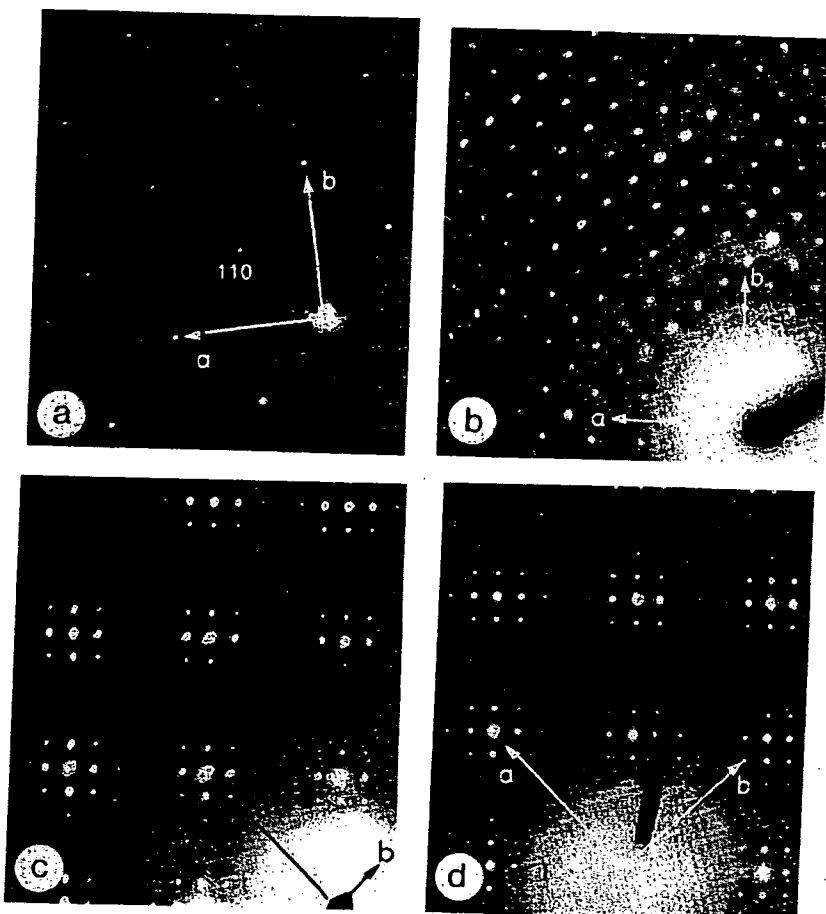


FIG. 1. Electron diffraction patterns of the (001) planes for $La_{2/3}Sr_{4/3}CuO_{3.33}$; (a) $n = 1$; (b) 4; (c) 5.6; (d) 6.

were refined successively and then simultaneously and the best value of $R = 0.081$ (Table IV) was obtained for a total occupa-

tion of the O_I sites, while vacancies and oxygen atoms were distributed over the O_{II} sites. The location of the vacancies preferentially on the O_{II} sites, at the same level as the copper atoms, can be considered as significant, on account of the relatively weak scattering factor of oxygen. This is confirmed by the high R value ($R = 0.153$) obtained for a total occupation of the O_{II} sites, vacancies and oxygen atoms being distributed on the O_I sites. The first results which are summarized in Table III show the atoms are located in positions very close to those usually observed in K_2NiF_4 type structures. The main difference with

TABLE III
 $La_{0.80}Sr_{1.20}O_{3.40}$: ATOM POSITIONS IN THE SUBCELL^a

Sites	x	y	z	B (\AA^2)
La				
{ Sr	4(e)	0	0	0.357 ± 0.001
Cu	2(a)	0	0	0.85
O_I	4(e)	0	0	0.168 ± 0.002
O_{II}	4(c)	0	0.5	1.68
				4.25

^a $a = 3.760 \text{ \AA}$; $c = 12.94 \text{ \AA}$.

TABLE IV
 $\text{La}_{0.8}\text{Sr}_{1.2}\text{CuO}_{3.4}$: OBSERVED AND
 CALCULATED INTENSITIES FOR ATOMIC
 POSITIONS OF TABLE III^a

$h \ k \ l$	I_{obs}	I_{calc}
0 0 2	4.0	4.0
1 0 1	13.0	15.1
0 0 4	17.0	16.9
1 0 3	164.0	156.1
1 1 0	114.0	115.1
1 1 2	0.1	1.7
0 0 6	29.0	23.6
1 0 5	27.0	23.5
1 1 4	35.0	34.6
2 0 0	44.0	49.8
2 0 2	0.1	0.4
1 1 6	26.0	25.2
2 1 1	3.9	3.8
1 0 7	12.0	11.1
2 0 4	10.3	8.2
0 0 8	6.6	5.3
2 1 3	48.0	48.1
2 0 6	15.8	18.1
2 1 5	8.1	9.4
1 1 8	9.0	7.5
1 0 9	0.1	1.7
2 2 0	9.0	12.4
2 2 2	0.1	0.1
0 0 10	0.1	0.8
3 0 1	0.1	0.7
2 1 7	6.0	7.0
2 2 4	3.3	3.0
2 0 8	7.6	6.9
3 0 3	7.0	8.8

^a Subcell, space group $I4/mmm$; $R = 0.081$.

the ideal structure concerns the existence of vacancies located in the same plane as the copper atoms (Fig. 2). Moreover, the high B value for oxygen of O_1 sites (4.2 \AA^2) suggests that in this plane oxygen and vacancies were ordered.

Calculations in the actual cell in space group $I4/m$, were undertaken with 136 possible reflections, including superstructure reflections. Using the position and distributions determined from the subcell, the R factor increased to 0.104, showing, of course, a weak contribution of the superstructure reflections to the R value. The

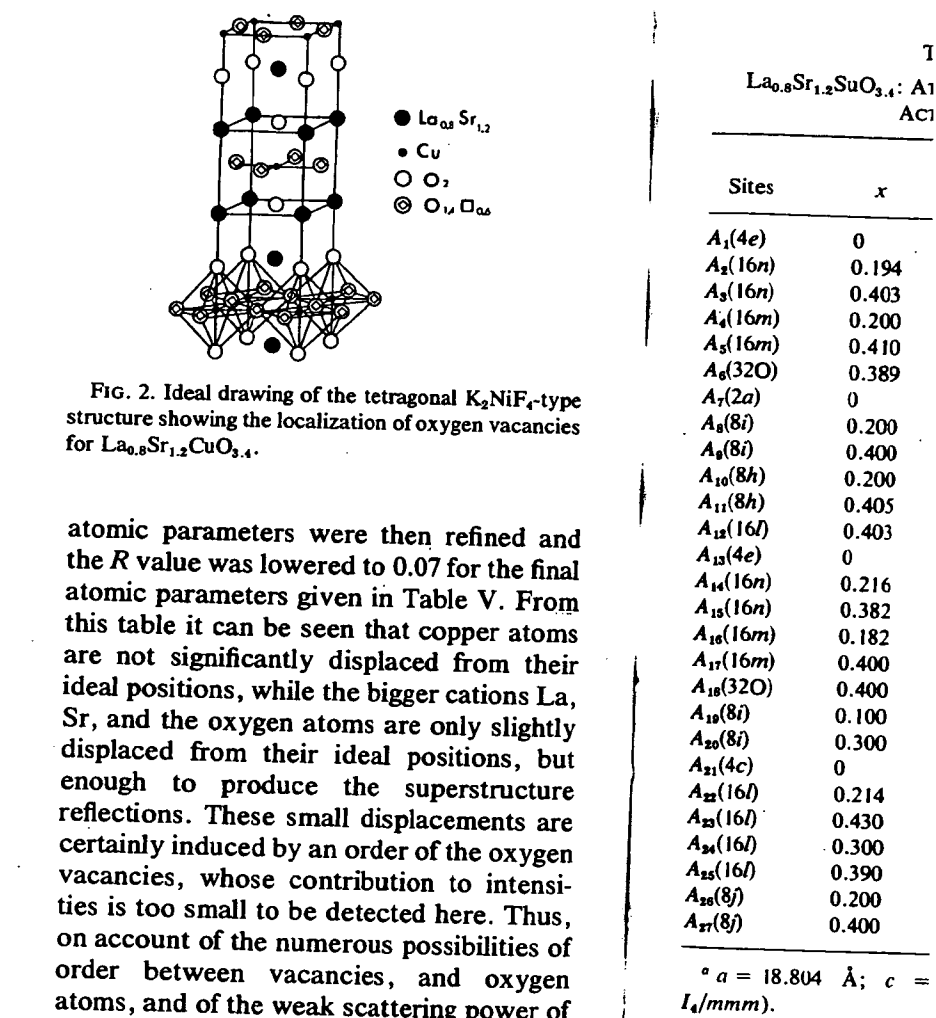


FIG. 2. Ideal drawing of the tetragonal K_2NiF_4 -type structure showing the localization of oxygen vacancies for $\text{La}_{0.8}\text{Sr}_{1.2}\text{CuO}_{3.4}$.

atomic parameters were then refined and the R value was lowered to 0.07 for the final atomic parameters given in Table V. From this table it can be seen that copper atoms are not significantly displaced from their ideal positions, while the bigger cations La, Sr, and the oxygen atoms are only slightly displaced from their ideal positions, but enough to produce the superstructure reflections. These small displacements are certainly induced by an order of the oxygen vacancies, whose contribution to intensities is too small to be detected here. Thus, on account of the numerous possibilities of order between vacancies, and oxygen atoms, and of the weak scattering power of these atoms, we did not try any hypothesis of distribution. Nevertheless, the very likely ordering of vacancies in the "copper plane," should also involve an ordering of lanthanum and strontium over the different sites. Refining the occupancy factors of La and Sr, led to an R value of 0.064 which is not very significant due to the weak contribution of La and Sr to the superstructure reflexions; a preferential occupation of the different sites is, however, likely: A_1 , A_4 , and A_5 would only be occupied by strontium, while lanthanum would occupy 90% of A_6 sites, the remaining strontium and lanthanum atoms being located statistically over the A_2 and A_3 sites.

Discussion

The stabilization, Cu(III) by only heating worthy of note. But characteristic of this existence of a Cu(III) ($x < 1$) which lies regions ($x = 0$ and x strongly related one to be explained by two competitive: the stoichiometric $K_2Ni_3La_2CuO_4$ and LaSrCu_3 form a related defect:

TABLE V
 $La_{0.6}Sr_{1.4}CuO_{3.4}$: ATOMIC PARAMETERS OF THE
 ACTUAL CELL^a

Sites	<i>x</i>	<i>y</i>	<i>z</i>	<i>B</i> (\AA^2)
$A_1(4e)$	0	0	0.347	0.35
$A_2(16n)$	0.194	0	0.359	1.00
$A_3(16n)$	0.403	0	0.356	0.39
$A_4(16m)$	0.200	0.200	0.357	0.32
$A_5(16m)$	0.410	0.410	0.358	1.00
$A_6(32O)$	0.389	0.192	0.357	0.86
$A_7(2a)$	0	0	0	0.80
$A_8(8i)$	0.200	0	0	0.51
$A_9(8i)$	0.400	0	0	0.43
$A_{10}(8h)$	0.200	0.200	0	0.31
$A_{11}(8h)$	0.405	0.405	0	1.00
$A_{12}(16l)$	0.403	0.205	0	0.37
$A_{13}(4e)$	0	0	0.168	1.00
$A_{14}(16n)$	0.216	0	0.168	1.00
$A_{15}(16n)$	0.382	0	0.168	1.00
$A_{16}(16m)$	0.182	0.182	0.172	1.00
$A_{17}(16m)$	0.400	0.400	0.168	1.00
$A_{18}(32O)$	0.400	0.202	0.163	1.00
$A_{19}(8i)$	0.100	0	0	1.00
$A_{20}(8i)$	0.300	0	0	1.00
$A_{21}(4c)$	0	0.500	0	1.00
$A_{22}(16l)$	0.214	0.100	0	1.00
$A_{23}(16l)$	0.430	0.100	0	1.00
$A_{24}(16l)$	0.300	0.200	0	1.00
$A_{25}(16l)$	0.390	0.310	0	1.00
$A_{26}(8j)$	0.200	0.500	0	1.00
$A_{27}(8j)$	0.400	0.500	0	1.00

^a $a = 18.804 \text{ \AA}$; $c = 12.941 \text{ \AA}$ (space group I_{4}/mm).

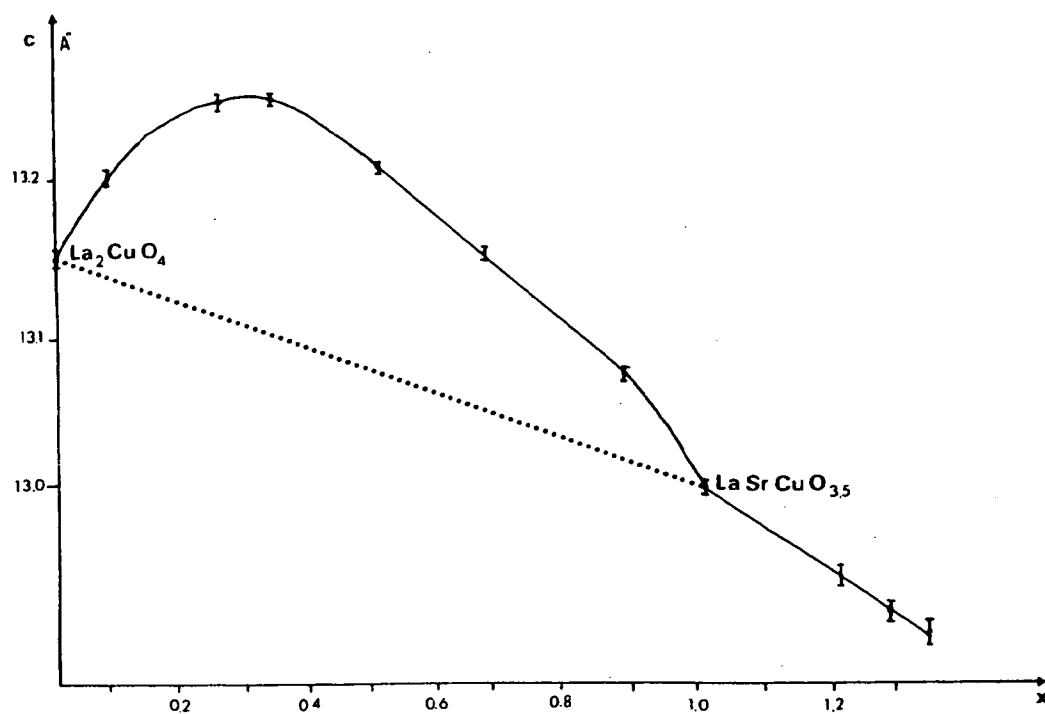
Discussion

The stabilization, in this system, of Cu(III) by only heating the oxides in air is worthy of note. But the most important characteristic of this system concerns the existence of a Cu(III) composition range ($0 < x < 1$) which lies between two Cu(II) regions ($x = 0$ and $x \geq 1$), for structures strongly related one to the other. This can be explained by two opposite effects which are competitive: the trend to preserve a stoichiometric K_2NiF_4 structure as for La_2CuO_4 and $LaSrCuO_4$ and the trend to form a related defect structure but with an

ordering of the oxygen vacancies. Thus, rather close to the stoichiometric compound La_2CuO_4 ($x < 1$), the trend to stoichiometry is favored and the vacancies formed from the nominal compositions involving only Cu(II) are partly balanced by the oxidation of Cu(II) to Cu III. For $x \geq 1$, i.e., rather far from stoichiometry, the La_2CuO_4 or " $LaSrCuO_4$ " stoichiometric compounds cannot be stabilized any more and orderings of the oxygen vacancies appear leading to different microphases as observed from the electron diffraction study, favoring Cu(II) with smaller coordinations (2, 5).

Structure is not, of course, the only factor governing the relative stability of Cu(II) and Cu(III) in these oxides. Kinetics play an important part for determining the ratio Cu(III)/Cu(II) in the richer Cu(III) oxides. For $0 < x < 1$, we have indeed noticed that the pure compounds could only be synthesized by heating at least 12 hr at the formation temperature (Table I) in order to ensure a good crystallization. Annealing the same samples at the same temperature, during longer periods (24 hr) allows us to prepare pure phases with the same structure, but with greater amount of Cu(III). The oxygen pressure will also influence the Cu(III)/Cu(II) ratios. Heating, for example, some Cu(III) samples at low temperature under vacuum, involves a decrease of Cu(III) amount without destroying the structure. In the same way, a reaction under oxygen allows us to increase the Cu(III) amount.

The influence of the Cu(III) amount can also be detected by considering the structural evolution, especially the *c* parameter, of these compounds as a function of composition (Fig. 3). This evolution is rather complex and quite different from that usually observed for single solid solutions. The substitution of strontium for lanthanum, should not affect this evolution, due to the similar sizes of these cations. It seems interesting to take the Cu(II) compounds as

FIG. 3. Evolution of the "c" parameter as a function of x .

a reference (dotted lines). Although we have only our compositions for comparison it can be seen that from $\text{La}_2\text{Cu}^{\text{II}}\text{O}_4$ to $\text{La}_{0.7}\text{Sr}_{1.3}\text{Cu}^{\text{II}}\text{O}_{3.35}$, a continuous decrease of a and c parameters could be foreseen for all Cu(II) compounds, as x increases, in agreement with the increase of oxygen vacancies. This evolution is not linear, probably due to ordering of the vacancies observed for different compositions. What is worthy of note is the large deviation from this law observed for the only compounds containing Cu(III) (continuous line): the c parameter is greater than that obtained from the "reference line" corresponding to the presence of Cu(II) only, while the a parameter is smaller. Moreover, the largest deviations are observed for $x = 0.33$ which corresponds to the maximum value of δ ($\delta = 0.119$), i.e., for the greatest amount of Cu(III). It can thus be observed that the c/a

ratio increases with the Cu(III)/Cu(II) ratio in agreement with the observations previously made by Goodenough *et al.* (3). Attempts to modify the a and c parameters for $x = 0.16$ and 0.5 , were successful: heating these compounds under vacuum at 500°C led to a decrease of c and a slight increase of a , while a decrease of the Cu(III)/Cu(II) ratio was confirmed.

Conclusion

The stabilization of a great number of oxygen vacancies in the K_2NiF_4 -type structure has been shown. It is easily explained by the ability of copper to show square and square-pyramidal coordinations. During the synthesis in air, two phenomena are competitive: the substitution of Cu^{3+} for Cu^{2+} , and ordering of oxygen and vacancies involving the existence of microphases.

The influence of the oxygen vacancies formation of these structures will be investigated. The relations between the properties and the structure will be studied.

References

- J. M. LONGO AND P. M. J. GOODENOUGH, *J. Solid State Chem.* **6**, 526 (1973).

The influence of the oxygen pressure on the formation of these structures will be investigated. The relations between the electrical properties and the structure of these oxides will be studied.

References

1. J. M. LONGO AND P. M. RACCAH, *J. Solid State Chem.* **6**, 526 (1973).
2. B. GRANDE, H. K. MÜLLER-BUSCHBAUM, AND M. SCHWEIZER, *Z. Anorg. Allg. Chem.* **428**, 120 (1977).
3. J. B. GOODENOUGH, G. DEMAZEAU, M. POUCHARD, AND P. HAGENMULLER, *J. Solid State Chem.* **8**, 325 (1973).
4. N. NGUYEN, L. ER-RAKHO, C. MICHEL, J. CHOISNET, AND B. RAVEAU, *Mater. Res. Bull.* **15**, 891 (1980).
5. S. N. RUDDLESDEN AND P. POPPER, *Acta Crystallogr.* **11**, 54 (1958).
6. C. H. R. L. TESKE AND H. K. MÜLLER-BUSCHBAUM, *Z. Anorg. Allg. Chem.* **371**, 325 (1969).

(II) ratio
; previous
(3). At
ters for
heating
t 500°C
increase
/Cu(II)

nber of
e struc-
plained
are and
During
ena are
 Cu^{3+} for
cancies
phases.

BRIEF ATTACHMENT G

IN THE UNITED STATES PATENT AND TRADEMARK OFFICE

In re Patent Application of

Applicants: Bednorz et al.

Serial No.: 08/479,810

Filed: June 7, 1995

For: NEW SUPERCONDUCTIVE COMPOUNDS HAVING HIGH TRANSITION
TEMPERATURE, METHODS FOR THEIR USE AND PREPARATION

Date: March 1, 2005

Docket: YO987-074BZ

Group Art Unit: 1751

Examiner: M. Kopecky

Commissioner for Patents
P.O. Box 1450
Alexandria, VA 22313-1450

FIRST SUPPLEMENTAL AMENDMENT

Sir:

In response to the Office Action dated July 28, 2004, please consider the
following:

ATTACHMENT G

THE OXYGEN DEFECT PEROVSKITE $\text{BaLa}_4\text{Cu}_5\text{O}_{13.4}$. A METALLIC CONDUCTOR

C. Michel, L. Er-Rakho and B. Raveau
Laboratoire de Cristallographie, Chimie et Physique des Solides, U.A. 251
ISMRa-Université de Caen, 14032 Caen Cedex, France

(Received March 14, 1985; Refereed)

ABSTRACT

A new oxygen defect perovskite $\text{BaLa}_4\text{Cu}_5\text{O}_{13.4}$, characterized by a mixed valence of copper has been isolated ; the parameters of the tetragonal cell are closely related to that of the cubic perovskite: $a = 8.644(4) \text{ \AA} = a_p \sqrt{3}$ and $c = 3.867(3) \text{ \AA} = a_p$. The X-ray diffraction study shows that the atoms are displaced from their ideal positions in the cubic cell, owing to the presence of ordered oxygen vacancies. The study of conductivity, magnetic susceptibility and thermoelectric power versus temperature shows that this oxide is a very good metallic conductor.

INTRODUCTION

Oxygen defect perovskites, have been more extensively studied these last years owing to their potential applications in catalysis, electrocatalysis or as gauges (1-3). In this respect mixed valence copper oxides offer a wide field for investigation : several perovskites (4) or perovskite-related structures have been isolated (5-6). These materials in which copper takes several coordinations simultaneously and a valence state intermediate between II and III can intercalate large amounts of oxygen according to the oxygen pressure and the temperature. Their electron transport properties ranging from semi-conductive to metallic (7) are closely correlated to the amount of intercalated oxygen.

The present paper deals with a new oxygen defect perovskite $\text{BaLa}_4\text{Cu}_5\text{O}_{13.4}$, which is like $\text{La}_2\text{Ba}_3\text{Cu}_6\text{O}_{14+\delta}$ (4) a mixed valence copper oxide but whose behavior is quite different.

EXPERIMENTAL

Synthesis

Samples were prepared in platinum crucible and in air from appropriate mixtures of dried oxides La_2O_3 , CuO and carbonate BaCO_3 . The mixtures were first heated a few hours at 900°C , ground and heated at 1000°C during several hours. They were then ground again, and mixed with an organic binder, compressed into bars and then slowly heated up to 1000°C . After 24 hours or more at 1000°C , the bars were finally quenched to room temperature. The use of a binder was necessary to avoid that the compressed bars break before

heating. In these conditions the compactness of bars was of about 80 %.

Chemical analysis

In order to determine the oxidation state of the transition metal ions, chemical analysis were carried out by iodometric titration using KI and by reduction in a flow of 25 % hydrogen in argon up to about 1000°C using a SETARAM microbalance for weight loss measurements.

Structural analysis

The cell parameters were determined from X-ray powder diffractograms registered with a Philips goniometer using Cu $K\alpha$ radiation. The space group was determined by electron diffraction using a JEOL 120CX electron microscope.

Magnetic and electrical measurements

The magnetic susceptibility was measured on powders by the Faraday method in the range 80-300K using a Cahn RG microbalance.

The conductivity was measured by the four points method on sintered bars. It was calculated by measuring the intensity/voltage ratio between the points in each current circulation direction in order to minimise the dissymmetry effect between the contacts. The Seebeck coefficient was measured on the same sintered bars held between two Pt heads.

Measurements were carried out up to 600K under an helium pressure of 200 mbars for T < 290K and in air for T > 290K in order to avoid possible departure of oxygen.

RESULTS AND DISCUSSION

The scanning of the system La₂O₃-BaO-CuO for the compositions corresponding to the molar ratio (La + Ba)/Cu = 1 allowed us to isolate a perovskite for La/Ba = 4. The X-ray diffraction pattern of this compound presents besides the intense lines which can be indexed in a cubic perovskite cell, extra lines which are rather weak. This feature is confirmed by the electron diffraction study, which shows superstructure reflections, leading to a tetragonal cell whose parameters are related to the cubic perovskite subcell (a_p) as follows :

$$a = a_p \sqrt{5} \quad c = a_p$$

all the lines of the X-ray diffraction patterns can be then indexed with accuracy in the tetragonal system with $a = 8.644(4)$ Å and $c = 3.867(3)$ Å. No reflection conditions are observed. The analysis of the oxygen content leads to the formulation BaLa₄Cu₅O_{13.4} involving the presence simultaneously of Cu(II) and Cu(III) in spite of the presence of numerous oxygen vacancies (10.7%). The measure of the density by pycnometry in benzene at 25°C ($d_{exp} = 7.05$) confirms this composition for one mole per cell ($d_{calc} = 7.03$). Thus it appears that the oxide BaLa₄Cu_{11.2}Cu_{III}_{2.80}O_{13.4} 1.6 exhibits a great similarity with the oxygen defect perovskite BaLa₃Cu_{15.25}Cu_{III}₁₊₂₈O_{14.6} previously described. However, this compound is very different from BaLa₃Cu₆O_{14.6}, from the point of view of the oxygen intercalation : no intercalation or desintercalation of oxygen has been observed by annealing this phase at low temperature (400°C to 500°C) and under different oxygen pressures up to 1 bar contrary to Ba₃La₃Cu₆O_{14.6}. In the same way, no oxygen loss has been observed by TGA measurements for temperatures up to 650, 750 and 850°C and under oxygen pressures of 0.02, 0.2 and 1 bar respectively.

Taking into account the fact that the fundamental lines are indexed in a cubic perovskite cell and are strong with respect to the superstructure lines it was interesting to determine whether the metallic atoms were displaced from their ideal positions in the perovskite, or if the superstructure lines

Vol.

were small but
stud posi
spac
king were
from Phkl angle
ideal of t
R = f
B(O)
from ties
(Tabl
from oxyge
0.083
1 Å².
veral

Atom
the s

in thi
rather
ction

1.6 1C
ty p v
ty fro
(Y = 4

of tem.

80 %.

metal ions,
I and by re-
ing a SETARAM

ctograms
pace group
microscope.

Faraday me-

intered bars.
the points
symmetry ef-
a the same

ssure of
ossible de-

s correspon-
erovskite
esents be-
cell, extra
tron dif-
o a tetra-
bcell (a_p)

then
and c =
of the oxy-
resence
umerous oxy-
in benzene
11 (d_{calc} -
1.6 exhibits
Cu^{III} 1+26.046
on : no inter-
ing this ph-
pressures up
oss has been
50°C and

indexed in a
cture lines
displaced
ture lines

were only due to the ordering of oxygen vacancies. However, owing to the small amount of oxygen vacancies it was not likely to determine the distribution of the oxygen atoms by X-ray powder diffraction. Thus the structural study was undertaken for the composition $\text{La}_4\text{BaCu}_5\text{O}_{15}$ just to determine the positions of the atoms with respect to the cubic perovskite subcell. Eight space groups were possible, they were reduced to three P4, P4 and P4/m taking into account the analogy with the perovskite structure. Calculations were carried out in the most symmetrical space group P4/m. For a ranging from 0 to 48° , 37 peaks i.e. 84 hkl were registered. The disparity between F_{hkl} and F hkl led us to introduce 139 hkl in the calculations. In the same angle range 13 diffraction peaks (14 hkl) were indexed in the cubic perovskite cell with $a = 3.867 \text{ \AA}$, and used in a calculation with the atoms in the ideal positions of the cubic perovskite cell, involving only a refinement of the thermal factors B; this first refinement led to a discrepancy factor, $R = E|I_{\text{obs}} - I_{\text{calc}}|/E|I_{\text{obs}}$, of 0.066 with $B(\text{La}, \text{Ba}) = 1.2 \text{ \AA}^2$, $B(\text{Cu}) = 2.6 \text{ \AA}^2$, $B(O) = 3.9 \text{ \AA}^2$. The high B values let us think that the atoms were displaced from their ideal positions. A calculation carried out with all the intensities in the P4/m space group and the same ideal positions and overall $B = 1 \text{ \AA}^2$ (Table 1a), led to $R = 0.35$ in agreement with this point of view. Starting from these ideal positions, and assuming a statistical distribution of the oxygen vacancies in the oxides $\text{BaLa}_4\text{Cu}_5\text{O}_{13.4}$, the R factor was lowered to 0.083, by refinement of the atomic parameters, the B factor being fixed at 1 \AA^2 . From the final atomic parameters (Table 1.b) it can be seen that several atoms are displaced from their ideal positions in the cubic perovskite.

TABLE I

Atomic Parameters of $\text{BaLa}_4\text{Cu}_5\text{O}_{13.4}$ (a) ideal positions (b) after refinement in the space group P4/m

Atom	Site	(a)			(b)		
		X	Y	Z	X	Y	Z
Ba, La	1(d)	0.5	0.5	0.5	0.5	0.5	0.5
Ba, La	4(k)	0.1	0.3	0.5	0.124(1)	0.277(1)	0.5
Cu	1(a)	0.0	0.0	0.0	0.0	0.0	0.0
Cu	4(j)	0.4	0.2	0.0	0.415(3)	0.168(2)	0.0
O	1(b)	0.0	0.0	0.5	0.0	0.0	0.5
O	2(e)	0.0	0.5	0.0	0.0	0.5	0.0
O	4(j)	0.3	0.4	0.0	0.261(7)	0.384(8)	0.0
O	4(j)	0.2	0.1	0.0	0.229(8)	0.063(6)	0.0
O	4(k)	0.4	0.2	0.5	0.428(10)	0.155(6)	0.5

Further refinements, concerning the ordered distribution of oxygen in this structure, which is most probable, were not carried out due to the rather low content of oxygen vacancies, and the too small number of reflections.

This oxide is a very good conductor: its conductivity is about $1.6 \cdot 10^3 (\Omega \text{ cm})^{-1}$ at room temperature. Figure 1 which represents the resistivity ρ versus temperature, shows that this oxide exhibits a metallic conductivity from 200 to 600K. The γ value deduced from the equation $\rho = \rho_0(1+\gamma t)$ ($\gamma = 4.1 \cdot 10^{-3} \text{ K}^{-1}$) is very close to that of free electrons ($\gamma = 3.7 \cdot 10^{-3} \text{ K}^{-1}$).

The molar magnetic susceptibility is very weak and nearly independent of temperature. This suggests a Pauli paramagnetism which is characteris-

shows
ratio
Seebe
is mo

tron
of th
preta

- 1.
- 2.
- 3.
- 4.
- 5.
- 6.
- 7.
- 8.
- 9.
- 10.

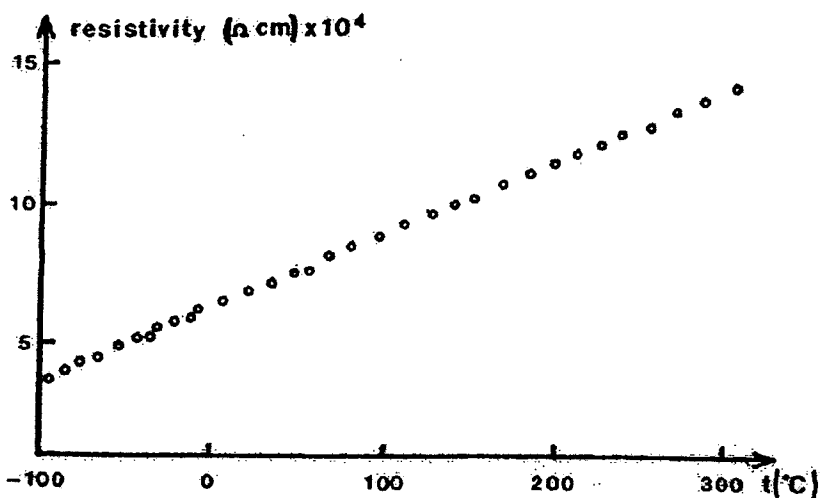


FIG. 1

Resistivity plotted as a function of temperature

tic of delocalized carriers. The Pauli susceptibility (8) calculated with $m^*/m = 1$ and for one carrier per Cu(III) ($\chi_M = 5.3 \cdot 10^{-5}$ e.m.u) is however one order of magnitude lower than the experimental value : $\chi_M = 6 \cdot 10^{-4}$ e.m.u. The increasing of the Pauli susceptibility up to the experimental value needs $m^*/m = 10$. This suggests a strongly correlated carriers gas (degenerated spin polaron gaz) which was introduced by Mott (9) to explain the magnetic susceptibility of LaCuO_3 and LaNiO_3 which are metals (10). At room temperature, the Seebeck coefficient is also very weak and positive ($\alpha = 9 \mu\text{VK}^{-1}$) and increases slightly with temperature ($\alpha_{500K} = 18 \mu\text{VK}^{-1}$) (Fig. 2). This

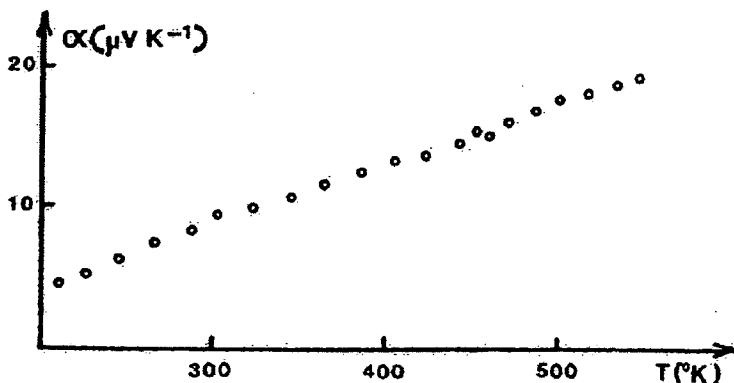


FIG. 2

Evolution of the thermoelectric power as a function of absolute temperature.

This

Nat. Res. Bull., 8, 647 (1973).

2

perature.

BRIEF ATTACHMENT H

IN THE UNITED STATES PATENT AND TRADEMARK OFFICE

In re Patent Application of
Applicants: Bednorz et al.
Serial No.: 08/479,810
Filed: June 7, 1995

For: NEW SUPERCONDUCTIVE COMPOUNDS HAVING HIGH TRANSITION
TEMPERATURE, METHODS FOR THEIR USE AND PREPARATION

Date: March 1, 2005
Docket: YO987-074BZ
Group Art Unit: 1751
Examiner: M. Kopecky

Commissioner for Patents
P.O. Box 1450
Alexandria, VA 22313-1450

FIRST SUPPLEMENTAL AMENDMENT

Sir:

In response to the Office Action dated July 28, 2004, please consider the
following:

ATTACHMENT H

REVUE DE CHIMIE MINÉRALE

Avec la collaboration de :

- ANIEL J. (Paris)
 ARMAND H. (Génève)
 AUBIN R. (Paris)
 BAPTILLETT N. (Berkeley)
 BERNARD J. (Paris)
 BERNARD L. (Berkeley)
 BERTAUT E. P. (Orsay)
 BESSETON J. (Orsay)
 BIVIAN D. J. M. (Belfast, Australie)
 BONHOMME R. (Orsay)
 BRONCHER W. (Aachen)
 BRUNCK-WAGNER J. H. (Tampa)
 CHANG T. L. (Bellinzona, Palerme)
 CHEK M. (Paris)
 COHEN-NADAR E. (Paris)
 COTTON P. A. (Cambridge, & M. University)
 COUSSEINS J. C. (Chamonix, Perrigny)
 DESCHAMPS A. (Cahn)
 DUNCAN J. P. (Wellington, New Zealand)
 FREUNDLICH W. (Paris)
 FUREKI K. (Tokyo)
 GALLAIS P. (Toulouse)
 GAMBLE P. A. (London, London)
 GIQUIERE P. A. (Québec, Québec)
 GILLIBRIDE R. J. (Hamilton, Ontario)
 GONZALEZ-QUIRK C. A. P. (Sewell)
 GOODENOUGH A. B. (Oxford)
 GRÖNYOULD B. (Oxford)
 GUTMANN V. (Wiesbaden)
 HABER J. (Krakow)
 HAENBWALD P. (Bernau)
 HANNAH N. B. (Bell Law, Murray Hill)
 HARALDEN H. (Oslo-Bislett)
 HEROLD A. (Nürnberg)
 HEUBEL J. (Lille)

Table des matières

HOIZZBERG P. (U. N. M., New York)	HOOPS R. (Glasgow)	HOGG R. (Paris)	HOGGEN R. A. (Stanford)	HURE J. (Commissariat à l'Energie Atomique)	JELLINEK F. (Chicago)	KLEMML W. (Münster in Westfalen)	KOLDITZ L. (Berlin)	LANG J. (Genève)	LARBIYNS J. (Paris)	MAURIN M. (Grenoble)	OSKAM A. (Amsterdam)	PALCZOWSKA W. (Warszawa)	POUCHARD M. (Bruxelles)	RABENAU A. (Stuttgart)	RAO C. N. R. (Bangalore)	REID A. F. (C. S. I. R. O., Port Melbourne)	ROUXEL J. (Paris)	SAUTO N. (Globe University)	SERRATOSA J. M. (Madrid)	SHUL'Z M. (Gomel'sk)	SIMON A. (Stuttgart)	SILIGHT A. Y. (Du Pont de Nemours Wilmington)	SPITZER V. (Meudon)	TAI A. P. (Nashua)	TAKIS S. (Kouki)	TARTI P. (Lille)	VILČEK A. (Prague)	WEIGER W. (Berlin)	WYATT J. (Prest)	ZOUETTE M. (Paris)
Sous la direction de A. CHARTEEN																														
Secrétaire Général : P. SILBER	Université Pierre-et-Marie-Curie — Chimie Minérale — Tour 44, 4, Place Jussieu, 75230 PARIS — CBDEX 05	Relations with Foreign Countries : P. HAGBNMULLER Directeur du Laboratoire de Chimie du solide du C.N.R.S. 351, cours de la Libération, 33405 TALENCE Cedex	C. D. R. — Centrale des Revues 11, rue Gossiaq, 92543 Montrouge Cedex, France. Tel. 6346-52-66	6 numéros par an — 6 issues a year — 6 Hefts pro Jahr	Parution : 10 mars, 10 mai, 10 juillet, 10 septembre, 10 novembre, 10 janvier	700 F																								
ABONNEMENTS — SUBSCRIPTIONS																														
C. D. R. — Centrale des Revues																														
11, rue Gossiaq, 92543 Montrouge Cedex, France. Tel. 6346-52-66																														
6 numéros par an — 6 issues a year — 6 Hefts pro Jahr																														
Parution : 10 mars, 10 mai, 10 juillet, 10 septembre, 10 novembre, 10 janvier																														
Taux d'abonnement annuel																														
Annual Subscription (including postage)																														
Jahresbezugspreis (inklusive Postage)																														
Envoy d'un spécimen sur simple demande. Specimen copy gratis upon request																														
The appearance of the code at the bottom or the first page of an article in this journal indicates the copyright owner's consent that copies of the article may be made for personal or internal use, or the personal or internal use of specific clients. This consent is given on the condition, however, that the article is not resold, nor is the same put into general circulation. Clearance Center, 27 Congress Street, Salem, Mass. 01970 U.S.A. (for non-members). For other users, permission to photocopy must be sought from the publisher. The present document contains no statement in either form or substance which authorizes copying or reproduction by anyone. The right of personal copying is granted for internal or personal use, except as allowed by section 107 or 108 of the U.S. Copyright Law. This permit does not extend to other kinds of copying, such as copying for general distribution, for advertising or promotional purposes, for creating new collective works, or for resale.																														
REVUE DE CHIMIE MINÉRALE — TOME 21 — 1984 — N° 4																														

(Received November 30, 1983).

**Oxygen intercalation
in mixed valence copper oxides related
to the perovskites**

by

Claude MICHEL and Bernard RAVEAU

Equipe Oxydes du Laboratoire de Cristallographie,
Chimie et Physique des Solides, L. A. 231, ISMRA,
Université, 14032 Caen Cedex, France.

ABSTRACT. — Intercalation of oxygen in ternary copper oxides has been studied for three series of compounds: $Ba_2La_xCuO_{4+x}$, $La_{2-x}A_xCuO_{4-x}$ and $La_{2-x}A_xCuO_{4-x+y}$ ($A = Ca, Sr, Ba$). These mixed valence copper oxides, characterized by the presence of Cu^{II} and Cu^{IV} simultaneously are oxygen defect compounds whose structure is closely related to that of the perovskite, and to those of the two members of the intergrowths stoichiometries $SrTiO_3$ and K_2NiF_4 , respectively. The localization of the oxygen vacancies in (0 0 1) planes of these structures makes that two of these families: $Ba_2Ca_xCuO_{4+x}$ and $La_{2-x}A_xCu_xO_{4-x+y}$ can be considered in their most reduced state as oxides with low dimensionality. The influence of oxygen intercalation on this structure is discussed. The electrical properties of these phases are described and discussed: they are strongly influenced by the intercalation process. A progressive transition from a P type semi-conductive to a P type semi-metallic or metallic state is indeed observed which depends on the oxygen pressure and on the nature of the oxides.

Résumé. — L'intercalation d'oxygène dans les oxydes ternaires de cuivre a été étudiée pour trois séries de composés : $Ba_2La_xCuO_{4+x}$, $La_{2-x}A_xCuO_{4-x}$ et $La_{2-x}A_xCuO_{4-x+y}$ ($A = Ca, Sr, Ba$). Ces oxydes de cuivre à valence mixte, caractérisés par la présence simultanée de Cu^{II} et Cu^{IV}, sont des composés déficients en oxygène dont la structure est étroitement liée celle de la perovskite et à celles des deux membres de la série d'intergrowths $SrTiO_3$ et K_2NiF_4 . La localisation des lacunes anioniques dans les plans (0 0 1) de ces structures fait que deux de ces familles : $Ba_2Ca_xCuO_{4+x}$ et $La_{2-x}A_xCu_xO_{4-x+y}$ peuvent être considérées, dans leur état le plus réduit, comme des oxydes de basse dimensionnalité. L'influence de l'intercalation d'oxygène dans la structure est décrite. Les propriétés électriques de ces phases sont décrites et discutées : elles sont fortement influencées par le processus d'intercalation. Une transition progressive d'un état semi-conducteur de type P à un état semi-métallique ou métallique de même type, qui dépend de la pression d'oxygène et de la nature des oxydes, est en effet observée.

INTRODUCTION

Intercalation of oxygen in an oxide, by a simple reversible exchange with O_2 in air or in a gaseous atmosphere can be used for different applications such as electrocatalysis, or gauge for materials with electrical properties sensitive to the oxygen content. Thus it appears that such oxides must exhibit rather large oxygen defects in their « reduced » form, and must be able to absorb oxygen from atmosphere tending towards a stoichiometric phase in their « oxidized » state. This phenomenon supposes a reversible change of the oxidation state and of the coordination number of the metallic atoms which participate to the framework of the oxides. In this respect, copper oxides are very good candidates, owing to the ability of copper to take several coordinations—octahedral, square pyramidal, square planar—and several oxidation states: +1, +2, +3. Cu(II) and Cu(III) must be especially considered owing to their possibility to take the same octahedral coordination in similar structures as shown from previous works on $La_2Cu^{\text{II}}O_4$ [1-2] and $LaSrCu^{\text{II}}O_4$ [3], which are isostructural with $X_2Ni^{\text{II}}P_4$. Ternary oxides $A_xCu^{\text{II}}O_3$ containing Cu(III) are more difficult to prepare than those with Cu(II), since oxygen pressures ranging from 1 bar [4-7] to several kbars [3-8] are most of the time necessary to synthesize these compounds. However, the presence of A elements like bismuth favours the formation of Cu(III) in normal pressure conditions [9-10]. The present paper deals with the soft intercalation of oxygen, i. e. at low pressure ($P \leq 1$ atm) and at low temperature ($T \sim 400-500^\circ\text{C}$) in three series of ternary copper oxides related to the perovskite [11-13] and belonging to the systems $La_xO_3-AxO-CuO$ with A = Ca, Sr, Ba. The influence of oxygen intercalation on the electron transport properties of these phases are discussed.

STRUCTURAL CONSIDERATIONS

Three families with an oxygen defect structure have been isolated in the systems $La_2O_3-AxO-CuO$:

— The oxygen defect perovskites $La_xBa_xCu_4O_{4+x}$.

— The oxygen defect intergrowths $Sr_xTi_xO_7$ type,

— The most reduced form which has been isolated for the defect perovskites $La_xBa_xCu_4O_{4+x}$, corresponds to the formulation $La_3Ba_3Cu_4O_{14}$. It is

structure (Fig. 1) can be described as an ordered oxygen defect perovskite. All the metallo sites corresponding to the stoichiometric perovskite are occupied by copper ions and lanthanum and barium ions respectively, whereas only 7/9 of the anionic sites are occupied in an ordered manner.

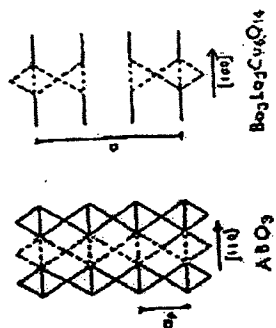


Fig. 1.—Schematic structure of a stoichiometric AB_2O_3 perovskite and the defect oxygen perovskite $Ba_2La_3Cu_4O_{14}$.

Considering the tetragonal cell of this compound ($a \approx c/\sqrt{2} = 5.525$ Å, $c \approx 3a_0 = 11.721$ Å), it can indeed be seen that the basal planes of the octahedra, parallel to (010) are preserved, that one apex out of two is missing at the levels $z = 1/6$ and $5/6$, whereas all the apices of these octahedra are missing at $z = 1/2$. It results that this reduced form can be considered as a true layer structure: double defect perovskite layers $[Ba_1.5La_0.5Cu_3O_7]$ built up from corner-sharing octahedra CuO_6 square pyramids CuO_5 and square groups CuO_4 , are observed whose cohesion is ensured by lanthanum ions located at $z = 1/2$. It is remarkable that such an oxide is characterized by a high Cu(II) content in spite of the high oxygen deficit content. Site potential calculations confirm that the Cu²⁺ ions are located preferentially on the octahedral sites. It must also be noted that this limit compound has not really been synthesized. By heating in air at 1 000°C for 24 h the mixture of La_2O_3 , CuO and $BaCO_3$ and quenching the samples at room-temperature a slight excess of oxygen is indeed observed corresponding to the formulation $La_3Ba_3Cu_4O_{14.10}$. The most reduced phase $La_3Ba_3Cu_4O_{14.03}$ is then synthesized by annealing the sample $La_3Ba_3Cu_4O_{14.10}$ at 400°C under low oxygen pressure ($\sim 5 \cdot 10^{-3}$ bar) during several hours.

The deviation from stoichiometry in the oxides $La_{2-x}A_xCu_4O_{6-x/2+2x}$ is more complex owing to the possibility of substitution of calcium or strontium for lanthanum, in a small homogeneity range ($0 \leq x \leq 0.14$ for

stays at constant structure

strontium and $x = 0.10$ for calcium). The most reduced oxide which has been isolated in this family corresponds to the formulation $\text{La}_2\text{Sr}_x\text{Cu}_2\text{O}_6$, $11 \times$ tetragonal cell ($a = 1.865 \text{ \AA}$, $c = 19.887 \text{ \AA}$), corresponds to a structure closely related to that of $\text{Sr}_2\text{Ti}_2\text{O}_7$ (fig. 2 a). Cu^{2+} ions are indeed located on the Ti^{4+} sites, La^{3+} and Sr^{2+} ions are located on the Sr^{2+} sites, whereas six anionic sites out of seven are occupied by oxygen in an ordered manner; thus, this oxide can be considered as an intergrowth of double oxygen perovskite layers and SrCO_3 type layers. The perovskite layers exhibit some similarity with those observed for $\text{La}_2\text{Ba}_3\text{Cu}_6\text{O}_{14}$: the basal planes of the octahedra parallel to $(0 \cdot 0 \cdot 1)$ are also preserved whereas at $z = 0$ and $z = 1/2$ all the apices of the oxygen octahedra are missing. However, the resulting configuration of the framework is different from $\text{La}_3\text{Ba}_5\text{Cu}_6\text{O}_{14}$. $\text{Cu}(II)$ exhibits here only one coordination which is square pyramidal. Nevertheless this oxide, like $\text{La}_3\text{Ba}_5\text{Cu}_6\text{O}_{14}$, must be considered as a structure with low dimensionality. It can indeed be described as built up from slabs $[\text{LaSrCu}_1\text{O}_6]_n$ parallel to $(0 \cdot 0 \cdot 1)$ whose cohesion is ensured by Sr^{2+} and La^{3+} ions located at $z = 0$ and $z = 1/2$. The $[\text{LaSrCu}_1\text{O}_6]_n$ slabs are themselves an intergrowth of SrO -type layers and corner-sharing square pyramid layers. Such slabs are in fact derived from the K_2NiF_4 structure: the latter corresponds indeed to the superposition of two $[\text{K}_2\text{Ni}_2\text{F}_6]_{10}$ slabs which would share the face of their square pyramids, forming NiF_6 octahedra (fig. 2 b). Like $\text{La}_2\text{Ba}_3\text{Cu}_6\text{O}_{14}$, $\text{La}_2\text{SrCu}_2\text{O}_6$ is

OXYGEN INTERCALATION IN COPPER OXIDES

characterized by a great stability in spite of its oxygen deficit structure: it is indeed synthesized by heating the stoichiometric mixture of CuO , La_2O_3 and SrCO_3 at $1050 \pm 100^\circ$ for 24 h in air and by quenching them at room temperature in order to avoid their oxidation at lower temperature. Contrary to $\text{La}_2\text{Ba}_3\text{Cu}_6\text{O}_{14}$, copper is in its lower oxidation state, $\text{Cu}(I)$ in this oxide.

The oxides $\text{La}_{2-x}\text{A}_x\text{CuO}_{4-\frac{2}{3}x+\frac{1}{3}}$ exhibit an oxygen deficit K_2NiF_4 type structure involving different coordinations of copper: octahedral, square pyramidal and eventually square planar (fig. 3). Their oxygen content

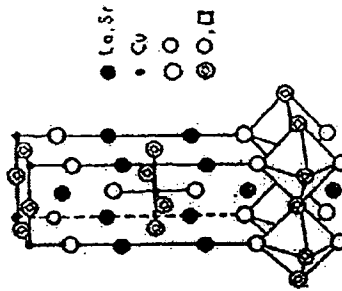


Fig. 3.—Perspective view of the structure of the oxides $\text{La}_{2-x}\text{SrxCuO}_{4-(1/3)x+(1/3)}$ with oxygen vacancies located in the basal plane of the octahedra.

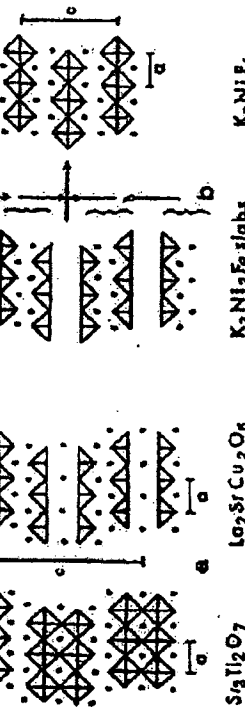


Fig. 2.

- a) Schematic structure of $\text{Sr}_2\text{Ti}_2\text{O}_7$ and $\text{La}_2\text{Sr}_2\text{Cu}_2\text{O}_8$ (projection on to $(1 \cdot 0 \cdot 0)$ plane), showing the oxygen vacancies.
- b) Schematic representation of $\text{K}_2\text{Ni}_2\text{F}_6$ plates sharing the surfaces of the NiF_6 pyramids to give the K_2NiF_4 structure.

TRANSACTIONS OF THE CERAMIC SOCIETY OF JAPAN

VOLUME 21 — 1984 — NO. 4

FEB 12, 1983 15:53
NMR : WISHTHINN RIBBLELLER
PHONE NO. : 301 595 9279
FEB. 12 2003 03:16PM PS
EBC 12 . 03 15:53

depends on the nature of the A ions ($A = \text{Ca}, \text{Sr}, \text{Ba}$) and on the substitution rate x which can lead to wide homogeneity range: $0 \leq x \leq 0.20$ for $A = \text{Ca}$ and $0 \leq x \leq 4/3$ for $A = \text{Sr}$. The most reduced phase which exhibits the highest deviation from stoichiometry has been synthesized in the case of strontium for $x = 4/3$: $\text{La}_{2-x}\text{Sr}_x\text{CuO}_3$.¹³ Contrary to the two other series, the oxygen vacancies are located in the basal plane of the octahedra which are parallel to the $(0 \cdot 0 \cdot 1)$ plane of the tetragonal cell ($a = 3.739 \text{ \AA}$, $c = 12.907 \text{ \AA}$). It must also be emphasized that this type of localization of the oxygen vacancies is always observed whatever the nature of the A ions, and whatever the rate of substitution x may be. However, symmetry changes and order-disorder phenomena in this plane may appear according to the nature of A and x value (table 1). So, the calcium and barium oxides are characterized by a monoclinic distortion of the tetragonal K_2NiF_4 structure, whatever the x value may be $0 \leq x \leq 0.20$; the same

series di creare niente

is true for the strontium compounds with $0 \leq x \leq 0.10$. Thus, the oxides corresponding to these homogeneity ranges exhibit an orthorhombic cell related to that of K_2NiF_4 in the following way: $a \approx b \approx aK_2NiF_4 \sqrt{2}/2$ and $c \approx cK_2NiF_4$.

TABLE I

The oxides $La_{1-x}A_xCuO_{4-\frac{1}{2}(x+1)}$: crystallographic data and analytical results (quenched materials).

	A	x	δ	a	b	c	Heating temperature °C
Ba	0	0.01	0.01	5.366	1.402	11.149	1,100
	0.1	0.02	0.02	5.361	1.380	11.201	1,100
	0.2	0.03	0.03	5.359	1.364	11.245	1,100
Cd	0.03	0.01	0.01	5.356	1.356	11.320	1,100
	0.1	0.02	0.02	5.351	1.387	11.150	1,100
	0.2	0.03	0.03	5.356	1.363	11.174	1,100
Sr	0.06	0.03	0.03	5.357	1.380	11.210	1,100
	0.16	0.04	0.04	5.351	1.368	11.200	1,000
	0.25	0.07	0.07	5.374	1.321	1,000	1,000
	0.13	0.11	0.11	5.375	1.326	11.247	1,000
	0.30	0.10	0.10	5.374	1.324	1,000	1,000
	0.46	0.075	0.075	5.375	1.320	1,000	1,000
	0.38	0.06	0.06	5.369	1.369	11.070	1,170
	1.0	0.05	0.05	5.361 ("")	1.362	11.002	1,200
	1.20	0.0	0.0	5 X 1.376	12.940	1,200	1,200
	1.33	0.0	0.0	5.375 ("")	12.907	1,200	1,200

(*) These a parameters are those of the tetragonal unitcell.

On the other hand, the strontium compounds exhibit a tetragonal symmetry similar to that of K_2NiF_4 or $LaSiCuO_4$ [3] for $0.10 < x < 1$ ($a \approx aK_2NiF_4$; $c \approx cK_2NiF_4$), whereas for $1 \leq x \leq 4/3$, superstructures appear on the electron diffraction patterns which involve tetragonal cells, with $a \approx b \approx aK_2NiF_4$, a ranging from 1 to 6 according to the composition, c remaining unchanged ($c \approx cK_2NiF_4$). These oxides are very stable in spite of the high deviation from stoichiometry; for instance $La_2Sr_xO_{4-\frac{1}{2}(x+1)}$ is prepared by heating a mixture of the compounds La_2O_3 , CuO and $SrCO_3$ at 1,200°C and quenching the phase at room temperature. It appears here that the most reduced phase exhibits also only $Cu(II)$ like $La_2SrCu_2O_6$ belonging to the second series. The oxides $La_{2-x}A_xCuO_{4-\frac{1}{2}(x+1)}$ appear very closely related to the second series formulated $La_{2-x}A_{x+\frac{1}{2}}Cu_xO_{6-\frac{1}{2}(x+1)}$ in that they can be considered as being respectively the members $n = 1$ and 2 of a series of "edges" of oxygen defect intergrowths between perovskites and

SrO structures, corresponding to the general formulation $A_{n+1}B_nO_{3n+1}$. However the behaviour of $La_{2-x}A_xCuO_{4-\frac{1}{2}(x+1)}$ is very different from the two other series in that it cannot be considered in its most reduced form as an oxide with low dimensionality.

OXYGEN INTERCALATION AND DEINTERCALATION: INFLUENCE ON THE STRUCTURE

Oxygen can be intercalated in these three series of oxides by simple annealing of the materials at low temperature, i. e. 400°C-500°C, under different oxygen pressures.

The oxygen defect perovskite $La_2Ba_2Cu_4O_{14.10}$ synthesized in air can absorb rather important oxygen amounts by annealing the samples at 400°C under oxygen pressure ranging from 10^{-2} to 1 bar as shown from table II. In the same way, oxygen can be desintercalated from the structure of $La_2Ba_2Cu_6O_{14.10}$ or from more oxidized compounds by simply annealing the samples always at 400°C under lower oxygen pressure, $5 \cdot 10^{-5}$ bar (table II). Thus it appears that the intercalated oxides $La_2Ba_2Cu_6O_{14.10}$

TABLE II

Evolution of δ as a function of the oxygen pressure after annealing the oxide $La_2Ba_2Cu_6O_{14.10}$ at 400°C.

P_O_2 (bar)	1.10^{-2}	10^{-1}	2.10^{-1}	5.10^{-1}	0.1	0.2	1
δ	0.03	0.19	0.25	0.31	0.33	0.37	0.43

exhibit a rather wide homogeneity range $0.05 \leq \delta \leq 0.43$. The intercalation of oxygen in this structure does not influence the cell parameters, since the most oxidized compound, $La_2Ba_2Cu_6O_{14.10}$, is characterized by parameters very similar to those of $La_2Ba_2Cu_6O_{14.10}$, $a = 5.529$ Å and $c = 11.729$ Å, whereas no parameter change with respect to the air synthesized oxide is observed when δ tends towards zero. It is of course not possible to localize the additional oxygen in the structure by X-ray diffraction; however site potential calculations [14], assuming that Cu^{2+} is octahedrally coordinated, show that this additional oxygen should be located between two square pyramids CuO_6 , i. e. at $z = 1/2$, between the layers described above, forming corner-sharing ribbons of CuO_6 octahedra running along c . The electron transport properties of these compounds, which will be discussed further, are in agreement with this hypothesis. The fact that

the c parameter does not vary, in spite of the intercalation of rather great amounts of oxygen is easily explained by the high oxygen defect content in the structure: the slabs $[Ba_1, La_0, Cu_3O_7]_n$ exhibit, themselves, oxygen defects, which may favour slight displacements of the copper and oxygen atoms along \vec{c} during oxygen intercalation, between the slabs, without changing the c parameter.

The oxygen intercalation in the second series, $La_{3-x}A_{1+x}Cu_2O_{6-\frac{1}{2}x+\frac{1}{2}}$, depends on the nature of the A ions, calcium or strontium, on the rate of substitution x , and on the oxygen pressure as shown from table III. It can

TABLE III
Crystallographic data and analytical results for the oxides
 $La_{3-x}A_{1+x}Cu_2O_{6-\frac{1}{2}x+\frac{1}{2}}$.

Quenched oxides (in air)	Annealed oxides (in O ₂)		
	O ₂ partial pressure	Composition	δ
$La_2SrCu_2O_6$	0	$a = 3.855 \text{ \AA}$ $c = 19.867 \text{ \AA}$	$La_2SrCu_2O_6$ $a = 3.865 \text{ \AA}$ $c = 20.063 \text{ \AA}$
$La_2Sr_1.05Cu_2O_6$	0.02	$a = 3.853 \text{ \AA}$ $c = 19.933 \text{ \AA}$	b
$La_2Sr_0.95Cu_2O_6$	0.04	$a = 3.859 \text{ \AA}$ $c = 19.956 \text{ \AA}$	$La_2Sr_1.05Cu_2O_6$ $a = 3.868 \text{ \AA}$ $c = 20.051 \text{ \AA}$
$La_2Ca_1.05Cu_2O_6$	0.02	$a = 3.825 \text{ \AA}$ $c = 19.404 \text{ \AA}$	$La_2Ca_1.05Cu_2O_6$ $a = 3.823 \text{ \AA}$ $c = 19.404 \text{ \AA}$

Indeed it is seen for the strontium oxides synthesized in air, like $La_2SrCu_2O_6$, that δ increases with the strontium content tending towards the formulation $La_{3-x}A_{1+x}Cu_2O_6$. It results that the Cu^{3+} content increases with the divalent A ion content, in order to compensate the oxygen vacancies due to the substitution of Si^{4+} or Ca^{2+} for La^{3+} . The annealing of the latter oxides at 400°C under an oxygen pressure of one bar shows the ability of these phases to intercalate oxygen, δ ranging from 0 to 0.29 for $La_{2-x}Sr_1+xCu_2O_{6-\frac{1}{2}x+\frac{1}{2}}$ whereas $0.02 \leq \delta \leq 0.08$ for $La_1, Ca_1, Cu_2O_{6-\frac{1}{2}x+\frac{1}{2}}$. One can see that the rate of intercalation is higher for the strontium oxides than for the calcium compound. Moreover it seems that in the strontium oxides the maximum rate of intercalation increases with the strontium content. Contrary to the oxides $La_2Ba_2Cu_2O_{14+x}$, the compounds $La_{2-x}Sr_1+xCu_2O_{6-\frac{1}{2}x+\frac{1}{2}}$ exhibit a variation of the interlayer distances: the c parameter of the tetragonal cell increases with the oxygen content δ , for a same x value. This influence of

intercalation on the c parameter, can be explained by the fact that the $[La_2-Sr_2Cu_2O_6]_n$ slabs, which are stoichiometric and formed of SiO_4 -type layers are more rigid than the $[Ba_1, La_0, Cu_3O_7]_n$ slabs, and are only displaced by the introduction of oxygen between them. However the behaviour of the oxides $La_{1.9}Cu_1.05O_6-\frac{1}{2}x+\frac{1}{2}$, where c parameter is independent of δ is not explained; nevertheless in this latter case δ remains rather weak ($\delta \leq 0.08$). The oxygen deintercalation of these oxides is similar to that observed for the first family: for instant heating the most oxidized compound $La_2Sr_2Cu_2O_{10}$ at 400°C under low oxygen pressures ($\sim 10^{-3}$ bar) leads progressively to the reduced phase $La_2SrCu_2O_8$.

The behaviour of the oxides $La_{3-x}A_xCu_2O_{6-\frac{1}{2}x+\frac{1}{2}}$ is much more complex owing to the wide homogeneity ranges observed for these oxides especially in the case of strontium. For instance, the δ values observed for the strontium oxides synthesized in air (table I) do not increase progressively with x contrary to $La_{2-x}Sr_1+xCu_2O_{6-\frac{1}{2}x+\frac{1}{2}}$, but increase up to $x \approx 1/3$ and then decrease again up to $x \approx 1$. These δ values are difficult to compare owing to the fact that the different compositions were not synthesized at the same temperature in order to obtain pure oxides. It is sure that equilibrium is rarely reached for this series. So, for $0 \leq x \leq 1$ the δ values given in table I correspond to heating times of 12 h and annealing these samples in the same conditions, but for longer times (24 h to 48 h) allowed us to prepare pure phases with the same structure but characterized by greater δ values. Thus it appears that kinetics plays an important part for oxygen intercalation in this phase at a given temperature and a given oxygen pressure. Like for the two other series, oxygen can be intercalated or deintercalated by annealing the samples synthesized in air, at 400°C under an oxygen pressure of one bar or under vacuum (10^{-3} bar) respectively. The curves $\delta = f(x)$ are given in figure 4 for the strontium compounds where they are compared with the sine $\delta = x/2$ which represents the maximum rate of intercalation available in this structure. It can be seen that oxygen can easily be deintercalated, tending towards the most oxygen deficit structure; it appears that intercalation tends to be maximum for low x values ($0 \leq x \leq 0.25$), whereas it is only partial for higher x values ($0.33 \leq x \leq 1.20$). 11% to 33% of the available anionic sites being only occupied in this latter composition range. From these results it seems that intercalation is governed by two opposite effects which are competitive: the trend to preserve a stoichiometric K_2NiF_4 structure as for $La_2Cu_2O_4$ and $LaSrCu_2O_4$, and the trend to form a related defect structure but with an ordering of the oxygen vacancies. Thus, rather close to the stoichiometric compound $La_2Cu_2O_4$ the trend to stoichiometry is favoured by partial oxy-

dation of Cu(II) to Cu(III), whereas rather far from La_2CuO_4 , for example for $x = 1$, the stoichiometric oxide $\text{LaSr}_x\text{CuO}_4$ [3] cannot be stabilized any more under normal oxygen pressure, and oxygen vacancies are favoured; the resulting great amount of anionic vacancies are ordered, leading to different microphases as observed by electron diffraction. The "a" parameter which characterizes the corresponding K_2NiF_4 -type tetragonal cell is generally not influenced by the intercalation-de-intercalation process except for high x values which exhibit superstructures. For such oxygen defect oxides, an order-disorder phenomenon of the oxygen vacancies appears in the (0 0 1) plane which contributes to the variation of the "a" parameter of the K_2NiF_4 subcell. It is for instance the case of the strontium oxide corresponding to $x = 1.20$. The sample quenched in air ($\delta = 0$) exhibits a superstructure in the (0 0 1) plane with a "a" subcell parameter of 1.76 Å (Table I). The annealing at 400°C in oxygen of this phase involves an important decrease of the rate of the oxygen vacancies ($\delta = 0.33$). It results that the order disappears, leading to a true tetragonal cell with a "a" greater than that of the quenched specimen ($a = 3.791$ Å), "c" being smaller ($c = 12.900$ Å). The evolution of the "a" parameter versus composition for quenched and annealed compounds is complex (Fig. 3). It results from the influence of several factors: copper (II) and oxygen vacancies contents, size of Sr^{2+} which is slightly larger than La^{3+} . For every "a" value, "c" increases with the rate of intercalation, i. e. with the $\text{Ca}^{3+}/\text{Cu}^{2+}$ ratio, except for high "x" values which exhibit order-disorder phenomena. This behavior is in agreement with the observation previously made by Goodenough *et al.* [3].

The evolution of "c" for $x > 0.25$ can be interpreted by two opposite effects: increasing due to substitution of Sr^{2+} for La^{3+} and decreasing due to oxygen vacancies. For small "x" values ($x < 0.25$) the number of oxygen vacancies remains low and tends towards zero so that "c" increases owing to the replacement of La^{3+} by Sr^{2+} . For $x > 0.25$ the number of oxygen vacancies becomes very large and its effect prevails on that of substitution $\text{Sr}^{2+}/\text{La}^{3+}$, involving a decrease of "c".

INFLUENCE OF THE INTERCALATION PROCESS ON THE ELECTRICAL PROPERTIES OF THE MIXED VALENCE COPPER OXIDES

Most of the oxides described above are characterized by the presence simultaneously of Cu(II) and Cu(III), and are thus mixed-valence oxides. The electron transport properties of these phases, which are *p* type semiconductors or *p* type semi-metals or metals are strongly influenced by the rate of intercalation.

The evolution of conductivity versus reciprocal temperature for different

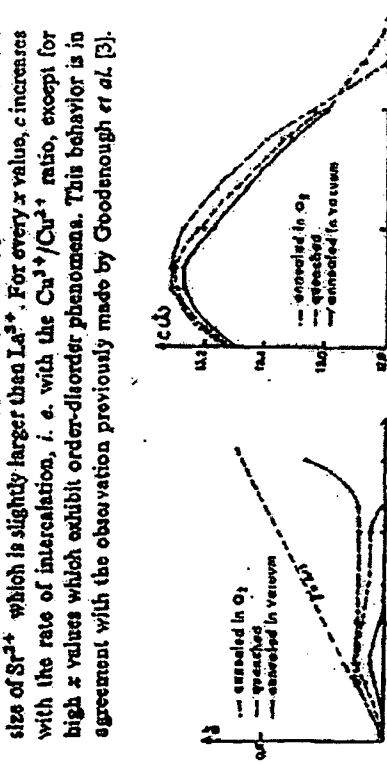


Fig. 4. — The oxide $\text{La}_{1-x}\text{Sr}_x\text{CuO}_{4-x/2}$: evolution of "c" as a function of "x" for oxides resulting from different thermal treatments.

Fig. 5. — The oxide $\text{La}_{1-x}\text{Sr}_x\text{CuO}_{4-x/2+1/2}$: evolution of the "c" parameter as a function of "x" for oxides resulting from different thermal treatments.

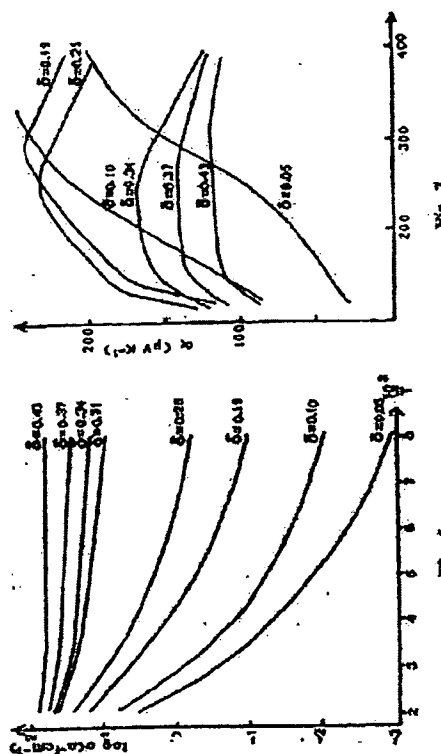


Fig. 6. — The oxide $\text{Ba}_{1-x}\text{La}_{1-x}\text{Sr}_x\text{CuO}_{4-x/2}$: variation of the conductivity (logarithmic scale) as a function of reciprocal temperature for different "x" values.

Fig. 7. — The oxide $\text{Ba}_{1-x}\text{La}_x\text{Cu}_x\text{O}_{4+x+1/2}$: variation of the thermoelectric power as a function of "T" for different "x" values.

Fig. 7.

Fig. 8. — The oxide $\text{Ba}_{1-x}\text{La}_x\text{Cu}_x\text{O}_{4+x+1/2}$: variation of the conductivity (logarithmic scale) as a function of reciprocal temperature for different "x" values.

δ values of the oxides $\text{La}_2\text{Ba}_3\text{Cu}_6\text{O}_{14+\delta}$ (Fig. 8) shows that the conductivity increases drastically with the intercalation of oxygen, contrary to the structure which remains unchanged. In the same way the thermoelectric power of these phases (Fig. 7) is very sensitive to the intercalation rate. These properties are interpreted by a conduction band model whose configuration is mainly determined by the splitting of the $3d$ Cu₁ orbitals by the crystal field [15] (Fig. 8 a). Every composition can indeed be considered as a mixing of the two limits: the reduced form $\text{Ba}_2\text{La}_3\text{Cu}_6\text{O}_{14}$ characterized by ribbons of one octahedron and two tetragonal pyramids running along c_1 , and the oxidized form $\text{Ba}_2\text{La}_3\text{Cu}_6\text{O}_{14}$ which exhibits infinite octahedral ribbons along c . The $\sigma_{x^2-y^2}^{\pm}$ bands result from Cu—O—Cu interactions and strong electron-electron interactions split the $d_{z^2}^{\pm}$ and $d_{x^2-y^2}^{\pm}$ levels by a few eV like the $\sigma_{x^2-y^2}^{\pm}$ and $\sigma_{z^2}^{\pm}$ bands. It results that the band structure of $\text{La}_2\text{Ba}_3\text{Cu}_6\text{O}_{14}$ (Fig. 8 b) is that of an insulator but this limit has not been synthesized; on the other hand, the only level configuration which can lead to a semi-metallic or metallic conduction for the limit $\text{Ba}_2\text{La}_3\text{Cu}_6\text{O}_{14}$ corresponds to a $d_{z^2}^{\pm}$ empty level located just above or across the filled

$\sigma_{x^2-y^2}^{\pm}$ band (Fig. 8 b). Thus, it appears that intercalation of oxygen which corresponds to a local change of copper coordination, will involve an increase of the density of the $d_{z^2}^{\pm}$ levels above the filled $\sigma_{x^2-y^2}^{\pm}$ band, i.e. an increase of the number of holes in the conduction band. The approximately linear evolution of $\log \sigma$ vs δ at 293 K is in agreement with this model. This progressive transition from a semi-conductive to a semi-metallic state can be explained by the Mott model [16] of quasi localized holes trapped at the top of the filled $3d_{x^2-y^2}^{\pm}$ band.

The oxides $\text{La}_{1-x}\text{A}_{1+x}\text{Cu}_2\text{O}_{6-\frac{1}{2}x+\delta}$ exhibit a similar behaviour [17]. From the evolution of the curves $\log \sigma = f(1/T)$, between 80 K and 300 K (Fig. 9) it can be seen that a continuous transition from a semi-conductive to a semi-metallic state is observed as the oxygen intercalation rate increases from $\delta = 0$ ($\text{La}_1\text{SrCu}_2\text{O}_6$) to $\delta = 0.29$ ($\text{La}_{1.06}\text{Sr}_{0.94}\text{Cu}_2\text{O}_{6.22}$). The conductivity depends also on the nature of the A ion which influences drastically the c parameter: the calcium oxide $\text{La}_{1.90}\text{Ca}_{0.10}\text{Cu}_2\text{O}_{6.97}$ is indeed much more conductor than the corresponding strontium oxide $\text{La}_{1.56}\text{Sr}_{1.44}\text{Cu}_2\text{O}_{6.17}$. The Seebeck coefficient curves $a = f(T)$ (Fig. 10) confirm this influence of intercalation: a increases continuously with T for

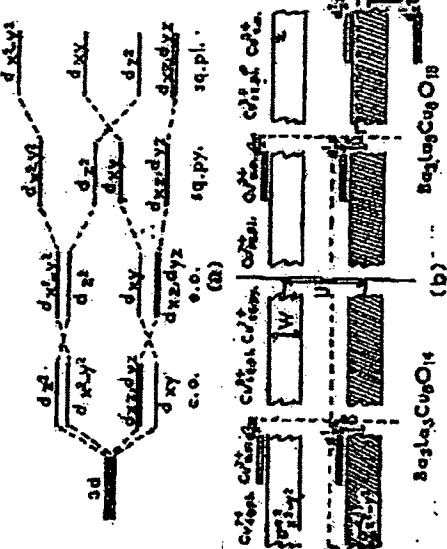


FIG. 8.

- a) Crystal field splittings for d -element in different environment; o. o.: compressed octahedron, e. o.: elongated octahedron, sq. pl.: square pyramidal, sq. pl.: square plane.
b) Schematic band diagram for $\text{Ba}_2\text{La}_3\text{Cu}_6\text{O}_{14}$ and $\text{Ba}_2\text{La}_3\text{Cu}_6\text{O}_{14}$; U denotes the intraatomic exchange energy, d_{z^2} and $d_{x^2-y^2}$ the splitting due to the axial distortion of the octahedron and W the estimated band width.

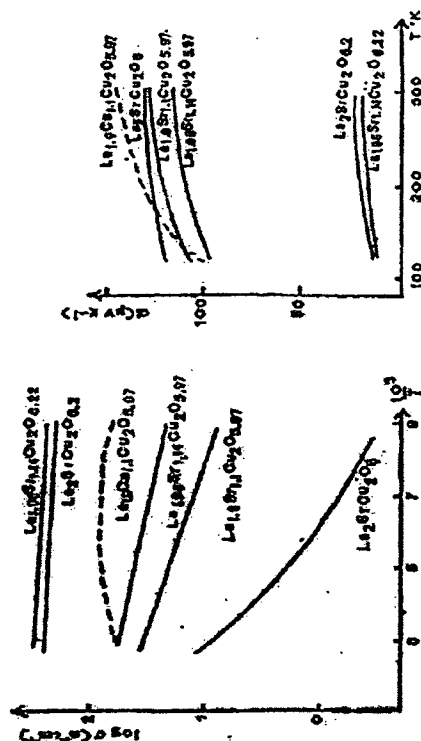


FIG. 9.

- Fig. 9. — The oxides $\text{La}_{1-x}\text{A}_{1+x}\text{Cu}_2\text{O}_{6-\frac{1}{2}x+\delta}$: evolution of the conductivity (logarithmic scale) vs T^{-1} for different compositions.

- Fig. 10. — The oxides $\text{La}_{1-x}\text{A}_{1+x}\text{Cu}_2\text{O}_{6-\frac{1}{2}x+\delta}$: evolution of its thermoelectric power $a = f(T)$ for different compositions.

FIG. 10.

- Fig. 10. — The oxides $\text{La}_{1-x}\text{A}_{1+x}\text{Cu}_2\text{O}_{6-\frac{1}{2}x+\delta}$: evolution of its thermoelectric power $a = f(T)$ for different compositions.

the small intercalation rates ($\delta = 0$ to 0.04) i.e. for small Cu^{2+} contents, whereas it becomes weak and nearly independent of the temperature, for high intercalation rates ($\delta = 0.20$ to 0.29), i.e. for high hole concentration. These properties very similar to those obtained for $\text{La}_2\text{Ba}_3\text{Cu}_6\text{O}_{14+\delta}$ can be explained by the same Mott model of holes trapped at the top of the $\sigma_{x^2-y^2}^{\pm}$ band. However the rather high conductivity of $\text{La}_2\text{SrCl}_2\text{O}_6$ in spite of the very weak Cu^{2+} content, $\delta \approx 0$ —let us think that the intra-atomic energy U is in this case of the same order of magnitude as the band width W , (fig. 11). In the same manner the relatively high and metallic conductivity of the calcium oxide $\text{La}_{1-x}\text{Ca}_{0.10}\text{Cu}_{2-x}\text{O}_{4.91}$ compared to the corresponding strontium oxide shows that the band width W , must be larger than U . In the calcium compound so that the overlapping of the two $\sigma_{x^2-y^2}^{\pm}$ bands gives rise to a higher mobility.

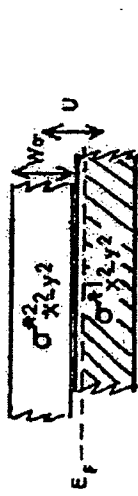


Fig. 11.—The oxides $\text{La}_{2-x}\text{A}_{1+x}\text{Cu}_{2-x}\text{O}_{6-\delta}$: schematic band diagram deduced from electron transport properties.

The highest conductivities are observed for the oxides $\text{La}_{2-x}\text{Sr}_x\text{CuO}_{4-\delta}$ [18]. For a given substitution rate x , the conductivity increases with the rate of intercalation δ as shown from figure 12 for temperature ranging from 80 K to 300 K. However the evolution of $\log \sigma$ vs $1/T$ as well as $\sigma \sim f(T)$ is more complex than the two other series: δ is not the only factor governing the electron transport properties of the phases. Three domains must in fact be distinguished: $0 < x \leq 0.16$, $0.16 < x \leq 0.50$ and $0.50 < x \leq 1.20$ for the oxides quenched in air and annealed in oxygen. The compounds of the first domain ($0 \leq x \leq 0.16$) are characterized by a semi-metallic behaviour and their properties can be interpreted by the model developed by Goodenough for La_2CuO_4 [19] involving the presence of holes in the filled band $\sigma_{z^2}^{\pm}$. The weak variation of conductivity which does not correspond to the metallic model $\rho = \rho_0(1 + \gamma)$ (fig. 12 a), as well as the thermoelectric power values (fig. 12) greater than those of a metal are in agreement with this model. The fact that the holes may be trapped on localized levels at the top of the $\sigma_{x^2-y^2}^{\pm}$ band according to the Mott Model is also confirmed by the fact that σ increases with temperature (fig. 13). The

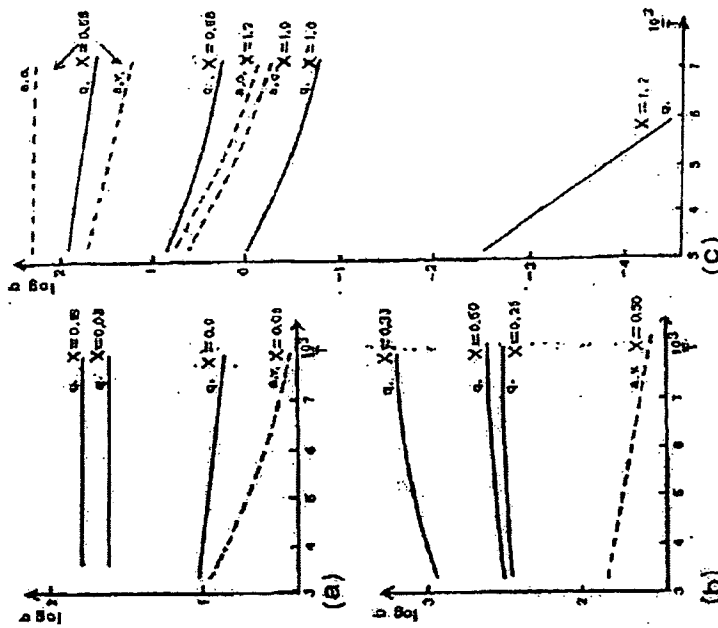


Fig. 12.—The oxides $\text{La}_{2-x}\text{Sr}_x\text{CuO}_{4-\delta}$: variation of the conductivity vs T^{-1} (a: quench-ed in air, a. o.; annealed in O_2 , a. v.; annealed in vacuum),
a) $0 < x \leq 0.16$; b) $0.16 < x \leq 0.50$; c) $0.5 < x \leq 1.20$.

oxides belonging to the second domain ($0.16 < x \leq 0.50$), exhibit a metallic conductivity (fig. 12 b) which increases with the intercalation rate: ρ increases linearly with temperature and the thermoelectric power values are weak and nearly temperature independent (fig. 13). The highest x compositions ($0.50 < x \leq 1.20$), exhibit for the less oxidized compounds synthesized in air ($\delta < 0.07$) a semiconductive behaviour: σ decreases drastically with δ (fig. 12 c), and comparatively α increases as δ decreases (fig. 13). These latter oxides and especially the compositions corresponding to $x = 0.88$, 1 and 1.2 exhibit a variation of the conductivity according to the Mott relation $\sigma = A \exp[-(QR_0T)^{1/4}]$ which characterizes a variable range hopp-

ing-on-the-capacitance model

ing of holes located in the $\sigma_{x_1-x_2}^{+}$ -band close to the Fermi level. It must be noted that the electrical properties of the oxides $\text{La}_{2-x}\text{Sr}_x\text{CuO}_{4-\delta/2+\delta}$ do not depend on the δ value only. So, for instance, the oxides corresponding to $0.33 \leq x \leq 1.0$ which have been annealed under an oxygen pressure of 1 bar exhibit the same δ value ($\delta \approx 0.11$), but are characterized by a decrease

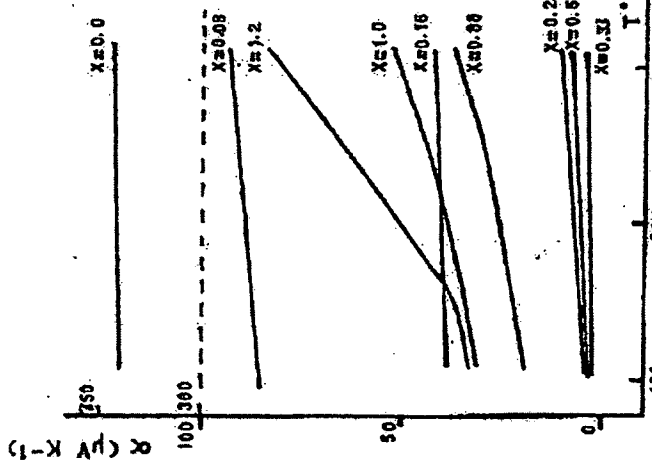


Fig. 13. — The oxides $\text{La}_{2-x}\text{Sr}_x\text{CuO}_{4-\delta/2+\delta}$: thermoelectric power vs T for quenched oxides with different x values.

of σ as x increases as shown figure 14. This shows the influence of the rate of anionic vacancies ($\delta/2-\delta$) on the carrier mobility. Moreover the distribution of the oxygen defects i. e.; the order-disorder phenomena, may influence the electron transport properties of these compounds. The great sensitivity of these compounds to oxygen makes that their electrical conductivity can vary drastically, under a given oxygen pressure owing to the intercalation or deintercalation of oxygen. For this reason

note 21 — 1984 — n° 4

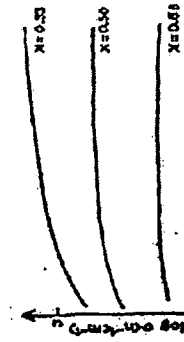


Fig. 14. — The oxides $\text{La}_{2-x}\text{Sr}_x\text{CuO}_{4-\delta/2+\delta}$: evolution of the conductivity as a function of reciprocal temperature for oxides annealed under an oxygen pressure of 1 bar ($\delta = 0.11$, $0.33 \leq x \leq 1.0$).

we have only discussed above the electrical properties of these phases at relatively low temperatures ($T < 300$ K), where all the compounds of the three families are not sensitive to intercalation or deintercalation. Such anomalies of the conductivity have indeed been observed for the oxides $\text{La}_{2-x}\text{Sr}_x\text{CuO}_{4-\delta/2+\delta}$, corresponding to $0 \leq x \leq 0.16$ and synthesized in air ($0 \leq \delta \leq 0.04$). One indeed observes (fig. 15), beyond 300 K under an oxygen pressure of 0.2 bar that σ decreases first drastically in the temperature range 300 K-420 K, and then increases again in the temperature range 420 K-650 K. The thermogravimetric curves of these phases, characterized successively by a weight loss and weight gain, show clearly that this behaviour results from deintercalation and intercalation of oxygen successively. Similar properties are observed for the oxides $\text{La}_{2-x}\text{Sr}_{1+x}\text{Cu}_2\text{O}_{6-\delta/2+\delta}$ synthesized in air for $x = 0.1$ and 0.14 (fig. 15) and for which the thermogravimetric measurements confirm the oxygen deintercalation-intercalation process. The reversibility of the intercalation process in these phases is illustrated by the evolution of the conductivity of $\text{La}_{1.9}\text{Cr}_{1.1}\text{Cu}_{2}\text{O}_{5.97}$ versus reciprocal

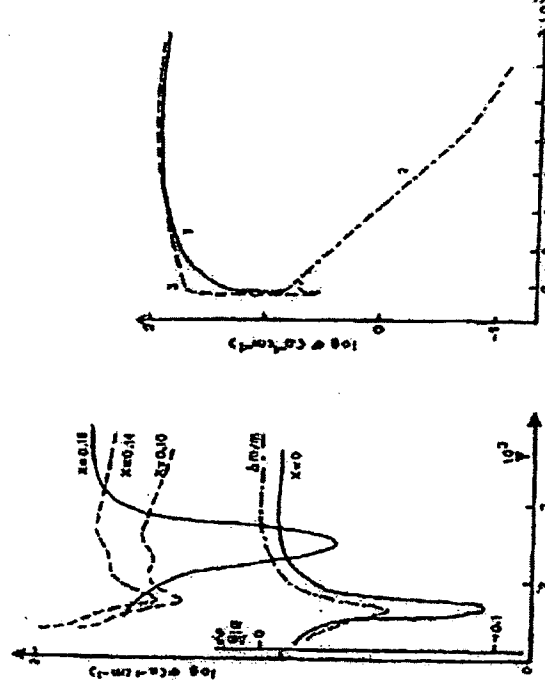


Fig. 15.

Fig. 15. — Variation of conductivity σ vs T ($T > 300\text{K}$) in air for some oxides in the $\text{La}_{1-x}\text{Sr}_x\text{O}_{1-\delta}$ series (solid line) and in the $\text{La}_{1-x}\text{Sr}_x\text{O}_{1-\delta} \cdot \text{Cu}_2\text{O}$ series (dotted line). A TG curve for $x = 0$ (first series), with the same temperature scale is given as example to illustrate the close relation between variation of conductivity and oxygen amount.

Fig. 16. — Variation of conductivity σ vs T for the oxides $\text{La}_{1-x}\text{Sr}_x\text{O}_{1-\delta}$ under different atmospheres:

- 1) — first heating under inert atmosphere,
- 2) — second heating under inert atmosphere,
- 3) — air introduction and second cooling (in air).

temperature under argon and air (fig. 16). The behaviour of this phase is indeed very different in argon and in air. The conductivity decreases under argon as soon as the temperature is greater than 300 K owing to the departure of oxygen and at about 370 K it decreases drastically. At this stage of the experiment, heating is stopped and the sample is cooled progressively down to 77 K . In this latter temperature range a semi-conductive behaviour is observed owing to the lower oxygen rate of intercalation. Heating again up to 300 K under argon leads to the same curve. However,

beyond 300 K , σ decreases again; this phenomenon is due to the fact that the thermodynamical equilibrium is not yet reached when we stop heating at 370 K . At 370 K argon is replaced by air, and heating is stopped. It can be seen that the conductivity increases immediately owing to the oxygen intercalation. The behaviour observed from 370 K to 77 K is then similar to that observed for the starting material.

REFERENCES

- [1] J. M. LARROU, P. M. RICCIANI, *J. Solid State Chem.*, 1973, 6, p. 576.
- [2] S. CHANDRA, H. MULLER-BIRCHMANN, M. SCHWEITZER, *Z. Anorg. Allg. Chem.*, 1977, 418, p. 130.
- [3] J. B. GOODENOUGH, O. DEJAYEAU, M. POUCHARD, P. HAENGMULLER, *J. Solid State Chem.*, 1973, 8, p. 325.
- [4] W. KLEIN, O. WHIRAKAWA, H. BROS, *Elektrochim. Ber. Dtsch. Phys. Chem.*, 1959, 63, p. 36.
- [5] K. HERRMANN, R. HOPPE, *Z. Anorg. Allg. Chem.*, 1968, 367, p. 249.
- [6] K. HERRMANN, R. HOPPE, *Z. Anorg. Allg. Chem.*, 1969, 367, p. 261.
- [7] K. HERRMANN, R. HOPPE, *Z. Anorg. Allg. Chem.*, 1969, 367, p. 270.
- [8] O. DEJAYEAU, C. PARENT, M. POUCHARD, P. HAENGMULLER, *Mai. Rev. Bélg.*, 1972, 7, p. 913.
- [9] N. ANTONIO, D. MACHIN, J. Chem. Soc. Dalton Trans., 1975, p. 1061.
- [10] H. N. MASON, R. JEANNERET, M. ZANNA, J. AUBRY, *Rev. Chim. Miner.*, 1976, 13, p. 440.
- [11] N. NEUVRE, L. BRAYARD, C. MICHEL, J. CHATINER, B. RAVEAU, *Mat. Res. Bull.*, 1980, 15, p. 891.
- [12] L. BRAYARD, C. MICHEL, J. PROVOST, B. RAVEAU, *J. Solid State Chem.*, 1981, 37, p. 151.
- [13] N. NEUVRE, J. CHATINER, M. HEAVER, B. RAVEAU, *J. Solid State Chem.*, 1981, 38, p. 120.
- [14] J. PROVOST, F. SYMONS, C. MICHEL, B. RAVEAU, *Synthetische Metall*, 1981, 4, p. 147.
- [15] J. PROVOST, F. SYMONS, C. MICHEL, B. RAVEAU, *Synthetische Metall*, 1981, 4, p. 157.
- [16] N. F. MORR, *Metat-Moderator Transfert*, Taylor and Francis, London, 1974.
- [17] N. NEUVRE, C. MICHEL, P. SPUDAK, B. RAVEAU, *Mai. Chem.*, 1982, 7, p. 413.
- [18] N. NEUVRE, P. SPUDAK, B. RAVEAU, *J. Phys. Chem. Solids*, 1983, 44, p. 189.
- [19] J. B. GOODENOUGH, *Mai. Res. Belg.*, 1973, 8, p. 423.

(Received December 12, 1981)

BRIEF ATTACHMENT I

IN THE UNITED STATES PATENT AND TRADEMARK OFFICE

In re Patent Application of
Applicants: Bednorz et al.
Serial No.: 08/479,810
Filed: June 7, 1995

Date: March 1, 2005
Docket: YO987-074BZ
Group Art Unit: 1751
Examiner: M. Kopec

For: NEW SUPERCONDUCTIVE COMPOUNDS HAVING HIGH TRANSITION
TEMPERATURE, METHODS FOR THEIR USE AND PREPARATION

Commissioner for Patents
P.O. Box 1450
Alexandria, VA 22313-1450

FIRST SUPPLEMENTAL AMENDMENT

Sir:

In response to the Office Action dated July 28, 2004, please consider the
following:

ATTACHMENT I



Thermal Analysis

Vol. 2

Inorganic Chemistry/Metallurgy
Earth Sciences
Organic Chemistry/Polymers
Biological Sciences/Medicine/Pharmacy

Editor

W. Hemminger
Institut für Werkstoffkunde
Universität Braunschweig
Federal Republic of Germany

SEP 25 1981
CATALOGING - PREP

1980



Birkhäuser Verlag
Basel · Boston · Stuttgart

Proceedings of the Sixth International
Conference on Thermal Analysis

Bayreuth, Federal Republic of Germany
July 6-12, 1980



T

Vol. 1 Theory
 Instrumentation
 Applied Sciences
 Industrial Applications

Vol. 2 Inorganic Chemistry/Metallurgy
 Earth Sciences
 Organic Chemistry/Polymers
 Biological Sciences/Medicine/Pharmacy

Vol. 2 Inor
 Eart
 Org:
 Biol

 Edit
 W. J
 Insti
 Uni
 Fed

B

CIP-Kurzaufnahme der Deutschen
Bibliothek

Thermal analysis. - Basel, Boston, Stuttgart:
Birkhäuser.

Bd. 1971 mit d. Erscheinungsorten: Basel,
Stuttgart. - Bd. 1977 im Verl. Heyden, Lon-
don, Bellmawr (NJ), Rheine.

ISBN 3-7643-1202-5

1980.

Vol. 2. Inorganic chemistry, metallurgy,
earth sciences, organic chemistry, polymers,
biological sciences, medicine, pharmacy:
proceedings of the 6. Internat. Conference
on Thermal Analysis, Bayreuth, Fed.
Republic of Germany, July 6-12, 1980/cd.
W. Hemminger. - 1980.

ISBN 3-7643-1086-3

NE: Hemminger, Wolfgang (Hrsg.); ICTA
(06, 1980, Bayreuth)

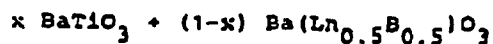
All rights reserved. No part of this publica-
tion may be reproduced, stored in a
retrieval system, or transmitted in any form
or by any means, electronic, mechanical,
photocopying, recording or otherwise, with-
out the prior permission of the copyright
owner.

© Birkhäuser Verlag Basel, 1980
ISBN 3-7643-1086-3
Printed in Switzerland

Although the use o
sions began in the r
of the effects of he
20th century. In t
broadly applicable
For a demonstratio
volume. From acad
quality control of i
tools for the scienti
field of endeavour.
others employ them
and chemical proc
Growth in the valu
number of natu
common ground a
application of the
a similar but broad
ing an opportunity
common interests:
of experts continue
ture, standards an
together ICTA an
to work, to find st
analysis. The end i

Onta
Miss

THERMAL BEHAVIOUR OF COMPOSITIONS IN THE SYSTEMS



V.S. Chincholkar* and A.R. Vyawahare

Department of Chemistry, Institute of Science, Nagpur

ABSTRACT

The effect of temperature on the dielectric constant (ϵ), $\tan \delta$ (loss tangent) and the ferroelectric properties of compositions in the systems $x \text{ BaTiO}_3 + (1-x) \text{ Ba}(\text{Ln}_{0.5}\text{B}_{0.5})\text{O}_3$ ($0 \leq x \leq 1$, Ln^{3+} = a rare earth cation and Y^{3+} , B^{5+} = $\text{Ta}, \text{Nb}, \text{V}$) reveal that in the Ta^{5+} system at $x = 0.8$, the ϵ_{\max} (ϵ at T_c) and T_c (the Curie-point) exhibit an increasing trend with decreasing ionic radii of the Ln^{3+} ions, whereas in the analogous Nb^{5+} system, an almost linear behaviour has been observed. In the V^{5+} system, the pure phases ($x = 0$) exhibit increasing trend of ϵ_{\max} and T_c values with decreasing rare earth cation size. Phases with $x = 0.8$, exhibit a break at Nd^{3+} in ϵ_{\max} values, in contrast to an increasing trend in T_c values with decreasing rare earth cation size. Similar behaviour is observed for the polarization data. The increasing trend in the T_c values in the direction $\text{Ta}^{5+}-\text{Nb}^{5+}-\text{V}^{5+}$ at $x = 0.8$ is perhaps reminiscent of the nephelauxetic effect.

The T_c values for these first order transitions have been confirmed by recording DTA curves against inert $\alpha\text{-Al}_2\text{O}_3$, the enthalpy change, however, being appreciably low in the present series.

INTRODUCTION

Recently emphasis has been placed on laser research and a concentrated effort has brought new and improved materials which can be used as hosts for transition. An important part of this effort has been directed towards finding potential laser materials having fluorescent energy states with long life times. In order to determine if symmetry conditions in

THERMAL ANALYSIS . ICTA 80 . BIRKHAUSER VERLAG, BASEL, BOSTON, STUTTGART

Feb. 17 2005 05:02PM PG

252

crystals also affect the life time of rare earth ion fluorescence, a series of ordered perovskite compounds having the general formula $A(B'_{0.5}B''_{0.5})O_3$ were studied [1]-[7]. However, temperature effects and doping characteristics were not studied. The present work concerns with the formation and the thermal characteristics of compositions in the systems $x BaTiO_3 + (1-x) Ba(Ln_{0.5}B'_{0.5})O_3$ where $0 \leq x \leq 1$, Ln^{3+} = a rare earth cation and B^{5+} = Nb^{5+} , Ta^{5+} and V^{5+} .

EXPERIMENTAL PROCEDURE

The compositions were prepared by the solid state reaction of the parent compounds (carbonates, oxides) at high temperature as described elsewhere [8], [9]. Room temperature X-ray structure was determined using Debye-Scherrer camera (14 cm diameter) and nickel-filtered Cu-K α radiation. Temperature effects on the dielectric constant (capacitance) and loss tangent ($\tan \delta$) were measured using a 716-C GR capacitance bridge together with type 1340-B type audiobeat frequency generator and 1231-B type u null detector and amplifier with 1231 P₅ type variable filter in a sample holder designed in this laboratory [10].

Modified [11] Sawyer-Tower type circuit was used to record hysteresis loops as a function of temperature in the above sample holder and a MOM Derivatograph was used to record DTA curves against $\alpha-Al_2O_3$ as reference.

RESULTS AND DISCUSSION

Tables 1-3 show the room temperature ϵ values as also the ϵ_{max} and the Curie-point (T_c) values evaluated from the capacitance measurements for compositions in the various systems. The temperature study was restricted to $x = 0.8$ compositions in the Ta^{5+} , Nb^{5+} systems and over the entire composition range in the V^{5+} system which exhibited the transition in the whole range of compositions. Table 4 shows these parameters at $x = 0$ for compositions in the V^{5+} system. In all the sys-

tems, an increase in ϵ with decreasing rare earth concentration of the lanthanide ions.

ϵ_{max} , P_s and T_c vs

Composition

$Ba(La_{0.1}Ta_{0.1}Ti_{0.8})$
$Ba(Nd_{0.1}Ta_{0.1}Ti_{0.8})$
$Ba(Sm_{0.1}Ta_{0.1}Ti_{0.8})$
$Ba(Gd_{0.1}Ta_{0.1}Ti_{0.8})$
$Ba(Dy_{0.1}Ta_{0.1}Ti_{0.8})$
$Ba(Y_{0.1}Ta_{0.1}Ti_{0.8})$

ϵ_{max} , P_s and T_c vs

$Ba(La_{0.1}Nb_{0.1}Ti_{0.8})$
$Ba(Nd_{0.1}Nb_{0.1}Ti_{0.8})$
$Ba(Sm_{0.1}Nb_{0.1}Ti_{0.8})$
$Ba(Gd_{0.1}Nb_{0.1}Ti_{0.8})$
$Ba(Dy_{0.1}Nb_{0.1}Ti_{0.8})$
$Ba(Y_{0.1}Nb_{0.1}Ti_{0.8})$

ϵ_{max} , P_s and T_c vs

$Ba(La_{0.1}V_{0.1}Ti_{0.8})$
$Ba(Nd_{0.1}V_{0.1}Ti_{0.8})$
$Ba(Sm_{0.1}V_{0.1}Ti_{0.8})$
$Ba(Gd_{0.1}V_{0.1}Ti_{0.8})$
$Ba(Dy_{0.1}V_{0.1}Ti_{0.8})$
$Ba(Y_{0.1}V_{0.1}Ti_{0.8})$

252

253

res-
ie
ver,
itu-
ie
rare-
in
vera-
tay
cm
te
;
re
'
with
in
id
re
DTA

stems, an increasing trend in ϵ_{max} as also T_c is observed with decreasing rare earth cation size, and is perhaps reminiscent of the lanthanide contraction.

Table 1

ϵ_{max} , P_s and T_c values for compositions in the Ta^{5+} system

Composition	$\epsilon_{25^\circ C}$	P_s [mc/cm ²]	ϵ_{max}	T_c [°C]
Ba(La _{0.1} Ta _{0.1} Ti _{0.8})O ₃	200	4.5	780	85
Ba(Nd _{0.1} Ta _{0.1} Ti _{0.8})O ₃	250	6.0	850	90
Ba(Sm _{0.1} Ta _{0.1} Ti _{0.8})O ₃	342	8.1	1050	92
Ba(Gd _{0.1} Ta _{0.1} Ti _{0.8})O ₃	480	8.5	1120	96
Ba(Dy _{0.1} Ta _{0.1} Ti _{0.8})O ₃	530	8.9	1400	100
Ba(Y _{0.1} Ta _{0.1} Ti _{0.8})O ₃	580	9.6	1830	110

Table 2

ϵ_{max} , P_s and T_c values for compositions in the systems Nb^{5+}

Ba(La _{0.1} Nb _{0.1} Ti _{0.8})O ₃	232	5.3	580	90
Ba(Nd _{0.1} Nb _{0.1} Ti _{0.8})O ₃	260	6.2	900	100
Ba(Sm _{0.1} Nb _{0.1} Ti _{0.8})O ₃	290	8.4	1100	107
Ba(Gd _{0.1} Nb _{0.1} Ti _{0.8})O ₃	380	9.2	1220	110
Ba(Dy _{0.1} Nb _{0.1} Ti _{0.8})O ₃	415	9.8	1350	115
Ba(Y _{0.1} Nb _{0.1} Ti _{0.8})O ₃	530	10.2	1600	118

Table 3

ϵ_{max} , P_s and T_c values for compositions in the V^{5+} system

Ba(La _{0.1} V _{0.1} Ti _{0.8})O ₃	170	4.5	1100	93
Ba(Nd _{0.1} V _{0.1} Ti _{0.8})O ₃	225	3.5	840	124
Ba(Sm _{0.1} V _{0.1} Ti _{0.8})O ₃	280	7.5	1130	130
Ba(Gd _{0.1} V _{0.1} Ti _{0.8})O ₃	350	8.2	1290	135
Ba(Dy _{0.1} V _{0.1} Ti _{0.8})O ₃	480	8.2	1600	135
Ba(Y _{0.1} V _{0.1} Ti _{0.8})O ₃	530	12.2	2200	125

Table 4

ϵ_{max} , P_s and T_c values for compositions in the V^{5+} system at $x = 0$				
$Ba(La_{0.5}V_{0.5})O_3$	60	--	--	--
$Ba(Nd_{0.5}V_{0.5})O_3$	20	7.8	260	154
$Ba(Sm_{0.5}V_{0.5})O_3$	30	10.7	500	168
$Ba(Gd_{0.5}V_{0.5})O_3$	35	11.3	850	175
$Ba(Dy_{0.5}V_{0.5})O_3$	25	12.5	1020	200
$Ba(Y_{0.5}V_{0.5})O_3$	40	17.9	1250	220

Covalency of the B-O bond is reported [12] to increase with decreasing rare earth cation size and may be responsible for the above occurrence. The behaviour, however, is linear in case of Nb^{5+} and non-linear in the case of Ta^{5+} , V^{5+} . Table 5 shows the T_f and ΔH values as evaluated from the DTA curves, for some representative samples.

Table 5

Composition	T_f [°C]	ΔH [cal mole ⁻¹]
$Ba(La_{0.1}Ta_{0.1}Ti_{0.8})O_3$	80	25
$Ba(La_{0.1}Nb_{0.1}Ti_{0.8})O_3$	90	45
$Ba(La_{0.1}V_{0.1}Ti_{0.8})O_3$	95	65

A glance at the ΔH values reveal dilution of the ΔH value of the 120°C transition of $BaTiO_3$ (46 cal/mole) [13] by the addition of Ta^{5+} phases, no change with addition of Nb^{5+} phases and a substantial increase with incorporation of V^{5+} phases.

Another significant result of the present study is the observation of increasing T_c (T_f) values with decreasing B^{5+} radii, keeping the Ln^{3+} ion fixed, in the sequence $Ta^{5+} - Nb^{5+} - V^{5+}$. Considering the energy level diagram of an octahedrally surrounded metal ion with configuration $(np)^6$, we expect Ta^{5+} to

be more ionic than the elec will be less justified by these ions T Jørgensen has that the elec $Nb^{5+} - V^{5+}$ and transition me cal bond becau Our results a;

Fifth ionizat;

Ion

V^{5+}
Nb^{5+}
Ta^{5+}

- [1] F. Galasso Report UAS
- [2] F. Galasso 81 (1959)
- [3] F. Galasso 83 (1961)
- [4] F. Galasso
- [5] F. Galasso
- [6] F. Galasso
- [7] F. Galasso
- [8] V.S. Chinc

254

255

be more ionically bonded than Nb^{5+} and V^{5+} . As a result of this the electron density in the t_{2g} -orbital of the Ta^{5+} ion will be less than that in the case of Nb^{5+} , V^{5+} . This is also justified by considering the fifth ionization potential of these ions T (Table 6) which also increases in this sequence. Jørgensen has concluded from the electron transfer spectra that the electron affinity increases in the sequence Ta^{5+} - Nb^{5+} - V^{5+} and from the reduced Racah parameters of several transition metal ions (nephelauxetic effect) that the chemical bond becomes more covalent in the sequence 5d-4d-3d group. Our results are consistent with the observations of Jørgensen.

Table 6
Fifth ionization potential and electron configuration of B^{5+} metal ions

Ion	Electron configuration	I_5 (eV)
V^{5+}	$3s^2 3p^6$	65
Nb^{5+}	$4s^2 4p^6$	52
Ta^{5+}	$5s^2 5p^6$	45

REFERENCES

- [1] F. Galasso, United Aircraft Corporation Laboratory, Report UAR-B10, Jan 1963
- [2] F. Galasso, L. Katz, and R. Ward, J.Amer.Chem.Soc. 81 (1959) 820
- [3] F. Galasso, J.R. Barrante, and L. Katz, J.Amer.Chem.Soc. 83 (1961) 2830
- [4] F. Galasso, and W.J. Darby, J.Phys.Chem. 66 (1962) 131
- [5] F. Galasso, and J. Pyle, J.Phys.Chem. 67 (1963) 533
- [6] F. Galasso, and J. Pyle, J.Phys.Chem. 67 (1963) 1561
- [7] F. Galasso, and J. Pyle, Inorg.Chem. 2 (1963) 482
- [8] V.S. Chincholkar, J.Inorg.Nucl.Chem. 34 (1972) 2973

Feb. 17 2005 05:04PM P10

256

- [9] K. Gade, and V.S. Chincholkar, J.Chem.Soc.(Dalton) 12 (1979) 1959
- [10] V.S. Chincholkar, Z.Angew.Chem. 26 (1970) 288
- [11] V.S. Chincholkar, Ph.D.Thesis. Pune University, 1967
- [12] R.S.Roth, J.Research NBS 58 (1957) 75
- [13] J. Volger, Philips Res.Rep. 7 (1952) 21
- [14] C.K.Jørgensen, "Absorption spectra and chemical bonding in complexes" Pergamon Press, 1962, pp. 147, 306 and 310-12

STUDIES

A.

Bhabha

* Present address: Forensic Science Laboratory, Bombay-8

The formation of
by Solid State re

$\text{La}_2(\text{C}_2\text{O}_4)_3$, La (The reaction occurs depending upon the kinetics of forms and MoO_3 is evaluated controlled mechanism activation energy mole^{-1} .

A reversible phase observed at 823 K x-ray diffraction

The solid state :
 $\text{La}_2(\text{C}_2\text{O}_4)_3$, La (to gain better understanding in general and the formation of triplex in particular.

Several $\text{La}_2(\text{MoO}_4)_3$ have been extensively studied, electrical, magnetic, kinetics and mechanical properties reported scantily; reactivity of the compounds to re-examine this detail.

THERMAL ANALYSIS . ICI

BRIEF ATTACHMENT J

IN THE UNITED STATES PATENT AND TRADEMARK OFFICE

In re Patent Application of

Applicants: Bednorz et al.

Serial No.: 08/479,810

Filed: June 7, 1995

For: NEW SUPERCONDUCTIVE COMPOUNDS HAVING HIGH TRANSITION
TEMPERATURE, METHODS FOR THEIR USE AND PREPARATION

Date: March 1, 2005

Docket: YO987-074BZ

Group Art Unit: 1751

Examiner: M. Kopc

Commissioner for Patents
P.O. Box 1450
Alexandria, VA 22313-1450

FIRST SUPPLEMENTAL AMENDMENT

Sir:

In response to the Office Action dated July 28, 2004, please consider the
following:

ATTACHMENT J

Model family of high-temperature superconductors: $Tl_mCa_{n-1}Ba_2Cu_nO_{2(n+1)+m}$
 $(m = 1, 2; n = 1, 2, 3)$

S. S. P. Parkin, V. Y. Lee, A. I. Nazzal, R. Savoy, T. C. Huang, G. Gorman, and R. Beyers

IBM Research Division, Almaden Research Center, 650 Harry Road,

San Jose, California 95120-6099

(Received 31 May 1988)

We describe the structures and superconducting properties of six compounds in the Tl-Ca-Ba-Cu-O system of the general form, $Tl_mCa_{n-1}Ba_2Cu_nO_{2(n+1)+m}$, where $m = 1$ or 2 and $n = 1, 2$, or 3 . One of the compounds displays the highest known superconducting transition temperature, $T_c = 125$ K. The structures of these compounds consist of copper perovskitelike blocks containing 1, 2, or 3 CuO₂ planes separated by one or two Tl-O layers and thus form a model family of structures in which both the size and separation of the copper oxide blocks can be independently varied. The superconducting transition temperature increases with the number of CuO₂ planes in the perovskitelike block for both the Tl-O monolayer and bilayer compounds. For each pair of compounds ($m = 1, 2$) with the same number of CuO₂ planes (same n), the transition temperatures are similar but are consistently 15–20 K lower in the materials with single Tl-O layers. Variations in the transition temperatures in the double and triple CuO₂-layer compounds are observed to correlate with increased densities of intergrowths of related structures.

Recently^{1–7} several new high-temperature superconductors have been synthesized in the Tl-Ca-Ba-Cu-O system, including $Tl_2Ca_2Ba_2Cu_3O_{10 \pm x}$, which displays the highest superconducting transition temperature yet found, $T_c = 125$ K.³ In this article we present data on the structures and superconducting properties of six compounds of the form $Tl_mCa_{n-1}Ba_2Cu_nO_{2(n+1)+m}$, where $m = 1$ or 2 and $n = 1, 2$, or 3 . The structures consist of copper perovskitelike blocks containing 1, 2, or 3 CuO₂ planes separated by one or two Tl-O layers. These compounds thus form a model family of structures in which both the size and separation of the copper blocks can be independently varied. We present data that establish that the superconducting transition temperature increases with the number of CuO₂ planes in the perovskitelike block for both the Tl-O monolayer and bilayer compounds. For each pair of compounds ($m = 1, 2$) with the same number of CuO₂ planes (same n), the transition temperature is 15–20 K lower in the material with single Tl-O layers. Variations in the transition temperatures in the double and triple CuO₂ layer compounds are observed to correlate with increased densities of intergrowths of related structures.

The samples were prepared by thoroughly mixing suitable amounts of Tl₂O₃, CaO, BaO₂, and CuO, and forming a pellet of this mixture under pressure. The pellet was then wrapped in gold foil, sealed in a quartz tube containing slightly less than 1 atm of oxygen, and baked for approximately 3 h at ≈ 880 °C. A wide range of starting compositions was studied. In most cases the resulting pellet was comprised of several phases. However, for certain ranges of starting compositions, the pellets contained only one superconducting phase of the form $Tl_mCa_{n-1}Ba_2Cu_nO_{2(n+1)+m}$ together with minor amounts (< $\approx 20\%$) of insulating oxides such as those of Cu, Ca-Cu, Ba-Cu, and Tl-Ba. The relative amounts of each phase depended on the annealing time and temperature and the rate of

cooling from this temperature. In particular, for slow cooling rates (≈ 100 °C/h) the composition of the major $Tl_mCa_{n-1}Ba_2Cu_nO_{2(n+1)+m}$ phase more closely matched that of the starting composition. The composition and microstructure of the pellets were determined from complementary powder x-ray diffraction, electron microprobe, electron diffraction, and high-resolution transmission electron microscopy (TEM) studies. The superconducting properties of each pellet were examined by resistivity and dc Meissner susceptibility studies. The latter was measured with a SHE SQUID magnetometer. Cooling in a field of 100 Oe, the magnitude of the Meissner susceptibility at 5.5 K ranged from 10% to 35% of the susceptibility of a perfect diamagnet of the same volume, neglecting small demagnetizing corrections. The magnitude of the diamagnetic shielding signal is very dependent on the distribution of the normal and superconducting phases within the multiphase pellets and in most cases did not give useful information. The susceptibility data revealed that for some pellets the presence of a minority superconducting phase resulted in the resistance of the pellet dropping to zero at substantially higher temperatures than the T_c of the majority superconducting phase. This type of behavior emphasizes the importance of determining the transition temperature from a flux exclusion measurement in this complex quinary system. These results are summarized in Table I.

We have previously described the preparation and properties of the three members of the $Tl_mCa_{n-1}Ba_2Cu_nO_{2(n+1)+m}$ family, namely $Tl_2Ca_2Ba_2Cu_3O_{10}$ (2:2:2:3),³ $Tl_2Ca_1Ba_2Cu_2O_8$ (2:1:2:2),³ and $Tl_1Ca_2Ba_2Cu_3O_9$ (1:2:2:3),⁴ which display superconducting transition temperatures of 125, 108, and 110 K, respectively. By systematically varying the starting composition of the pellets, the related compounds, $Tl_2Ca_0Ba_2Cu_1O_x$ (2:0:2:1), $Tl_1Ca_0Ba_2Cu_1O_x$ (1:0:2:1), and $Tl_1Ca_1Ba_2Cu_2O_x$ (1:1:2:2) were synthesized. The unit cells for each phase

**Model family of high-temperature superconductors: $Tl_m Ca_{n-1} Ba_2 Cu_n O_{2(n+1)+m}$
($m = 1, 2$; $n = 1, 2, 3$)**

S. S. P. Parkin, V. Y. Lee, A. I. Nazzal, R. Savoy, T. C. Huang, G. Gorman, and R. Beyers
*IBM Research Division, Almaden Research Center, 650 Harry Road,
 San Jose, California 95120-6099*
 (Received 31 May 1988)

We describe the structures and superconducting properties of six compounds in the Tl-Ca-Ba-Cu-O system of the general form, $Tl_m Ca_{n-1} Ba_2 Cu_n O_{2(n+1)+m}$, where $m = 1$ or 2 and $n = 1, 2$, or 3. One of the compounds displays the highest known superconducting transition temperature, $T_c = 125$ K. The structures of these compounds consist of copper perovskitelike blocks containing 1, 2, or 3 CuO_2 planes separated by one or two Tl-O layers and thus form a model family of structures in which both the size and separation of the copper oxide blocks can be independently varied. The superconducting transition temperature increases with the number of CuO_2 planes in the perovskitelike block for both the Tl-O monolayer and bilayer compounds. For each pair of compounds ($m = 1, 2$) with the same number of CuO_2 planes (same n), the transition temperatures are similar but are consistently 15–20 K lower in the materials with single Tl-O layers. Variations in the transition temperatures in the double and triple CuO_2 -layer compounds are observed to correlate with increased densities of intergrowths of related structures.

Recently^{1–7} several new high-temperature superconductors have been synthesized in the Tl-Ca-Ba-Cu-O system, including $Tl_2 Ca_2 Ba_2 Cu_3 O_{10 \pm x}$, which displays the highest superconducting transition temperature yet found, $T_c = 125$ K.³ In this article we present data on the structures and superconducting properties of six compounds of the form $Tl_m Ca_{n-1} Ba_2 Cu_n O_{2(n+1)+m}$, where $m = 1$ or 2 and $n = 1, 2$, or 3. The structures consist of copper perovskitelike blocks containing 1, 2, or 3 CuO_2 planes separated by one or two Tl-O layers. These compounds thus form a model family of structures in which both the size and separation of the copper blocks can be independently varied. We present data that establish that the superconducting transition temperature increases with the number of CuO_2 planes in the perovskitelike block for both the Tl-O monolayer and bilayer compounds. For each pair of compounds ($m = 1, 2$) with the same number of CuO_2 planes (same n), the transition temperature is 15–20 K lower in the material with single Tl-O layers. Variations in the transition temperatures in the double and triple CuO_2 layer compounds are observed to correlate with increased densities of intergrowths of related structures.

The samples were prepared by thoroughly mixing suitable amounts of $Tl_2 O_3$, CaO , BaO_2 , and CuO , and forming a pellet of this mixture under pressure. The pellet was then wrapped in gold foil, sealed in a quartz tube containing slightly less than 1 atm of oxygen, and baked for approximately 3 h at ≈ 880 °C. A wide range of starting compositions was studied. In most cases the resulting pellet was comprised of several phases. However, for certain ranges of starting compositions, the pellets contained only one superconducting phase of the form $Tl_m Ca_{n-1} Ba_2 Cu_n O_{2(n+1)+m}$ together with minor amounts (< $\approx 20\%$) of insulating oxides such as those of Cu, Ca-Cu, Ba-Cu, and Tl-Ba. The relative amounts of each phase depended on the annealing time and temperature and the rate of

cooling from this temperature. In particular, for slow cooling rates (≈ 100 °C/h) the composition of the major $Tl_m Ca_{n-1} Ba_2 Cu_n O_{2(n+1)+m}$ phase more closely matched that of the starting composition. The composition and microstructure of the pellets were determined from complementary powder x-ray diffraction, electron microprobe, electron diffraction, and high-resolution transmission electron microscopy (TEM) studies. The superconducting properties of each pellet were examined by resistivity and dc Meissner susceptibility studies. The latter was measured with a SHE SQUID magnetometer. Cooling in a field of 100 Oe, the magnitude of the Meissner susceptibility at 5.5 K ranged from 10% to 35% of the susceptibility of a perfect diamagnet of the same volume, neglecting small demagnetizing corrections. The magnitude of the diamagnetic shielding signal is very dependent on the distribution of the normal and superconducting phases within the multiphase pellets and in most cases did not give useful information. The susceptibility data revealed that for some pellets the presence of a minority superconducting phase resulted in the resistance of the pellet dropping to zero at substantially higher temperatures than the T_c of the majority superconducting phase. This type of behavior emphasizes the importance of determining the transition temperature from a flux exclusion measurement in this complex quinary system. These results are summarized in Table I.

We have previously described the preparation and properties of the three members of the $Tl_m Ca_{n-1} Ba_2 Cu_n O_{2(n+1)+m}$ family, namely $Tl_2 Ca_2 Ba_2 Cu_3 O_{10}$ (2:2:2:3),³ $Tl_2 Ca_1 Ba_2 Cu_2 O_8$ (2:1:2:2),³ and $Tl_1 Ca_2 Ba_2 Cu_3 O_9$ (1:2:2:3),⁴ which display superconducting transition temperatures of 125, 108, and 110 K, respectively. By systematically varying the starting composition of the pellets, the related compounds, $Tl_2 Ca_0 Ba_2 Cu_1 O_x$ (2:0:2:1), $Tl_1 Ca_0 Ba_2 Cu_1 O_x$ (1:0:2:1), and $Tl_1 Ca_1 Ba_2 Cu_2 O_x$ (1:1:2:2) were synthesized. The unit cells for each phase

TABLE I. Summary of properties of $Tl_mCa_{n-1}Ba_2Cu_nO_x$

Conc. ratio	Tl	Relative composition				Lattice parameters	Superlattice wave vector (\mathbf{k})	T_c (K)
		Ca	Ba	Cu	O	a (Å)	c (Å)	
1:0:2:1	1.2	0.0	2	0.7	4.8	$Tl_1Ca_{n-1}Ba_2Cu_nO_x$ $P4/mmm$	3.869(2) 9.694(9)	a b
1:1:2:2	1.1	0.9	2	2.1	7.1	$Tl_1Ca_{n-1}Ba_2Cu_nO_x$ $P4/mmm$	3.8505(7) 12.728(2)	$\langle 0.29, 0, 0.5 \rangle$ 65-85
1:2:2:3	1.1	0.8	2	3.0	9.7	$Tl_1Ca_{n-1}Ba_2Cu_nO_x$ $P4/mmm$	3.8429(6) 15.871(3)	$\langle 0.29, 0, 0.5 \rangle$ 100-110
2:0:2:1	1.9	0.0	2	1.1	6.4	$Tl_2Ca_{n-1}Ba_2Cu_nO_x$ F/mmm^c	$a = 5.445(2)$ $b = 5.492(1)$	$\langle \overline{0.08}, 0.24, 1 \rangle^c$ b
2:0:2:1 ^d	1.8	0	2	1.1	6.4	$Tl_2Ca_{n-1}Ba_2Cu_nO_x$ F/mmm^c	$a = 5.4634(3)$ $b = a$	$\langle \overline{0.08}, 0.24, 1 \rangle^c$ 20
2:0:2:1	1.8	0.02	2	1.1	6.3	$Tl_2Ca_{n-1}Ba_2Cu_nO_x$ $I4/mmm$	3.8587(4) 23.152(2)	$\langle \overline{0.16}, 0.08, 1 \rangle^e$ 15-20
2:1:2:2	1.7	0.9	2	2.3	8.1	$Tl_2Ca_{n-1}Ba_2Cu_nO_x$ $I4/mmm$	3.857(1) 29.39(1)	$\langle 0.17, 0, 1 \rangle$ 95-108
2:2:2:3	1.6	1.8	2	3.1	10.1	$Tl_2Ca_{n-1}Ba_2Cu_nO_x$ $I4/mmm$	3.822(4) 36.26(3)	$\langle 0.17, 0, 1 \rangle$ 118-125

^aNo superlattice spots observed.^bNometallic or weakly metallic samples with no superconducting transition observed in resistivity and magnetic susceptibility studies for temperatures down to 4.2 K.^cThe symmetry of the structure is *orthorhombic* if the observed superlattice is ignored. Taking the superlattice into account lowers the symmetry to *monoclinic*.^dSample prepared from a Cu-rich starting composition, $Tl_2Ba_2Cu_2$.^eThe superstructure is identical to that for the orthorhombic 2:0:2:1 polymorph.

were determined from powder x-ray diffraction patterns extending from $2\theta = 3^\circ$ to 70° and verified by electron diffraction studies. These studies showed that all of the $Tl_mCa_{n-1}Ba_2Cu_nO_{2(n+1)+m}$ compounds have tetragonal cells at room temperature. The $Tl_1Ca_{n-1}Ba_2Cu_nO_{2n+3}$ compounds contain Tl-O monolayers, resulting in primitive tetragonal cells, whereas the $Tl_2Ca_{n-1}Ba_2Cu_nO_{2n+4}$ compounds contain Tl-O bilayers, resulting in body-centered tetragonal cells. The lattice parameters and symmetries of the various structures are included in Table I. As discussed later, the 2:0:2:1 compound also has an orthorhombic polymorph. As shown in Fig. 1, each oxide has a single peak in the low-angle portion ($3^\circ \leq 2\theta \leq 10^\circ$) of its x-ray diffraction pattern which results from the large c/a ratio in each structure. These peaks, (001) for $m=1$ and (002) for $m=2$, serve as fingerprints with which each of the compounds within the

$Tl_mCa_{n-1}Ba_2Cu_nO_{2(n+1)+m}$ family can be uniquely identified. The peak systematically shifts to lower angles as n increases within both the $Tl_1Ca_{n-1}Ba_2Cu_nO_{2n+3}$ and $Tl_2Ca_{n-1}Ba_2Cu_nO_{2n+4}$ families, consistent with an expansion of the unit cell along the c axis by the addition of extra CuO_2 and Ca planes. The peaks are in all cases at lower angles in the $Tl_2Ca_{n-1}Ba_2Cu_nO_{2n+4}$ compounds compared to the corresponding $Tl_1Ca_{n-1}Ba_2Cu_nO_{2n+3}$ compound, consistent with the increased number of Tl-O layers in the $Tl_2Ca_{n-1}Ba_2Cu_nO_{2n+4}$ compounds. The peaks are asymmetrically broadened to low angles because of geometrical aberrations in the focusing condition resulting from the flat specimens used.⁸ The arrangement of the cations in the various compounds is shown in Fig. 2. The positions of the oxygen atoms are inferred by comparison with related structures in the $La_{2-x}Sr_xCuO_4$, $YBa_2Cu_3O_x$, and $Bi_2Sr_2Ca_1Cu_2O_x$ families.⁹⁻¹¹ The six structures are comprised of Cu perovskitelike blocks containing one, two, or three CuO_2 planes sandwiched between Tl-O monolayers (1:0:2:1, 1:1:2:2, and 1:2:2:3 compounds) or bilayers (2:0:2:1, 2:1:2:2, 2:2:2:3 compounds). The Ba cations are located in planes adjacent to the Tl-O unit and the Ca cations form planes within the interior of the Cu perovskitelike unit.

Since the preparation, structure, and properties of the double and triple CuO_2 layer oxides appear to be much less complex than those of the single CuO_2 layer oxides for both the monolayer and bilayer Tl-O compounds, we will discuss these groups of compounds separately. As described earlier, for each of the $n=2$ and $n=3$ compounds a single tetragonal structure was found. An important structural feature of these compounds observed by TEM, scanning electron microscopy (SEM), and electron microprobe studies are intergrowths of structures related to the primary phase by the addition or removal of CuO_2 or Tl-O layers. For some samples SEM images showed contrast striations $\approx 5-10 \mu m$ in width within individual

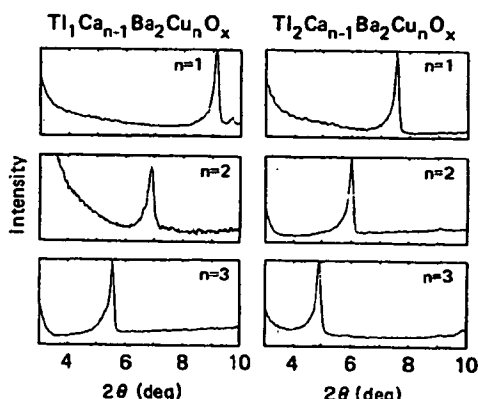


FIG. 1. Low-angle section of the powder x-ray diffraction patterns for the six phases $Tl_mCa_{n-1}Ba_2Cu_nO_{2(n+1)+m}$ ($m=1, 2$; $n=1, 2, 3$).

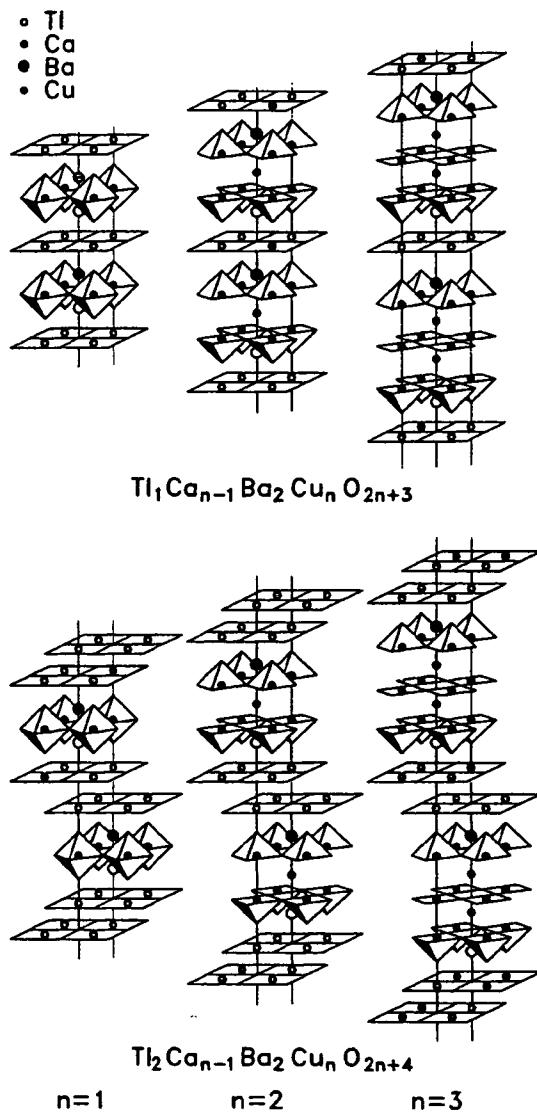


FIG. 2. Nominal structures of the six $Tl_m Ca_{n-1} Ba_2 Cu_n O_{2(n+1)+m}$ phases for $n = 1, 2$ and $m = 1, 2, 3$.

grains which result from intergrowths of regions with different proportions of heavy atoms. TEM studies revealed the existence of intergrowths on much finer length scales, as demonstrated in Fig. 3 for a sample prepared from a starting composition of $Tl_{0.85} Ca_1 Ba_2 Cu_2$. Figure 3(a) shows a selected area diffraction pattern along b^* which indicates that this grain contains both 1:1:2:2 and 1:2:2:3 phases. Indeed Meissner data on this sample [included in Fig. 4(d)] indicate two superconducting transitions with $T_c = 65$ and ≈ 105 K, consistent with the presence of extended regions of two distinct phases. Coincidentally, the c lattice parameters of the 1:1:2:2 and 1:2:2:3 phases are almost exactly in the ratio of 4/5 so that every fifth 1:2:2:3 $h0l$ spot coincides with every fourth 1:1:2:2 $h0l$ spot in Figure 3(a). High-resolution TEM micrographs in Figs. 3(b) and 3(c) show intergrowths of the

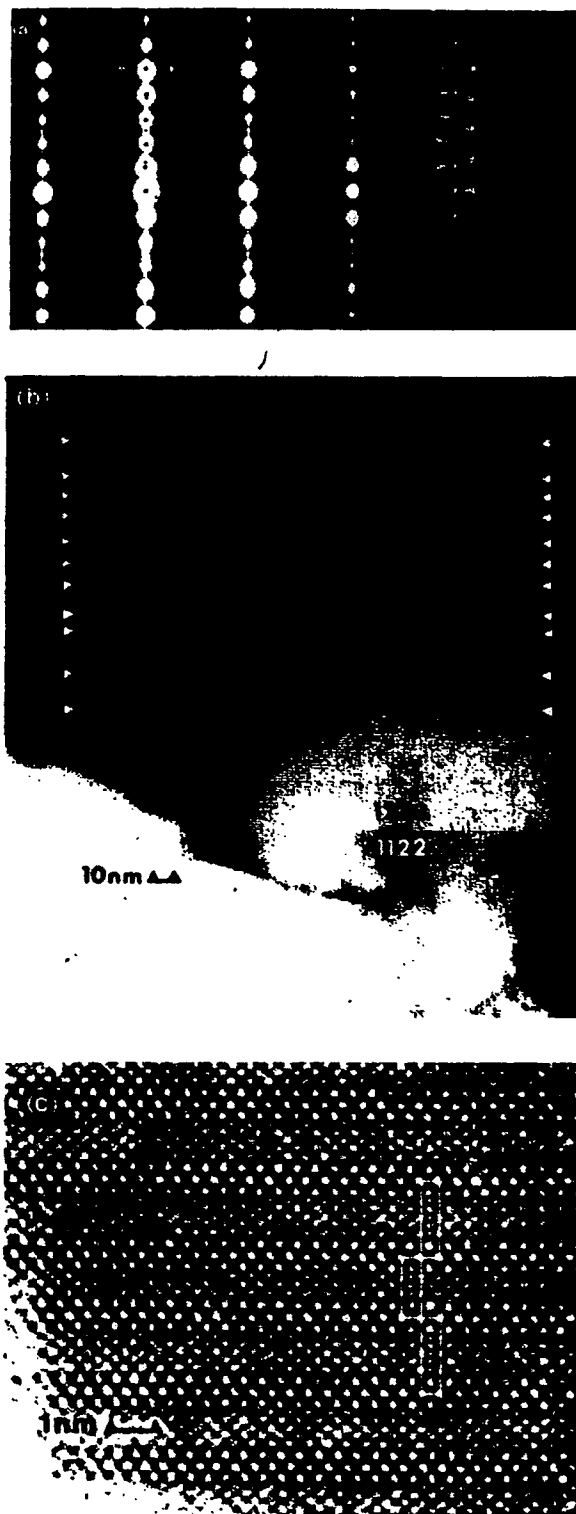


FIG. 3. (a) [010] selected area diffraction (SAD) pattern and (b) corresponding image of crystallites containing regions of 1:2:2:3 and 1:1:2:2. The arrows in (b) denote unit-cell thick intergrowths of 1:1:2:2 in 1:2:2:3. (c) High-resolution transmission electron micrograph of one unit-cell thick 1:1:2:2 intergrowth in 1:2:2:3.

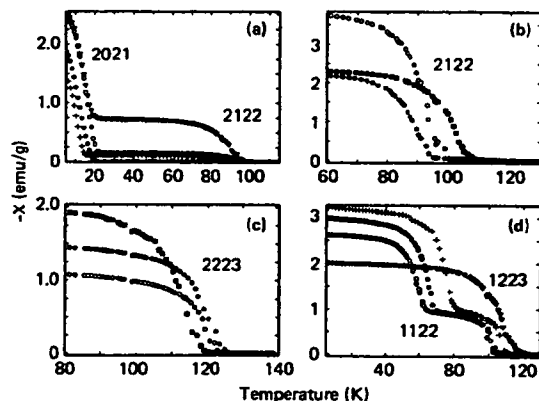


FIG. 4. Meissner susceptibility vs temperature for an applied field of 100 Oe for materials with starting cation composition, (a) $Tl_2Ba_2Cu_2$ (●), $Tl_2Ca_{0.05}Ba_2Cu_{1.05}$ (○, +), and $Tl_2Ca_{0.15}Ba_2Cu_{2.15}$ (▼); (b) $Tl_1Ca_2Ba_2Cu_3$ (●), $Tl_2Ca_1Ba_2Cu_2$ (○), and $Tl_{2.25}Ca_1Ba_2Cu_2$ (■); (c) $Tl_1Ca_2Ba_2Cu_3$ (■), $Tl_1Ca_{2.5}Ba_1Cu_3$ (○), and $Tl_1Ca_3Ba_1Cu_3$ (●); (d) $Tl_{0.85}Ca_1Ba_2Cu_2$ (○), $Tl_1Ca_1Ba_2Cu_2$ (●, +), and $Tl_{0.85}Ca_2Ba_2Cu_3$ (▼). The phases present in the pellet giving rise to the diamagnetic susceptibility are (a) 2:0:2:1 and 2:1:2:2, (b) 2:1:2:2, (c) 2:2:2:3, and (d) 1:1:2:2 and 1:2:2:3.

1:1:2:2 and 1:2:2:3 phases on length scales extending from $\approx 1\mu m$ down to one unit cell. The intergrowths are randomly distributed along the stacking axis. Isolated intergrowths comprising four CuO_2 planes were found in some samples (see Fig. 5) but no evidence was found for extended intergrowths comprising greater than three CuO_2 layers in these or other samples especially prepared from Cu- and Ca-rich starting compositions. A second type of intergrowth was observed in samples of the 1:2:2:3 phase in which an extra Tl -O plane was occasionally inserted between the Cu perovskitelike units, creating local regions of the 2:2:2:3 phase. Microprobe data show that the Tl content is systematically high in the compounds containing single Tl -O layers and systematically low in those com-



FIG. 5. High-resolution TEM image of an isolated four- CuO_2 -layer intergrowth. The markers denote the positions of the Cu columns.

pounds with Tl -O bilayers (see Table I) thus suggesting that intergrowths of Tl -O monolayers in the Tl -O bilayers materials and Tl -O bilayers in the Tl -O monolayer compounds are a general feature of these materials.

Meissner data (see Fig. 4) established that T_c can take a range of values for all of the double and triple CuO_2 layer compounds— $T_c = 95-108$ K for 2:1:2:2, $T_c = 118-125$ K for 2:2:2:3, $T_c = 65-85$ K for 1:1:2:2, and $T_c = 100-110$ K for 1:2:2:3. For a given compound, x-ray diffraction and microprobe studies did not detect any obvious difference between the samples with different transition temperatures. TEM studies, however, showed a clear correlation between the density of intergrowths and T_c . For the 2:1:2:2, 2:2:2:3, and 1:2:2:3 phases the material with no intergrowths displayed the highest transition temperature, whereas for the 1:1:2:2 compound the sample with the lowest density of intergrowths had the lowest T_c . As the density of intergrowths increased we observed that T_c systematically decreases or increases, respectively. It is possible that the structural or electronic modifications caused by the intergrowths are directly responsible for the decreased transition temperatures. Alternatively the presence of the intergrowths may simply reflect a means whereby the system accommodates, to some extent, off-stoichiometry in the cation sites which in turn may influence T_c . It is difficult to determine whether it is the local change in structure or composition which is responsible for the decrease in T_c since these are concurrent changes.

A second important structural feature found in all of the double and triple CuO_2 layer compounds is the presence of weak superlattice reflections in the selected area electron diffraction patterns. These reflections are considerably weaker than those previously found in the $Bi_2Sr_2Ca_1Cu_2O_x$ compound¹²⁻¹⁶ and indicate different structural modulations than those in the $Bi_2Sr_2Ca_1Cu_2O_x$ compound. The patterns can be described by a set of symmetry-related wave vectors, k . Each wave vector describes a pair of reflections symmetrically disposed a reciprocal distance $|k|$ along k on either side of each Bragg peak, which would be consistent with a sinusoidal modulation of the charge density along this direction.¹⁷ The possibility that each k corresponds to a different crystal variant with lowered symmetry is unresolved. The Tl -O monolayer and bilayer families each display a distinctive pattern of superlattice reflections, shown schematically in Figs. 6(a) and 6(b). One example of electron diffraction patterns showing the superlattice reflections is given in Fig. 7 for the 1:1:2:2 phase.

The structure and properties of the single CuO_2 layer compounds are more sensitive to the preparation conditions than those of the double and triple CuO_2 layer compounds. When prepared from a $Tl_2Ba_2Cu_1$ starting composition, the 2:0:2:1 compound has a face-centered orthorhombic cell and is not superconducting. The material is heavily twinned with twin planes of {110} type in the orthorhombic cell. This cell is related to the tetragonal cell by a rotation of $\approx 45^\circ$ about the c axis with a and b increased in size by a factor of $=\sqrt{2}$. However when the 2:0:2:1 compound is prepared from a Cu-rich starting composition, $Tl_2Ba_2Cu_2$, the compound is superconduct-

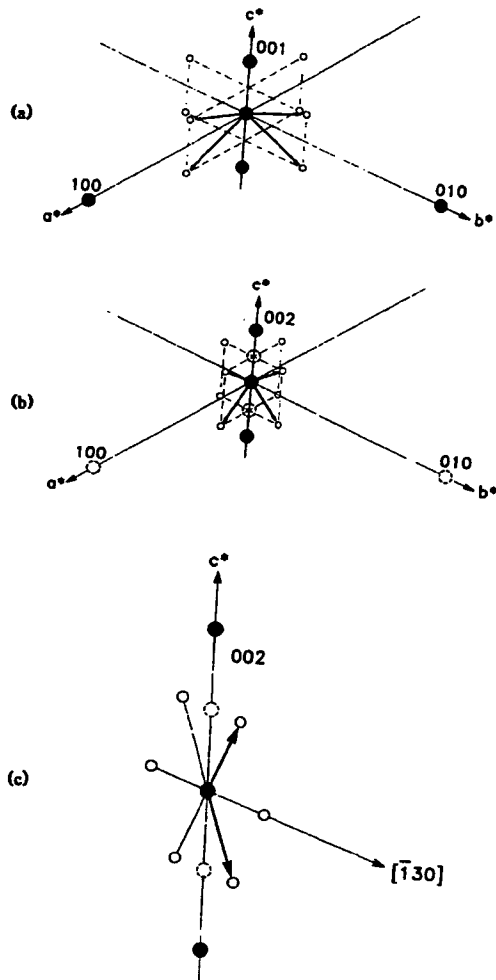


FIG. 6. Schematic diagram of the arrangement of superlattice reflections about the fundamental reflections for (a) the 1:1:2:2 and 1:2:2:3 phases, (b) the 2:1:2:2 and 2:2:2:3 phases, (c) the 2:0:2:1 phase. The fundamental reflections are shown as solid circles, and those which are systematically absent are shown as dashed circles. The superstructure is shown by open circles and the corresponding wave vectors by bold arrows.

ing at ≈ 20 K. While x-ray data indicate the structure is pseudotetragonal, transmission electron micrographs reveal a tweed pattern which is consistent with local orthorhombic distortion. A tetragonal polymorph with no evidence from TEM studies of either an average or local orthorhombic distortion can be formed by preparing the compound from a pellet containing a small amount of Ca ($Tl:Ca:Ba:Cu = 2:y:2:1+y$, with $y = 0.05-0.15$). This polymorph is also superconducting with a T_c which is independent of the amount of Ca in the starting composition but weakly dependent on the annealing time— $T_c = 15$ and 20 K for anneal times at 880°C of 3 and 9 h, respectively. As suggested by the Meissner data in Fig. 4(a) these pellets contain, in addition to the tetragonal 2:0:2:1 phase, a substantial amount of the 2:1:2:2 phase which increases as the proportion of Ca in the starting composition is increased. There is a sufficient amount of this phase that the resistance of these pellets actually drops to zero at

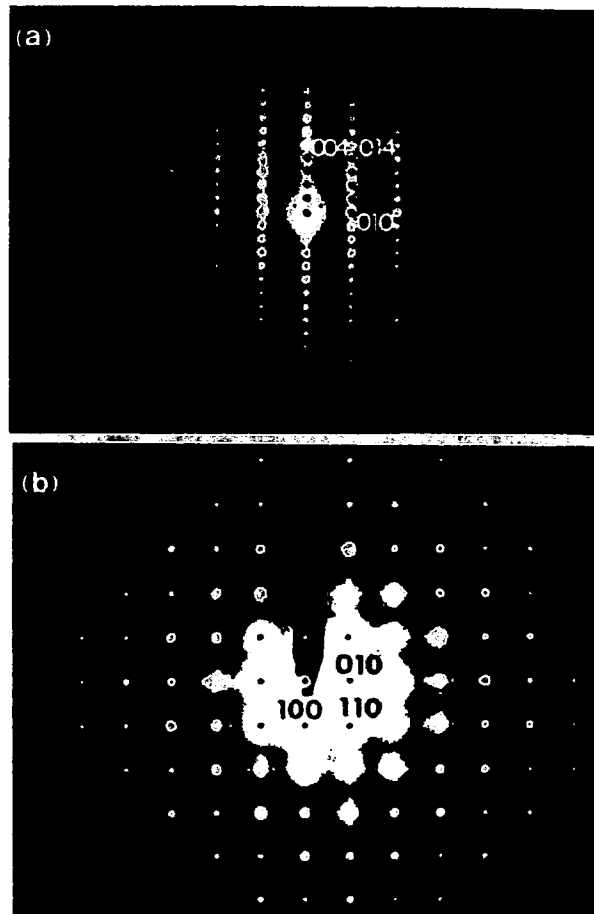


FIG. 7. (a) $\langle 100 \rangle$ and (b) $\langle 001 \rangle$ selected area diffraction patterns from crystallites of 1:1:2:2 showing superlattice reflections.

$T_c = 100$ K. The Meissner data in Fig. 4(a) show that for $y = 0.05$ the ratio of 2:1:2:2 to 2:0:2:1 is about 8% and for $y = 0.15$ the ratio is increased to $\approx 30\%$. Electron microprobe analysis shows that only a small amount of Ca (≈ 0.2 at.%) is incorporated into the 2:0:2:1 grains and consequently the role of the Ca doping in changing the structure and properties of the 2:0:2:1 material is unclear. Moreover there are reports that the 2:0:2:1 phase can be prepared without Ca with a transition temperature as high as ≈ 85 K.⁵ Both polymorphs of the 2:0:2:1 structures display a similar superlattice with an approximate wave vector, $\mathbf{k} = [0.08, 0.24, 1]$ in the orthorhombic setting. Taking the superlattice into account lowers the symmetry of both the orthorhombic and tetragonal structures to monoclinic with the c axis being unique. As shown in Fig. 8 this superstructure is different from those found in the double and triple CuO_2 layer compounds.

The other member of the $Tl_m\text{Ca}_{n-1}\text{Ba}_2\text{Cu}_n\text{O}_{2(n+1)+m}$ family which contains single CuO_2 layers, the 1:0:2:1 phase, has a primitive tetragonal cell and is not superconducting for the wide range of preparative conditions considered in this study, including growth from Cu-rich or Ca-doped starting compositions. No superstructures have been observed in these crystals so far.

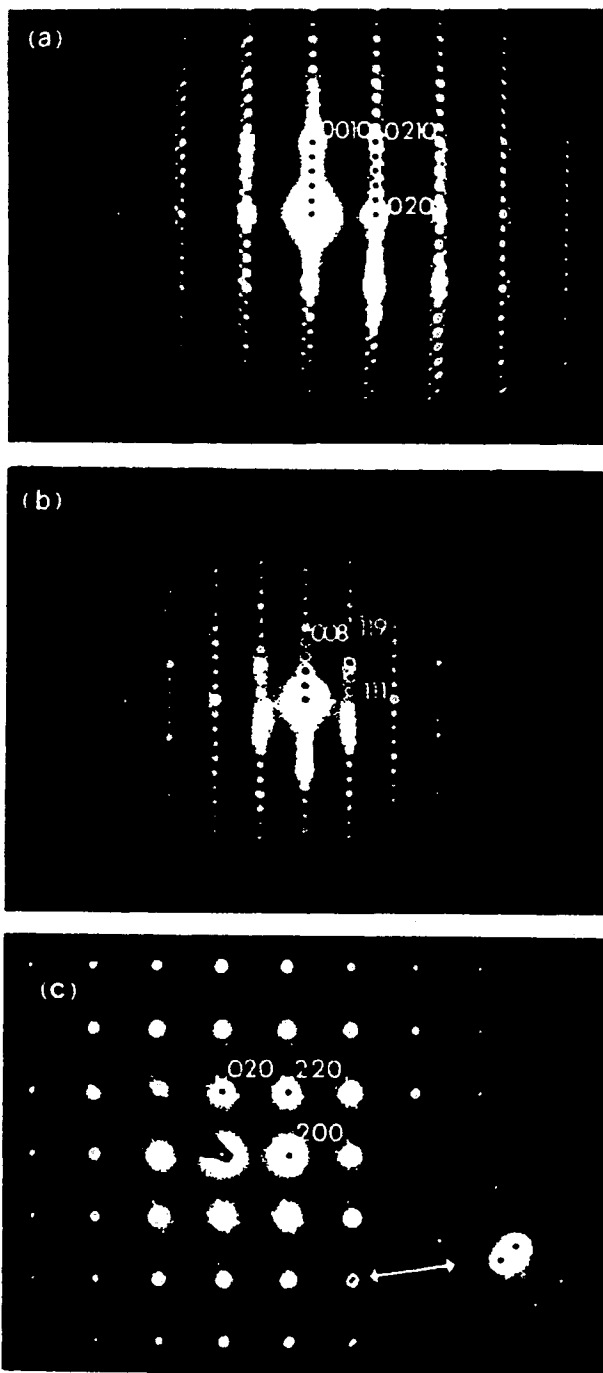


FIG. 8. (a) [100], (b) [110], and (c) [001] selected area diffraction patterns from a crystallite of 2:0:2:1.

As shown in Table I there is no obvious correlation of superlattice structure with the superconducting properties of the $Tl_mCa_{n-1}Ba_2Cu_nO_{2(n+1)+m}$ compounds. Note that in the closely related compound, $Bi_2Sr_1Ca_2Cu_2O_x$, it has recently been proposed that the observed incommensurate superlattice corresponds to a distortion of both the Bi-O and CuO₂ planes resulting from ordered vacancies

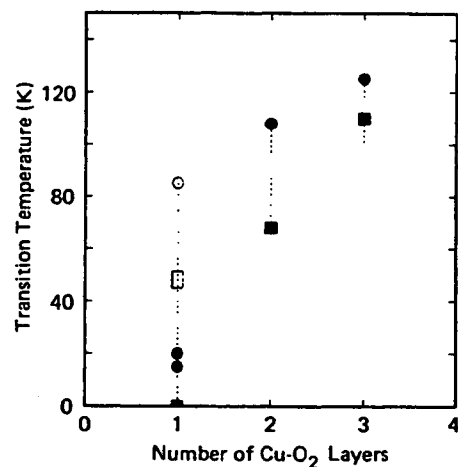


FIG. 9. Dependence of T_c on the number of CuO₂ planes within the Cu perovskitelike unit for the $Tl_1Ca_{n-1}Ba_2Cu_nO_{2n+3}$ (■) and $Tl_2Ca_{n-1}Ba_2Cu_nO_{2n+4}$ (●, this work; ○, Ref. 5) series of compounds. The dashed vertical lines correspond to the variations in T_c found for each phase. □ corresponds to data for $(Tl, Bi)_1(Ca, Sr)_2Cu_1O_x$ (Ref. 21).

on the Sr sites.¹⁶ The vacancies are postulated to determine the carrier density on the CuO₂ planes and so influence the T_c in a manner similar to that first noted by Schafer, Penney, and Olsen for the $La_{2-x}Sr_xCuO_{4-y}$ compounds.¹⁸ The number of different superlattice structures found in the Tl-Ca-Ba-Cu-O system provides a more extensive basis with which to test such hypotheses. Indeed it may be significant that, as shown in Table I, there are important variations in stoichiometry away from the ideal stoichiometries expected for the various $Tl_mCa_{n-1}Ba_2Cu_nO_{2(n+1)+m}$ phases. In particular, the [Tl]/[Ba] ratio is higher for the $n=1$ compounds compared to those for $n=2$ and $n=3$. Band-structure calculations of both the $Tl_mCa_{n-1}Ba_2Cu_nO_{2(n+1)+m}$ compounds and $Bi_2Sr_1Ca_2Cu_2O_x$ indicate that the stoichiometry of the Tl-O and Bi-O layers would have a profound impact on the carrier density in these materials.^{19,20} The extent of off-stoichiometry on the cation or the oxygen sites in the Tl-Ca-Ba-Cu-O phases requires further study. Note also that one group has recently prepared a complex material of the form $(Tl, Bi)_1(Ca, Sr)_2Cu_1O_x$ with the 1:0:2:1 structure which appears to superconduct at temperatures of up to 50 K (Ref. 21). The variation of properties of the single CuO₂ layers compounds provides a fertile area for further study and highlights the difficulties in preparing these multicomponent oxides in a controlled manner.

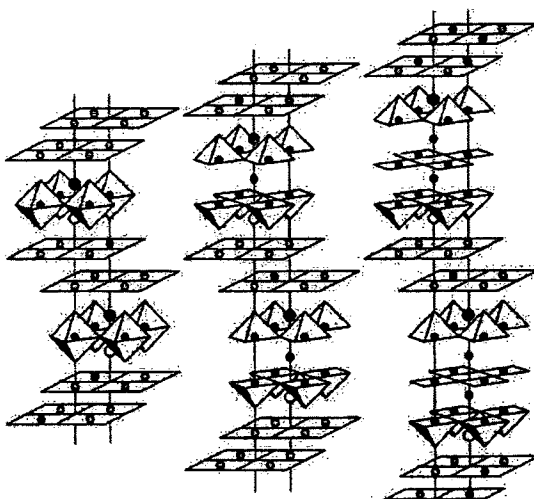
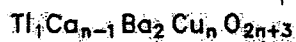
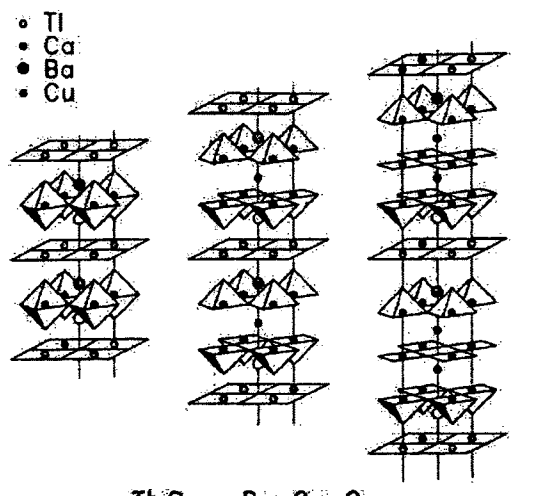
In conclusion, these studies have shown that the superconducting transition temperature increases with the number of CuO₂ planes in the perovskitelike unit for both the $Tl_1Ca_{n-1}Ba_2Cu_nO_{2n+3}$ and $Tl_2Ca_{n-1}Ba_2Cu_nO_{2n+4}$ structures (Fig. 9). A similar dependency is found in both series of compounds with an increased spread of T_c as the number of CuO₂ planes is reduced. The range of T_c in the double and triple CuO₂ layer compounds correlates with the density of intergrowth defects. No such defects have been observed so far in the single CuO₂ layer compounds,

even when doped with Ca. One might speculate that in this case the variation in transition temperature may result from variations in cation or oxygen site occupancy. The increase in T_c as n increases may be accounted for by various theories, including several based on the BCS theory¹⁹ and others invoking more exotic mechanisms such as the resonating-valence-bond model.²² The variety of structures and properties in the Tl-Ca-Ba-Cu-O system provides a model family of compounds with which various

theories of high-temperature superconductivity can be evaluated.

We are indebted to S. J. La Placa, F. Herman, and J. B. Torrance for many useful discussions. We thank C. C. Torardi, R. B. Flippen, and R. M. Hazen for discussions regarding the 2:0:2:1 compound. We are grateful to Professor Sinclair at Stanford for the use of his electron microscope.

-
- ¹Z. Z. Sheng and A. M. Hermann, *Nature (London)* **332**, 138 (1988); **332**, 55 (1988).
 - ²R. M. Hazen, L. W. Finger, R. J. Angel, C. T. Prewitt, N. L. Ross, C. G. Hadidiacos, P. J. Heaney, D. R. Veblen, Z. Z. Sheng, A. El Ali, and A. M. Hermann, *Phys. Rev. Lett.* **60**, 1657 (1988).
 - ³S. S. Parkin, V. Y. Lee, E. M. Engler, A. I. Nazzal, T. C. Huang, G. Gorman, R. Savoy, and R. Beyers, *Phys. Rev. Lett.* **60**, 2539 (1988).
 - ⁴S. S. Parkin, V. Y. Lee, A. I. Nazzal, R. Savoy, R. Beyers, and S. J. La Placa, *Phys. Rev. Lett.* **61**, 750 (1988).
 - ⁵C. C. Torardi, M. A. Subramanian, J. C. Calabrese, J. Gopalakrishnan, K. J. Morrissey, T. R. Askew, R. B. Flippen, U. Chowdry, and A. W. Sleight, *Science* **240**, 631 (1988).
 - ⁶M. A. Subramanian, J. C. Calabrese, C. C. Torardi, J. Gopalakrishnan, T. R. Askew, R. B. Flippen, K. J. Morrissey, U. Chowdry, and A. W. Sleight, *Nature (London)* **332**, 420 (1988).
 - ⁷S. Kondoh, Y. Ando, M. Onoda, and M. Sato, *Solid State Commun.* **65**, 1329 (1988).
 - ⁸W. Parrish, *X-ray and Electron Methods of Analysis* (Plenum, New York, 1968).
 - ⁹J. M. Tarascon, Y. Le Page, P. Barboux, B. G. Bagley, L. H. Greene, W. R. McKinnon, G. W. Hull, M. Giroud, and D. M. Hwang, *Phys. Rev. B* **37**, 9382 (1988).
 - ¹⁰S. A. Sunshine, T. Siegrist, L. F. Schneemeyer, D. W. Murphy, R. J. Cava, B. Batlogg, R. B. van Dover, R. M. Fleming, S. H. Glarum, S. Nakahara, R. Farrow, J. J. Krajewski, S. M. Zahurak, J. V. Waszczak, J. H. Marshall, P. Marsh, L. W. Rupp, and W. F. Peck, *Phys. Rev. B* **38**, 893 (1988).
 - ¹¹J. B. Torrance, Y. Tokura, S. J. LaPlaca, T. C. Huang, R. J. Savoy, and A. I. Nazzal, *Solid State Commun.* **66**, 703 (1988).
 - ¹²T. M. Shaw, S. A. Shivanshankar, S. J. LaPlaca, J. J. Cuomo, T. R. McGuire, R. A. Roy, K. H. Kelleher, and D. S. Yee, *Phys. Rev. B* **37**, 9856 (1988).
 - ¹³D. R. Veblen, P. J. Heaney, R. J. Angel, L. W. Finger, R. M. Hazen, C. T. Prewitt, N. L. Ross, C. W. Chu, P. H. Hor, and R. L. Meng, *Nature (London)* **332**, 334 (1988).
 - ¹⁴E. A. Hewat, M. Dupuy, P. Bordet, J. J. Capponi, C. Chaillet, J. L. Hodeau, and M. Marezio, *Nature (London)* **333**, 53 (1988).
 - ¹⁵H. W. Zandbergen, Y. K. Huang, M. J. V. Menken, J. N. Li, K. Kadokawa, A. A. Menovsky, G. van Tendeloo, and S. Amelinckx, *Nature (London)* **332**, 620 (1988).
 - ¹⁶P. L. Gai and P. Day (unpublished).
 - ¹⁷P. M. De Wolff, *Acta Crystallogr. Sec. A* **30**, 777 (1974).
 - ¹⁸M. W. Shafer, T. Penney, and B. L. Olsen, *Phys. Rev. B* **36**, 4047 (1987).
 - ¹⁹M. S. Hybertson and L. F. Mattheiss, *Phys. Rev. Lett.* **60**, 1661 (1988).
 - ²⁰F. Herman, R. V. Kasowski, and W. Y. Hsu, *Phys. Rev. B* **38**, 204 (1988); F. Herman, R. V. Kasowski, S. J. La Placa, and S. S. Parkin (unpublished).
 - ²¹P. Haldar, A. Roig-Janicki, S. Sridhar, and B. C. Giessen (unpublished).
 - ²²J. M. Wheatley, T. C. Hsu, and P. W. Anderson, *Nature (London)* **333**, 121 (1988).



n=1 n=2 n=3

FIG. 2. Nominal structures of the six $Tl_mCa_{n-1}Ba_2Cu_nO_{2(n+1)+m}$ phases for $n=1, 2$ and $m=1, 2, 3$.

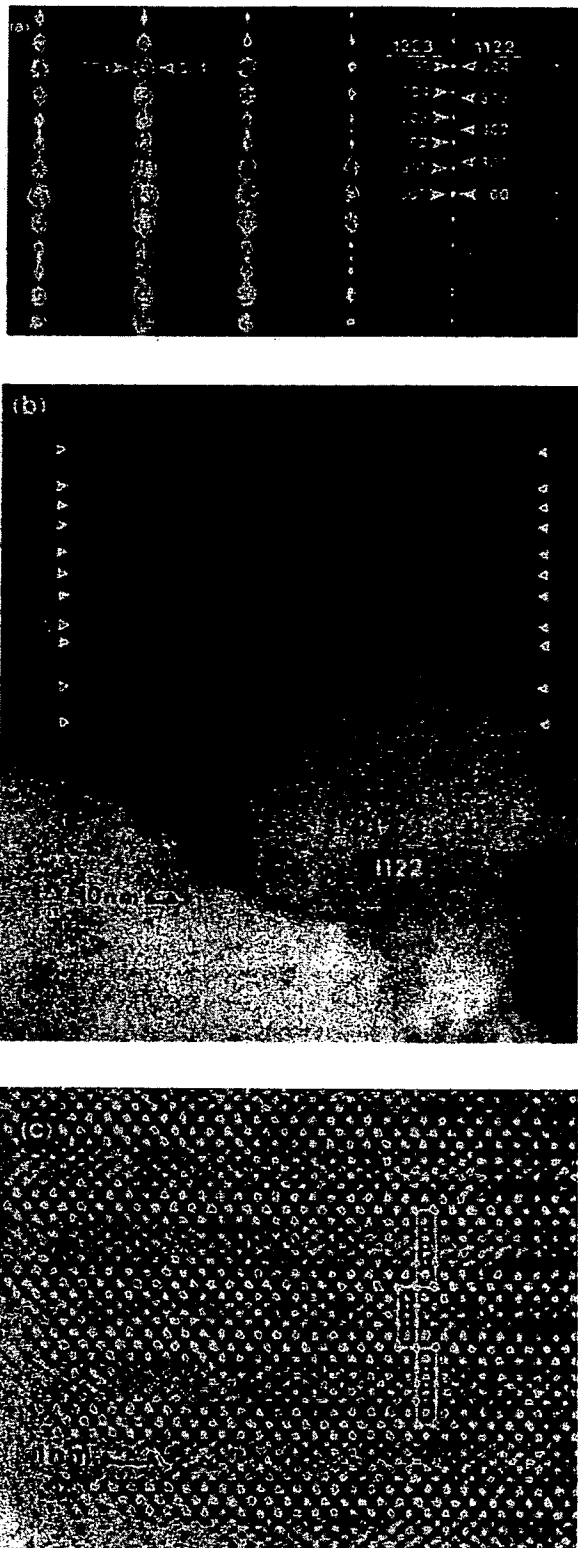


FIG. 3. (a) [010] selected area diffraction (SAD) pattern and (b) corresponding image of crystallites containing regions of 1:2:2:3 and 1:1:2:2. The arrows in (b) denote unit-cell thick intergrowths of 1:1:2:2 in 1:2:2:3. (c) High-resolution transmission electron micrograph of one unit-cell thick 1:1:2:2 intergrowth in 1:2:2:3.

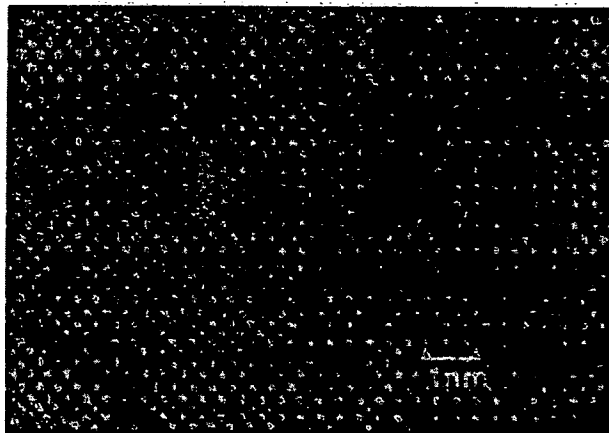


FIG. 5. High-resolution TEM image of an isolated four- CuO_2 -layer intergrowth. The markers denote the positions of the Cu columns.

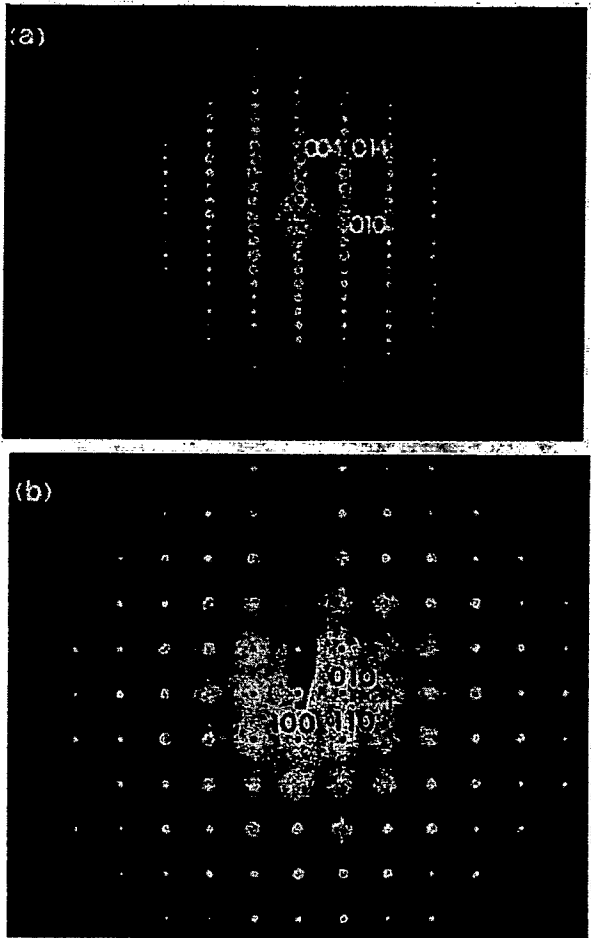


FIG. 7. (a) [100] and (b) [001] selected area diffraction patterns from crystallites of 1:1:2:2 showing superlattice reflections.

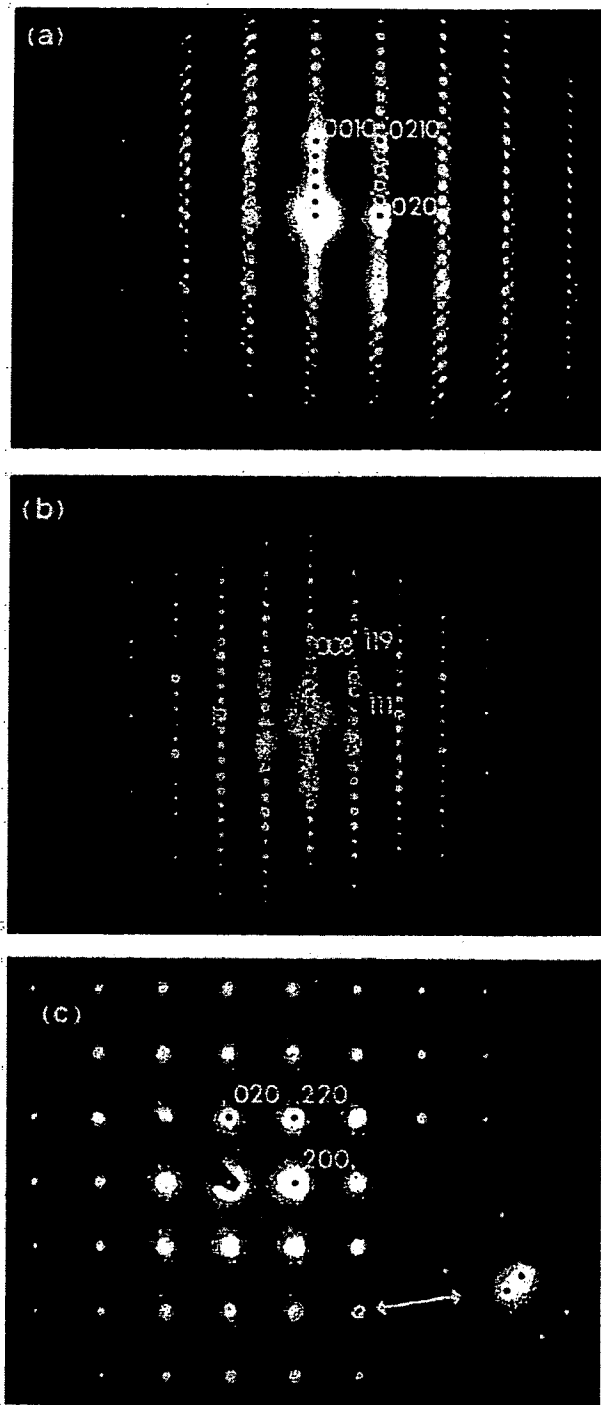


FIG. 8. (a) [100], (b) [110], and (c) [001] selected area diffraction patterns from a crystallite of 2:0:2:1.

BRIEF ATTACHMENT K

IN THE UNITED STATES PATENT AND TRADEMARK OFFICE

In re Patent Application of

Applicants: Bednorz et al.

Serial No.: 08/479,810

Filed: June 7, 1995

For: NEW SUPERCONDUCTIVE COMPOUNDS HAVING HIGH TRANSITION
TEMPERATURE, METHODS FOR THEIR USE AND PREPARATION

Date: March 1, 2005

Docket: YO987-074BZ

Group Art Unit: 1751

Examiner: M. Kopecky

Commissioner for Patents
P.O. Box 1450
Alexandria, VA 22313-1450

FIRST SUPPLEMENTAL AMENDMENT

Sir:

In response to the Office Action dated July 28, 2004, please consider the
following:

ATTACHMENT K

A New High- T_c Oxide Superconductor without a Rare Earth Element

Hiroshi MAEDA, Yoshiaki TANAKA, Masao FUKUTOMI and Toshihisa ASANO

National Research Institute for Metals, Tsukuba Laboratories, Ibaraki 305

(Received January 22, 1988; accepted for publication January 23, 1988)

We have discovered a new high- T_c oxide superconductor of the Bi-Sr-Ca-Cu-O system without any rare earth element. The oxide $\text{Bi}_2\text{Sr}_1\text{Ca}_1\text{Cu}_2\text{O}_x$ has T_c of about 105 K, higher than that of $\text{YBa}_2\text{Cu}_3\text{O}_7$, by more than 10 K. In this oxide, the coexistence of Sr and Ca is necessary to obtain high T_c .

KEYWORDS: oxide superconductor, Bi-Sr-Ca-Cu-O system, rare earth, high T_c , new stable superconductor

Soon after the discovery of high- T_c superconductors of the layered perovskites $(\text{LaBa})_2\text{CuO}_4$ ¹⁾ and $(\text{LaSr})_2\text{CuO}_4$ ²⁾ with T_c of about 40 K, $\text{YBa}_2\text{Cu}_3\text{O}_7$ ³⁾ with T_c of 94 K was synthesized. The discovery of these materials stimulated many researchers to investigate new oxide superconductors of still higher T_c and extensive studies have been carried out to search for these oxides. Up to now, however, no new stable superconductors with T_c higher than that of $\text{YBa}_2\text{Cu}_3\text{O}_7$ have been reported. The values of T_c have not improved by the substitution of other rare earth elements for yttrium.

In order to find high- T_c superconductors, we believe that it is important to investigate other classes of oxides which do not include rare earth elements. This led us to study the superconducting oxide system including the Vb-element group such as Bi and Sb of trivalent elements, and we discovered a new high- T_c superconducting material $\text{Bi}_2\text{Sr}_1\text{Ca}_1\text{Cu}_2\text{O}_x$. This oxide has T_c of about 105 K, being higher than that of $\text{YBa}_2\text{Cu}_3\text{O}_7$, by more than 10 K.

The value of T_c in the Bi-Sr-Cu-O oxide system which does not include Ca is very low being about 8 K.^{4,5)} In order to obtain high T_c , the coexistence of Sr and Ca in the Bi oxide system is found to be absolutely necessary.

The Bi-Sr-Ca-Cu-O oxide samples were prepared from powder reagents of Bi_2O_3 , SrCO_3 , CaCO_3 and CuO . The appropriate amounts of powders were mixed, calcined at 800–870°C for 5 h, thoroughly reground and then cold-pressed into disk-shape pellets (20 mm in diameter and 2 mm in thickness) at a pressure of 2 ton/cm². Most of the pellets were sintered at about 870°C in air or in an oxygen atmosphere and then furnace-cooled to room temperature.

The electrical resistivity was measured by the standard four-probe method for a bar-shaped specimen of about $1 \times 2 \times 20$ mm³ cut out from the pellets. Magnetization measurements were carried out with a vibrating sample magnetometer. The temperature was measured by Au7%Fe-Chromel thermocouples. Figure 1 shows the resistivity vs temperature curves of $\text{Bi}_2\text{Sr}_1\text{Ca}_1\text{Cu}_2\text{O}_x$ oxides thus prepared. Specimen (a) was sintered at a relatively low temperature of 800°C for 8 h while specimen (b) was sintered at a higher temperature of 882°C for 20 min followed by annealing at 872°C for 9 h. In the case of the lower sintering temperature, the onset temperature (T_c^{onset}) of the superconducting transition is about 83 K and the zero resistance state (T_c^{off}) is reached at 75 K (low- T_c

phase). On the other hand, in the case of a higher sintering temperature, a high- T_c phase appears, the onset temperature of which is about 120 K and T_c extrapolated to zero resistance is as high as 105 K. The value of T_c^{off} is higher than that of $\text{YBa}_2\text{Cu}_3\text{O}_7$, by more than 10 K. Since a little amount of the low- T_c phase still remained in the sample, a complete zero resistance state is achieved at 75 K which corresponds to that of the low- T_c phase. We have not succeeded in synthesizing the oxides with a single phase of the high- T_c material at this moment. From our preliminary experiments, we know that sintering at high temperatures for a short duration of time is effective enough to increase the relative amount of the high- T_c phase. This may indicate that the high- T_c phase is stable at elevated temperatures.

Figure 2 shows the magnetization vs temperature curve for the specimen (b) in Fig. 1 which was sintered at the higher temperatures. A Meissner effect showing a perfect diamagnetic state is observed exactly in the same temperature range as in curve (a) shown in Fig. 1. We conclude, therefore, that the present high- T_c phase is indeed superconducting.

The high- T_c phase appears near the composition ratios of $\text{Bi}:\text{Sr}:\text{Ca}=1:1:1$. As the composition deviates from

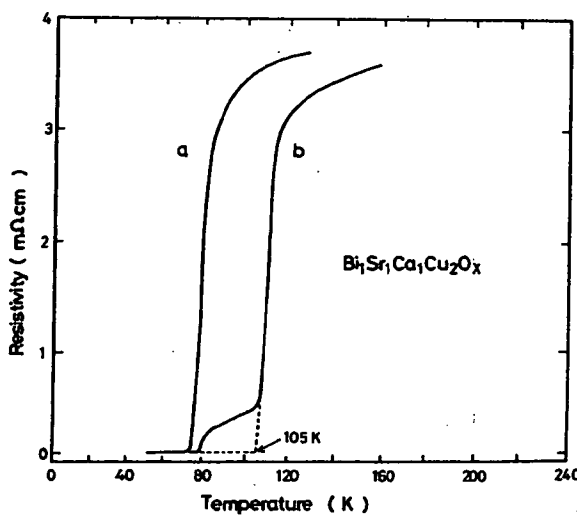


Fig. 1. Temperature dependence of resistivities in $\text{Bi}_2\text{Sr}_1\text{Ca}_1\text{Cu}_2\text{O}_x$ oxides (a) sintered in air at 800°C for 8 h, then cooled in a furnace and (b) sintered at 882°C for 20 min followed by annealing at 872°C for 9 h.

A New High- T_c Oxide Superconductor without a Rare Earth Element

Hiroshi MAEDA, Yoshiaki TANAKA, Masao FUKUTOMI and Toshihisa ASANO

National Research Institute for Metals, Tsukuba Laboratories, Ibaraki 305

(Received January 22, 1988; accepted for publication January 23, 1988)

We have discovered a new high- T_c oxide superconductor of the Bi-Sr-Ca-Cu-O system without any rare earth element. The oxide $\text{BiSrCaCu}_2\text{O}_x$ has T_c of about 105 K, higher than that of $\text{YBa}_2\text{Cu}_3\text{O}_7$, by more than 10 K. In this oxide, the coexistence of Sr and Ca is necessary to obtain high T_c .

KEYWORDS: oxide superconductor, Bi-Sr-Ca-Cu-O system, rare earth, high T_c , new stable superconductor

Soon after the discovery of high- T_c superconductors of the layered perovskites $(\text{LaBa})_2\text{CuO}_4$ ¹⁾ and $(\text{LaSr})_2\text{CuO}_4$ ²⁾ with T_c of about 40 K, $\text{YBa}_2\text{Cu}_3\text{O}_7$ ³⁾ with T_c of 94 K was synthesized. The discovery of these materials stimulated many researchers to investigate new oxide superconductors of still higher T_c and extensive studies have been carried out to search for these oxides. Up to now, however, no new stable superconductors with T_c higher than that of $\text{YBa}_2\text{Cu}_3\text{O}_7$ have been reported. The values of T_c have not improved by the substitution of other rare earth elements for yttrium.

In order to find high- T_c superconductors, we believe that it is important to investigate other classes of oxides which do not include rare earth elements. This led us to study the superconducting oxide system including the Vb-element group such as Bi and Sb of trivalent elements, and we discovered a new high- T_c superconducting material $\text{BiSrCaCu}_2\text{O}_x$. This oxide has T_c of about 105 K, being higher than that of $\text{YBa}_2\text{Cu}_3\text{O}_7$ by more than 10 K.

The value of T_c in the Bi-Sr-Cu-O oxide system which does not include Ca is very low being about 8 K.^{4,5)} In order to obtain high T_c , the coexistence of Sr and Ca in the Bi oxide system is found to be absolutely necessary.

The Bi-Sr-Ca-Cu-O oxide samples were prepared from powder reagents of Bi_2O_3 , SrCO_3 , CaCO_3 and CuO . The appropriate amounts of powders were mixed, calcined at 800–870°C for 5 h, thoroughly reground and then cold-pressed into disk-shape pellets (20 mm in diameter and 2 mm in thickness) at a pressure of 2 ton/cm². Most of the pellets were sintered at about 870°C in air or in an oxygen atmosphere and then furnace-cooled to room temperature.

The electrical resistivity was measured by the standard four-probe method for a bar-shaped specimen of about $1 \times 2 \times 20 \text{ mm}^3$ cut out from the pellets. Magnetization measurements were carried out with a vibrating sample magnetometer. The temperature was measured by Au7%Fe-Chromel thermocouples. Figure 1 shows the resistivity vs temperature curves of $\text{BiSrCaCu}_2\text{O}_x$ oxides thus prepared. Specimen (a) was sintered at a relatively low temperature of 800°C for 8 h while specimen (b) was sintered at a higher temperature of 882°C for 20 min followed by annealing at 872°C for 9 h. In the case of the lower sintering temperature, the onset temperature (T_c^{onset}) of the superconducting transition is about 83 K and the zero resistance state (T_c^{off}) is reached at 75 K (low- T_c

phase). On the other hand, in the case of a higher sintering temperature, a high- T_c phase appears, the onset temperature of which is about 120 K and T_c extrapolated to zero resistance is as high as 105 K. The value of T_c^{off} is higher than that of $\text{YBa}_2\text{Cu}_3\text{O}_7$ by more than 10 K. Since a little amount of the low- T_c phase still remained in the sample, a complete zero resistance state is achieved at 75 K which corresponds to that of the low- T_c phase. We have not succeeded in synthesizing the oxides with a single phase of the high- T_c material at this moment. From our preliminary experiments, we know that sintering at high temperatures for a short duration of time is effective enough to increase the relative amount of the high- T_c phase. This may indicate that the high- T_c phase is stable at elevated temperatures.

Figure 2 shows the magnetization vs temperature curve for the specimen (b) in Fig. 1 which was sintered at the higher temperatures. A Meissner effect showing a perfect diamagnetic state is observed exactly in the same temperature range as in curve (a) shown in Fig. 1. We conclude, therefore, that the present high- T_c phase is indeed superconducting.

The high- T_c phase appears near the composition ratios of $\text{Bi}:\text{Sr}:\text{Ca}=1:1:1$. As the composition deviates from

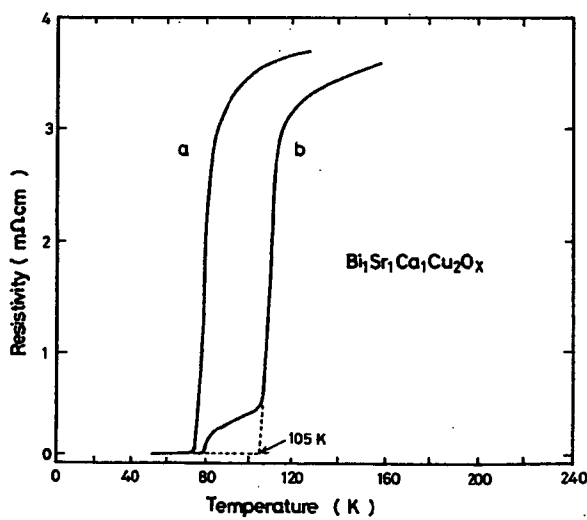


Fig. 1. Temperature dependence of resistivities in $\text{Bi}_{1-x}\text{Sr}_x\text{Ca}_{1-x}\text{Cu}_x\text{O}_x$ oxides (a) sintered in air at 800°C for 8 h, then cooled in a furnace and (b) sintered at 882°C for 20 min followed by annealing at 872°C for 9 h.

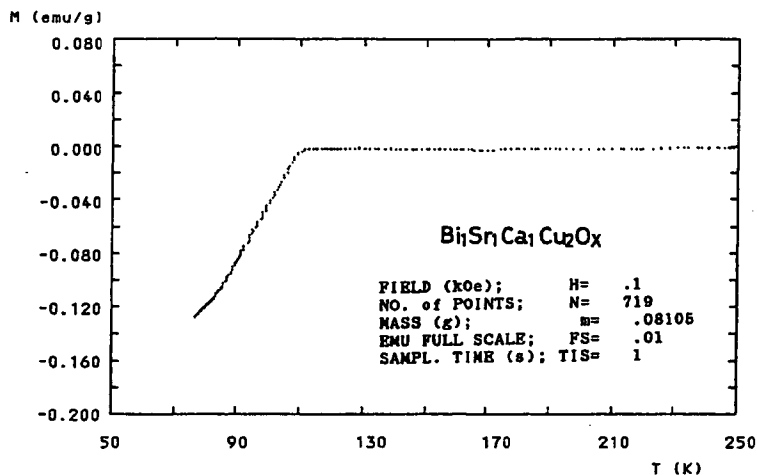


Fig. 2. Magnetization of $\text{Bi}_1\text{Sr}_1\text{Ca}_1\text{Cu}_2\text{O}_x$ for the sample (b) in Fig. 1 in a field of 100 Oe.

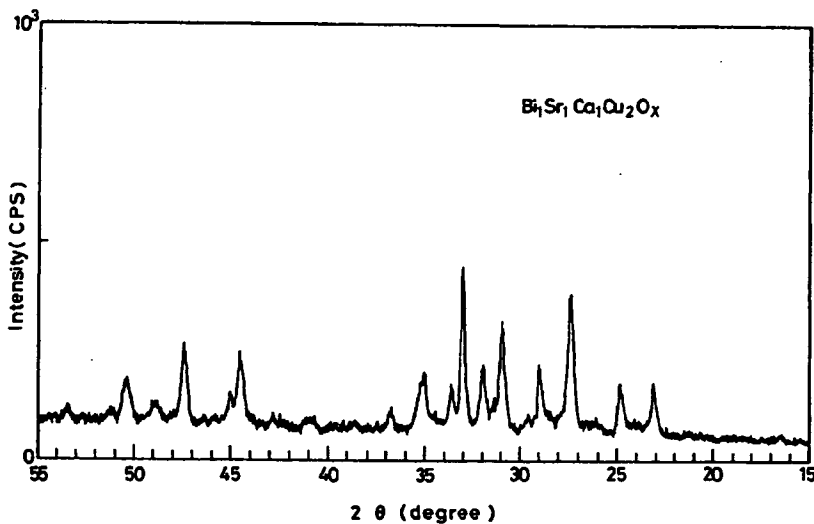


Fig. 3. X-ray ($\text{Cu } \text{K}\alpha$) diffraction pattern of the $\text{Bi}_1\text{Sr}_1\text{Ca}_1\text{Cu}_2\text{O}_x$ oxide superconductor for the sample (b) in Fig. 1.

this ratio, a low- T_c phase tends to appear irrespective of the sintering conditions. In $\text{Bi}_1\text{Sr}_1\text{Ca}_1\text{Cu}_y\text{O}_x$ oxides, the oxide of $y=1$ is not superconducting. According to the results of the X-ray diffraction analyses, the starting material corresponding to the composition of $\text{Bi}_1\text{Sr}_1\text{Ca}_1\text{Cu}_2\text{O}_x$ seems to form a single phase. While in the nominal composition of oxides with $y>2$, unreacted CuO remained in the sample. A typical X-ray diffraction pattern for the oxide of $y=2$ (sample (b) in Fig. 1) is shown in Fig. 3. Although the structure of this oxide is not identified yet, it appears to be different from those of $(\text{LaSr})_2\text{CuO}_4$ and $\text{YBa}_2\text{Cu}_3\text{O}_7$.

This material having high T_c above 105 K may have potential application in various industrial fields in the near future. It should be noted that these oxides are extremely stable in water and moisture and that no change in the superconducting properties has been observed even after the thermal cyclings between 4 K and room temperature or above.

Furthermore, the oxide has two phases with different

T_c and their structures seem to be different from those of high- T_c oxide superconductors discovered up to now. We believe that this new oxide will contribute greatly to elucidating the high- T_c superconducting mechanism.

Acknowledgements

We would like to thank Dr. M. Uehara for the measurements of magnetization and Dr. K. Ogawa for his useful discussions.

References

- 1) J. G. Bednorz and K. A. Müller: *Z. Phys.* **B64** (1986) 189.
- 2) S. Uchida, H. Takagi, K. Kitazawa and S. Tanaka: *Jpn. J. Appl. Phys.* **26** (1987) L1.
- 3) M. K. Wu, J. R. Ashburn, C. J. Torng, P. H. Hor, R. L. Meng, L. Gao, Z. J. Haang, Y. Q. Wang and C. W. Chu: *Phys. Rev. Lett.* **58** (1987) 908.
- 4) J. Akimitsu, A. Yamazaki, H. Sawa and H. Fujiki: *Jpn. J. Appl. Phys.* **26** (1987) L2080.
- 5) C. Michel, M. Hervieu, M. M. Borel, A. Grandin, F. Deslandes, J. Provost and B. Raveau: *Z. Phys.* **B68** (1987) 421.

BRIEF ATTACHMENT L

IN THE UNITED STATES PATENT AND TRADEMARK OFFICE

In re Patent Application of

Applicants: Bednorz et al.

Serial No.: 08/479,810

Filed: June 7, 1995

For: NEW SUPERCONDUCTIVE COMPOUNDS HAVING HIGH TRANSITION
TEMPERATURE, METHODS FOR THEIR USE AND PREPARATION

Date: March 1, 2005

Docket: YO987-074BZ

Group Art Unit: 1751

Examiner: M. Kopc

Commissioner for Patents
P.O. Box 1450
Alexandria, VA 22313-1450

FIRST SUPPLEMENTAL AMENDMENT

Sir:

In response to the Office Action dated July 28, 2004, please consider the
following:

ATTACHMENT L

The resulting map (Fig. 1e) shows that the absorption feature has a mean W of 0.2 nm and stretches from roughly north to south across the entire emission line region, corresponding to a length of >30 kpc (the map presents only the area with good signal-to-noise ratio). Its spatial width is rather uncertain, because it is unresolved in the east-west direction ($<1.5''$). It cannot be narrower than $0.5''$ because otherwise even a 100% obscuration would be washed out by our beam into a relative depression of $<25\%$ (0.25 nm). So we assume a projected size of 10×10 kpc 2 for the absorber, with a deconvolved equivalent width of about 0.5 nm.

Such an absorber can either consist of one or more clouds located well in front of 4C41.17 (if the blueshift of the absorption is cosmological, the absorber sits at a comoving distance of 5 Mpc). On the other hand, the velocity in the EELR itself is large enough to cover this blueshift; otherwise we would be unable to detect the feature. Thus, a dense, partially ionized cloud at the edge of 4C41.17 could equally explain the absorption. In this latter case more detailed observations are necessary for a physical interpretation. We therefore would like to pursue the former possibility of a physically separated absorber. Such clouds—commonly known as Lyman-forest clouds—and their properties have been extensively studied in the absorption line spectra of high redshift quasars.

For comparison we make use of a spectrum¹⁴ of the quasar Q0000-263 ($z = 4.11$), the Lyman-forest of which covers the λ range of our observation. We smoothed the original spectrum (resolution, 0.1 nm) to our instrumental resolution of 1.0 nm. The comparison between smoothed and original spectrum reveals that any absorption feature as deep as that observed in 4C41.17 typically consists of two or more narrow absorption lines. We have to realize therefore, that our 'absorption cloud' is likely to be a superposition of several individual Lyman-forest clouds. Nevertheless, we believe that the outline of the absorber in the W map (Fig. 1e) is most likely to be determined by one single cloud which made the feature strong enough to become detectable, and we assign half of the measured equivalent width (0.25 nm) to this cloud. Assuming a Doppler parameter $b = 35$ km s $^{-1}$ and $N_{\text{H}}/N_{\text{H}_2} = 10^{-4}$ as typical for Lyman clouds of that depth (refs 1, 3), we find a column density $N_{\text{H}} \sim 10^{15}$ cm $^{-2}$. A cigar-shaped cloud of 40 kpc length and 10 kpc diameter would contain a total hydrogen mass of $\sim 3 \times 10^7 M_{\odot}$.

What is the probability of detecting such an absorption feature in front of 4C41.17? Both the smoothed spectrum of Q0000-263 (ref. 14) and the standard $dN(W, z)/dz$ relation¹⁵ yield ~ 25 features with $W > 0.4$ nm on each line of sight and within one z unit at the observed wavelength. Considering the 'useful' wavelength range of ~ 1.2 nm (the blue half of the width of the emission line) in our search for line features, and the area of the EELR inspected of ~ 20 arcsec 2 , the probability of detecting a cloud of a typical size of a few arcsec 2 is close to 1.

In conclusion, we believe that we have succeeded in obtaining the first direct observation of a Lyman absorption cloud. Either this cloud belongs directly to the mass concentration around 4C41.17 or it is a physically separated foreground object. In the latter case it would represent the population of Lyman-forest clouds known from the absorption spectra of quasars. In either case, our observations indicate that the relevant absorbers have projected sizes of some 100 kpc 2 and an elongated shape, like a cigar or a sheet seen almost edge-on in the case of 4C41.17. □

Received 23 September 1992; accepted 19 January 1993.

- Chaffee, F. H., Folta, C. R., Beckhoff, J. & Weymann, R. J. *Astrophys. J.* **304**, 116–123 (1986).
- Carswell, R. F., Webb, J. K., Baldwin, J. A. & Atwood, B. *Astrophys. J.* **319**, 709–722 (1987).
- Rauch, M. et al. *Astrophys. J.* **390**, 387–404 (1992).
- Foltz, C. B., Weyman, R. J., Chaffee, H. J. & Chaffee, F. H. *Astrophys. J.* **281**, L1–L4 (1984).
- Smette, A. et al. *Astrophys. J.* **369**, 39–62 (1992).
- Tyler, D. *Astrophys. J.* **321**, 69–79 (1987).
- Pettini, M., Hunstead, R. W., Smith, L. J. & Mar, D. P. *Mon. Not. R. astr. Soc.* **246**, 545–564 (1990).
- Ikeuchi, S. in *Dark Matter in the Universe* (eds Salo, H. & Kotoma, H.) 50–62 (Springer, Berlin, 1990).

- Spinrad, H. in *Epoch of Galaxy Formation* (eds Frenk, C. S. et al.) 39–56 (Kluwer, Dordrecht, 1988).
- Lilly, S. *Astrophys. J.* **333**, 161–167 (1988).
- Chambers, K. C., Miley, G. K. & van Breugel, W. *Astrophys. J.* **363**, 21–39 (1990).
- Melsheimer, K. & Hippel, H. *Astr. Astrophys.* **284**, 455–471 (1992).
- Röser, S. & Bastian, U. *PPM Star Catalogue* (Spectrum Akad., Heidelberg, 1991).
- Webb, J. K. et al. *ESO Messenger* **63**, 15–18 (1988).
- Murdoch, H. S., Hunstead, R. W., Pettini, M. & Blades, J. C. *Astrophys. J.* **309**, 19–32 (1986).

ACKNOWLEDGEMENTS. We thank R. Carswell for the spectrum of Q0000-263 and H. Röser for discussions.

Superconductivity at 94 K in $\text{HgBa}_2\text{CuO}_{4+\delta}$

S. N. Putilin^a†, E. V. Antipov^a, O. Chmaissem^a
& M. Marezio^b‡

^a Chemical Department, Moscow State University,
119899 Moscow, Russia

^b Laboratoire de Cristallographie CNRS-LJF, BP 166,
38042 Grenoble Cedex 09, France

‡ AT&T Bell Laboratories, Murray Hill, New Jersey 07974, USA

FOLLOWING the discovery¹ of high-transition-temperature (high- T_c) superconductivity in doped La_2CuO_4 , several families of related compounds have been discovered which have layers of CuO_2 as the essential requirement for superconductivity: the highest transition temperatures so far have been found for thallium-bearing compounds². Recently the mercury-bearing compound $\text{HgBa}_2\text{RCu}_2\text{O}_{6+\delta}$ (Hg-1212) was synthesized³ (where R is a rare-earth element), with a structure similar to the thallium-bearing superconductor $\text{TlBa}_2\text{CaCu}_2\text{O}_7$ (Tl-1212), which has one TlO layer and two CuO_2 layers per unit cell, and a T_c of 85 K (ref. 2). But in spite of its resemblance to Tl-1212, Hg-1212 was found not to be superconducting. Here we report the synthesis of the related compound $\text{HgBa}_2\text{CuO}_{4+\delta}$ (Hg-1201), with only one CuO_2 layer per unit cell, and show that it is superconducting below 94 K. Its structure is similar to that of Tl-1201 (which has a T_c of <10 K)⁴, but its transition temperature is considerably higher. The availability of a material with high T_c but only a single metal oxide (HgO) layer may be important for technological applications, as it seems that smaller spacing between CuO_2 planes leads to better superconducting properties in a magnetic field⁵.

The samples were prepared by solid state reaction between stoichiometric mixtures of $\text{Ba}_2\text{CuO}_{3+\delta}$ and yellow HgO (98% purity, Aldrich). The precursor $\text{Ba}_2\text{CuO}_{3+\delta}$ was obtained by the same type of reaction between BaO_2 (95% purity, Aldrich) and CuO (NormaPur, Prolabo) at 930 °C in oxygen, according to the procedure described by De Leeuw *et al.*⁶. The powders were ground in an agate mortar and placed in silica tubes. All these operations were carried out in a dry box. After evacuation, the tubes were sealed, placed in steel containers, as described in ref. 3, and heated for 5 h to reach ~ 800 °C. The samples were then cooled in the furnace, reaching room temperature after ~ 10 h.

The formation of the new phase $\text{HgBa}_2\text{CuO}_{4+\delta}$ was revealed by X-ray powder analysis, performed with a Guinier-Hägg focusing camera and $\text{Fe K}\alpha$ radiation (1.93730 Å). Finely powdered silicon ($a = 5.43088$ Å at 25 °C) was used as an internal standard. The intensities of the reflections were evaluated by means of an automatic film scanner and indexed on a tetragonal cell with lattice parameters $a = 3.8797$ (5) Å, $c = 9.509$ (2) Å and assignment $Z = 1$. No systematic absences were observed, leading to the number of molecules per unit cell of the space group $P4/mmm$. The c parameter corresponded to the value calculated from the formula $c \approx 9.5 + 3.2(n - 1)$, similar to that deduced for the $\text{TlBa}_{2-n}\text{Cu}_n\text{O}_{2n+3}$ homologous series. We took this as a strong indication that the powder pattern corresponded to that of the first member of the $\text{HgBa}_2\text{R}_{n-1}\text{Cu}_n\text{O}_{2n+2+\delta}$ series.

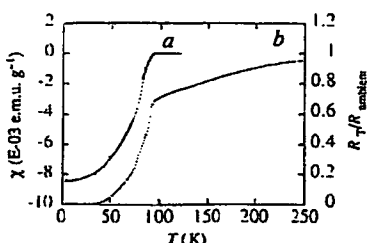


FIG. 1 AC magnetic susceptibility χ (a) and normalized resistivity (b) as a function of temperature for $\text{HgBa}_2\text{CuO}_{4+\delta}$.

Scanning electron microscopy using a JEOL SM 840A equipped with an energy-dispersive spectroscopy (EDS) attachment revealed that the sample was well crystallized with particle sizes of several micrometres. EDS analysis of several well crystallized, flat and oriented grains was performed. Beside Hg, Ba, Cu and O, no other element was detected in the spectra. The average metal ratio found for eight grains was $\text{Hg}:\text{Ba}:\text{Cu} = 28(1):47(2):25(1)$, where the numbers between parentheses are the standard deviations. Determination of the oxygen content by EDS analysis was not possible, so it was estimated by structural analysis and iodometric titration. The cation stoichiometry is in qualitatively good agreement with the proposed formula of the new compound.

Alternating-current magnetic susceptibility measurements between 4.2 and 120 K, done without any additional oxygen treatment, showed that $\text{HgBa}_2\text{CuO}_{4+\delta}$ samples undergo a transition from paramagnetic to diamagnetic with an onset as high as 94 K (Fig. 1a, where the susceptibility is in electromagnetic units g^{-1}). The estimated magnetic susceptibility at 4.2 K corresponds to >50% of the ideal diamagnetic values.

The resistivity was measured between 4.2 and 250 K by the four-probe technique. The sample was a pressed pellet which was annealed in oxygen for 2 h. The temperature dependence of the normalized resistivity, shown in Fig. 1, exhibits a sharp drop at T_c , but the transition is broad and it reaches the value of zero resistance only at 35 K. This behaviour indicates that the sample is not homogeneous.

To determine the structure of $\text{HgBa}_2\text{CuO}_{4+\delta}$, X-ray powder data were collected by a $\theta/2\theta$ STADI P diffractometer in transmission mode. The experimental conditions were as follows: 2θ range $= 6-115^\circ$ (0.02° steps) with fixed counting time 60 s and a rotating sample. An absorption correction was applied and the sample thickness was calculated from the primary beam absorption ($\mu R = 1.7$, where μ is absorption coefficient and R is thickness). The structural refinements were done by the Rietveld method. The initial positional parameters were deduced from a structural model containing the sequence $(\text{Hg})(\text{BaO})(\text{CuO}_2)(\text{BaO})(\text{Hg})$. After convergence (intensity discrepancy factor, $R_I = 0.039$), a Fourier difference map revealed that the position at $(\frac{1}{2}, \frac{1}{2}, 0)$ of the Hg layer was partially occupied. During the final cycle of refinement, the occupancy factor of a third oxygen atom placed in this position was varied together with the positional and thermal parameters for all atoms (except for the thermal parameter of O(3) which was kept fixed at 1.0 \AA^2). The final intensity (R_I) and profile (R_p) discrepancy factors based on 84 reflections were $R_I = 0.0367$ and $R_p = 0.116$, with a GOF (goodness of fit) = 0.33.

The final positional and thermal parameters together with the relevant interatomic distances are given in Table 1. Observed, calculated and difference diffraction patterns are shown in Fig. 2. A schematic representation of the structure is shown in Fig. 3. Preliminary structural refinements based on powder neutron diffraction data support the presence of oxygen in the O(3) position with an occupancy factor slightly larger than that found by X-ray powder diffraction data. The neutron data also

TABLE 1 Crystallographic data for $\text{HgBa}_2\text{CuO}_{4+\delta}$

Positional, thermal and occupancy parameters						
Atom	Position	x	y	z	$B_{iso} (\text{\AA}^2)$	Occupancy
Hg	1a	0	0	0	2.55 (5)	1.00
Ba	2h	0.5	0.5	0.2979 (1)	1.43 (4)	1.00
Cu	1b	0	0	0.5	0.88 (9)	1.00
O(1)	2e	0.5	0	0.5	0.4 (3)	1.00
O(2)	2g	0	0	0.206 (2)	2.2 (3)	1.00
O(3)	1c	0.5	0.5	0	1.0	0.10 (3)

Selected interatomic distances (Å)						
Hg-O(2) (x2)	1.95 (2)	Cu-O(1) (x4)	1.940 (1)	Ba-O(1) (x4)	2.730 (1)	
Hg-O(3)*	2.742 (1)	Cu-O(2) (x2)	2.79 (2)	Ba-O(2) (x4)	2.880 (5)	
				Ba-O(3)*	2.831 (1)	

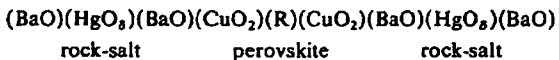
Data obtained using monochromatized $\text{CuK}\alpha_1$ radiation ($\lambda = 1.54056 \text{ \AA}$), giving $a = 3.87766(4) \text{ \AA}$, $c = 9.5073(1) \text{ \AA}$.

* Partially occupied sites.

confirm the large value for the mercury thermal factors. As in the case of the X-ray data, the anisotropic model shows a very slight difference between $B_{11} = B_{22}$ and B_{33} , the thermal factors along x , y and z respectively.

$\text{HgBa}_2\text{CuO}_{4+\delta}$ has a structure related to that of Hg-1212 (ref. 3). Its lattice parameters correspond to four-layered packing along the c -axis of a unit cell: $a = a_{\text{per.}}$, $c = 2a_{\text{per.}}$ (where $a_{\text{per.}}$ is the parameter of the perovskite subcell) and its structure contains the sequence $(\text{CuO}_2)(\text{BaO})(\text{HgO}_8)(\text{BaO})(\text{CuO}_2)$. The Cu cations are octahedrally coordinated, while the coordination of the other cations depends upon the value of δ . This, as obtained from powder X-ray data, is 0.10(3). An important consequence is that most of the Hg cations have two oxygen atoms near them in a 'dumb-bell' configuration, an appropriate coordination for Hg^{2+} cations. Because δ is small and different from zero (within about three standard deviations) X-ray powder data alone are insufficient to determine which sites of the rock-salt positions in the HgO layer are occupied and how they affect the Hg coordination. The extra oxygen atoms are needed in order to increase the average oxidation number of the Cu and to create the concentration of holes necessary for superconductivity. Iodometric titration performed with a large excess of KI leads to 16% of Cu^{3+} , corresponding to $\delta = 0.08$.

Similarly, the structure of $\text{HgBa}_2\text{RCu}_2\text{O}_{6+\delta}$ (the second member of the $\text{HgBa}_2\text{R}_{n-1}\text{Cu}_n\text{O}_{2n+2+\delta}$ series) can be described as six-layered blocks made of rock-salt and perovskite-type structures. In the structure of Hg-1212 the layer sequence is:



The CuO_2 monolayer in Hg-1201 has been replaced by the $(\text{CuO}_2)(\text{R})(\text{CuO}_2)$ block. As a consequence the Cu cations are

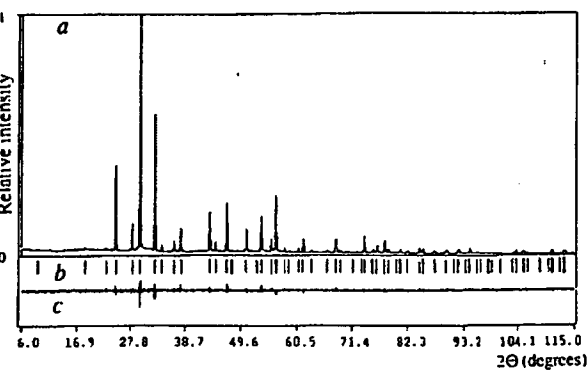


FIG. 2 Observed (a), calculated (b) and difference (c) powder patterns after Rietveld refinement for $\text{HgBa}_2\text{CuO}_{4+\delta}$.

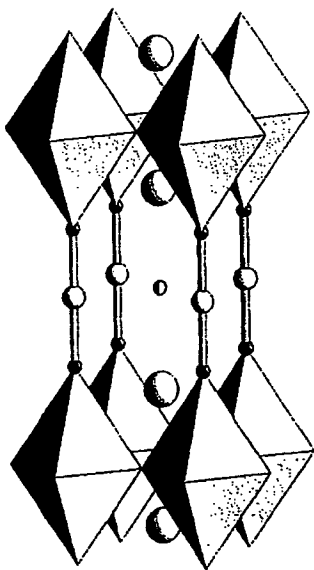


FIG. 3 Structure of $\text{HgBa}_2\text{CuO}_{4+\delta}$. The large, medium and small circles represent the Ba, Hg and O atoms, respectively. The Cu atoms are inside the octahedra. Note that the partially occupied oxygen O(3) site on the Hg layer is represented by a partially filled circle.

pyramidal coordination. The coordination of the Ba and Hg cations in Hg-1212 is similar to that of the same cations in Hg-1201. The R cations are surrounded by 8 oxygen atoms arranged as a prism. The valence of the Cu cations depends upon the value of δ and the valence of the R cations: if the same Cu valence or hole concentration as in Hg-1201 is needed to induce the superconducting state in Hg-1212, then the R cations should be 2^+ and δ_{1212} should be appreciably greater than δ_{1201} . For the previously reported Hg-1212, R was a mixture of Eu and Ca, and δ was not precisely determined³. It is possible that δ was not large enough to compensate for the higher valence of the R cations and to transfer the needed extra charges to CuO_2 layers.

As stated above, the structural arrangement of $\text{HgBa}_2\text{CuO}_{4+\delta}$ is similar to that of $\text{TlBa}_2\text{CuO}_{5-\delta}$, except for the oxygen stoichiometry of the HgO_8 and $\text{TiO}_{1-\delta}$ layers respectively. For the former, δ is very small and this depletion is possible because the dumb-bell coordination is appropriate for the Hg^{2+} cations. For the latter, the $\text{TiO}_{1-\delta}$ layer is only slightly oxygen depleted, creating the appropriate coordination for the thallium cations, resulting in either a distorted octahedron or a five-coordinated polyhedron. These different requirements for attaining the optimal concentration of holes are due to the different preferred coordination geometries of the Tl^{3+} and Hg^{2+} cations.

The first member of the latter series (Tl-1201) has been reported and found to become superconducting at <10 K (ref. 4). By doping the Ba sites with La this value can be increased to 52 K (ref. 7). The second member of the mono-Tl series becomes superconducting at 85 K (ref. 2). This increase is a general rule for the first few members of this series of compounds. If this behaviour holds for the Hg-series, the second member could reach values for T_c as high as those of the thallium.

The possible advantages for technical applications of $\text{HgBa}_2\text{CuO}_{4+\delta}$, in analogy with one-Tl-layer materials, would be due to the relatively short distance between CuO_2 layers. This might lead to lower anisotropy of the superconducting properties and to higher flux-melting temperatures than those of two-TlO-layer superconductors⁵.

Received 18 December 1992; accepted 12 February 1993.

1. Bednorz, J. G. & Müller, K. A. *Z. Phys.* **864**, 189–193 (1986).
2. Parkin, S. S. P. *et al.* *Phys. Rev. B* **38**, 6531–6537 (1988).
3. Putlin, S. N., Bryntse, I. & Antipov, E. V. *Mat. Res. Bull.* **26**, 1299–1307 (1991).
4. Copatkarshen, I. K., Yakhini, J. V. & Iyer, R. M. *Physica C* **175**, 183–186 (1991).
5. Kim, D. H. *et al.* *Physica C* **177**, 431–437 (1991).
6. De Leeuw, D. M., Mutsers, C. A. H. A., Lengerets, C., Smorenburg, H. C. A. & Rommers, P. J. *Physica C* **152**, 39–49 (1988).
7. Subramanian, M. A., Kwei, G. H., Parise, J. B., Goldstone, J. A. & Von Dreele, R. B. *Physica C* **166**, 19–24 (1990).

ACKNOWLEDGEMENTS. The authors thank R. V. Shapchenko and J. L. Tholence for their collaboration. S.N.P. thanks O. Massenet for a grant to attend the Laboratoire de Cristallographie of the CNRS, Grenoble. S.N.P. and E.V.A. are supported by grants from the Project "Polisk" of the Russian Scientific Council on Superconductivity.

Dependence of aggregate morphology on structure of dimeric surfactants

R. Zana* & Y. Taimon

Department of Chemical Engineering, Technion-Israel Institute of Technology, Haifa 32000, Israel

SURFACTANT molecules in water form organized assemblies of various shapes, such as micelles and bilayer lamellae, which are of interest as analogues of biological structures, as model systems for studying complex phase behaviour and because of their technological importance, for example to the food and paint industries. The polar head groups are usually arranged randomly at the surface of these assemblies. We have studied the effect on the microstructure of these assemblies of imposing constraints on the head-group spacing. We investigate the structures formed by 'double-headed' surfactants in which two quaternary ammonium species ($\text{C}_m\text{H}_{2m+1}\text{N}^+(\text{CH}_3)_2$) are linked at the level of the head groups by a hydrocarbon spacer (C_sH_{2s}). Here we report the microstructures formed by these dimeric surfactants with $m = 12$ and $s = 2, 3$ or 4 in aqueous solution, by rapidly cooling the micellar solutions and investigating the vitrified structures with transmission electron microscopy. The surfactants with a short spacer ($s = 2, 3$) form long, thread-like and entangled micelles even at low concentrations, whereas the corresponding monomeric ammonium surfactants can form only spherical micelles. The dimeric surfactants with $s = 4$ form spheroidal micelles. Thus short spacers (which impose reduced head-group separation) appear to promote lower spontaneous curvature in the assemblies. This approach may afford a new way to control amphiphilic self-aggregation.

Conventional surfactant molecules generally comprise two distinct parts that are incompatible with each other: one polar head and either one or two alkyl chains. These molecules tend to self-associate in water, where they produce micellar solutions in the dilute range, and lyotropic mesophases at higher concentrations. Whatever the structure, the surfactant polar heads are located at the interface between the hydrocarbon and water regions. Their relative positions and distances are determined mainly by their electrostatic interactions, and also by the packing requirements of the disordered alkyl chains^{1–3}. In caesium or rubidium soaps at low temperature in the presence of water, for example the head groups form well developed hexagonal or rectangular crystalline arrays⁴. Generally, however, they are arranged randomly, and little is known of their packing geometry or the width of their spacing distribution.

To investigate the effect of a perturbation of the local arrangement of polar heads on the micellar and mesomorphic properties

* To whom correspondence should be addressed in Haifa. On leave of absence from Institut Charles Sadron (CNRS), 6 rue Boussingault, 67083 Strasbourg Cedex, France.

BRIEF ATTACHMENT M

IN THE UNITED STATES PATENT AND TRADEMARK OFFICE

In re Patent Application of
Applicants: Bednorz et al.
Serial No.: 08/479,810
Filed: June 7, 1995

Date: March 1, 2005
Docket: YO987-074BZ
Group Art Unit: 1751
Examiner: M. Kopec

For: **NEW SUPERCONDUCTIVE COMPOUNDS HAVING HIGH TRANSITION
TEMPERATURE, METHODS FOR THEIR USE AND PREPARATION**

Commissioner for Patents
P.O. Box 1450
Alexandria, VA 22313-1450

FIRST SUPPLEMENTAL AMENDMENT

Sir:

In response to the Office Action dated July 28, 2004, please consider the
following:

ATTACHMENT M

Superconductivity near 70 K in a new family of layered copper oxides

R. J. Cava, B. Batlogg, J. J. Krajewski, L. W. Rupp, L. F. Schneemeyer, T. Siegrist, R. B. vanDover, P. Marsh, W. F. Peck, Jr, P. K. Gallagher, S. H. Glarum, J. H. Marshall, R. C. Farrow, J. V. Waszczak, R. Hull & P. Trevor

AT&T Bell Laboratories, Murray Hill, New Jersey 07974, USA

A new family of high-temperature superconductors is described, with the general formula $Pb_2Sr_2ACu_3O_{8+\delta}$. Although they have the planes of CuO_5 square pyramids characteristic of the other copper-oxide superconductors, the new compounds belong to a distinct structural series, with wide scope for elemental substitution. Their unusual electronic configuration also gives new insight into the role of charge distribution among the structural building blocks in controlling superconductivity.

SINCE the first observation¹ of high-transition-temperature (high- T_c) superconductivity in La-Ba-Cu-O, progress in the understanding of this remarkable phenomenon has been coupled to the discovery of new materials. Until now, three families of copper-oxide-based high- T_c superconductors have been identified, based on $(La,M)_2CuO_4$, $LaBa_2Cu_3O_7$, and $(Tl,Bi)_{m/2}(Ba,Sr)_2Ca_{n+1}Cu_nO_{m+2n+2}$ (ref. 2). (Here M represents a metal cation that may substitute on some La sites, and Ln represents a lanthanide.) Here we report the discovery of a new family of planar copper-oxide superconductors with general formula $Pb_2Sr_2ACu_3O_{8+\delta}$ (where A is a lanthanide or a mixture of Ln + Sr or Ca), and describe the synthesis, crystal structure and properties of prototype compounds. We find, for example, that one preliminary optimal composition $Pb_2Sr_2Y_{0.5}Ca_{0.5}Cu_3O_8$ has a superconducting T_c of 68 K. The new family displays the same kind of rich substitutional chemistry as is observed for $LaBa_2Cu_3O_7$, with the phase forming for Y and at least La, Pr, Nd, Sm, Eu, Gd, Dy, Ho, Tm, Yb and Lu, spanning the entire rare-earth series. Wide ranges of large-metal-atom solid solution and oxygen stoichiometry are observed, suggesting many possible avenues to be explored for the optimization of superconducting properties.

Superconductivity is induced in the host compounds $Pb_2Sr_2LnCu_3O_{8+\delta}$ ($\delta = 0$) either by partial substitution of a divalent ion (such as Sr or Ca) on the lanthanide site, or possibly by the accommodation of excess oxygen ($\delta > 0$), or a combination of both. The compounds can be synthesized only under mildly reducing conditions, which are necessary to maintain Pb in a 2+ oxidation state. Oxidation of $\delta = 0$ compounds is possible, but only at low temperatures, where decomposition to a Pb(IV)-containing perovskite is sluggish. Remarkably, the formal average oxidation state of copper in the superconductors is less than 2+, but a clear structural distinction between different types of copper layers leads us to hypothesize that holes are nonetheless present on electronically active CuO pyramidal planes.

Synthesis

The preparative conditions for the new materials are considerably more stringent than for the previously known copper-based superconductors. Direct synthesis of members of this family by reaction of the component metal oxides or carbonates in air or oxygen at temperatures below 900 °C is not possible because of the stability of the oxidized $SrPbO_3$ -based perovskite. Successful synthesis is accomplished by the reaction of PbO with pre-reacted (Sr, Ca, Ln) oxide precursors. The precursors are prepared from oxides and carbonates in the appropriate metal ratios, calcined for 16 hours (in dense Al_2O_3 crucibles) at 920–980 °C in air with one intermediate quenching. Some of the

$Pb_2Sr_2LnCu_3O_{8+\delta}$ compounds can be prepared in air from $PbO + LnSr_2Cu_3O_x$ precursor mixtures, which are not reacted at temperatures below ~850 °C. For example, single-phase $Pb_2Sr_2YCu_3O_{8+\delta}$ ($\delta = 0$) can be prepared by reacting PbO with $YSr_2Cu_3O_x$ at 920 °C for 1 h, followed by quenching. Slower cooling results in partial decomposition through oxidation. Short reaction times are generally sufficient to obtain single-phase products. The same air-heating/quenching process does not appear to work, however, for $Pb_2Sr_2LaCu_3O_{8+\delta}$ or $Pb_2Sr_2LuCu_3O_{8+\delta}$.

The best synthetic conditions found so far involve the reaction of PbO with the cuprate precursors in thoroughly mixed pressed pellets. Reaction temperatures are between 860 and 925 °C, for times between 1–16 h, in a flowing gas stream of 1% O_2 in N_2 , a mildly reducing atmosphere. For $Pb_2Sr_2Y_{1-x}Ca_xCu_3O_{8+\delta}$, for example, single-phase materials are obtained for $0 \leq x \leq 0.5$ in 1% O_2 after heating overnight at 865 °C and cooling in the gas stream to room temperature in 15 minutes. Using higher temperatures, higher p_{O_2} in the gas stream or higher Ca contents of the starting mixture results in the intergrowth of 123-type $YSr_2(Pb,Cu)_3O_x$ with the new compound, or the formation of an $SrPbO_3$ -based second phase. Similar procedures are successful for other Sr/rare-earth/Ca combinations. The oxygen contents of $Pb_2Sr_2Y_{1-x}Ca_xCu_3O_{8+\delta}$ for $0 \leq x \leq 0.50$, prepared under these conditions, are measured by reduction in H_2 and are uniformly $\delta = 0 \pm 0.1$. Ca is employed as a dopant on the Ln site because it has an ionic size similar to the intermediate rare-earths. We have not yet found synthetic conditions under which $Pb_2Sr_{2+x}Ln_{1-x}Cu_3O_{8+\delta}$ solid solutions can be prepared as single-phase polycrystalline samples that are good bulk superconductors, although superconducting single crystals of that stoichiometry have been prepared.

Single crystals of the superconducting compounds were grown from PbO- and CuO-rich melts using a similar precursor technique. Melt compositions were generally $Pb_{3.5}Sr_2YCu_4O_x$. Following a 30-min soak at 1,025 °C, samples were cooled at 2 °C min⁻¹ in the 1% O_2 atmosphere to temperatures between 800 and 400 °C, and were then rapidly cooled to room temperature in the same gas stream. Crystals are plate-like in habit, but are generally more equiaxed than those of $LaBa_2Cu_3O_7$.

Stoichiometry and crystal structure

Compounds of stoichiometry $Pb_2Sr_2LnCu_3O_8$ ($\delta = 0$) are not bulk superconductors, although we often observe small amounts of superconductivity (1% or less) in materials of that stoichiometry prepared either by the quench or by the 1%- O_2 synthetic techniques. The non-bulk superconductivity may be due to inhomogeneities in either oxygen content or Sr/Ln distribution.

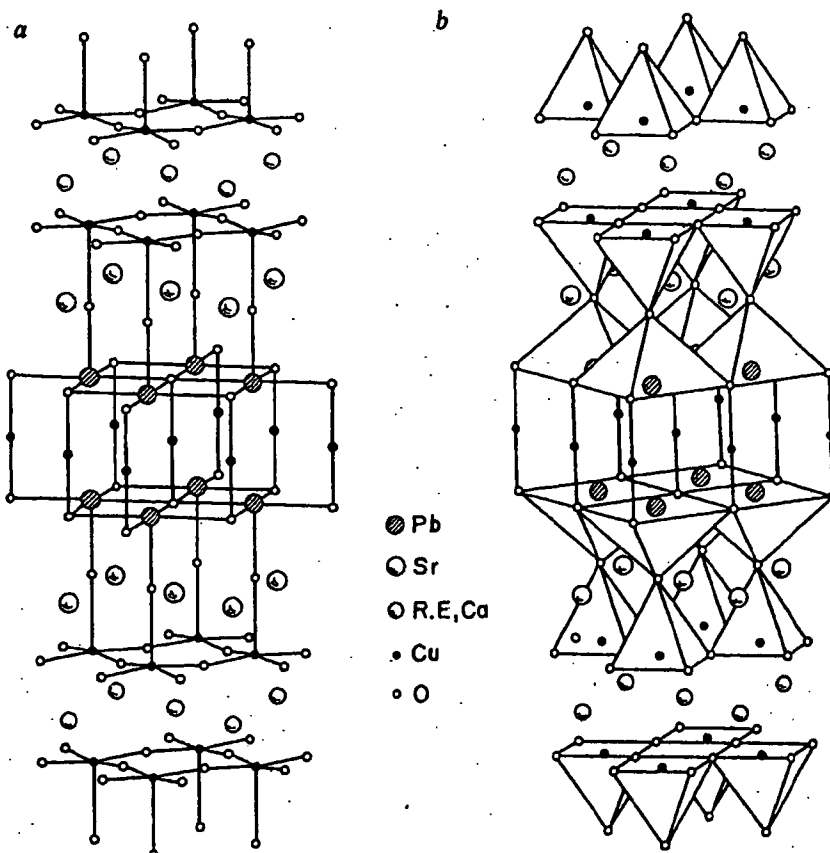


Fig. 1 Two representations of the crystal structure for the new superconducting compounds, for the case of $Pb_2Sr_{2.24}Nd_{0.76}Cu_3O_{8+\delta}$. Representation *a* emphasizes the Cu-O and Pb-O bonding scheme, and representation *b* emphasizes the manner in which Cu-O and Pb-O coordination polyhedra are arranged.

The range of oxygen contents possible for these compounds is remarkable. $Pb_2Sr_2YC_{u_3}O_{8+\delta}$, $\delta=0$, for example, can be oxidized by heating in O_2 to temperatures below 500 °C for short times (2–4 h) to δ values of ~1.6, retaining the same basic crystal structure. We have observed values as large as $\delta=1.8$ for $Pb_2Sr_2Y_{0.75}Ca_{0.25}Cu_3O_{8+\delta}$. Oxidation at temperatures higher than 500 °C, or for longer reaction periods, generally results in decomposition to the $SrPbO_3$ -based perovskite. Powder samples of $Pb_2Sr_2YC_{u_3}O_{8+\delta}$ with large values of δ are not superconducting. Single crystals of the $Pb_2Sr_{2+x}Ln_xCu_3O_{8+\delta}$ type are superconductors with transition temperatures between 10 and 70 K. These crystals may have non-zero values of δ but have not yet been fully characterized. The range of T_c s observed suggests a complex and interesting relationship between T_c , δ and the Sr:Ln ratio.

Powder X-ray diffraction indicates that the new phases have an orthorhombic unit cell which is based on a many-layer perovskite structure. The characteristic X-ray pattern for the prototype compound $Pb_2Sr_2YC_{u_3}O_8$ is presented in Table 1. The compound deviates only slightly from tetragonal symmetry. The simplest cell consistent with the X-ray pattern is *c*-centred, with lattice parameters $a=5.40$, $b=5.43$, and $c=15.74$ Å. Systematic absences are consistent with a *c*-centred cell down to the detectability limit of 1% maximum intensity. The orthorhombic cell gives an excellent fit to the powder diffraction pattern but a hint of a shoulder on the high 2θ side of the 314 reflection indicates that the true symmetry may be weakly monoclinic. Although the lattice parameters for this family of compounds are very similar to those reported for $TlBa_2Ca_2Cu_3O_8$ (ref. 3), the crystal structures are quite different. Electron microscope investigations indicate that for some crystals, weak (but sharp) reflections are present which violate the *c*-centring. Furthermore, these studies show the presence of long-period, long-range-ordered superlattices in the *a*-*b* plane, suggesting that a variety of structural distortions and stoichiometry-driven atom-ordering schemes can occur.

The crystal structure of compounds in this family, determined for a superconducting Nd-based single crystal of approximate stoichiometry $Pb_2Sr_{2.24}Nd_{0.76}Cu_3O_{8+\delta}$ (determined by structure refinement) is shown in Fig. 1. The crystal employed in the structural determination was twinned, as expected from the pseudo-tetragonal symmetry. The atomic coordinates are reported in the *c*-centred orthorhombic cell to be consistent with the powder data, but a primitive cell with *a* and *b* rotated by 45° and reduced by $\sqrt{2}$ gives an equally good description of the single-crystal data. The very small scattering cross-section of oxygen precludes determination of δ by refinement. The data are well fitted by the structural model (refinement parameter $R=3.7\%$), but a microscopic explanation of the orthorhombic symmetry is not apparent; if the origin is primarily in the oxygen sublattice we would not be able to detect it in the X-ray structure determination.

The basis of the structure comprises infinite planes of corner-shared CuO_5 pyramids separated by eight-coordinate rare-earth atoms, as are common to all the presently known copper-based superconductors with $T_c>50$ K. The four in-plane copper-oxygen distances are ~1.9 Å, and the distance to the apical oxygen is ~2.3 Å, both of which are very similar to those observed in $YBa_2Cu_3O_7$. The structural components unique to the new class of materials are the $PbO-CuO_5-PbO$ planes shown in the centre of the Fig. 1. For $\delta=0$, Pb has a distorted flattened square pyramid coordination (sharing edges with adjacent pyramids), with the lone pair pointing toward the vacant sixth site of the coordination octahedron. The PbO_5 pyramids are separated by a single copper layer, which, for $\delta=0$, is oxygen-free, and displays an O-Cu-O coordination characteristic of Cu^{1+} (Cu-O distance ~1.8 Å), as is observed in non-superconducting $YBa_2Cu_3O_6$. During the low-temperature oxidation process, oxygen is apparently accommodated in this copper layer, resulting in a large expansion of the *c* axis. The PbO_5 and CuO_5 pyramidal planes are joined by the common oxygens at their apices. The Sr atoms are coordinated to nine oxygens, as in $(La,$

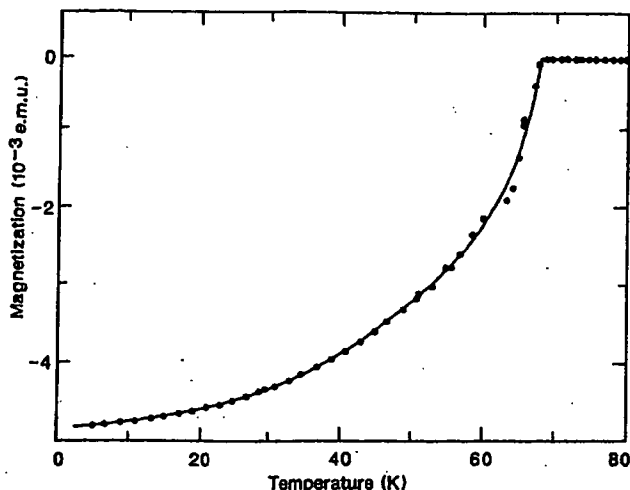


Fig. 2 Magnetization data (d.c. field-cooled at 25 Oe) for $\text{Pb}_2\text{Sr}_2\text{Y}_{0.5}\text{Ca}_{0.5}\text{Cu}_3\text{O}_8$.

Sr_2CuO_4 , and the Ln site is eight-coordinate, as in the $\text{LnBa}_2\text{Cu}_3\text{O}_7$ family, sandwiched between the CuO_5 pyramidal planes. In the superconducting compound $\text{Pb}_2\text{Sr}_2\text{Y}_{1-x}\text{Ca}_x\text{Cu}_3\text{O}_{8+\delta}$, Ca partially substitutes for Y in the eight-coordinate site.

The crystal structures of all the known copper-oxide-based superconductors are generally described as many-layered perovskites. The similarities and differences among them are most easily illustrated in terms of the stacking sequences of rocksalt-like (AO) and perovskite-like (BO₂) layers². Taking, for example, representatives from the superconductor families that have double CuO₅ pyramidal layers, the stacking sequences are:

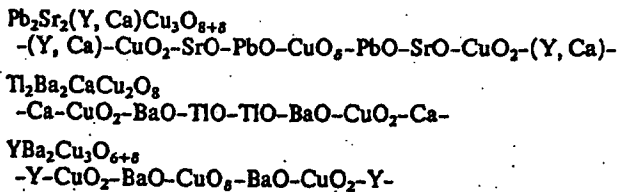


Table 1 Characteristic X-ray powder diffraction pattern for $\text{Pb}_2\text{Sr}_2\text{YC}_3\text{O}_8$

hkl	d	I/I_0	hkl	d	I/I_0
001	15.74	7	116	2.164	11
002	7.87	3	025	2.057	12
003	5.25	2	205	2.050	10
004	3.94	10	008	1.967	7
110	3.831	11	220	1.915	25
111	3.722	24	118, 009	1.750	2
112	3.444	1	027, 207	1.730	1
005	3.148	11	224	1.722	2
113	3.094	11	130	1.717	2
114	2.745	100	310, 131	1.708	3
020	2.717	43	311	1.699	2
200	2.701	43	225	1.636	3
021	2.677	7	133	1.632	3
201	2.662	7	313	1.625	1
006	2.623	6	028	1.593	11
023	2.412	1	208, 119	1.591	11
203	2.401	1	134	1.574	18
024	2.236	2	314	1.568	14
204	2.227	1			

Cu K α radiation, 0–60° 2θ c-centred orthorhombic cell, preliminary indexing, true symmetry may be weakly monoclinic. Lattice parameters $a = 5.4019(15)$, $b = 5.4333(15)$, $c = 15.7388$.

The new superconductors, then, can be seen to be intimately related in structure to those previously described. They can be considered as related to $\text{Tl}_2\text{Ba}_2\text{CaCu}_3\text{O}_8$ by insertion of a single CuO_8 layer between adjacent polarizable AO layers, or related to $\text{YBa}_2\text{Cu}_3\text{O}_{6+\delta}$ by sandwiching of the CuO_8 'chain' layer by two PbO layers. We believe that it is the electronic screening of the CuO_2 planes from the CuO_8 layers by the PbO layers that makes the new superconductors of considerable interest. Furthermore, we expect these materials to be even more anisotropic in their physical properties than those previously known, as the double pyramidal CuO_2 -A- CuO_2 layers are widely separated.

Superconducting properties

We have studied the composition dependence of the superconducting properties of compounds in the series $\text{Pb}_2\text{Sr}_2\text{Y}_{1-x}\text{Ca}_x\text{Cu}_3\text{O}_8$ for $0 \leq x \leq 0.75$, by estimating the flux expulsion measured on cooling in a field of 25 Oe in a d.c. SQUID magnetometer (S.H.E. model 905). The greatest flux expulsion occurs for $x = 0.5$, and is ~20% of the ideal value (see Fig. 2). Because flux becomes trapped in the pores of these low-density ceramics, this is an underestimate of the true volume fraction of superconductivity. For $x \geq 0.5$, the materials were not entirely single-phase, with one or more impurity peaks having a maximum intensity of 5% of the strongest peak in the powder X-ray pattern. This, coupled with the estimate of the volume fraction of superconductivity, suggests that the optimal superconducting composition may have x somewhat greater than 0.5. This could be achieved if different synthetic methods can be found that allow a larger range of solid solution to be attained. We have measured the normal-state susceptibility (in a 20-kOe field) for temperatures below 400 K of apparently single-phase samples (no unindexed X-ray lines to 0.5% maximum intensity) of the non-superconducting endmember $\text{Pb}_2\text{Sr}_2\text{YC}_3\text{O}_8$ and superconducting $\text{Pb}_2\text{Sr}_2\text{Y}_{0.625}\text{Ca}_{0.375}\text{Cu}_3\text{O}_8$. The susceptibility of the superconductor (χ) is essentially temperature independent ($\chi \approx 1 \times 10^{-4}$ e.m.u. per mole formula unit), with only a slight decrease at low temperatures. This temperature dependence is similar to that of high-quality $\text{YBa}_2\text{Cu}_3\text{O}_7$, and is characterized by the absence of a Curie-Weiss contribution. Furthermore, this supports our conclusion that the copper atoms between the PbO layers are Cu^{+4} . Post-oxidation at 500 °C results in oxidation of this copper to magnetic Cu^{+2} . $\text{Pb}_2\text{Sr}_2\text{YC}_3\text{O}_8$ appears to be magnetic (~0.5 μB per Cu atom), but further studies are necessary to clarify whether this is intrinsic or is due to the presence of highly magnetic impurity phases that are undetectable by X-ray diffraction.

Figure 3 shows the temperature dependence of the resistivity for a single crystal of $\text{Pb}_2\text{Sr}_2\text{Dy}_{1-x}\text{Ca}_x\text{Cu}_3\text{O}_{8+\delta}$. The midpoint of the superconducting transition is at 51.5 K (indicated by an arrow in Fig. 3), although there is a small foot which gives a zero-resistance T_c of 46 K. Above T_c the temperature

Table 2 Crystallographic data for $\text{Pb}_2\text{Sr}_{2.24}\text{Nd}_{0.76}\text{Cu}_3\text{O}_{8+\delta}$

Atom	Position	x	y	z	$B_{\text{iso}} [\text{\AA}^2]$
Pb	4l	1/2	0	0.38858(4)	1.09(2)
Sr	4k	0	0	0.22184(9)	0.74(4)
Nd, Sr*	2a	0	0	0	0.69(3)
Cu1	2d	0	0	1/2	0.86(9)
Cu2	4l	1/2	0	0.11074(13)	0.46(5)
O1	4l	1/2	0	0.2546(8)	1.5(5)
O2	4k	0	0	0.384(3)	13(5)
O3	8m	1/4	1/4	0.0995(5)	0.9(3)

Orthorhombic cell (pseudotetragonal substructure); $a = 5.435(1)\text{\AA}$, $b = 5.463(1)\text{\AA}$, $c = 15.817(3)\text{\AA}$; space group $Cmmm$, $z = 2$; observed reflections 707, $R_w = 0.037$.

* Mixed occupancy site: (1) Sr, 0.76(1) Nd.

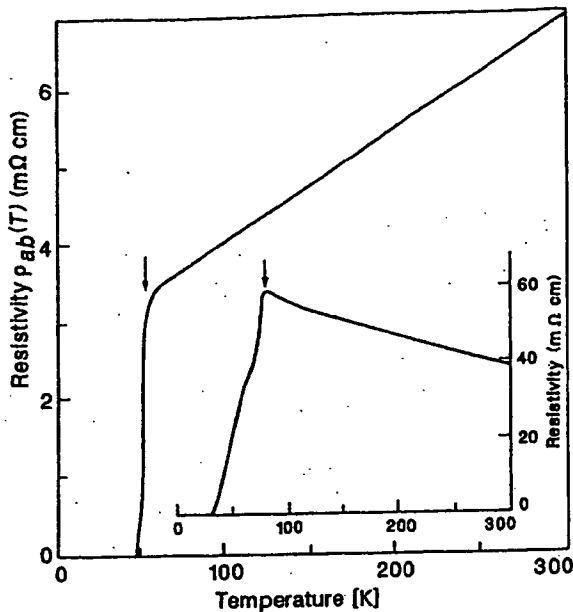


Fig. 3 Resistivity in the a - b plane as a function of temperature for a single crystal of $Pb_2Sr_2(Dy,Ca)Cu_3O_{8+\delta}$. Inset, typical temperature-dependent resistivity for a polycrystalline sample of $Pb_2Sr_2(Y,Ca)Cu_3O_8$.

dependence is fairly linear, but near T_c there is a region of positive curvature which, along with the resistivity foot, we attribute to small inhomogeneities in the metal and/or oxygen distribution. The scale of the resistivity is a factor of ten greater than for previous oxide superconductors. It is not yet clear whether this is an intrinsic property.

A typical resistivity curve for a ceramics sample is shown in the inset to Fig. 3, illustrating the typically broad transitions observed. The transition in this sample begins at 79 K (arrow) but zero resistance is achieved (within instrumental accuracy) as 32 K. Note that the resistivity scale is again quite high. We attribute the breadth of the transition and the negative normal-state temperature coefficient to inhomogeneity in the metal and/or oxygen distribution, rather than to exogenous phases at the grain boundaries. The behaviour of this system seems to be very similar to that of $(La,Sr)_2CuO_4$ (ref. 4).

Electronic aspects

Given that the average formal copper valence of previously known superconductors has always been greater than +2, the new superconductors are unique and, at first sight, anomalous. For the series $Pb_2Sr_2Y_{1-x}Ca_xCu_3O_8$, the average formal copper valence increases from 1.67 in the non-superconducting $x=0$ member to ~ 1.92 at the maximum Ca concentration studied. At our current estimate of the optimal superconducting composition ($x=0.5$), the average formal valence is 1.83. The linear coordination of the copper atom sandwiched between the PbO sheets, characteristic of Cu^{1+} , and the probable electronic isolation of this layer from the conducting CuO pyramidal planes, imply that the formal charge formulation becomes $Pb_2Sr_2YCu^{1+}Cu^{2+}_2O_8$ in the non-superconducting compound. When Ca is substituted for Y, we propose that holes are accommodated only in the CuO_3 planes, and at the $x=0.5$ stoichiometry the formal charge formulation becomes $Pb_2Sr_2Y_{0.5}Ca_{0.5}Cu^{1+}Cu^{2+}_2O_8$, which is consistent with the cur-

rent assumption for previously known high- T_c materials that holes are present in the CuO_3 pyramidal planes.

For $Pb_2Sr_2ACu_3O_{8+\delta}$ compounds with $\delta > 0$, excess oxygen must be accommodated near the Cu^{1+} planes, and a more complex hole-doping scheme may be operating. We expect that in that case the compound does not respond in a simple fashion to the change in charge through doping of a rigid band; the oxygen inserted in the bonding neighbourhood of the reduced Cu and Pb ions may create the electronic states in which the charge is partly or fully accommodated.

This new family of compounds has a unique crystal structure, yet it also reflects a concept common to all copper-oxide-based superconductors. By now it is well established that superconductivity is associated with layers of Cu - O octahedra, pyramids and squares. The remaining structural building blocks are seen as the electron acceptors which induce the holes necessary for superconductivity in the Cu - O layers. For $YBa_2Cu_3O_{6+\delta}$, for example, we have shown in detail how the CuO_3 chains act as charge reservoirs, and how superconductivity depends on charge transfer between chains and planes⁵.

To illustrate the concept of local charge distribution, one may rewrite the formulae of the high- T_c copper-oxide superconductors as follows: $YBa_2Cu_3O_6[CuO_3]$; $Sr_2CaCu_2O_6[Bi_2O_3]$; $Ba_2CaCu_2O_6[Tl_2O_2]$; $Sr_2(Y, Ca)Cu_2O_6[Pb_2CuO_{2+\delta}]$; where the structural components in square brackets act as reservoirs which control the charge on the superconducting Cu - O planes. The PbO - CuO_3 - PbO reservoir layer is likely to be exceptionally flexible in accommodation of charge, and we therefore expect that a relationship between T_c and oxygen stoichiometry as unusual as that for $YBa_2Cu_3O_{6+\delta}$ will eventually be observed. The wide ranges of metal-atom and oxygen-atom stoichiometries in this new family of superconductors are of considerable interest, and warrant further study with the aim of understanding and optimizing the superconducting properties.

We thank D. W. Murphy and K. Rabe for helpful discussions.

Received 21 October; accepted 28 October 1988.

1. Bednorz, J. G. & Müller, K. A. Z. Phys. B64, 189-193 (1986).
2. Saini, A.; Beech, P.; Marzocci, M. & Cava, R. J. Physics C (in the press).
3. Parth, S. S. P. et al. Phys. Rev. Lett. 61, 750-753 (1988).

4. Van Dover, R. B.; Cava, R. J.; Batlogg, B. & Rickman, E. A. Phys. Rev. B35, 5337-5339 (1987).
5. Cava, R. J. et al. Physics C (in the press).

BRIEF ATTACHMENT N

IN THE UNITED STATES PATENT AND TRADEMARK OFFICE

In re Patent Application of
Applicants: Bednorz et al.
Serial No.: 08/479,810
Filed: June 7, 1995

Date: March 1, 2005
Docket: YO987-074BZ
Group Art Unit: 1751
Examiner: M. Kopec

For: NEW SUPERCONDUCTIVE COMPOUNDS HAVING HIGH TRANSITION
TEMPERATURE, METHODS FOR THEIR USE AND PREPARATION

Commissioner for Patents
P.O. Box 1450
Alexandria, VA 22313-1450

FIRST SUPPLEMENTAL AMENDMENT

Sir:

In response to the Office Action dated July 28, 2004, please consider the
following:

ATTACHMENT N

LANDOLT-BÖRNSTEIN

Numerical Data and Functional Relationships
in Science and Technology

New Series

Editor in Chief: K.-H. Hellwege

Group III: Crystal and Solid State Physics

Volume 4
Magnetic and Other Properties
of Oxides and Related Compounds

Part a

J. B. Goodenough · W. Gräper · F. Holtzberg · D. L. Huber
R. A. Lefever · J. M. Longo · T. R. McGuire · S. Methfessel

Editors: K.-H. Hellwege and A. M. Hellwege



Springer-Verlag Berlin · Heidelberg · New York 1970

N **LANDOLT-BÖRNSTEIN**

S

Zahlenwerte und Funktionen
aus Naturwissenschaften und Technik

Neue Serie

Gesamtherausgabe: K.-H. Hellwege

Gruppe III: Kristall- und Festkörperphysik

Band 4

Magnetische und andere Eigenschaften
von Oxiden und verwandten Verbindungen

Teil a

J. B. Goodenough · W. Gräper · F. Holtzberg · D. L. Huber
R. A. Lefever · J. M. Longo · T. R. McGuire · S. Methfessel

Herausgeber: K.-H. Hellwege und A. M. Hellwege



1970

Springer-Verlag Berlin · Heidelberg · New York 1970

3 Crystallographic and magnetic properties of perovskite and perovskite-related compounds*)

3.0 Introduction — Einleitung

3.0.1 General remarks — Allgemeines

The perovskites form a family of compounds having a crystal structure similar to that of the mineral perovskite, CaTiO_3 . There are two classes of materials crystallizing with this general structure type: primarily ionic materials having the ideal chemical formula ABX_3 , (A = larger cation, B = smaller cation, X = anion), and alloys having the ideal formula $\text{M}^{\text{e}}\text{XM}^{\text{f}}_3$, (X = interstitial atom, M^{e} and M^{f} are metal atoms). Of these two classes, the former is much larger and the more important.

The stability of the ABX_3 perovskite structure is primarily derived from the electrostatic (Madelung) energy achieved if cations occupy corner-shared octahedra. Thus the first prerequisite for a stable ABX_3 perovskite is the existence of stable, polar octahedral-site building blocks. This, in turn, requires that the B cation have a preference for octahedral coordination and that there be an effective charge on the B cation. Since any A cation must occupy the relatively large anionic interstice created by corner-shared octahedra, a second prerequisite is an appropriate size for the A cation. Where it is too large, the B-X bond length cannot be optimized, and hexagonal stacking with face-shared octahedra becomes competitive. Where the A cation is too small, A-X bonding stabilizes structures having a smaller anionic coordination about the A cation. Thus ABX_3 perovskites are commonly found in fluorides and oxides having B cations with a preference energy for octahedral coordination. By contrast, the chlorides and sulfides, having larger anions, not only require the largest A cations, but also form layer structures, where the A cations are missing, because they have anionic d orbitals energetically available for orbital hybridization.

There are many perovskite-related structures, and these have been included in these tables. For example, the structure can tolerate mixed systems such as $\text{A}_{1-x}\text{A}'_x\text{BX}_3$ and $\text{AB}_{1-x}\text{B}'_x\text{X}_3$, A-cationic vacancies \square as in $\square_{1-x}\text{A}_x\text{BX}_3$, and cationic ordering as in $\text{A}_2\text{BB}'\text{X}_6$. Although anion-deficient perovskites have been reported many times, the anion vacancies \oplus are probably not distributed randomly. In compounds containing Fe^{3+} ions, for example, they appear to condense in pairs at individual B -site octahedra to convert the local anion interstice from an octahedron to a tetrahedron. In

Die Perowskite sind eine Gruppe von Verbindungen mit der gleichen Kristallstruktur wie das Mineral Perowskit, CaTiO_3 . Man unterscheidet zwei Klassen von Substanzen, die in diesem allgemeinen Strukturtyp kristallisieren: in erster Linie Ionenverbindungen mit der idealen chemischen Formel ABX_3 (A = größeres Kation, B = kleineres Kation, X = Anion) und Legierungen mit der idealen Formel $\text{M}^{\text{e}}\text{XM}^{\text{f}}_3$ (X = Zwischengitteratom, M^{e} und M^{f} = Metallatome). Von diesen beiden Klassen ist die erstere wesentlich umfangreicher und wichtiger.

Die Stabilität der ABX_3 -Perowskitstruktur beruht in erster Linie auf der elektrostatischen (Madelung-) Energie, die dann zustande kommt, wenn Kationen Oktaeder mit gemeinsamen Ecken besetzen. So ist die Existenz von stabilen, polaren Oktaeder-Bausteinen die erste Voraussetzung für ein stabiles ABX_3 -Perowskit. Dies wiederum erfordert, daß das B -Kation die Oktaeder-Koordination bevorzugt und daß beim B -Kation eine effektive Ladung existiert. Da ein jedes A -Kation die relativ große Anionen-Lücke besetzen muß, die zwischen Oktaedern mit gemeinsamen Ecken entsteht, ist die passende Größe des A -Kations die zweite Voraussetzung. Wenn das A -Kation zu groß ist, läßt sich der optimale B-X -Bindungsabstand nicht erreichen, und eine hexagonale Packung von Oktaedern mit gemeinsamen Flächen kann ebenso auftreten. Wenn das A -Kation zu klein ist, ergibt die A-X -Bindung Strukturen mit einer kleineren Anionen-Koordination um das A -Kation. Daher sind ABX_3 -Perowskite gewöhnlich unter den Fluoriden und Oxiden zu finden, in denen die B -Kationen Oktaeder-Koordination energetisch bevorzugen. Dagegen erfordern Chloride und Sulfide, die größere Anionen haben, nicht nur die größten A -Kationen, sondern sie bilden, weil sie anionische d -Elektronenbahnen mit der richtigen Energie für eine Bahn-Hybridisierung haben, auch Schichtstrukturen, bei denen die A -Kationen ganz fehlen.

Es gibt viele dem Perowskit verwandte Strukturen, die in diese Tabellen aufgenommen wurden. Zum Beispiel können gemischte Systeme wie $\text{A}_{1-x}\text{A}'_x\text{BX}_3$ und $\text{AB}_{1-x}\text{B}'_x\text{X}_3$ mit dieser Struktur auftreten, weiter A -Kationenlücken \square wie in $\square_{1-x}\text{A}_x\text{BX}_3$ und geordnete Kationen wie in $\text{A}_2\text{BB}'\text{X}_6$. Über Perowskite mit Anionenlücken ist schon häufig berichtet worden, vermutlich sind die Anionenleerstellen \oplus nicht willkürlich verteilt. In Verbindungen, die Fe^{3+} -Ionen enthalten, scheinen sie z. B. paarweise im Oktaeder eines einzelnen B -Platzes zusammenzutreffen und die

*) This work was sponsored by the U. S. Air Force.

compon
it is mor
anions
defici
cations,
contain
across v
edges (
iciencies
alloys.
B-occu
perovs
cation
an inte
(Fig. 2:
stackin
nal sta
cies (E
(AX)_m
rocksa
stacke
also oc
an A c
struct
with i
classif
and I
rather
for ex
18). S
of the

T
ing pl
BaTi
ferro
cond
ducti
lator
a pati
trans
ture ABX
mult
[Sm
ferr
ed f
Ba,
perc
and
mag
of t
mag
app
tura
tha

*)]

compounds containing Ti^{4+} ions, on the other hand, it is more probable that local rearrangements of the anions form trigonal bipyramidal sites. Anion-deficient, ionic materials in which there are no A-cations, such as $\square WO_{3-x}$, have been shown to contain $\square BX_3$ blocks connected by "shear" planes across which the occupied octahedra share common edges (Fig. 22). On the other hand, anion deficiencies may occur randomly in the $M^eX_{1-x}M^f_x$ alloys. B-cation defects cannot occur, because the B-occupied octahedra form the basis of the ABX_3 -perovskite structure. Where there are apparent B-cation vacancies, as in $A_mB_{m-1}X_{sm}$, there is either an interleaving of perovskite layers with A_2X_2 layers (Fig. 23) or an interleaving of cubic (perovskite) stacking of AO_3 layers with regularly spaced hexagonal stackings at which are located the B-ion vacancies (Fig. 24). Similarly, the series of compounds $(AX)_m(ABX_3)_n$ crystallize with an interleaving of rocksalt layers (Fig. 25). Interleaving of cubic-stacked AO_3 layers and hexagonal-stacked layers also occurs in ABX_3 compounds having too large an A cation to be accommodated by the perovskite structure (Fig. 3). Finally, there are a few alloys with interesting magnetic properties that can be classified as $A_2BB'X_6$ compounds if the symbols B and B' are allowed to represent atomic clusters rather than single cations. These are illustrated, for example, by the alloy $Al_2(AlCo_{12})(Co_8)B_6$ (Fig. 18). Sections 3.1 and 3.2 are devoted to descriptions of the perovskite and perovskite-related structures.

The ABX_3 perovskites exhibit several interesting physical properties such as ferroelectricity (as in $BaTiO_3$), ferromagnetism (as in $SrRuO_3$), weak ferromagnetism (as in $LaFeO_3$ or $HoFeO_3$), superconductivity (as in $SrTiO_{3-x}$), a large thermal conductivity due to exciton transport ($LaCoO_3$), insulator-to-metallic transitions of interest for thermistor applications (as in $LaCoO_3$), fluorescence compatible with laser action (as in $LaAlO_3:Nd$), and transport properties of interest for high-temperature thermoelectric power (as in La_2CuO_4). A few ABX_3 perovskites have been found that are simultaneously antiferromagnetic and ferroelectric [Sm 16, Mi 7, Sm 9]. The simultaneous occurrence of ferroelectricity and ferromagnetism has been reported for systems like $Sr_{0.25}La_{0.75}MnO_3$ - $ATiO_3$ ($A = Ba, Pb, Bi_{0.5}K_{0.5}$) [To 3, To 6]. Many of the $M^eX_{1-x}M^f_x$ perovskite alloys are ferromagnetic or ferrimagnetic, and a few exhibit first-order ferrimagnetic-to-ferromagnetic transitions. Nevertheless, the significance of the entire perovskite family for the field of magnetism*) lies not yet in their technological applications, but in their provision of an isostructural series of compounds having outer d electrons that are localized and spontaneously magnetic in

dortige Anionenlücke von einem Oktaeder in einen Tetraeder umzuwandeln. Bei Verbindungen, die Ti^{4+} -Ionen enthalten, ist es dagegen wahrscheinlicher, daß die lokale Anordnung der Anionen trigonale Doppelpyramiden-Plätze bildet. Für Ionenverbindungen mit Anionenlücken, die keine A-Kationen haben, wie $\square WO_{3-x}$, ist gezeigt worden, daß sie $\square BX_3$ -Blöcke enthalten, die durch „Gleit“-ebenen verbunden sind, in denen die besetzten Oktaeder gemeinsame Kanten innehaben (Fig. 22). In $M^eX_{1-x}M^f_x$ -Legierungen können jedoch Anionenlücken auch beliebig auftreten. B-Kationenlücken können nicht vorkommen, weil die von B besetzten Oktaeder die Basis der ABX_3 -Perowskitstruktur bilden. Wo scheinbare B-Kationenleerstellen auftreten, wie in $A_mB_{m-1}X_{sm}$, sind entweder A_2X_2 -Schichten zwischen Perowskischichten eingeschoben (Fig. 23), oder kubische (Perowskit-) Anordnungen von AO_3 -Schichten wechseln mit regelmäßig verteilten hexagonalen Anordnungen, in denen die B-Ionenlücken auftreten, ab (Fig. 24). Ähnlich kristallisieren die Verbindungen der Reihe $(AX)_m(ABX_3)_n$ mit einer Einschiebung von Steinsalzschichten (Fig. 25). Einschiebungen von kubisch gepackten AO_3 -Schichten und hexagonal gepackten Schichten treten auch in solchen ABX_3 -Verbindungen auf, deren A-Kation für die Perowskit-Struktur zu groß ist (Fig. 3). Schließlich gibt es einige wenige Legierungen mit interessanten magnetischen Eigenschaften, die als $A_2BB'X_6$ -Verbindungen eingeordnet werden können, wenn man unter den Symbolen B und B' Atomgruppen statt einzelner Kationen versteht. Dies gilt z. B. für die Legierung $Al_2(AlCo_{12})(Co_8)B_6$ (Fig. 18). Die Abschnitte 3.1 und 3.2 sind der Beschreibung der Perowskit- und verwandter Strukturen gewidmet.

Die ABX_3 -Perovskite weisen einige interessante physikalische Eigenschaften auf, wie Ferroelektrizität (in $BaTiO_3$), Ferromagnetismus (in $SrRuO_3$), schwachen Ferromagnetismus (in $LaFeO_3$ oder $HoFeO_3$), Supraleitfähigkeit (in $SrTiO_{3-x}$), große Wärmeleitfähigkeit durch Excitonentransport (in $LaCoO_3$), für Thermistoren interessante Übergänge zwischen Nichtleiter und metallischem Leiter (in $LaCoO_3$), für Laser-Anwendungen geeignete Fluoreszenz (in $LaAlO_3:Nd$), und Transporteigenschaften, die für Thermospannungen bei hohen Temperaturen von Interesse sind (in La_2CuO_4). Einige wenige ABX_3 -Perovskite wurden gefunden, die sowohl ferromagnetisch als auch ferroelektrisch sind [Sm 16, Mi 7, Sm 9]. Das gleichzeitige Auftreten von Ferroelektrizität und Ferromagnetismus wurde bei Systemen wie $Sr_{0.25}La_{0.75}MnO_3$ - $ATiO_3$ ($A = Ba, Pb, Bi_{0.5}K_{0.5}$) [To 3, To 6] beschrieben. Viele $M^eX_{1-x}M^f_x$ -Perowskitlegierungen sind ferromagnetisch oder ferrimagnetisch, und einige zeigen Übergänge erster Ordnung von Ferri- zu Ferromagnetismus. Trotzdem liegt die Bedeutung der gesamten Perowskit-Familie für den Magnetismus*) noch nicht in der technologischen Anwendung, sondern im Vorhandensein einer isostrukturellen Reihe von Verbin-

*) The technologically important dielectric properties are outside the scope of this summary. See Vol. III/3 of the New Series of Landolt-Börnstein.

*) Die technologisch wichtigen dielektrischen Eigenschaften liegen nicht im Rahmen dieser Zusammenstellung. Siehe Band III/3 der Neuen Serie des Landolt-Börnstein.

one member, collective and spontaneously magnetic in another, and collective and Pauli paramagnetic in yet another. This permits a systematic experimental investigation of the properties of the d electrons on passing through the transition from a localized character, where crystal-field plus superexchange and/or double-exchange theories apply, to an uncorrelated (except below a superconducting transition temperature) collective-electron character, where the conventional band theory applies. In addition, the simplicity of the perovskite ABX_3 structure minimizes competitive magnetic interactions between neighboring magnetic cations. Therefore from a study of magnetic order, as revealed by neutron diffraction, together with detailed structural information, as revealed by x-ray diffraction, it has been possible to test the semi-empirical rules for 180° cation-anion-cation isotropic superexchange interactions between localized electrons, the double-exchange hypothesis, antisymmetric exchange, and predictions of magnetic order and spontaneous atomic moments due to collective electrons.

Section 3.3 presents the general phenomenological exchange Hamiltonian for localized electrons and summarizes the microscopic models for isotropic superexchange, double exchange, and antisymmetric exchange. From these models, general rules for the interactions responsible for magnetic order are developed for comparison with the tabulated magnetic data.

Section 3.4 presents the fundamental physical concepts needed to construct a qualitative phase diagram for the outer d electrons as a function of the number n_l of electrons per relevant orbital, the magnitude of a nearest-neighbor transfer energy b , and the temperature T . It also summarizes the various characters of several physical properties imparted by outer electrons to show how they can be used to distinguish the electronic phases in different perovskites. Information from the tabulated data is used to show the influence of covalence and intra-atomic exchange, which help determine the parameter b , on the character of the electrons. Spontaneous collective-electron magnetism is seen to occur only in a narrow transitional interval of b between localized-electron magnetism and collective-electron Pauli paramagnetism.

Section 3.5 provides schematic energy diagrams for the alloys $M^oXM^f_3$. These are shown to be useful guides to predictions of the magnitudes of the atomic moments and the magnetic order.

dungen mit äußeren d -Elektronen, die lokalisiert und spontan magnetisch in einer Verbindung, kollektiv und spontan magnetisch in einer anderen, und kollektiv und Pauli-paramagnetisch in noch einer weiteren sind. Dies erlaubt systematische experimentelle Untersuchungen der Eigenschaften der d -Elektronen, indem man von einem lokalisierten Zustand, in dem Kristallfeld plus Superaustausch- und/oder Doppelaustausch-Theorien gelten, zu einem Zustand unkorrelierter Kollektivelektronen (außer bei Temperaturen unterhalb des Übergangs zur Supraleitung) übergeht, in dem die konventionelle Bändertheorie anzuwenden ist. Weiterhin führt die Einfachheit der Perowskit- ABX_3 -Struktur zu minimalen konkurrierenden Wechselwirkungen zwischen benachbarten magnetischen Kationen. Aufgrund der Untersuchung der magnetischen Ordnung, die man durch die Neutronenbeugung kennt, und einer genauen Kenntnis der Struktur, wie man sie durch Röntgenbeugung gewonnen hat, war es deshalb möglich, die halb-empirischen Gesetze über die isotrope 180° -Kation-Anion-Kation-Superaustausch-Wechselwirkung zwischen lokalisierten Elektronen, die Doppelaustausch-Hypothese, den antisymmetrischen Austausch und Voraussagen für magnetische Ordnung und spontane Atom-Momente, die von Kollektivelektronen herühren, zu prüfen.

Der Abschnitt 3.3 enthält den allgemeinen phänomenologischen Hamilton-Austausch-Operator für lokalisierte Elektronen und faßt die mikroskopischen Modelle für den isotropen Superaustausch, den Doppelaustausch und den antisymmetrischen Austausch zusammen. Aus diesen Modellen werden allgemeine Regeln für die Wechselwirkungen, die für die magnetische Ordnung verantwortlich sind, zum Vergleich mit den tabellierten Daten entwickelt.

Der Abschnitt 3.4 enthält die grundlegenden physikalischen Ideen, die für die Herstellung eines qualitativen Phasendiagramms für die äußeren d -Elektronen als Funktion der Elektronenzahl n_l pro betreffenden Bahnzustand, der Größe einer Übertragungsenergie b zwischen nächsten Nachbarn und der Temperatur T notwendig sind. Außerdem werden hier verschiedene Charakteristika einiger durch die äußeren Elektronen gegebenen physikalischen Eigenschaften zusammengestellt, um zu zeigen, wie man mit ihrer Hilfe die elektronischen Phasen verschiedener Perowskite unterscheiden kann. Auf Grund der tabellierten Werte wird der Einfluß von Kovalenz und intra-atomarem Austausch, die den Parameter b mitbestimmen, auf den Charakter der Elektronen gezeigt. Spontane Magnetisierung der Kollektivelektronen tritt, wie man sieht, nur in einem schmalen Übergangsintervall von b zwischen dem Magnetismus lokalizierter Elektronen und dem Pauli-Paramagnetismus der Kollektivelektronen auf.

Der Abschnitt 3.5 enthält schematische Energiediagramme für die Legierungen $M^oXM^f_3$. Es wird gezeigt, daß sie zu brauchbaren Voraussagen über die Größe der Atom-Momente und die magnetische Ordnung führen können.

ert
ag,
de-
in
na-
en-
em
lus
eo-
ek-
alb
em
ist.
xit-
den
ne-
der
ro-
der
ing
ilb-
on-
ung
us-
us-
ord-
lek-

hä-
itor
opi-
sch,
hen
den
die
ind,
ent-

iden
ines
n d-
pro
ber-
und
wer-
urch
chen
wie
ver-
Auf
von
die
kter
rung
ur in
chen
dem
onen

rgie-
d ge-
r die
ische

In the introductions to the sections 3.2 ... 3.5 we have referenced the principle theoretical contribution discussed, but no attempt was made to do this systematically for the experimental contributions, which are thoroughly referenced in the tables. — In the crystallographic tables, the crystal parameters quoted either represent the most complete analysis, in our judgment, or belong to the most complete set of parameters for a series of similar compounds. They do not necessarily represent the historical reference that established the unit-cell dimensions.

Literature was considered up to 1969.

Finally, we would like to thank DAVID MAHONEY for his willing assistance, the library and publications personnel of Lincoln Laboratory for their efficient support, and Mrs. G. E. BOYD for her help with all the foreign references.

In den Einleitungen zu den Abschnitten 3.2 ... 3.5 haben wir die grundlegenden theoretischen Beiträge, die diskutiert werden, mit Literaturhinweisen versehen; für die experimentellen Beiträge haben wir dies nicht systematisch durchzuführen versucht, da die entsprechenden Tabellen vollständig mit Literaturhinweisen versehen sind. — In den kristallographischen Tabellen stellen die angeführten Kristallparameter entweder die nach unserer Beurteilung vollständigste Analyse dar, oder sie gehören zum vollständigsten Satz von Parametern für eine Reihe ähnlicher Verbindungen. Sie geben nicht notwendigerweise den historischen Literaturhinweis, der die Dimensionen der Einheitszelle festlegte.

Die Literatur wurde bis 1969 berücksichtigt.

Schließlich möchten wir DAVID MAHONEY für seine bereitwillige Hilfe, den Angestellten der Bibliothek und der Veröffentlichungsabteilung des Lincoln-Laboratoriums für ihre wirksame Unterstützung und Mrs. G. E. BOYD für ihre Hilfe bei der ausländischen Literatur danken.

3.0.2 Symbols and units used in tables and figures

Crystallographic structure

symmetry

$a, b, c [\text{\AA}]$

$\alpha, \beta, \gamma [\text{deg}]$

$\Theta_{\text{trans}}, \Theta_{\text{ord}} [\text{^\circ K}]$

$\Theta_D [\text{^\circ K}]$

$T_{\text{melt}} [\text{^\circ K}]$

c_{ij}

ϵ_i

$r_{A,B,B'} [\text{\AA}]$

symmetry classification for perovskite structures: C = cubic, H = hexagonal, R = rhombohedral, O = orthorhombic ($a < c/\sqrt{2}$), O' = orthorhombic ($c/\sqrt{2} < a$), T = tetragonal, M = monoclinic, Tr = triclinic

lattice parameters

angle between crystallographic axes

crystallographic transition and ordering temperatures

Debye temperature

melting temperature

elastic constants

crystalline strains

radius of A, B, B' cation

Magnetic properties (static measurements)

see magnetic structure type from Fig. 26

atomic moment and component of atomic moment parallel to net ferromagnetic

moment in numbers of Bohr magnetons: $p_A = n_A \mu_B$

net magnetization per molecule in numbers of Bohr magneton: $p_m = \bar{n}_m \mu_B$

$n_{\text{eff}} = \sqrt{8} C_m$ is the effective paramagnetic moment: $p_{\text{eff}} = n_{\text{eff}} \mu_B$

Curie temperature

Néel temperature; extrapolated Néel temperature

temperature for spin reorientation

paramagnetic Curie temperature ($\Theta_p < 0$ if antiferromagnetic coupling)

temperature below which parasitic n_A^A deviates appreciably from 0.05

molar Curie constant determined from Curie-Weiss law $\chi_m = C_m/(T - \Theta_p)$

specific paramagnetic susceptibility

molar paramagnetic susceptibility

atomic moment, atomic moment of element A

molecular moment (of molecule xy)

effective paramagnetic moment: $p^* = \sqrt{\chi_m T}$

isotropic exchange constant of Eq. (16) for near-neighbor interactions

Ln-Fe interaction parameter defined by

$M(t) = \sigma_0(0) B(t) [1 + (d/t)]$, where $t = T/\Theta_C$ and $B(t)$ is the Brillouin function

domain wall energy density

net near-neighbor Weiss molecular field constant: $H_{\text{wi}} = \sum_{j=1}^5 W_{ij} M_j$

σ { [Gauss cm ³ /g] { [emu/g]	magnetic moment per gram = specific magnetization
σ_0 [emu/g]	specific parasitic (weak) magnetization as obtained from $\sigma = \sigma_0 + \chi_g H_a$
σ_{sp}	spontaneous specific magnetization
H_a [Oe]	externally applied field
H_{crit} [Oe]	critical applied field for antiferromagnetic-ferromagnetic transition or for spin-flop transition
H_c	coercivity
α	cant angle
b_1, b_2 [dyn/cm ²]	magnetoelectric coefficients
λ_{100}	magnetostriction constant for [100] direction: $\lambda_{100} = -4b_1/3(c_{11} - c_{12})$
C_{ijk}	components of the tensor describing the quadratic dependence of magnetization on applied field: Eq. (36)
μ_B	the Bohr magneton = 5585 emu/g
T [erg/g]	torque: $T = \sigma \times H_a$
Magnetic properties (resonance measurements)	
H_A	effective crystalline-anisotropy field
H_{ex}	exchange field
H_D	spin-canting field (Dzialoshinskii field)
H_{int}	internal magnetic field at the nucleus
H_n	axial hyperfine field arising from nuclear polarization
H_{hyp}	hyperfine field $I \cdot A \cdot S$, where I = nuclear spin, S = net atomic spin, and the components of the interaction tensor are $A_s, A_{ns}, A_\sigma, A_\pi, A_{2p}$.
$f_s^A, f_\sigma^A, f_\pi^A$	fraction of unpaired p_σ or p_π electron spins involved in covalent bonding: $f_s^A = 2SA_s/A_{ns} = \frac{1}{3}N_e^2\lambda_s^2, f_\sigma^A = 2SA_\sigma/A_{2p} = \frac{1}{3}N_e^2\lambda_\sigma^2, f_\pi^A = 2SA_\pi/A_{2p} = \frac{1}{3}N_e^2\lambda_\pi^2$. See Eq. (4) for $N_e, N_t, \lambda_s, \lambda_\sigma, \lambda_\pi$.
$\epsilon, \Delta E$	nuclear quadrupole coupling constant and quadrupole splitting
F_{ij}, G_{ij}	dipolar and quadrupolar magnetoelastic coefficients: $\delta g_i = \sum_{j=1}^6 F_{ij} \epsilon_j$ and $d_i = \sum_{j=1}^6 G_{ij} \epsilon_j$, where $\mathcal{H}_{\text{spin-lattice}} = \mu_B H_a \cdot \delta g \cdot S + S \cdot d \cdot S$
ν_R [Hz]	resonance frequency for NMR
$\Delta\nu$ [Hz]	half-line width
T_1 [sec]	nuclear spin-lattice relaxation time
T_2 [sec]	nuclear spin-spin relaxation time
T_{1e} [sec]	nuclear spin-lattice relaxation time during a locking pulse
Optical measurements	
n	index of refraction
ϵ_0	low-frequency dielectric constant
ϱ [$^{\circ}$ /cm]	Faraday rotation
ν_{TO}, ν_{LO} [Hz]	frequency of transverse and longitudinal optical modes
Transport measurements	
Θ_{cs}	superconducting critical temperature
E_F	Fermi energy
E_a	activation energy for a small-polaron hop
ϱ [Ω cm]	electrical resistivity
S [μ V/ $^{\circ}$ K]	Seebeck coefficient
e [esu]	magnitude of the electronic charge
c, n_i, n_{\pm} [cm ⁻³]	charge-carrier density
μ [cm ² /Vsec]	charge-carrier mobility
τ [sec]	charge-carrier collision time
m^* [g]	charge-carrier effective mass
D_0 [cm ² /sec]	charge-carrier diffusion coefficient at $E_a = 0$
N_{\pm}	density of unoccupied states: $2(2\pi m_{\pm}^* k T/h^2)^{3/2}$
General properties	
T [$^{\circ}$ K]	temperature
p	pressure
c_p	specific heat at constant pressure

 A
A
B
C
D
D
E
F
F
H
I
L
M
N
n
C
F
F
P
P
F
S
S
C
J
i
S
S
C
J
i

Abbreviations for text and indices

AFMR	antiferromagnetic resonance
APR	acoustic paramagnetic resonance
BPW	Bethe-Peierls-Weiss method
C, cub	cubic
DS	Danielson-Stevens method
DTA	differential thermal analysis
ESR	electron spin resonance = paramagnetic resonance
f.c.	face-centered permutation
FMR	ferromagnetic resonance
F_B	ferromagnetic with reduced n_A
H, hex, hex (nL)	hexagonal, hexagonal n-layer structure
I.R.	infrared
Ln	Lanthanon = any of the rare-earth elements
MF	molecular field approximation
M, mon	monoclinic
NAR	nuclear acoustic resonance
NMR	nuclear magnetic resonance
ncub	noncubic
O, O', orth	orthorhombic ($O: a < c/\sqrt{2}$; $O': c/\sqrt{2} < a$)
P&S	reference to preparation and structural information
Prep.	reference to material preparation
Prop.	reference to material properties
pscub	pseudocubic
psmon	pseudomonoclinic
R, rh	rhombohedral
RW	Rushbrooke-Wood method
S. G.	space group
S.S.	solid solution
T, tetr	tetragonal
Tr, tr	triclinic

3.1 Descriptions of stoichiometric ABX_3 and $\text{M}^{\text{c}}\text{XM}^{\text{f}}_3$ structures

3.1.1 The ideal perovskite structure

The ideal perovskite structure has the cubic unit cell of Fig. 1 with space group Pm3m. Fig. 1(a) shows the corner-sharing octahedral units (BX_6 array in ABX_3 , and XM^{f}_6 array in $\text{M}^{\text{c}}\text{XM}^{\text{f}}_3$), which form the stable skeleton of the structure. The A cation (or M^{c} atom) occupies the body-center position. Fig. 1(b) shows the unit cell with the A cation (or M^{c} atom) at the origin, or corner position. This shows the face-centered-cubic character (with Cu₃Au-type order) of the AX_3 or $\text{M}^{\text{c}}\text{M}^{\text{f}}_3$ subarrays. Fig. 1(c) shows the cubic perovskite on an hexagonal basis, with the c axis along the cubic [111] direction. The alternate AX_3 and B' ionic layers each have cubic stacking. Also indicated is the ordering of B and B' layers in the ordered $\text{A}(\text{B}_{2/3}^{\text{i}}\text{B}_{1/3}^{\text{o}})\text{X}_3$ structures.

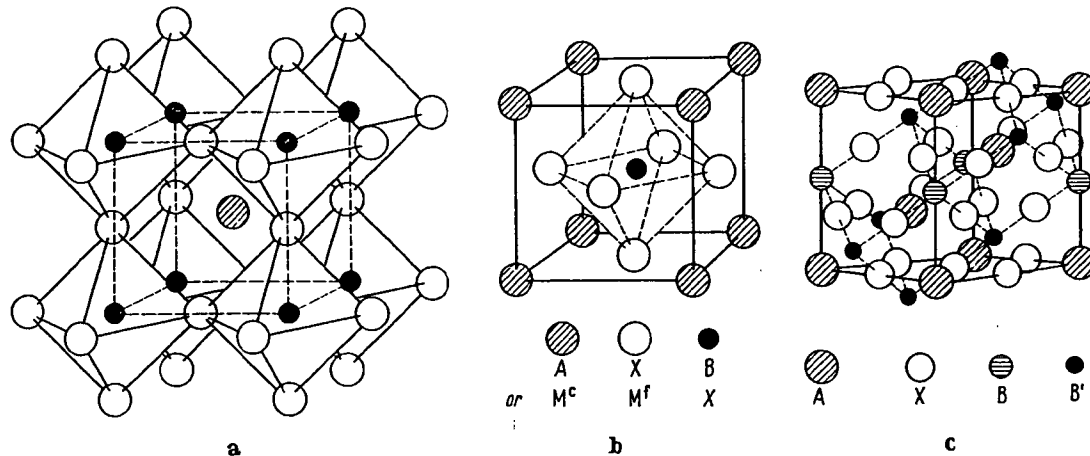


Fig. 1. ABX_3 , $\text{M}^{\text{c}}\text{XM}^{\text{f}}_3$. Ideal perovskite structure: a) B cation (or X atom) at origin. b) M^{c} atom (or A cation) at origin. c) A cation at origin in hexagonal basis [Ga10].

The alloys M^aXM^b₃ are stabilized by covalent M-X bonding and by metallic M-M bonding, so that they are generally cubic. Only in phases exhibiting complex magnetic order are there distortions to lower symmetry. On the other hand, the ABX₃ perovskites, which are primarily stabilized by the Madelung energy, are rarely cubic at normal temperatures. Madelung energy calculations are available [Ro15a, Sa2b, Mi1].

Although cubic at high temperatures, most ABX₃ compounds exhibit distortions to lower symmetry below some temperature Θ_{trans} as a result of atomic displacements. Such displacive transitions can be described by a finite set of normal vibrational modes that become soft, their vibrational frequency increasing with $T > \Theta_{\text{trans}}$. From LANDAU's [La2] theory of phase transitions, it may be argued [Ha1, Co2] that at a second-order displacive transition, the frequency of one normal mode becomes zero. Thus the occurrence of ferroelectricity in perovskite-type crystals such as BaTiO₃ has been correlated both theoretically and experimentally [An2, Co1, Ba17, Co28, Ne8, Sh26] with the existence of a transverse optic mode of lattice vibration having wave number $k \approx 0$ and a temperature-dependent frequency $\omega \sim (T - \Theta_{\text{trans}})^{1/2}$.

Similarly, in the case of LaAlO₃ softening of a single normal mode can produce the R̄3c-to-cubic transition, and this transition is probably second-order. Investigation [Ha1] of the atomic displacements involved in other distortions from cubic symmetry, on the other hand, has shown that several normal modes are involved, and these displacive transitions are first-order.

SrTiO₃ exhibits a tetragonal (D_{4h}¹⁸ with $c/a = 1.00056$) to cubic transition at $\Theta_{\text{trans}} = 110 \text{ }^{\circ}\text{K}$ [Ly2, Ri5] that appears to illustrate the softening of a triply degenerate phonon at the R point of the Brillouin zone in the cubic phase. For $T < \Theta_{\text{trans}}$, it splits into two zone-center phonons having a frequency dependence $\omega \sim (\Theta_{\text{trans}} - T)^{0.31}$ [Fi2]. In the presence of an external electric field E_a , the symmetry is further reduced to C_{4v} if $E_a \parallel c$ -axis, or C_{2v} if $E_a \perp c$ -axis, and the critical modes have the same symmetry as the ferroelectric TO modes. "Anticrossing" of the modes occurs for $E_a = 1.5 \text{ kV/cm}$ and 15 kV/cm [Ne7, Wo19]. Thus the observed [He5] maximum in the electric susceptibility of SrTiO₃ at very low temperatures does not appear to be associated with a ferroelectric transition.

Theoretical interest in the analytic description of these phase transitions continues [Go1a, Mu4a, Ta14a, Th3].

The physical origins of the various crystallographic distortions may be separated into three parts: relative ionic sizes, electron ordering among localized electrons, and electron ordering among collective electrons.

3.1.2 The influence of relative ionic sizes

3.1.2.1 Tolerance factor

The first prerequisite for a stable perovskite structure is the existence of a stable BX₃ skeletal subarray. If the B-cation radius is $r_B < 0.51 \text{ \AA}$ in oxides, for example, the B cation does not achieve its optimum B-O separation in an octahedral site and therefore stabilizes a structure with a smaller anion coordination. The Al³⁺ ion is borderline, being stable in four, five or six coordination. However, Ga³⁺, Ge⁴⁺ and V⁵⁺ ions are definitely more stable in tetrahedral sites at ambient pressures.

Given the BX₃ skeletal subarray, additional stabilization is achieved by accommodating a large A cation within this skeleton. Because there is an optimum A-X bond length, the presence of an A atom generally distorts the BX₃ array so as to optimize the A-X bonding. However, if this distortion is too large, then other space groups become competitive. GOLDSCHMIDT [Go2] defined the tolerable limits on the size of the A cation via a tolerance factor

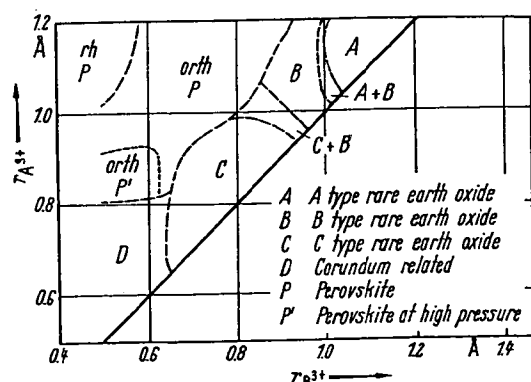
$$t = (r_A + r_X)/\sqrt{2}(r_B + r_X) \quad (1)$$

where r_A , r_B , r_X are empirical radii of the respective ions. By geometry, the ideal cubic structure should have $t = 1$. The perovskite structure occurs only within the range $0.75 < t < 1.00$. However, this is not a sufficient condition, since the A and B cations must, in themselves, be stable in twelvefold (12 or 8 + 4 or 6 + 6) and sixfold coordinations. This sets lower bounds for the cationic radii. In oxides these bounds are $r_A > 0.90 \text{ \AA}$ and $r_B > 0.51 \text{ \AA}$. In addition, MEGAW [Me5] noted that, if $0.75 < t < 0.9$, a cooperative buckling of the corner-shared octahedra to optimize the A-X bond lengths enlarges the unit cell; on the other hand, if $0.9 < t < 1$, such buckling may not be found, although small distortions to rhombohedral symmetry occur. These structures are to be distinguished from perovskites that exhibit additional distortions as a result of electron ordering. The cubic phase is found at high temperatures or where the A-X bond is more ionic (especially if $t \approx 1$).

Where the A cation is too small ($r_A < 0.9 \text{ \AA}$) to accommodate twelve nearest neighbors, a structure in which the A and B cations are both six-coordinated becomes competitive. From the phase diagram of Fig. 2 for the oxides A^aB^bO₃, which has been adapted from SCHNEIDER, ROTH, and WARING [Sc13], the initial competition is the C-M₂O₃ structure, which contains two unusual types of corner-shared, six-coordinated sites. The C-M₂O₃ structure consists of a face-centered-cubic array of cations with anions occupying $\frac{1}{8}$ of the tetrahedral interstices in an ordered manner. Thus each cation has six out of eight near-neighbor anions at the corners of a circumscribing cube: $\frac{1}{2}$ of the cations have two anions missing at the ends of a body diagonal and $\frac{1}{2}$ of the cations have two anions missing at the end of a face diagonal of the circumscribing cube. This arrangement minimizes the electrostatic repulsive forces between the cations.

3.1 ABX₃ perovskite structure

Fig. 2. General $r_A - r_B$ phase diagram for $A^{3+}B^{3+}O_3$ compounds based on ionic-size considerations. Exceptions may occur where considerations other than ionic radii r_A, r_B become important, as in the case $A = Bi$. A similar plot for $A^{3+}B^{4+}O_3$ perovskites is not useful because secondary considerations are amplified by ferroelectric distortions and the possibility of different layer sequences where larger A cations are present. [Adapted from *Sc13*].



Given smaller A cations, however, electrostatic screening between face-shared octahedra can be achieved by displacements of the cations away from the shared face, and the structure competitive with perovskite is generally built from an hexagonal-close-packed anion array, which has octahedral holes sharing common faces along the c -axis. With one octahedral hole per anion and a cation/anion ratio 2/3, the cations are ordered among these holes so as to minimize the electrostatic energy. If the A and B cations carry the same charge, as in $A^{3+}B^{3+}O_3$, only pairs of cations share common octahedral-site faces and there is no ordering of A and B within the cationic array. This allows the electrostatic force between two cations sharing a common octahedral face to be reduced by displacements of the cations away from each other, thus distorting the octahedra. The result is the corundum structure of Al_2O_3 . If the cations A and B carry different charges, as in $A^{2+}B^{4+}O_3$, then the A and the B cations order into alternate puckered cationic (111) planes of the rhombohedral corundum structure to form the ilmenite structure. However, where there is a large difference in the cationic charges, as in $Li^+Sb^{5+}O_3$ and $Li^+Nb^{5+}O_3$, two other alternatives become competitive: (1) The A^{3+} ions order in strings of face-shared octahedra so as to permit the B^{3+} -ion octahedra to share only edges with near-neighbor occupied octahedra. This structure is illustrated by $LiSbO_3$ [Ed1]. (2) After ordering B^{3+} and Li^+ ions within each cationic (111) plane of the corundum structure in such a way that B^{3+} and Li^+ ions share common octahedral-site faces, each A^{3+} cation is then displaced into the far face of its octahedron, where it is equally spaced from B^{3+} cations above and below so long as the B^{3+} cations remain in the centers of their octahedra. This is the structure of paraelectric $LiNbO_3$ and $LiTaO_3$ [Ab3].

Where the A cation is too large ($t > 1.0$), the close-packed AX₃ layers of Fig. 1(c) tend to change their stacking sequence from cubic to hexagonal. However, the change from the all-cubic stacking of the rhombohedral perovskite structure to the all-hexagonal stacking of the hexagonal (hex. 2L) CsNiCl₃ structure goes via the three intermediate steps shown in Fig. 3 [Lo1]. The first step is the hexagonal BaTiO₃ structure of Fig. 3(c). It is a six-layer structure with stacking sequence *a-b-c-a-c-b-a*, corresponding to one hexagonal stacking out of three. In this structure (hex. 6L), two-out-of-three B cations form pairs sharing a common octahedral-site face, and one-out-of-three B cation shares only common octahedral-site corners as in the perovskite structure. Many ordered compounds $A_3B_2B'O_9$ are known to have this structure. The second step, illustrated by the hexagonal BaMnO₃ structure of Fig. 3(d), alternates hexagonal and cubic stackings with the sequence *a-b-c-b-a*. This four-layer structure (hex. 4L), contains only B-cation pairs sharing common octahedral-site faces. The electrostatic forces between paired B-cations in B-cation pairs sharing common octahedral-site faces. The electrostatic forces between paired B-cations in Figs. 3(c), (d) displace the paired cations from one another along the c axis, exactly as in the corundum

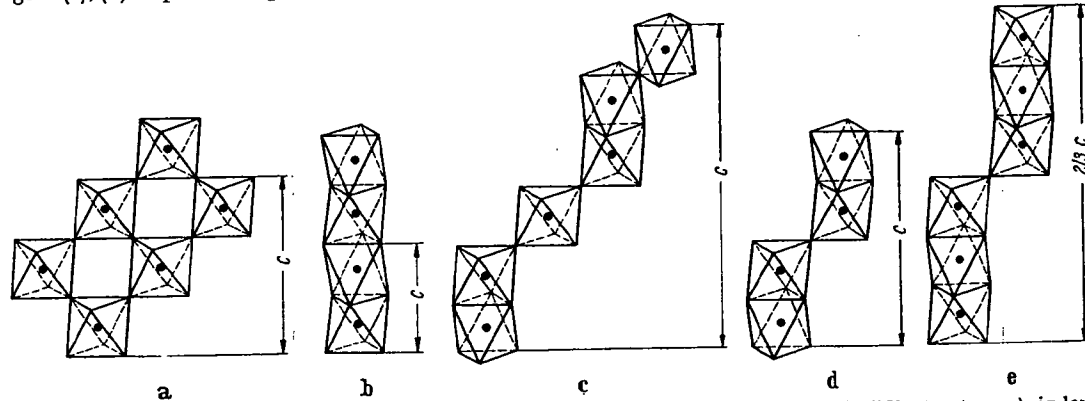


Fig. 3. Stable structures intermediate to a) cubic perovskite and b) the two-layer hexagonal CsNiCl₃ structure, c) six-layer hexagonal BaTiO₃ structure, d) four-layer hexagonal BaMnO₃ structure, e) nine-layer hexagonal BaRuO₃ structure. [Adapted from *Ca2*].

structure. The third step is the nine-layer (hex. 9L) structure of BaRuO₃, which has two hexagonal stackings out of three in the sequence *a-b-c-b-c-a-c-a-b-a*. Here the B cations form strings of three sharing common octahedral-site faces along the *c*-axis. Electrostatic forces displace the two end-member B cations away from the center B cation of each string, as shown in Fig. 3(e). Because cubic stacking is stabilized by hydrostatic pressure, it is possible to convert under pressure and high temperature the hexagonal structures to the perovskite structure through the successive sequence of steps. This is well illustrated by the Ba_{1-x}Sr_xRuO₃ system as shown in Fig. 4(a). These particular intermediate structures appear to be stabilized by the cation displacements, but at the cost of alternating the stacking sequence. The (hex. 4L) structure, which has the maximum alternation of stacking, is not always found, and the intermediate structures tend to be stabilized by smaller B cations, as illustrated in Fig. 4(b).

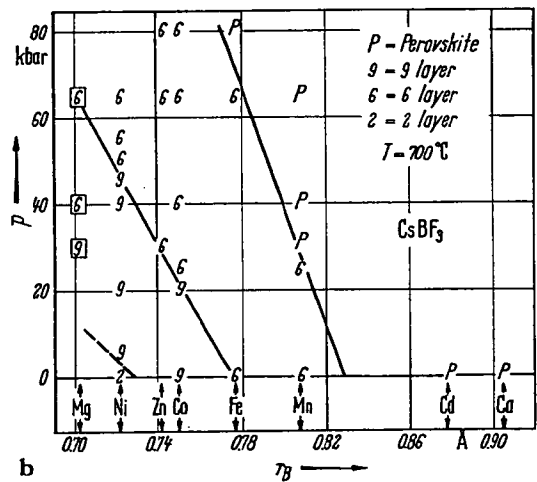
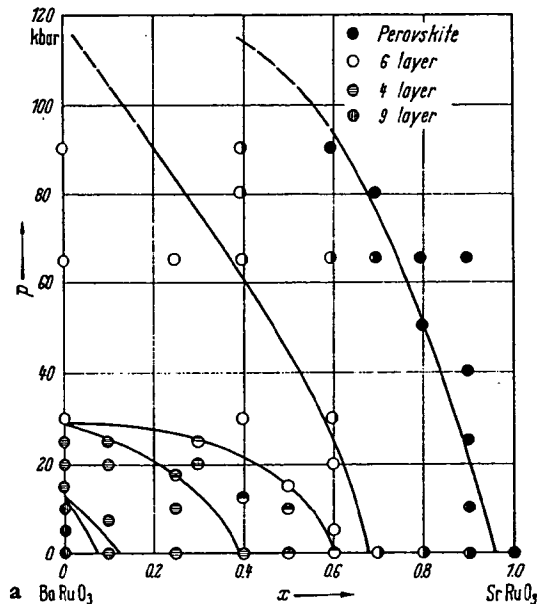


Fig. 4. a) Ba_{1-x}Sr_xRuO₃, P - x phase diagram where P is hydrostatic pressure [Lo1], b) structural phase diagram of CsBF₃ compounds [Lo1b].

3.1.2.2 O-orthorhombic structure

Cooperative buckling of corner-shared octahedra, although indexed on a monoclinic pseudocell in earlier work, may produce the orthorhombic primitive cell of Fig. 5 containing four formula units. It was first identified in single crystals of GdFeO₃, [Ge1] and later confirmed [Co21]. Powder photographs taken with CrK_α radiation could be indexed on the monoclinic pseudocell containing a single GdFeO₃ molecule, which is the origin of the earlier classification. The pseudocell dimensions of GdFeO₃ are $a = c = 3.87 \text{ \AA}$, $b = 3.83 \text{ \AA}$, $\beta = 92.8^\circ$, where $2b_{\text{pseudocell}} = c_{\text{true cell}}$. The true orthorhombic cell is referred to in the tables as O-orthorhombic and is distinguished from the O'-orthorhombic structure by a lattice-parameter ratio

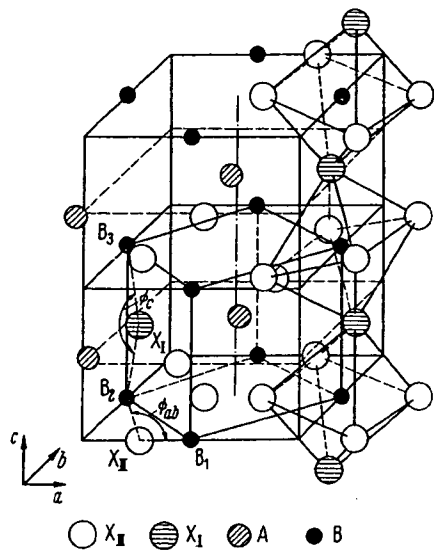


Fig. 5. GdFeO₃, O-orthorhombic structure.
 $\phi_{ab} = \frac{a}{B_1 X_{II} B_3}$, $\phi_c = \frac{c}{B_2 X_I B_3}$.
 Fig. from [Ve12], structure [Ge1], coordinates [Co21].

ion	position	coordinates		
		<i>x</i>	<i>y</i>	<i>z</i>
Gd ³⁺	4(c)	-0.018	0.060	$\frac{1}{2}$
Fe ³⁺	4(b)	$\frac{1}{4}$	0	0
O ²⁻	4(c)	0.05	0.470	$\frac{1}{2}$
O ²⁻ _{II}	8(d)	-0.29	0.275	0.05

$c/a > \sqrt{2}$, where $a < b$. The O'-orthorhombic structure, which has $c/a < \sqrt{2}$, is the result of a superposed Jahn-Teller (with or without spin-orbit coupling) distortion. It is also to be distinguished from ferroelectric O_B⁺-orthorhombic and O_B⁰-orthorhombic distortions in which each B cation is removed from the center of symmetry of its interstice. Other orthorhombic distortions have been reported for NdGaO₃ [Br26] and NaCoF₃ [Ok5].

The O-orthorhombic unit cell has the probable space group Pbnn with A cations in positions 4(c): $\pm(x, y, \frac{1}{2}; \frac{1}{2} - x, \frac{1}{2} + y, \frac{1}{2})$, the B cations in 4(b): $(\frac{1}{2}, 0, 0; \frac{1}{2}, 0, \frac{1}{2}; 0, \frac{1}{2}, 0; 0, \frac{1}{2}, \frac{1}{2})$, eight anions X_{II} in 8(d): $\pm(x, y, z; \frac{1}{2} - x, \frac{1}{2} + y, \frac{1}{2} - z; \bar{x}, \bar{y}, \frac{1}{2} + z; \frac{1}{2} + x, \frac{1}{2} - y, \bar{z})$, and the remaining four anions X_I in 4(c). Coordinates for the ions in GdFeO₃ are also given in Fig. 5.

The buckling of the corner-shared octahedra decreases the cation-anion-cation angle Φ from 180°. If the B cations and the anions are distinguished as B₁($\frac{1}{2}, 0, 0$), B₂($0, \frac{1}{2}, 0$), B₃($\frac{1}{2}, 0, \frac{1}{2}$), X_{II}($\frac{1}{2} + x, \frac{1}{2} - y, \bar{z}$), and X_I($\frac{1}{2} - x, \frac{1}{2} + y, \frac{1}{2}$), then the two representative angles are $\Phi_{ab} = (B_1 - X_{II} - B_2)$ and $\Phi_c = (B_2 - X_I - B_3)$. GILLEO [Gi4] has estimated that in La(Co_{0.2}Mn_{0.8})O₃ these angles are $\Phi_{ab} = 150^\circ \pm 3^\circ$ and $\Phi_c = 177^\circ \pm 3^\circ$ with B₁ - O_{II} = 1.95 Å, B₂ - O_{II} = 2.10 Å, B₁ - O_I = B₃ - O_I = 1.96 Å. The angles in GdFeO₃ are similar.

3.1.2.3 Rhombohedral structures

Where there is no buckling of the octahedra, the perovskites ABX₃ may have a small deformation from cubic to rhombohedral symmetry. Where this deformation does not enlarge the unit cell, it is possible to index it either on a unit cell containing two formula units, as shown in Fig. 6, or on a unit cell containing one formula unit. The corresponding rhombohedral angles are $\alpha \approx 60^\circ$ or $\alpha \approx 90^\circ$. In the early literature, detailed anion positions were not known, and it was common to use the smaller cell with $\alpha \approx 90^\circ$. However, the anions are generally displaced so as to require the larger unit cell of Fig. 6, which has $\alpha \approx 60^\circ$.

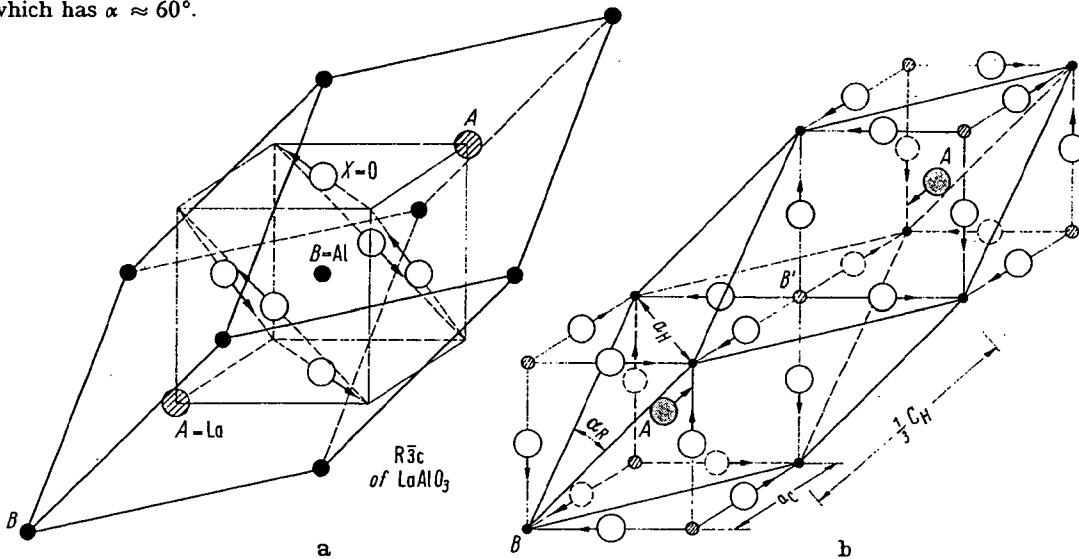


Fig. 6. Rhombohedral ABX₃ structures: a) anion shifts for symmetry R $\bar{3}$ c; b) the simplest ionic displacements, corresponding to symmetry R $\bar{3}$ m for ordered A₂BB'X₄ structures having $r_{B'} > r_B$ [Ra3].

Anion displacements from their ideal positions may be of three different types: (1) AX₃(111) planes remain equidistant from neighboring B-cation (111) planes, leaving all the B-cations equivalent. Within these planes, three A-X distances are reduced and three are enlarged via cooperative rotations of the B-cation octahedra, as shown in Fig. 6(a). (2) The anions may move within pseudocubic {110} planes including the B-B axes so as to create two distinguishable B positions: B positions having a shorter B-X separation and B' positions having a larger B'-X separation. This gives the symmetry R $\bar{3}$ m, which allows the A cations to be displaced along the [111] axis so as to make the separations B-A ≠ B'-A. (3) In the most general case, the anion displacements may be decomposed into R $\bar{3}$ c and R $\bar{3}$ m components. The resulting symmetry R $\bar{3}$ also gives distinguishable B and B' positions via its R $\bar{3}$ m component.

Although the distinction between these possibilities has been determined in only a few cases, it appears that R $\bar{3}$ c can be anticipated unless there is a physical reason for creating two distinguishable positions B and B'. This conclusion is based on the fact that LaAlO₃ has been shown to have the symmetry R $\bar{3}$ c by neutron diffraction, [De14] nuclear quadrupole resonance [Mu5], electron-spin resonance, [Ki3] and x-ray techniques [Ge4b, De17]. It is strongly supported by the observation [Ra3] that LaCoO₃ has the symmetry R $\bar{3}$ c at low temperatures, where all of the trivalent cobalt are in their low-spin state, but has the symmetry R $\bar{3}$ at higher temperatures where thermal activation creates a nearly equal population of high-spin and low-spin cobalt ions. These are crystallographically distinguishable, via different ionic radii, as B and B'.

3.1.3 The influence of localized-electron ordering

3.1.3.1 Crystal-field theory

Crystal-field theory rests on the assumption that the outer electrons to be described are localized at discrete atomic positions. This assumption is valid for outer *f* electrons; it is valid for *d* electrons in fluorides and in many oxides. Given this assumption, the Schroedinger equation $\mathcal{H}\psi = E\psi$ that describes the localized orbitals and their energies contains the Hamiltonian

$$\mathcal{H} = \mathcal{H}_0 + V_{el} + V_{cub} + (V_{LS} + V_{ncub} + V_\lambda + \sum_j V_{ij}) \quad (2)$$

where \mathcal{H}_0 is the Hamiltonian for a hydrogen-like, spherical potential, V_{el} is the atomic correction for spherical symmetry that enters if there is more than one outer *d* electron, and V_{cub} is the energy correction due to the cubic component of the crystalline fields. For outer *d* electrons, V_{el} and V_{cub} are generally ≈ 1 eV, and the ion is in a high-spin or a low-spin state depending upon the relative magnitudes of these two terms. In the case of 3*d* electrons, the perturbations listed within the parentheses are all < 0.1 eV, and they must be considered simultaneously. $V_{LS} = \lambda \mathbf{L} \cdot \mathbf{S}$ is the spin-orbit coupling energy, and covalent mixing reduces slightly the parameter λ from its free-atom value. V_{ncub} is the noncubic component of the crystalline field, V_λ is the elastic coupling energy associated with cooperative local distortions, and V_{ij} is the magnetic exchange energy coupling localized atomic moments on neighboring cations.

Solution of the zero-order equation $\mathcal{H}_0\psi = E\psi$ gives hydrogenic wave functions $f_{l,m} = R_l(r) Y_l^m(\theta, \phi)$. From the spherical harmonics $Y_l^m(\theta, \phi)$, the *d* electrons ($l = 2$) have the following angular dependence and azimuthal-angular-momentum quantum number *m* derived from $L_z f = -i \hbar \partial f / \partial \phi = m \hbar f$:

$$\begin{aligned} f_A &\sim (3z^2 - r^2)/r^2 &= (3 \cos^2 \theta - 1); & m = 0 \\ (f_D \pm i f_E) &\sim 2(zx \pm iy)/r^2 &= \sin 2\theta \exp(\pm i\phi); & m = \pm 1 \\ (f_B \pm i f_C) &\sim (x^2 - y^2 \pm izy)/r^2 &= \sin^2 \theta \exp(\pm i2\phi); & m = \pm 2 \end{aligned} \quad (3)$$

where θ, ϕ are conventional spherical coordinates. The perturbation V_{el} reflects the fact that outer electrons of parallel spin are excluded from one another and therefore screen each other less from the positive atomic nucleus than do those of antiparallel spin. This correction is responsible for Hund's highest-multiplicity rule for the free atoms. It influences the radial part of the wave function, and hence the relative energies of states of different spin, but not the angular part.

Given the cartesian axes at a B cation formed by the principal axes of its octahedral interstice, the five *d* orbitals of Eq. (3) are separated into two symmetry groups; f_A and f_B , which are directed along the cartesian axes toward near-neighbor anions, have E_g symmetry and are referred to as e_g orbitals; f_C, f_D , and f_E , which are more stable because they are directed away from the near-neighbor anions, have T_{2g} symmetry and are referred to as t_{2g} orbitals. The principal contribution to the cubic-field splitting 10 Dq of T_{2g} and E_g energies is due to covalent mixing, not to electrostatic energies as calculated on a point-charge model. If covalent mixing with the near-neighbor anionic and A-cationic orbitals is introduced, then the crystalline localized orbitals of t_{2g} and e_g symmetry become

$$\begin{aligned} \psi_t &= N_t(f_t - \lambda_n \phi_n + \lambda_A \phi_A) \\ \psi_e &= N_e(f_e - \lambda_s \phi_s - \lambda_\sigma \phi_\sigma) \end{aligned} \quad (4)$$

where f_t and f_e are linear combinations of the atomic f_C, f_D, f_E and f_A, f_B orbitals. The symmetrized anionic p_n, s and p_σ orbitals are ϕ_n, ϕ_s and ϕ_σ ; the symmetrized A-cationic s, p orbitals are ϕ_A . The covalent-mixing parameters $\lambda_n, \lambda_s, \lambda_A, \lambda_\sigma$ are roughly proportional to the overlap integral for atomic orbitals on neighboring ions and inversely proportional to their energy separation. Initially, the energy separations of cationic *d* and ϕ_σ or ϕ_n are given by $E_M - E_I$, the difference between the Madelung energy and ionization potentials for the "effective" ionic charges, so that by symmetry

$$10Dq = \Delta_M + (\lambda_\sigma^2 - \lambda_n^2)(E_M - E_I), \lambda_n < \lambda_\sigma \quad (5)$$

where Δ_M is any electrostatic contribution to 10 Dq. The one-electron crystal-field splitting of the *d*-state manifold is shown in Fig. 7(a). The relationship $\lambda_n < \lambda_\sigma$ has been confirmed by nuclear magnetic resonance studies of KMnF₃, KNiF₃, and K₂NiCrF₆ [Sh30, Hu4]. In these experiments the fractional occupancies by unpaired spins of the 2*s*, 2*p*_σ, and 2*p*_π orbitals are:

$$fx_s \equiv 2SA_s/A_{2s} \sim N_s^2 \lambda_s^2, \quad fx_\sigma = 2SA_\sigma/A_{2p} \sim N_\sigma^2 \lambda_\sigma^2, \quad fx_\pi = 2SA_\pi/A_{2p} \sim N_\pi^2 \lambda_\pi^2$$

where A_s is the isotropic component and A_σ, A_π the anisotropic components of the hyperfine interaction tensor A_{ij} entering the nuclear spin-electron spin coupling energy $\sum_i I_i \cdot A_{ij} \cdot S_j$. Interpretation of the phenomenological parameters $\lambda_n, \lambda_\sigma$ and 10 Dq has been discussed extensively [Hu4].

With more than one outer *d* electron or *d* hole, it is necessary to introduce V_{el} , which is responsible for Hund's highest multiplicity rule (highest net *S* and *L*) for the free atoms. For four outer electrons, the atomic ground term is therefore ⁵D. In a crystal, this rule may break down as a result of the crystalline

field
may
with
(4ex)

Fig.
a) L
Hu
sio:
Sir
is :
pa:
per:
the
va:
sta

o1
t2
ti

fields. Schematically, the Hund splitting Δ_{ex} for states of different spin and the one-electron splitting $10 Dq$ may be represented on the same energy diagram, as shown in Fig. 7(b). It follows from this figure that with four to eight outer d electrons, the magnitude of the net ground-state spin depends upon whether ($\Delta_{\text{ex}} - 10 Dq$) is positive or negative. If $\Delta_{\text{ex}} > 10 Dq$, the ion is in a high-spin state; if $\Delta_{\text{ex}} < 10 Dq$,

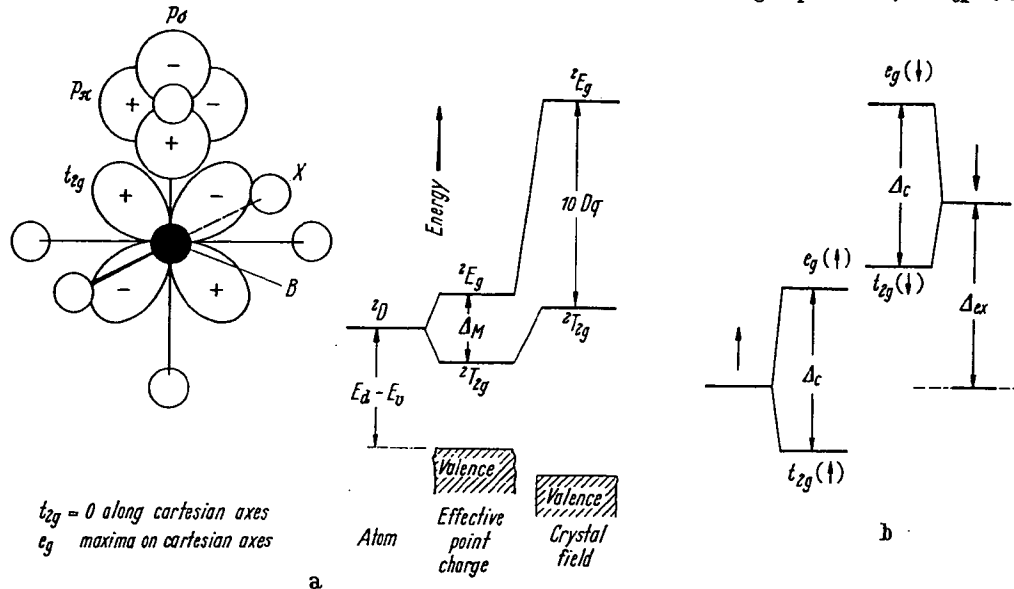


Fig. 7. One-electron crystal-field splitting of the d -state manifold of a transition-metal B cation in a cubic perovskite: a) $\Delta_{\text{ex}} = 0$ and b) schematically for $\Delta_{\text{ex}} \neq 0$, corresponding to more than one outer d electron.

Hund's rule breaks down and the ion is in a low-spin state. Since Δ_{ex} decreases with larger radial extension of the crystalline wave functions, it decreases with increasing covalent-mixing parameters λ_{cr} , λ_{in} . Simultaneously, from Eq. (5) it follows that $10 Dq$ increases with increasing covalency. Therefore there is a critical amount of covalent bonding beyond which Hund's rule breaks down. Covalency with a particular anionic sublattice increases with cationic charge and on going to the right through any long period of the periodic table. In oxides with the perovskite structure, only divalent and trivalent ions of the first long period are high-spin. Of these, trivalent nickel is low-spin and trivalent cobalt exhibits a variable high-spin to low-spin population as a function of temperature.

In general, it is necessary to use a multi-electron notation for the outer d electrons. Whereas atomic D states are split by the crystalline fields as shown in Fig. 7, atomic F states are split as shown in Fig. 8.

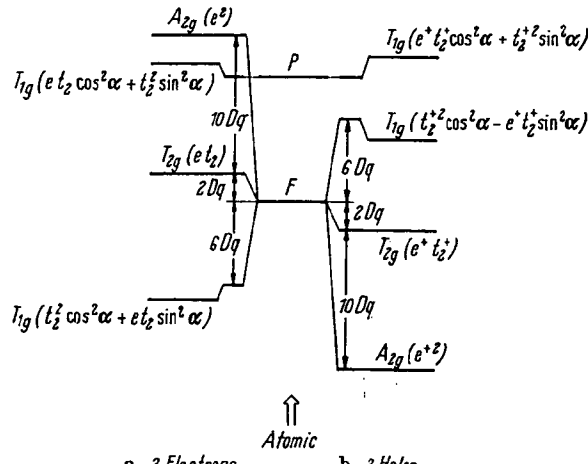


Fig. 8. Octahedral-site splitting of atomic F states: a) two-electron 3F states and b) two-hole 3F states.

Because the operator $L_z = -i\hbar\partial/\partial\phi$ is imaginary, the crystal-field splitting of f_B and f_C quenches the orbital angular momentum associated with these orbitals, so that the e_g orbitals have $m = 0, 0$ and the t_{2g} orbitals have $m = 0, \pm 1$. An isomorphism between f_C , f_D , f_E and atomic P orbitals simplifies calculation of V_{LS} . It is possible to treat the t_{2g} orbitals as atomic P orbitals if the sign of the spin-orbit-coupling

parameter λ is reversed [Gr9]. Therefore ground states having an orbital degeneracy and $m \neq 0$ are split by V_{LS} into $(2J + 1)$ multiplet states corresponding to states of different $J = L + S$. However, the order of the levels is inverted (largest J lowest for less than five d electrons, smallest J lowest for more than five d electrons) because of the change in sign of λ . According to the Landé interval rule, the separation between states J and $J + 1$ is $|\lambda| (J + 1)$. The first-order multiplet splittings, which do not include mixing of higher states of similar symmetry, are shown in Fig. 9 for Fe^{2+} and Co^{2+} ions. Note that the term is now identified by its symmetry character T_{2g} or T_{1g} rather than by its atomic orbital-momentum character D or F . Tab. 1 summarizes the various symmetry notations for different spin states.

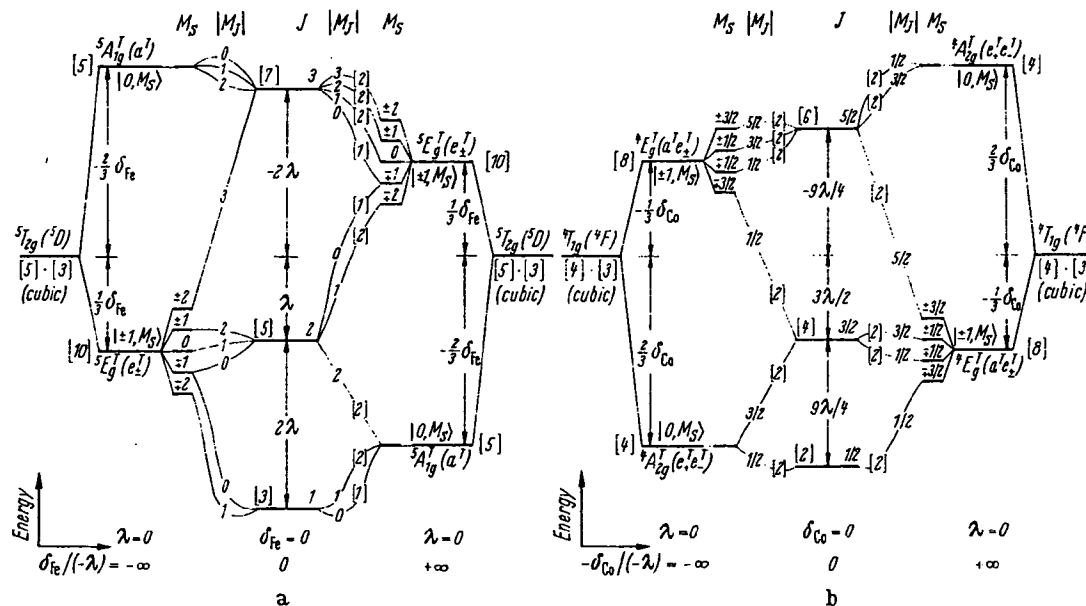


Fig. 9. Schematic spin-orbit plus trigonal-field, or tetragonal-field, splittings of cubic-field levels as a function of the ratio $\delta/(-\lambda)$ for a) $^5T_{2g}$ level of Fe^{2+} and b) $^4T_{1g}$ level of Co^{2+} .

Spin-orbit coupling introduces an axial symmetry to the charge distribution, where the spin (or atomic-moment) defines the axis. Therefore, if there is a noncubic component to the crystalline field ($V_{\text{n cub}} \neq 0$), then there is a spin-lattice interaction via the orbital-lattice interaction that introduces a magnetic anisotropy. For localized electrons, this is a local, one-ion anisotropy. Conversely, if the spins are ordered below some transition temperature, then the local interstices have time to relax about the noncubic charge distribution, thereby distorting the octahedral site. Therefore there is an intimate connection between the noncubic symmetry and the magnitude of the multiplet splitting. The noncubic component is usually parametrized as

$$V_{\text{n cub}} = \delta (L_z^2 - \frac{1}{3}), \quad (6)$$

and Fig. 9 includes the total perturbation $V_{LS} + V_{\text{n cub}}$ of the one-electron and two-electron ground states.

With one or two holes in a half-shell, the one-electron and two-electron energy diagrams are inverted. In these cases $M_L = \sum_i m_i = 0$, so that $V_{LS} = 0$, and there is no multiplet splitting.

Tab. 1 also displays the general ground-state wave functions for a magnetically ordered phase having collinear spins. The coefficients a_1, a_2, a_3 of the Kramers' doublets and b_1, b_2 of the singlets all depend upon the relative magnitudes of the five perturbation terms $V_{LS} + V_{\text{n cub}} + V_\lambda + \mathcal{H}_Z$ where \mathcal{H}_Z is the Zeeman energy due to the internal molecular field resulting from magnetic order. The molecular-field approximation is used for the first-order, isotropic magnetic-coupling energy \mathcal{H}_{ex} , which is the dominant term in $\sum_j V_{ij}$ [see discussion of Eq. (13)]. This gives

$$\mathcal{H}_Z \approx 2 J_p \langle S \rangle S_z \quad (7)$$

where J_p , the sum of all near-neighbor exchange parameters, can be determined from the temperature dependence of the magnetic susceptibility and z is along the axis of the average spin $\langle S \rangle$ on the neighboring cations. This term contributes to the spectroscopic-splitting factor g , and hence to the net atomic moment, if $V_{LS} \neq 0$. In Tab. 1, the components of the wave functions are designated by the notation $|M_L, M_S\rangle$, where M_L, M_S are the azimuthal quantum numbers for the net orbital and spin moments.

Tab. 1. Lowest terms and ground state wave function for octahedral-site cations having n localized outer d electrons

n	Ion	<i>t⁶e_g</i>	<i>V_{a1}</i>	<i>V_{cub}</i>	<i>V_{LS}</i>	<i>V_{LS} + V_{cub}(δ < 0) + ℳ_Z</i>	<i>V_{LS} + V_{cub}(δ > 0) + ℳ_Z</i>
1	Ti ³⁺ , V ⁴⁺ , W ⁵⁺ , Re ⁶⁺	<i>t¹e₀</i>	<i>2D</i>	<i>2T_{2g}</i>	<i>J = 1/2</i>	<i> +1, +1/2></i>	<i>a₁ 0, +1/2> + a₃ +1, -1/2></i>
2	V ³⁺ , Cr ⁴⁺ , Mo ⁵⁺	<i>t²e₀</i>	<i>3F</i>	<i>3T_{1g}</i>	<i>J = 2</i>	<i> +1, +1></i>	<i>b₁ +1, -1> + b₂ 0, 0> + b₃ -1, +1></i>
3	V ²⁺ , Cr ³⁺ , Mn ⁴⁺ , Mo ³⁺	<i>t³e₀</i>	<i>4F</i>	<i>4A_{2g}</i>	<i>J = 1/2</i>	<i> 0, +3/2></i>	<i> 0, +3/2></i>
4	Cr ²⁺ , Mn ³⁺	<i>t³e₁</i>	<i>5D</i>	<i>5E_g</i>	<i>J = 2</i>	<i>⁵B_{1g} 0, +2></i>	<i>⁵A_{1g} 0, +2></i>
5	Fe ^{IV} , Ru ^{IV} , Os ^{IV}	<i>t⁴e₀</i>	<i>3T_{1g}</i>	<i>J = 0</i>	<i>b₁ +1, -1> + b₂ 0, 0> + b₁ -1, +1></i>	<i>b₁ ' +1, -1> + b₂' 0, 0> + b₁' -1, +1></i>	
5	Mn ²⁺ , Fe ³⁺	<i>t³e₂</i>	<i>6S</i>	<i>6A_{1g}</i>	<i>J = 1/2</i>	<i> 0, +1/2></i>	<i> 0, +1/2></i>
5	I ^{IV}	<i>t⁵e₀</i>	<i>2T_{2g}</i>	<i>J = 1</i>	<i>a₁ 0, +1/2> + a₃ +1, -1/2></i>	<i>a₁' 0, +1/2> + a₃' +1, -1/2></i>	
6	Fe ³⁺ , Co ³⁺	<i>t⁴e₂</i>	<i>5D</i>	<i>5T_{2g}</i>	<i>J = 1</i>	<i>a₁ -1, +2> + a₂ 0, +1> + a₃ +1, 0></i>	<i>b₁ +1, -1> + b₂ 0, 0> + b₁ -1, +1></i>
6	Co ^{III} , Rh ^{III} , Pt ^{IV}	<i>t⁶e₀</i>	<i>1A_{1g}</i>	<i>J = 0</i>	<i> 0, 0></i>	<i> 0, 0></i>	
7	Co ²⁺	<i>t⁶e₂</i>	<i>4F</i>	<i>4T_{1g}</i>	<i>J = 1/2</i>	<i>a₁ -1, +3/2> + a₂ 0, +1/2> + a₃ +1, -1/2></i>	<i>a₁' -1, +3/2> + a₂' 0, +1/2> + a₃' +1, -1/2></i>
7	Ni ^{III}	<i>t⁶e₁</i>	<i>2E_g</i>	<i>J = 1/2</i>	<i>²B_{1g} 0, +1/2></i>	<i>²A_{1g} 0, +1/2></i>	
8	Ni ²⁺ , Pd ²⁺	<i>t⁶e₂</i>	<i>3F</i>	<i>3A_{2g}</i>	<i>J = 1</i>	<i> 0, +1></i>	<i> 0, +1></i>
9	Cu ²⁺	<i>t⁶e₃</i>	<i>2D</i>	<i>2E_g</i>	<i>J = 1/2</i>	<i>²B_{1g} 0, +1/2></i>	<i>²A_{1g} 0, +1/2></i>

3.1.3.2 Jahn-Teller distortions

If the cubic-field ground state of the B cation is an orbitally two-fold-degenerate E_g state, then the t_{2g} orbitals are either full or half-filled, so that $M_L = 0$, and there is no spin-orbit coupling ($V_{LS} = 0$). JAHN and TELLER [Ja6] have shown that, if there is no perturbation available to remove a ground-state orbital degeneracy, then there will be a spontaneous distortion to lower local symmetry below some transition temperature $\Theta_{\text{trans}} < T_{\text{melt}}$ where T_{melt} is the melting point. Since the energy gained by a local distortion is reduced by the work done against the elastic restoring forces of the crystal, transition temperatures Θ_{trans} are small for isolated ions. However, if all of the B cations are similar, then cooperative distortions are possible, and the net energy gained per ion is much greater because of the elastic-coupling energy V_λ of Eq. (2). Such a cooperative phenomenon is characterized by thermal hysteresis and a definite (usually first-order) transition temperature. Since they are due to electronic ordering, such transitions are martensitic.

VAN VLECK [Va15] pointed out that the normal vibrational modes that split an E_g electronic state are themselves twofold-degenerate with symmetry E_g . One mode gives the interstice a tetragonal distortion, the other an orthorhombic distortion. It follows that, from first-order theory, there is no static distortion of the interstice, only a dynamic coupling between the electronic charge density and the vibrational modes. Moreover, this dynamic coupling greatly enhances the two E_g vibrational modes and gives a dynamic splitting of the electronic E_g state. This mechanism has important consequences for the acoustic properties and, as discussed in 3.3, for the sign of the magnetic superexchange coupling.

Inclusion in the theory of higher-order coupling terms and anharmonic elastic terms shows that a static, tetragonal ($c/a > 1$) distortion of the interstice is stable below some Θ_{trans} [Ka10]. This sign for the static distortion was first established experimentally through the interpretation [Go15] and further study of cooperative tetragonal-to-cubic transitions in spinel systems. However, application to the perovskites requires a solution of the lowest-energy cooperative distortion via inclusion of the elastic-coupling energy V_λ . GOODENOUGH [Go6] proposed that individual tetragonal ($c/a > 1$) octahedra order their long axes alternately along [100] and [010] axes of the pseudocubic cell. KANAMORI [Ka10] generalized this solution to include an orthorhombic component to the local-octahedron distortions. This gives B-B separations within (001) planes having a long (l) and a short (s) B-X separation and along the [001] axis two intermediate (m) B-X separations where $s < m < (l + s)/2$. This prediction was later verified by HEPWORTH and JACK [He9] for $\square \text{MnF}_3$, and by OKAZAKI [Ok1] for KCuF_3 (see Fig. 10). Superposition of this distortion on an O-orthorhombic cell stabilizes the unique axis along the orthorhombic c -axis, and

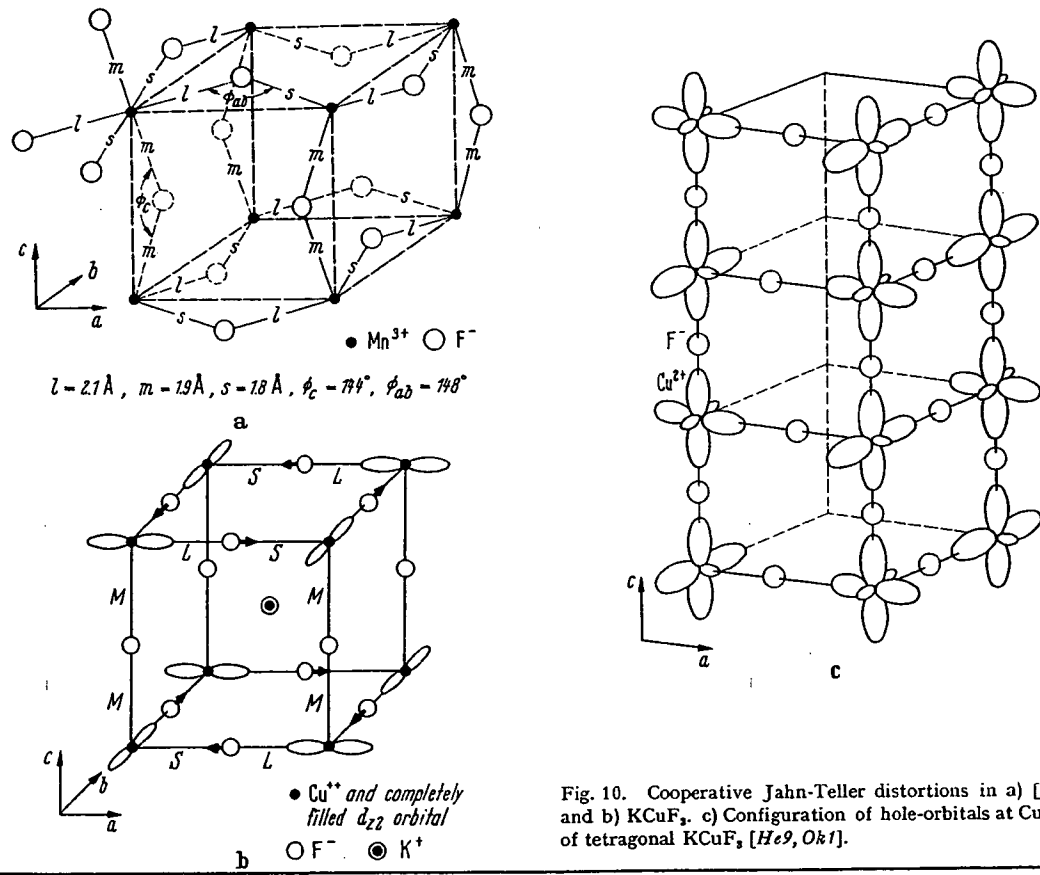


Fig. 10. Cooperative Jahn-Teller distortions in a) $\square \text{MnF}_3$, b) KCuF_3 , c) Configuration of hole-orbitals at Cu^{2+} ions of tetragonal KCuF_3 [He9, Ok1].

the axial ratios of the O-orthorhombic cell are transformed from $a < c/\sqrt{2}$ to $c/\sqrt{2} < a$. To signal the fact that a Jahn-Teller distortion (with or without spin-orbit coupling) has been superposed on a distortion due to relative ionic sizes, the notation O'-orthorhombic is used in Tab. 2 wherever $c/\sqrt{2} < a$.

The important B cations that exhibit dynamic and static JAHN-TELLER stabilizations in the absence of spin-orbit coupling are: Cu²⁺ $^2E_g(t_{2g}^6e_g^2)$, Cr²⁺ and Mn³⁺ $^5E_g(t_{2g}^3e_g^1)$, Ni^{III} $^2E_g(t_{2g}^6e_g^1)$, where Roman numerals are used for the valence state of a low-spin cation. Tab. 2 shows that O'-orthorhombic symmetry above a magnetic-ordering temperature is associated with these ions, provided the d electrons are localized, and only with these ions, with the exception of LaVO₃ and CeVO₃, where sharply enhanced distortions appear abruptly below Θ_N [Ro13; Go10]. The cubic $^3T_{1g}$ state of V³⁺ is orbitally threefold-degenerate, so that it may induce small distortions above Θ_N , larger distortions below Θ_N (see discussion Go14). LaNiO₃ remains R̄3c because the e_g electrons are collective. In La₂Li_{0.5}Ni_{0.5}O₄ crystals, on the other hand, the ordered Ni^{III} ions have localized e_g electrons, and there is a tetragonal ($c/a > 1$) distortion. The sign of this distortion is manifest by the large c/a ratio. Strictly speaking, this is not a Jahn-Teller distortion, since the K₂NiF₄ structure is tetragonal, but ordering of the localized electron of unpaired spin in the tetragonal field distorts the Ni^{III} octahedra to tetragonal symmetry with axes parallel to the unique axis. Pure Jahn-Teller distortions can be distinguished from distortions associated with spin-orbit coupling because they are independent of magnetic order and generally occur at a Θ_{trans} above the magnetic-ordering temperature.

3.1.3.3 Spin-orbit coupling

B cations having cubic-field ground-state terms T_{2g} or T_{1g} are orbitally threefold-degenerate with $M_L = 0, \pm 1$, so that $V_{LS} \neq 0$. The combined perturbations $V_{LS} + V_{ncub}$ separate into secular equations for different M_J , as shown in Fig. 9. With a single outer electron, the $^2T_{2g}$ cubic-field term is split in two, the energies for different M_J shifting by

$$\begin{aligned} E_{3/2} &= \frac{1}{2}\delta - \frac{1}{2}\lambda \\ E_{1/2}^{\pm} &= -\frac{1}{2}\delta + \frac{1}{2}\lambda \pm \frac{1}{2}\{\delta^2 + \lambda\delta + (\frac{1}{2}\lambda)^2\}^{1/2} \end{aligned} \quad (8)$$

where $\lambda > 0$. In a cubic field

$$E_{3/2} = E_{1/2}^- = E_{1/2}^+ - \frac{1}{2}\lambda, \quad (9)$$

and spin-orbit coupling leaves an orbitally twofold-degenerate ground state. Therefore it is necessary to consider an additional Jahn-Teller stabilization via $V_{ncub} + V_\lambda + \mathcal{H}_Z$. GOODENOUGH [Go14] has shown that it is necessary to consider two temperature regions: $T > \Theta_N$ and $T < \Theta_N$, where Θ_N is the temperature below which the spins order collinearly. In the paramagnetic domain $T > \Theta_N$, the molecular fields vanish ($\langle S \rangle = 0$) and, from Eq. (7), $\mathcal{H}_Z = 0$. In this case, the ground-state energy varies as (δ^2/λ) . Since the work done against elastic restoring forces is $q_2\delta^2$, there is a spontaneous Jahn-Teller distortion, corresponding to $\delta > 0$, at a $\Theta_{trans} > \Theta_N$ only if the product λq_2 is relatively small. In the magnetically ordered state ($T < \Theta_N$), on the other hand, there is an internal molecular field H_{int} at each atom, which produces a Zeeman splitting of the orbitals of different spin. The magnitude of this splitting depends upon the spectroscopic splitting factor, which has the components

$$g_{||} = 2 - 2g_1(\delta/\lambda) \text{ and } g_{\perp} = 2 + g_1(\delta/\lambda) \quad (10)$$

where $g_1 > 0$. Therefore the Zeeman splitting in the molecular fields is maximized by making $\delta < 0$ and having the spins parallel to the unique axis defined by δ . Further, this energy is linear in δ , so that a spontaneous distortion should occur at some $\Theta_{trans} < \Theta_N$. A similar argument holds for the orbitally twofold-degenerate $J = 1$ and $J = \frac{1}{2}$ states of octahedral-site Fe²⁺ $^5T_{2g}$ and Co²⁺ $^4T_{1g}$.

In summary, if multiplet splitting leaves a ground state with a twofold, accidental orbital degeneracy, then there is a spontaneous Jahn-Teller distortion at some Θ_{trans} that removes this degeneracy. If $\Theta_{trans} > \Theta_N$, then $\delta > 0$. However, this alternative requires special crystallographic conditions that do not appear to be met in perovskites. On the other hand, a $\Theta_{trans} \leq \Theta_N$ and $\delta < 0$ can be generally anticipated wherever the spins order collinearly and the d electrons are localized. Further, from Eqs. (3) and (6), it follows that T_{2g} states (one outer t_{2g} electron) have $\delta < 0$ if the site symmetry is tetragonal ($c/a > 1$), whereas T_{1g} states (two outer t_{2g} electrons) have $\delta < 0$ if it is tetragonal ($c/a < 1$). Alternatively, distortions of the site symmetry may be to trigonal symmetry. A $\delta < 0$ corresponds to $\alpha < 60^\circ$ for T_{2g} states, to $\alpha > 60^\circ$ for T_{1g} states. These relationships are also summarized in Tab. 1. Experimentally, Fe²⁺ $^5T_{2g}$ octahedra become trigonal ($\alpha < 60^\circ$) below Θ_N , as exhibited by KFeF₃, whereas Co²⁺ $^4T_{1g}$ octahedra become tetragonal ($c/a < 1$) below Θ_N , as exhibited by KCoF₃. Where $\Theta_{trans} = \Theta_N$, the magnetic-ordering temperature may be first-order. In addition, the spontaneous distortions introduce large magnetostriction and magnetic anisotropy.

The cubic-field ground state of V³⁺ $^3T_{1g}$ is orbitally threefold-degenerate. As a result, any spontaneous distortion must correspond to $\delta < 0$, i.e., tetragonal ($c/a < 1$) or trigonal ($\alpha > 60^\circ$). However, as in the other cases a $\Theta_{trans} \lesssim \Theta_N$ is to be expected in the perovskite structure. The V³⁺ ion generally occurs in an O-orthorhombic perovskite, and superposition of a tetragonal ($c/a < 1$) distortion with coincident unique axes again results in O'-orthorhombic symmetry. The perovskite LaVO₃ exhibits an abrupt contraction of the c-axis on cooling through Θ_N .

3.1.4 The influence of collective-electron ordering

3.1.4.1 Band theory

Conventional band theory rests on three principal assumptions: (1) A description of the outer electrons may be built up from solutions of a single electron moving in a periodic potential. (2) Multiplet structure on individual atoms may be disregarded. (3) Electron-phonon interactions may be treated as a small perturbation. For an infinite crystal, the unperturbed solution of running waves in a periodic potential gives the Bloch functions and energies

$$\psi_{\mathbf{k}m} = \exp(i\mathbf{k} \cdot \mathbf{r}) u_{\mathbf{k}m}(\mathbf{r}); E_{\mathbf{k}} = E_0 + \hbar^2 k^2 / 2m^* \quad (11)$$

where $\hbar\mathbf{k}$ is the momentum of an electron of effective mass m^* and $u_{\mathbf{k}}(\mathbf{r})$ is a periodic function. In the tight-binding approximation appropriate for narrow bands, the Bloch functions are

$$\psi_{\mathbf{k}}(\mathbf{r}) = 1/\sqrt{N} \sum_{n=1}^N \exp(i\mathbf{k} \cdot \mathbf{R}_n) w(\mathbf{r} - \mathbf{R}_n)$$

where $w(\mathbf{r} - \mathbf{R}_n)$ is a localized wave function for the atom at \mathbf{R}_n defined by

$$w(\mathbf{r} - \mathbf{R}_n) = 1/\sqrt{N} \sum_n \exp[i\mathbf{k} \cdot (\mathbf{r} - \mathbf{R}_n)] u_{\mathbf{k}}(\mathbf{r})$$

and $u_{\mathbf{k}}(\mathbf{r})$ is a localized crystalline orbital. At the Brilloin-zone boundaries defined by

$$2\mathbf{k} \cdot \mathbf{K} + |\mathbf{K}|^2 = 0, \quad (12)$$

where \mathbf{K} is a reciprocal lattice vector, there are energy discontinuities in energy-momentum space. In polar insulators, this introduces an energy gap E_g between occupied, primarily anionic states and empty, primarily cationic states. Cooperative displacements δ of the cationic sublattice relative to the anionic sublattice may increase this gap, thereby stabilizing the total energy of the occupied states by $\epsilon_2 \delta^2$. Since the resulting elastic-strain energy is $q_2 \delta^2$, there can be a spontaneous displacement only for the exceptional case $q_2 < \epsilon_2$ and a ground state corresponding to a small distortion parameter δ . In this case vibrational entropy may stabilize the higher symmetry at the higher temperatures. This differs from the usual criterion for spontaneous distortions, where a term linear in δ is identified. There appear to be two situations occurring in perovskites where the requirement $q_2 < \epsilon_2$ is met: (1) Where B-cations have empty d orbitals, there is a critical range of covalent-mixing parameters through which the site preference changes from octahedral to tetrahedral. In this range q_2 is very small for B-cation displacements within an octahedron that reduce the coordination number from six towards four. The origin of the small q_2 is a balance of the electrostatic energy lost and covalent-bond energy gained on going to smaller anion coordination. (2) The high polarizability of the outer core electrons of Pb²⁺ and Bi³⁺ ions makes q_2 relatively small, so that displacements that permit a relatively large ϵ_2 can occur spontaneously.

What distinguishes these spontaneous distortions from those due to an ordering of localized electrons is the displacement of the cations from the centers of symmetry of their interstices. (The Jahn-Teller distortions, with or without spin-orbit coupling, leave the cations in the centers of symmetry of their interstices.) Unlike the structures, such as corundum, where pairs of octahedra share a common face, these cationic displacements from the centers of symmetry of their interstices do not follow from point-charge electrostatic arguments. In polar insulators, these displacements lead to ferroelectricity or anti-ferroelectricity, and they often induce displacements of neighboring cations. Further, where the requirement $q_2 \approx \epsilon_2$ occurs just above Θ_{trans} , there must be a strong interaction of the bonding (mostly anionic) electrons with those vibrational modes that anticipate the cooperative ionic displacements below Θ_{trans} . These "soft" vibrational modes impart several anomalous physical properties, including a high electric susceptibility.

3.1.4.2 Distortions due to B-X bonding

Transition-metal cations having no outer d electrons have the following site preferences:

Sc ³⁺	Ti ⁴⁺	V ⁵⁺	Cr ⁶⁺	Mn ⁷⁺
Y ³⁺	Zr ⁴⁺	<u>Nb⁵⁺</u>	<u>Mo⁶⁺</u>	Tc ⁷⁺
Hf ⁴⁺	Ta ⁵⁺	<u>W⁶⁺</u>	<u>Re⁷⁺</u>	

where cations at the left of each row have definite octahedral-site (or larger anion coordination) preference and those to the right have definite tetrahedral-site preference. Those underlined by a solid line may be stabilized in the octahedral sites of a perovskite-type structure, but they tend to induce spontaneous ferroelectric or antiferroelectric distortions, the ions moving cooperatively out of the centers of symmetry of their interstices. The ions underlined by dashed lines only occur in ordered perovskites $A_2BB' O_6$ and $A_3BB' O_9$. In general, they are found in tetrahedral sites or in strongly distorted octahedral sites. However, in the ordered perovskites they are able to strongly polarize the anion near neighbors so as to stabilize the octahedral symmetry.

3.1 ABX₃ perovskite structure

It is significant that spontaneous ferroelectric distortions are only induced by B cations if these are transition-metal cations having empty d orbitals. It is also significant that the change from octahedral-site to tetrahedral-site preference is associated with a relative stabilization of the d orbitals (larger atomic number in any long period) as well as with a decrease in ionic size. (The ionic radii decrease in the order Y³⁺, Sc³⁺, Hf⁴⁺, Zr⁴⁺, Ta⁵⁺, Nb⁵⁺, Ti⁴⁺, W⁶⁺, Mo⁶⁺, Re⁷⁺, V⁵⁺, Tc⁷⁺, Cr⁶⁺, Mn⁷⁺). The greater the relative stability of the d orbitals, the larger are the parameters λ_{σ} and λ_{π} of Eq. (4), and these are enhanced by any displacement that decreases a B-X separation. Such an enhancement stabilizes the occupied states at the expense of the d states, and a net stabilization can occur if the d states are empty. Also the smaller the cationic size, the smaller the elastic resistance to displacements within an octahedral interstice. (Phenomenological ionic models for the ferroelectric distortions have also been given [Me7, Ha33].)

There are three B-cation displacements relative to their octahedral interstices that would simultaneously stabilize the occupied anionic p_{π} orbitals relative to the unoccupied t_{2g} orbitals: (1) *Tetragonal symmetry*. Displacements along an [001] axis that create alternate long and short B-X distances along this axis would stabilize s, p_{σ} and the two p_{π} orbitals per anion on this axis and strongly polarize the charge density toward the short B-X separation. (2) *Orthorhombic symmetry*. Displacement along a [110] axis that created two shortest and two longest B-X distances would stabilize the s, p_{σ} and the two p_{π} orbitals per anion on two out of the three cartesian axes. (3) *Rhombohedral symmetry*. Displacement along a [111] axis would stabilize the s, p_{σ} and the two p_{π} orbitals per anion on all the anions. These three possibilities are illustrated in Fig. 11.

Such distortions also induce changes in the A-X separations, and the particular cooperative distortion that is stabilized depends upon the character of the A-X bonding. The covalency contribution to the A-X bond increases with formal A cationic charge; for a fixed charge it decreases with increasing atomic number of the A cation down any column of the periodic table. If A-X covalent bonding is relatively strong and the perovskite is distorted to O-orthorhombic symmetry, all ferroelectric distortions may be quenched because the p_{π} orbitals are stabilized by σ -bonding with the A cations. This appears to be illustrated by CaTiO₃, and almost so by SrTiO₃. On the other hand, if the A atom is stabilized by a polarization of its outer core electrons (Pb²⁺ and Bi³⁺ as discussed in 3.1.4.3), then a tetragonal, ferroelectric distortion is stabilized so as to allow a cooperative displacement of the A and B cations, the A cation moving along the [001] axis to stabilize two p_{π} orbitals per anion not on [001] axes. This is illustrated by the PbTiO₃ structure of Fig. 12. If the covalency contribution to the A-X bonding is relatively weak, then the B-X covalency contribution should dominate. For large A cations ($t > 0.9$), this would stabilize a ferroelectric, rhombohedral distortion at lowest temperatures, as illustrated by BaTiO₃. As the temperature increases, successive distorted structures ($R_B^F \rightarrow O_B^F \rightarrow T_B^F \rightarrow C$) introduce incremental additions to the entropy. However, a small A cation and weak A-X covalency contribution may lead to a ferroelectric distortion superposed on the O-orthorhombic structure to give the O_B^F -orthorhombic structure of CdTiO₃, or NaTaO₃, shown in Fig. 13. Even more complex distortions are found in NaNbO₃, [Vo6]. The room-tem-

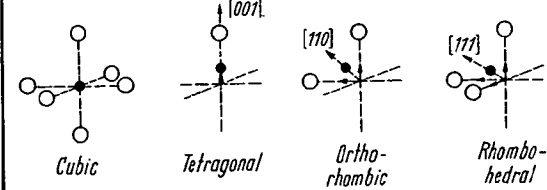


Fig. 11. Possible B-cationic displacements within their octahedra in ferroelectric or antiferroelectric distortions.

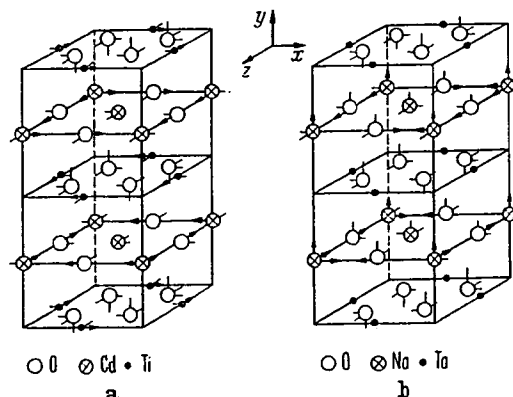


Fig. 12. Tetragonal PbTiO₃; a) environment of Ti and b) environment of Pb [Sh21].

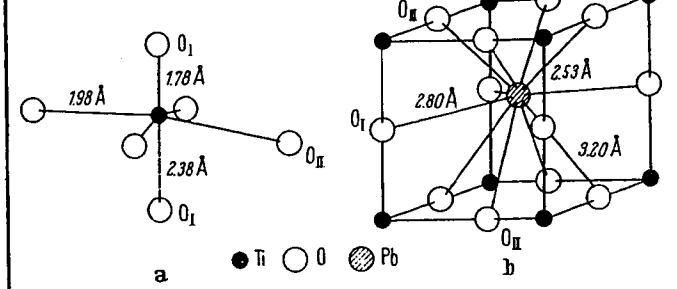


Fig. 13. Ionic displacements in a) CdTiO₃ and b) NaTaO₃ [Ka22].

perature form has parallel pairs of (001) NbO₂ planes coupled antiparallel to give an antiferroelectric phase, as shown in Fig. 14. The Na atoms are also displaced antiparallel to one another.

3.1.4.3 Distortions due to core polarization : Pb²⁺ and Bi³⁺

Lead and bismuth are heavy ions, and the 6s orbitals are sufficiently more stable than the 6p orbitals that Pb²⁺ and Bi³⁺ ions are commonly stable. However, the outer 6s² core electrons have a relatively large radial extension, making the ionic radius large, and this reduces the overlap of the 6p orbitals with the orbitals on near-neighbor anions. This reduction in overlap reduces the strength of the A-X bond. However, hybridization of 6s and 6p orbitals, which costs the energy separation of 6s and 6p orbitals, produces a polarization of the outer-core electrons, so that the effective ionic radius is much smaller on one side of the cation than on the other. This permits the formation of a much more stable bond on one side of the cation, and the energy gained in this bonding may be greater than the hybridization energy required to polarize the core. It is for this reason that Pb²⁺ and Bi³⁺ ions are stabilized in many crystals with an asymmetric anion coordination.

There are three possible displacements of the A cations that would stabilize the anion p_n orbitals (which σ-bond with the A cations): (1) *Tetragonal symmetry*. Displacement of the A cations along [001] axes to stabilize the two p_n orbitals per anion not on [001] axes, as found for PbTiO₃ (see Fig. 12). (2) *Orthorhombic symmetry*. Displacement of the A cations along [110] axes to stabilize strongly one p_n orbital per anion on [001] axes and less strongly one p_n orbital per anion not on [001] axes. The smallest induced distortion of the B-cation octahedra occurs for an antiferroelectric displacement of the type illustrated by PbZrO₃, Fig. 15. (3) *Rhombohedral symmetry*. Displacement of the A cations along [111] axes to stabilize strongly one p_n orbital per anion. To be cooperative, such a distortion must be ferroelectric, as in BiFeO₃, Fig. 16. Further, since the A cation is moved toward a B cation, there is an electrostatic repulsion between them that displaces the B cation from the center of symmetry of its interstice.

Given spontaneous distortions due to A-cation displacements, there remains the possibility that electron ordering among localized d electrons on B cations can superpose an additional distortion. Whether this is the origin of the triclinic symmetry reported for ferromagnetic BiMnO₃, where Mn³⁺ is a Jahn-Teller ion, is not known.

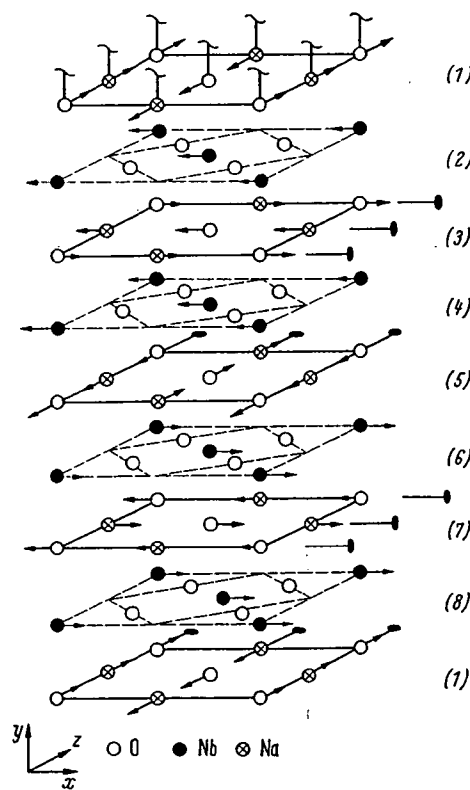


Fig. 14. Ionic displacements in orthorhombic NaNbO₃. The shifts of the anions in NbO₂ planes and the small z-shifts of the Nb ions have been omitted for clarity [Vog].

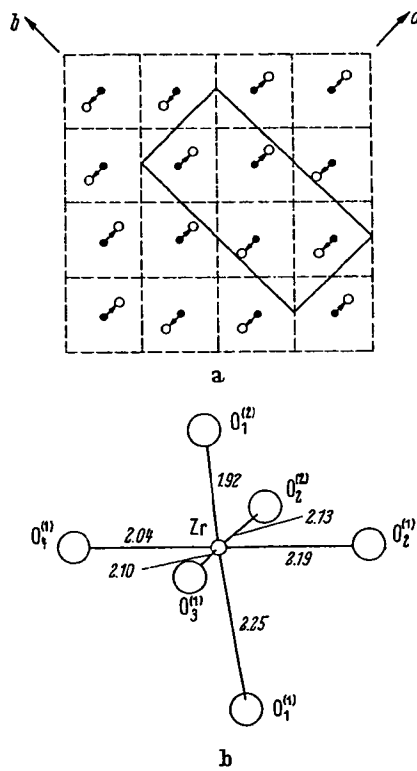


Fig. 15. a) Pb-ion shifts ($\approx 0.26 \text{ \AA}$) in a (001) plane of anti-ferroelectric PbZrO₃. b) Distorted Zr octahedra as a result of simultaneous anion displacements. Zr-O distances are given in \AA [Saß, Joß].

se,

als
ely
th
d.
ls,
on
ne
gy
alsals
[1]
io-
ver
ed
by
ze
D,
enxc-
ter
n-

3.1.4.4 Competitive phases

A few compounds have atomic radii compatible with the formation of a perovskite phase and yet are stabilized in other structures at ordinary temperature and pressure. Two important competitive structures of this type are represented by YAlO_3 and PbRuO_3 . Both of these compounds convert to the perovskite structure under hydrostatic pressure.

The hexagonal YAlO_3 structure of Fig. 17(a) consists of close-packed layers having the sequence $b-a-b'-a-b-c-b'-c-b$, where b is an A-cation layer, b' is a B-X layer with anions stacked beneath A cations (b stacking) and B cations in the trigonal bipyramids formed by face-shared tetrahedra in the hexagonal $a-b-a$ or $c-b-c$ anion-stacking sequence. The structure apparently forms because both the A cations and the B cations simultaneously approach the lower limit for cationic size: $r_B = 0.51 \text{ \AA}$, $r_A = 0.90 \text{ \AA}$. The small Al^{3+} ion is relatively stable in the five-fold coordination of the trigonal-bipyramidal sites, and the small Y^{3+} ion is more stable in an eightfold (or 6 + 2) coordination instead of a twelvefold (or 9 + 3) coordination. These site preferences reflect an increased stabilization of the bonding, anionic orbitals as a result of closer cation-anion distances.

The antiferromagnetic, ferroelectric compound YMnO_3 has a similar structure, but with an a -axis $\sqrt{3}$ larger than that of YAlO_3 to give six molecules per unit cell. The Mn^{3+} ion can be stabilized in a trigonal-bipyramidal site because it has four outer d electrons with configuration $e_g^2 e_g^2 a_1^0$, where the empty a_1 orbital is directed along the c -axis to bond covalently with the two collinear oxygen ions. The larger unit cell and the ferroelectricity are reflected in the complex magnetic order shown in Fig. 17(b). Below T_N , exchange striction favors antiferromagnetic Mn-O-O-Mn interactions. The ferroelectric transition that occurs above 600 °C is apparently due to the relatively large size of the Mn^{3+} ion, which creates a large enough interstice for the Y^{3+} ion that it is stabilized by a displacement from the center of symmetry of its interstice so as to lower its near-neighbor anion coordination from eight toward seven.

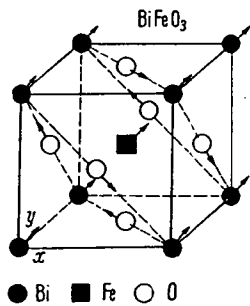


Fig. 16. Structure of BiFeO_3 showing displacements in perovskite subcell [M10].

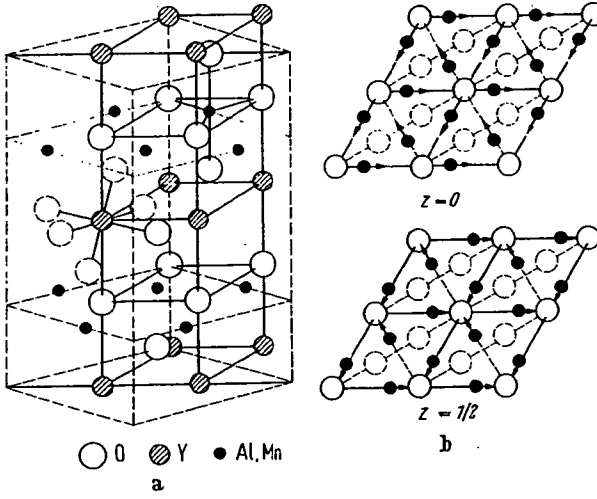


Fig. 17. a) Comparison of the unit cells of YAlO_3 (solid lines) and YMnO_3 (dashed lines). b) Magnetic structure of YMnO_3 [Be36, Be39].
 $a = 3.67 \text{ \AA}$, $c = 10.52 \text{ \AA}$ for YAlO_3 .

Cubic PbRuO_3 gives an x-ray pattern of the pyrochlore structure, corresponding to chemical formula $\text{A}_2\text{B}_2\text{O}_7$, and therefore may be written as $\text{Pb}_2\text{Ru}_2\text{O}_7\oplus$. This structure is competitive with the perovskite structure in several $\text{PbB}^{3+}\text{O}_3$ compounds. It has been shown [Lo4] that the anion vacancies \oplus are located at the centers of Pb^{2+} -ion tetrahedra sharing common corners and that the electrostatic repulsion between the Pb ions may be counteracted by a transfer of the two outer-core electrons per Pb ion to the \oplus sites, which act as traps for four electrons per vacancy. Thus the outer core electrons at the Pb^{2+} ions induce a completely new structure rather than a ferroelectric-type displacement of the A-cations within the perovskite structure. This new structure contains B cations in corner-shared octahedra, as in perovskite, but the B-X-B angle is reduced to about 135°. This structure is also stabilized in AgSbO_3 [Sc22] presumably because there is a small effective charge on the Ag^{+} ions. The pyrochlore $\text{A}_2\text{B}_2\text{O}_7$ structure itself is competitive if attempts are made to force a low valence state on one of the cations.

B
gi
nc
st
of
cli
lo
Fi
ra
ar
tr
sh
ac

A
ti
ci
ci
P
n
tl
A

3.1.5 Structures encountered with ordered B, B' cations

3.1.5.1 Same B atom

There are three ways of creating two different cations from the same atom:

(1) Two A cations of different valence can create two different valence states of the same B atom, and these may order at lower temperature as a result of different cationic charge. The ordering temperature may be quite low, since only electron transfers are required for cationic ordering. This is illustrated by $(La_{0.5}Ca_{0.5})(Mn^{3+}_{0.5}Mn^{4+}_{0.5})O_3$, which has the Mn³⁺, Mn⁴⁺ ordering in a rocksalt-type array. Because Mn³⁺($t_{2g}^2e_g^1$) is a Jahn-Teller ion having localized outer d electrons, there is also a cooperative distortion to tetragonal ($c/a > 1$) symmetry of the Mn³⁺-occupied octahedra, and the ordering of these distortions gives a macroscopic distortion to tetragonal ($c/a < 1$) symmetry (see Fig. 26).

(2) Where the energy difference between the high-spin and low-spin states of the B cation are nearly equal, the populations of the two energy states approach each other at higher temperatures. In LaCoO₃, high-spin Co³⁺ and low-spin Co^{III} are separated by only $E_{3+} - E_{III} \approx 0.08$ eV, and the populations of the two spin states are nearly equal at 400°K. This temperature is sufficiently low that ordering of the two different spin states occurs above this temperature, and the symmetry changes from R̄3c to R̄3 [Ra3]. In this case, it is the difference in ionic size and covalent bonding, which results in a difference in the effective ionic charge—not the formal ionic charge—that is the driving force for the ionic ordering.

(3) Disproportionation of B^{m+} cations into B^{(m-1)+} and B^{(m+1)+} cations may create ions of different size and charge that become ordered. This is illustrated by □PdF₃, which has been shown by magnetic susceptibility measurements to be Pd²⁺Pd^{IV}F₆ [Ba19]. (The A cation is missing.) Such a disproportionation permits the formation of (PdF₆)²⁻ clusters in which the anionic orbitals are stabilized by strong covalent mixing with the σ-bonding 4d orbitals of e_g symmetry. This is accomplished by a shifting of the F⁻ ions toward the Pd⁴⁺ ions and away from the Pd²⁺ ions. Simultaneously, the anionic shift reduces covalent mixing in the occupied, antibonding 4d orbitals of e_g symmetry at the Pd²⁺ ions. These orbitals are therefore localized and further stabilized by intra-atomic exchange (Hund splitting), so that each Pd²⁺ ion carries an atomic moment of $2\mu_B$. Were there no disproportionation, the single electron per low-spin Pd^{III} ion would occupy antibonding e_g orbitals that were more unstable than the occupied, localized e_g orbitals at the Pd²⁺ ions. However, the transformation $2Pd^{III} \rightarrow Pd^{2+} + Pd^{IV}$ costs ionization energy, and this is usually too large (as in LaNiO₃) for disproportionation to occur.

3.1.5.2 Different B atoms

There are many examples of ordered B, B' structures in compounds having different B atoms: A₂⁺B³⁺O₆, A₂⁺B³⁺+B'⁵⁺O₆, A₂⁺B³⁺+B'⁶⁺O₆, A₂⁺B³⁺+B'⁷⁺O₆; A₂⁺B³⁺+B'⁴⁺O₆, A₂⁺B³⁺+B'⁵⁺O₆, and A₂⁺B₂⁺B'⁶⁺O₉. In the A₂BB'X₆ group, ordering is on alternate (111) planes of B cations, in the A₃B₂B'X₉ group the B' cations occupy every third B-cation (111) layer, Fig. 1(c). The probability for an ordered arrangement of the B, B' cations is determined by the differences between their ionic charges and their ionic radii [Fe22, Fe23, Ga1, Ga10]. To first approximation, the order-disorder transition temperature Θ_{ord} induced by the charge difference Δq = (q' - q) at cations B' and B is $\Theta_{ord} \sim (\Delta q)^2$. Thus superstructure has been observed in all the known compounds having $(\Delta q)^2 = 36$ and 16, whereas those having $(\Delta q)^2 = 4$ are disordered unless there is a relatively large difference in ionic sizes. The minimum difference in ionic size that results in ordered A₂⁺B³⁺+B'⁵⁺O₆ compounds is $|r_B - r_{B'}|/r_B \approx 0.09$, and this has been achieved where B' = Nb or Ta, having empty d orbitals for the formation of stable (B'O₆)⁷⁻ clusters, while the B cation has no relatively stable, empty d orbitals.

Given the formation of (B'X₆) octahedra, a confusion arises as to where the structure corresponds to an ordered A₂BB'X₆ perovskite built up of corner-shared octahedra plus A cations and where it corresponds to the isostructural (NH₄)₃FeF₆ structure, which consists of discrete (B'X₆) octahedra separated by A and B cations. (The cubic K₂NaAlF₆ structure with space group T_h⁶(Pa3) is similar to (NH₄)₃FeF₆, but has a lower symmetry because there are very small rotations of the (B'X₆) octahedra.) Some authors [Fe22] select as a criterion for the perovskite structure the cationic radius ratio $r_B/r_A < 0.8$ where $r_B > r_{B'}$. This decision is based on the observation that a plot of the cubic lattice parameter a_0 vs. B-cation radius r_B is a straight line for $r_B/r_A < 0.8$, but bends over for $r_B/r_A > 0.8$. However, this probably reflects the ratio at which electrostatic forces inhibit (or reverse) any A-cation displacements rather than the ratio at which discrete (B'X₆) octahedra are formed. For most physical properties this criterion is probably arbitrary.

Without electron-ordering distortions superposed on the size effects, ordered A₂BB'X₆ perovskites can be described by either the O-orthorhombic cell of Fig. 5 or by the rhombohedral R̄3 (or R̄3m) cell of Fig. 6. Where $\alpha = 60^\circ$, a tetramolecular cubic cell may be chosen provided the A cations are not displaced from their ideal positions. Like cubic (NH₄)₃FeF₆, the cubic cell has the space group O_h⁶(Fm3m) with B cations in 4(b) ($\frac{1}{2}, \frac{1}{2}, \frac{1}{2}$); f.c., A cations in 8(c) $\pm (\frac{1}{4}, \frac{1}{4}, \frac{1}{4})$; f.c., B' cations in 4(a) (0, 0, 0); f. c., and X-anions in 24(e) $\pm (u, 0, 0; 0, u, 0; 0, 0, u)$; f.c. with $0.2 < u < 0.25$. However, even where $\alpha = 60^\circ$, motions of the A cations along the [111] axes may occur, thereby destroying the cubic symmetry.

If an electron-ordering transition superposes a distortion at every other octahedron of Fig. 5, either the B or the B' octahedra remaining cubic, cooperative elastic interactions between the distorted octahedra give a further reduction in symmetry. The resulting monoclinic cell [Fi9, Bl8], which is pseudotriclinic, is not to be confused with the pseudomonoclinic symmetry reported in early work for the O-orthorhombic structures. The origin of the superposed electron-ordering transition could be either a Jahn-Teller ordering of localized electrons or a ferroelectric-type displacement of the anions about a (B'X₆) octahedron.

Several Ca₂B³⁺Ta⁵⁺O₆ and Sr₂B³⁺Nb⁵⁺O₆ perovskites having B = rare-earth atom exhibit the monoclinic symmetry of a distorted O-orthorhombic cell [Fi8]. Since the 4f electrons at the rare-earth ions are localized, it is tempting to attribute this to a Jahn-Teller distortion with spin-orbit coupling. Although Fig. 9 shows that the octahedral site splitting of one-electron 4f orbitals gives orbitally threefold-degenerate levels having an accidental degeneracy that is not removed by spin-orbit coupling, nevertheless there are two reasons why this explanation cannot be correct: (1) There is no magnetic ordering of the 4f electrons at room temperature and (2) Sr₂GdNbO₆ shows the distortion even though Gd³⁺ has a half-filled 4f⁷ shell, which has no orbital degeneracy associated with the ground state. It is therefore concluded that the additional distortions are due to the potentially ferroelectric cations Nb⁵⁺ and Ta⁵⁺.

3.1.5.3 Complex alloys A₂BB'X₆, where B = M₁₃, B' = M₈

Several complex interstitial alloys have a formal structural relationship to the ordered perovskite A₂BB'X₆ as well as interesting magnetic properties. In this group, having space group Fm3m, the B position is occupied by a thirteen-atom cluster consisting of a metal atom at position 4(a) at the center of a cubo-octahedral, twelve-atom cluster of M atoms at positions 48(h); the B' position is occupied by a simple cube of eight M' atoms at 32(f). The three principal axes of each cluster are along the cubic axes of the perovskite cell, as shown schematically in Fig. 18, so that each X atom at positions 24(e) has eight near neighbors. The eight A atoms of the tetra-molecular cell are at the 8(c) positions. The 4(b) position at the center of the M'₈ clusters is empty. Alloys with this structure include the ferromagnetic borides Al₂[(AlM₁₃)(M'₈)]B₆, where M = Fe, Co, Ni, as well as Cr₂₃C₆.

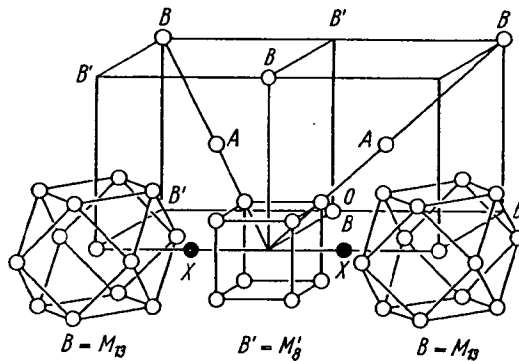


Fig. 18. One quadrant of the A₂BB'X₆ structure showing the atomic positions of the B = M₁₃ and B' = M'₈ clusters [We19].

3.1.6 First-order magnetic transition in M^cXM^f₃ perovskites

Many perovskites M^cXM^f₃ exhibit first-order phase changes at magnetic-ordering transitions. Most of these are reported to be cubic-to-cubic transitions, but in ZnCMn₃ it is a tetragonal (ferrimagnetic)-to-cubic (ferromagnetic) transition. These crystallographic changes are induced by a complex interplay of collective electrons in overlapping bands. Because of the intimate connection with the magnetic properties and because of the necessarily speculative character of any model at this time, discussion of these compounds is deferred to 3.5.

3.1.7 Data: Crystallographic properties of ABX₃, A₂BB'X₆, A₃B₂'BX₉ and A(B_xB'_yB''_z)X₃ compounds with perovskite or perovskite-related structure (Tab. 2)

Tab. 2.

Within any section, the compounds are in general first ordered according to the atomic number of the B cation and then by the basicity of the A cation. For the ordered perovskites of Tab. 2 b, c, d, the compounds are further ordered by the atomic number of the other B cation. The order of the sections is as follows:

Tab. 2a — ABX₃

A²⁺LiH₃
A(H₂O)(Li_{1/3})₃; A = I⁻¹, Br⁻¹
A⁺B²⁺X₃; X = F⁻¹, Cl⁻¹, Br⁻¹
A⁺B⁴⁺O₃; B = V, Nb, Sb, Ta, I, Pa, U
A²⁺B⁴⁺O₃; B = Ti, V, Cr, Mn, Fe, Co, Ni, Ge, Zr, Mo, Tc, Ru, Sn, Ce, Pr, Hf, Re, Ir, Pb, Th, U, Np, Pu
A²⁺B⁴⁺X₃ or A³⁺B³⁺X₃; X = S or Se, B = Ti, Zr, Ta, In, Ga
A³⁺B³⁺O₃; B = Al, Sc, Ti, V, Cr, Mn, Fe, Co, Ni, Ga, Y, Nb, Rh, In, Ho, Er, Tm, Yb, Lu

Tab. 2b — A₂BB'X₆

A₂BB³⁺X₆; X = F⁻¹, Cl⁻¹, B³⁺ = Al, Sc, Ti, V, Cr, Mn, Fe, Co, Ni, Cu, Ga, Ag, In, Ce, Pr, Au, Tl
A²⁺A³⁺B³⁺B⁴⁺O₆; B⁴⁺ = Ti, Ir
A₂BB⁴⁺O₆; B⁴⁺ = Ti, Mn, Ge, Zr, Ru, Ir
B⁵⁺ = V, Nb, Sb, Ta, Bi, Pa, Pu
B⁶⁺ = Mo, Te, W, Re^{6+,5+}, Os^{6+,5+}, U^{6+,5+}, Np⁶⁺, Pu⁶⁺
B⁷⁺ = Tc, Re, Os, I

Tab. 2c — A₃BB'₂O₉

A₃BB'₂O₉; B⁵⁺ = Nb, Ru, Sb, Ta
La₃Co₂B⁵⁺O₉; B⁵⁺ = Nb, Sb
A₃B₂B⁶⁺O₉; B⁶⁺ = Mo, W, Re, U

Tab. 2d — A²⁺(B_xB'_yB''_z)O₃

3.1 ABX_3 perovskite structure

Symmetry: C = cubic, H = hexagonal, M = monoclinic, O = orthorhombic ($a < c/\sqrt{2}$), O' = orthorhombic ($c/\sqrt{2} < a$), R = rhombohedral, T = tetragonal, Tr = triclinic.
Remarks: for abbreviations, see p. 131.

Tab. 2a. ABX_3 compounds

Compound	Sym.	a Å	b Å	c Å	angle	Ref.	Remarks	Magnetic Data
$\text{A}_2+\text{Li}^+ + \text{H}_3\text{I}^-$								
BaLiH_3	C	4.023						
	C	4.02						
BaLiD_3	C	3.833						
SrLiH_3	C	3.796						
EuLiH_3	C	3.996						
BaLiF_3	C							
$\text{A}(\text{H}_2\text{O})(\text{Li}_{1/2})_3$; A = I-I, Br ⁻¹	C	4.296						
$\text{I}(\text{H}_2\text{O})(\text{Li}_{1/2})_3$	C	3.99						
$\text{Br}(\text{H}_2\text{O})(\text{Li}_{1/2})_3$	C							
$\text{A}+\text{B}^{3+}\text{X}_3$; X = F ⁻¹ , Cl ⁻¹ , Br ⁻¹								
CsMgF_3	H	6.04						
	H	6.16						
	T	9.39						
RbMgF_3	M	8.19						
KMgF_3	C	3.973						
	O	5.363						
NaMgF_3	O	5.503						
	T	3.942						
	C	3.955						
NH_4MgF_3	C	4.06						
	H	7.278						
CsMgCl_3	O	6.954						
KMgCl_3	C	4.523						
	C	4.457						
CsCaF_3	C	8.76						
RbCaF_3	C	5.396						
KCaF_3	C							
CsCaCl_3	H	7.297						
CsTiCl_3	H							

Goodenough/Longo

3.1 ABX₃ Perowskit-Struktur

[Lit. S. 275]

Compound	Sym	$\frac{a}{\text{\AA}}$	$\frac{b}{\text{\AA}}$	$\frac{c}{\text{\AA}}$	angle	Ref.	Remarks	Magnetic Data
<i>A⁺B³⁺X₃; X = F⁻¹, Cl⁻¹, Br⁻¹ (continued)</i>								
CsVCl ₃	H	7.23		6.03			Se1b Gr8a Se1b	Hex (2L), P & S [Yd1] Hex (2L), optical and magnetic properties Hex (2L), P & S [Yd1]
RbVCl ₃	H	7.04		6.0			C ₀₂₇	
KVCl ₃	H	6.90		5.98			C ₀₂₇	
RbCrF ₃	T	6.149		8.088		V ₀₁	P & S [Co27]	
KCrF ₃	T	6.04		8.01		V ₀₁		
NaCrF ₃	C	4.158				C ₀₂₇		
(NH ₄)CrF ₃	T	8.544		7.968		Sc1	$T = 500^\circ\text{C}$, P & S [Ed2, V ₀₁ , Kn3, Y ₀₁ , Pe2a] Neutron diffraction	
TiCrF ₃	T	5.695		7.639	$\beta = 87^\circ 48'$	V ₀₁	a and b axis said to double	
CsCrCl ₃	T	6.232		7.954		V ₀₁		
RbCrCl ₃	H	6.194		8.064		V ₀₁		
CsMnF ₃	H	7.249		6.228		V _{d1}	Hex (2L), P & S [Se2] Hex (2L) pseudohexagonal	
	H	7.03		6.08		Se2		
RbMnF ₃	C	6.213		15.074		Za1	$\Theta_N = 54^\circ\text{K}$, P & S [Si14, Be19, Co25, Ho17], cubic to $T = 20^\circ\text{K}$ electron diffraction [Pi1], optical properties [Si28, St30], NMR [Mi4, We11], AFMR [Wi14], magnetic properties [Le3, Le4, Se1]. S.S. with K and Na [Be19a]	
KMnF ₃	C	4.328				L ₀₁ b	High pressure phase, P & S [Sy1] P & S [Si14, Be19, Co25, Ho17], cubic to $T = 20^\circ\text{K}$	
	C	4.2396				Wa8	[T ₀₄], dielectric properties [Ig1, Ch4a], compressibility [St29], I.R. spectra [Ax2, Pe5], bibliography [Fr10a]	
	C	4.186				Be3	P & S [Be14, Si14, Cr4, Be2, Be4, Kn3, Ok2, Ok3, Ok4, Be53, Ok6, Ho17, Gu1a], S.S. with Co + Ni [Ha28], I.R. spectra [Ax2, Pe5, Yo2], bibliography [Fr10a]	
NaMnF ₃	O	5.885		5.885		Be3	$T = 95^\circ\text{K}$, $(c/a > \sqrt{2})$ $184 > T > 84^\circ\text{K}$ [Be3, De3, Ok6]	
	O	5.900		5.900		Be3	$T = 65^\circ\text{K}$, $(c/a < \sqrt{2})$ $T < 84^\circ\text{K}$ [Be3, De3, Ok6]	
	O	5.568		5.760		Si14	Prep. [Ho17, Be19b], a and b axis doubled [Si14], P & S [Mag]	
(NH ₄)MnF ₃	C	4.238				Si14	P & S [C ₀₄ , Ho17, Co25], neutron diffraction [Pi1]	
TiMnF ₃	C	4.250				Ki9	Hex (9L), $\Theta_N = 69^\circ\text{K}$, AFMR [Ke1, Sh5]	
CaMnCl ₃	H	7.288		27.44		Ke7	Hex (6L), $\Theta_N = 86^\circ\text{K}$, AFMR & ESR [Ke1, Sh3, Sh5]	
RbMnCl ₃	H	7.164		17.798		Ke7		
KMnCl ₃	T	10.024		9.972		Cr6	Cubic $T > 458^\circ\text{C}$, AFMR & ESR [Ke1, Sh5]	
								6

3.1 ABX₃ perovskite structure

Compound	Sym	<i>a</i> Å	<i>b</i> Å	<i>c</i> Å	angle	Ref.	Remarks	Magnetic Data
<i>A</i> ⁺ <i>B</i> ²⁺ <i>X</i> ₃ ; <i>X</i> = F ⁻¹ , Cl ⁻¹ , Br ⁻¹ (continued)								
CsFeF ₃	H C C	6.158 4.283 4.173		14.855		Kel9 Lo1b Wa12	Hex (6L), structure [Ba5], Θ_c = 60 °K [Po9a, Po9b] High pressure phase F & S [Ke19], neutron diffraction [Wa14], cubic $T > 97$ °K, tetr. 97 $> T > 86$ °K, orth. 86 $> T > 45$ °K, mon. $T < 45$ °K [Te17]	6
RbFeF ₃	C	4.122				Ok6	F & S [Kn3, Ma29, Ok2, Ok3, Ok4], neutron diffraction [Sc1]	
KFeF ₃	C	4.108	5.672	7.890	$\alpha = 89^\circ 51'$	Ok6 Tr2	$T = 78$ °K, rhombohedral $T < 121$ °K F & S [Vo1, Ma9, Po9a]	6
NaFeF ₃	O C	5.495 4.177				Po9a Vo1	P & S [Po9a]	6
NH ₄ FeF ₃	C	4.188				Yd1	Hex (2L), P & S [Se2a]	6
TlFeF ₃	H	7.237				Se2a	Hex (2L)	
CsFeCl ₃	H	7.060				Ba5	Hex (2L), magnetic properties [Ru6], P & S [Ba4]	6
RbFeCl ₃	H	6.194				Lo1b	Hex (6L), high pressure phase P & S [Ru8, Cr4], S.S. with Mg [Sh1a]	6
CsCoF ₃	H	6.09				Ru6	P & S [Kn3, Ma29, Ok2, Ok3, Ok4, Ru8, Cr4]	6
RbCoF ₃	H	4.116				Ok6	I.R. spectra [Ax1, Ax2, Pe5, Yo2, Pe2a]	6
KCoF ₃	C	4.069				Ok6	$T = 78$ °K P & S [Ru8, Og2, Tu5, Ma10]	6
	T	4.057				Ru6	P & S [Ru8, Og2, Tu5, Ma10]	6
NaCoF ₃	O	5.420	5.603	4.049	7.792	Ru6	P & S [Cr4, Ru8]	6
NH ₄ CoF ₃	C	4.127				Ru6	P & S [Ru8]	6
TlCoF ₃	C	4.138				Yd1	Hex (2L), complete structure and magnetic prop-	
CsCoCl ₃	H	7.202		6.032		Yd1	erties [So1]	
RbCoCl ₃	H	6.996		5.996		En1	Hex (2L)	
CsNiF ₃	H	6.236		5.225		Ba2	Hex (2L)	
	H	6.15		22.32		Lo1b	Hex (9L), high pressure phase Hex (6L) high pressure form: Θ_c = 111 °K	
RbNiF ₃	H	6.05		14.54		Lo1b	Hex (6L), P & S [Si14], Θ_c = 139 °K, magnetic	
	H	5.843		14.31		Ru5	properties [Si19b, Mc1a, Sm32, Sm31, Sh1, Go3, Ku2, Go1a], S.S. with Co [Bo13, Su11, Pi16], optical properties [Sm32, Sm31, Sm21, Sm22, Sh1, Ty1, Pi8, Pi14, Pi15, Za1a, Be19c, Pi16], Raman scattering [Ch14a], NMR [Sm32a]	
KNiF ₃	C	4.074				Ka4	High pressure phase, P & S [Sy1]	6
	C	4.015				Ok6	F & S [Ok3, Ok4, Kn3, Ma10, Ru5, Ok2], I.R. spec-	6
	C	4.002				Ok6	tra [Pe5, Ba17a]	
							$T = 78$ °K	

3.1 ABX₃ Perowskit-Struktur

[Lit. S. 275]

Compound	Sym	$\frac{a}{\text{\AA}}$	$\frac{b}{\text{\AA}}$	$\frac{c}{\text{\AA}}$	angle	Ref.	Remarks	Magnetic Data
$A^+B^{2+}X_3; X = F^{-1}, Cl^{-1}, Br^{-1}$ (continued)								
NaNiF ₃	O	5.360.	5.524	7.688		Ru8	P & S [Og2, Ru5, Ok5]	in 3.3.4, Tab. 6
NH ₄ NiF ₃	C	8.145			14.37	Ru5	P & S [Ru8]	6
TiNiF ₃	H	5.87				Ko4	Hex (6L)	6
CsNiCl ₃	C	4.10				Ko4	High pressure phase, P & S [Sj7]	
(CH ₃) ₂ NNiCl ₃	H	7.169		5.940		Yd1	P & S [As4], structure determination	
CsNiBr ₃	H	9.019		6.109		St44	Hex (2L)	
CsCuF ₃	H	7.488		12.480		As4	Related to Hex (2L)	
RbCuF ₃	H	12.55		11.56		Ba2	Related to Hex (2L), optical properties [Sc10a]	
KCuF ₃	T	6.001		7.894		Ru6	Optical properties [Sc10a]	
	T	5.855		7.846		Ru6	P & S [Ed2, Kn3, Ok1, Ok2, Ok6], neutron diffraction [Ti4]	
NaCuF ₃	T	4.121		3.913		T = 78 °K	[Sc1], optical properties [Pe2a, Oe1, Sc10a]	
NH ₄ CuF ₃	M	11.01	11.37	7.521		P & S [Ru3]	P & S [Ru3]	
TiCuF ₃	T	6.09		7.78		Cr4	Related to Hex (2L), P & S [Sc7, We9] magnetic properties $\Theta_p = -3.5^\circ\text{K}$, μ_{eff} (300 °K) = 1.95 μ_B [Ric, Fi2]	
CsCuCl ₃	T	6.083		7.866		Ru6	Not perovskite, magnetic properties $\Theta_N = 17.5^\circ\text{K}$ [Ma1, Sh5]	
	H	7.20		18.00		Yd1	Not perovskite, magnetic properties $\Theta_N = 17.5^\circ\text{K}$ [In3]	
KCuCl ₃	M	4.029	13.785	8.736	$\beta = 97^\circ 20'$	Ki10	Hex (6L), high pressure phase	
NH ₄ CuCl ₃	M	4.066	14.189	9.003	$\beta = 97^\circ 30'$	Ba1	P & S [Cr4, Lu1]	
KCuBr ₃	M	4.05	14.43	9.30	$\beta = 96^\circ 5'$	Ba1	Hex (6L) high temperature form	
CsZnF ₃	T	9.90		9.05		Kn3	P & S [Lu1, Ma29], thermal conductivity [Su8], optical properties: Ni, Mn [Fe11, Fe15], I.R. spectra [Yo2, Pe2a]	
RbZnF ₃	H	6.09		14.67		Tu5	P & S [Lu1, Ru8, Ba1, Ma9, Ma10, Sc10]	
	C	4.110				Cr4		
KZnF ₃	H	5.896		14.44		De22		
	C	4.055				Yd1	Hex (6L)	
NaZnF ₃	O	5.404	5.569	7.743		Ch15	Nuclear quadrupole resonance [Vo0]	
NH ₄ ZnF ₃	C	4.115				Ch15	Cubic $T > 155^\circ\text{C}$, ferroelectric transition at 155°C	
AgZnF ₃	C	3.98						
TiZnF ₃	H	5.934						
CsGeCl ₃	R	5.444			$\alpha = 89^\circ 38'$			
	C	5.475						

3.1 ABX₃ perovskite structureCh15 | Cubic $T > 155^{\circ}\text{C}$, ferroelectric transition at 155°C

Compound	Sym	a Å	b Å	c Å	angle °	Ref.	Remarks	Magnetic Data
$\text{A}^{+}\text{B}^{3+}\text{X}_3$; $\text{X} = \text{F}^{-1}, \text{Cl}^{-1}, \text{Br}^{-1}$ (continued)								
CsSrF ₃	C	5.589				Yd1	[Be22a, Bu3a] no cell dimensions	
CsSrCl ₃						Prep. + Prop. [Ba20, Fi3]		
CsPdF ₃						K11 Vo1 Ba5b	P & S [Co27a] Mn emission [K11], P & S [Co27a] P & S [Ma29, Br9, K11, Co27a, Co26, Vo1], Mn emission [K11]	
CsCdF ₃	C	4.47				Co27a Co27a Fe20 Si3 Na15	$T_{\text{melt}} = 765^{\circ}\text{C}$ Slight distortion [Na15], P & S [Si3] Hex (6L) P & S [Na19]	
RbCdF ₃	C	4.395				D65 D65 Bo31		
KCdF ₃	T	6.101				Na15 Na15 Sc9	P & S [Na19, Na18] P & S [Na19]	
(NH ₄)CdF ₃	T	4.368				Mo2 Mo2	Phase transition at 40°C [Sa2a] Cubic $T > 47^{\circ}\text{C}$ [Mo2]	
TiCdF ₃	C	4.400						
CsCdCl ₃	C	5.20						
H								
CsCdBr ₃	C	7.418						
		10.70						
CsSnCl ₃	C	5.58						
CsSnBr ₃	C	5.94						
CsEuF ₃	C	4.77						
CsHgCl ₃	C	10.88						
CsHgBr ₃	C	5.77						
CsPbF ₃	C	4.81						
CsPbCl ₃	T	5.590						
CsPbBr ₃	C	5.599						
A ⁺ B ⁵⁺ O ₃		5.874						
AVO ₃								
RbNbO ₃	O	5.720	5.739	3.984		F67 Wo15	Not perovskite, A = Na, K, Rb, Cs and Ag Not perovskite Structure [Ka19, Vo4, Vo5], crystal growth [Bu2, Sh25], optical properties [Ka8, Ch13]; S.S. with: BaTiO ₃ [Br2], NaNbO ₃ [Du3, Te8c], Li [Ni2a]	
KNbO ₃						W015	$T = 260^{\circ}\text{C}$, Tetr. $435 > T > 225^{\circ}\text{C}$, S.S. with KTaO ₃ (see KTaO ₃)	
	T	4.00				W015 Sh23 Ad1	$T = 500^{\circ}\text{C}$, cubic $T > 435^{\circ}\text{C}$ $T = -140^{\circ}\text{C}$, neutron diffraction $2\text{Na} + \text{Nb}_2\text{O}_5$	
	C	4.024						
	R	4.016						
	C	4.2						
Na ₂ NbO _{2.6}								

Compound	Sym	$\frac{a}{\text{\AA}}$	$\frac{b}{\text{\AA}}$	$\frac{c}{\text{\AA}}$	angle	Ref.	Remarks	Magnetic Data in 3.3.4, Tab.
A⁺B³⁺O₃ (continued)								
NaNbO ₃	O	5.505	5.568	15.518		Vo6	Structure determined, P & S [Vo4, Vo5, We10, Ba18, Fe7, Wo15]; S.S. with: KNbO ₃ [Du3, Te8c], NaTaO ₃ [Iw4, Iw7, Is4], SrNb ₂ O ₆ [Is16, Te7], CdTiO ₃ [Le2], AgNbO ₃ [Br24], Cd and Sr [Te8b]	
NaNbO ₃	O	5.51	5.57	7.77		Wo17	50 kV/cm applied to crystal; other phase transformations [Te6, So1b, Le5, Fr1, Sh20a, Cr6a, So1a, Is5a]; heat of transformations [Te8a]	
Na _{0.97} K _{0.025} NbO ₃	O	5.528	5.582	7.782		We10	Structure determined	
LiNbO ₃	H	5.1483	7.888	13.8631		Ab4	Not perovskite, see text	
AgNbO ₃	M	7.888	7.888	15.660	$\beta = 90^\circ 34'$	Fy2	S.S. with KNbO ₃ [Wo5]	
AgSbO ₃	C	3.595				Fy2	$T = 550^\circ \text{C}$, cubic	
RbTaO ₃	C	10.32				Sc22	Defect pyrochlore	
KTaO ₃	T	3.92						
	C	3.9885						
NaTaO ₃	O	5.494	5.513	7.751		Sm11	[Fe7] says not perovskite	
	C	3.929				Vo4	P & S [Vo5], crystal growth [Sh25, Wi4, We13], optical properties [Fr20, Pr2, Di7, Di8, Be27, Ar1, Pe4, Jo15, Sh20, Ra7, Sc5, St20, La7a], Faraday rotation [Ba7], electrooptic properties [Fr20, Fa7, Fa8, Fr21, Fr22, Ge13, Zo2], S.S. with: KNbO ₃ [Fu3, Ha2, Ch13, Ge9, We12, We14, Di6, Hi2a, La7a], Ca [Se4]; Raman spectrum [Fr1a, Pe6, Fr1b]; ESR: Eu, Gd [Un1], Fe, Ni [Ha9a, We18b]; ultrasonic attenuation [Ba17b]; Nuclear spin resonance [Gr7a]	
	H	5.154						
CuTaO ₃	M	7.862	7.862	13.783		Ka22	Crystal structure, P & S [Vo4, Vo5], S.S. with: NaNbO ₃ [Is14, Is7]	
AgTaO ₃	C	3.949	3.949	7.914	$\beta = 90^\circ 21'$	Is5	630 °C, cubic $T \geq 630^\circ \text{C}$, tetr. 630 $> T > 550^\circ \text{C}$	
	C	4.674	4.674			Ab2	Not perovskite, neutron diffraction [Ab2] (see text)	
CsIO ₃	R	4.541	4.541			Sh12	Actually Cu _{0.5} TaO ₃ , see "Bronze" section	
RbIO ₃	M	8.94	8.94		$\alpha = 89^\circ 44'$	Fy2	P & S [Br27]	
KIO ₃	R	4.410	4.510		$\beta = 89^\circ 12'$	Bo30	P & S [Na15]	
TlIO ₃	R	4.510	9.18		$\alpha = 89^\circ 25'$	Na16	Perovskite (?), P & S [Na15]	
NH ₄ IO ₃	C	4.368	4.368		$\alpha = 89^\circ 20'$	Sm3	P & S [Ri9]	
CsPaO ₃	C					Kes	Na15	

3.1 ABX₃ perovskite structure

Compound	Sym	<i>a</i> Å	<i>b</i> Å	<i>c</i> Å	angle	Ref.	Remarks	Magnetic Data in 3.3.4, Tab.
A ³⁺ B ⁵⁺ O ₈ (continued)								
KPaO ₃	C	4.341	5.97	8.36		Ke5		
NaPaO ₃	O	5.82	4.323			Ke5		
RbUO ₃	C	4.290				Ke12	P & S [Ru3a, Ip1], Prop. [Ke13]	6
KUO ₃	C	5.775	5.905	8.25		Ke12	P & S [Ru3a, Ch1b], Prop. [Ke13]	6
NaUO ₃	O					Ke12	P & S [Ru3a], Prop. [Ke13]	6
A ³⁺ B ⁴⁺ O ₈								
BaTiO ₃	C	4.012				Me1	T = 200 °C, cubic 120 < T < 1372 °C [Ed5], cubic T > 133 °C [We1a], high temperature phase [Me4, Me6, Me2, Ka23]	
	T	3.994			4.034	Me1	T = 20 °C, tetragonal 5 < T < 120 °C; structure determination by x-rays [Ev2, Ev3, Ev4, Ch2], by neutrons [Sh18, Fr4], by electron microscope [Pi2]; P & S [De1, Sa5], further remarks:*)	
	O	5.682	5.669	3.990		V05	T = -10 °C, orthorhombic -90 < T < 5 °C [Ka24]	
	R	3.998				Ka24	T = -100 °C, rhombohedral T < -90 °C	
	H	5.735			14.05	Bu4	Flex (6L); structure determination [Bu4, Ev1]. Further remarks:**)	
	C	3.905				Me4	T = 293 °K; cubic T > 110 °K, thermal expansion α = 9.4 · 10 ⁻⁶ Å/deg., may be tetr. with c/a = 1.00008 [Ly2]	
	T	3.8972				Ly2	T = 100 °K, Tetr. 65 < T < 110 °K, c/a = 1.00056, on single crystal [Ly2]. Further remarks:***) See page 156	
	O				3.8991	Ly2	a:b:c 0.9998:1:1.0002, orthorhombic 35 < T < 65 °K [Ly2]	
	R					Ly2	Possibly rhombohedral at 10 °K	

*) Complete bibliography to 1961 [Ha7]; Raman scattering [Di8, Du2, Pa6, Pi3, Ri8, Di8a, Ro1/9a]; study of structural changes [Ca4, Co15a, Fo6, Me6, Sc8, Ka24, We1a]; pressure dependence of dielectric properties [Go27, Ka1, Le9, Me23, Mo7, Mo8, Po3, Po4, Po5, Po6, Sa3]; radiation damage [Sc6, We2]; refractive index [Sa11, Ho3a]; thermal conductivity [Di8, Ma23, Su7, In20]; surface layers [Or1, Le12, Ho10, Du1, Cr2, Ca1, Br1]. Optical properties [Mu11, Mu12, Mu13, V68, V69, Ha15, J01, Co30, Sh24, Ra4, Po7, Na8, K13, Ba9, We1a]; propagation [Gr10]; ESR: Ti [Da4, Ta4, Ta6], Mn [Ik1, Ik2, Ik3, Ve10], Pt [Si3], Eu [Ta7, Ta8], Gd [Bu7, Ta3, Ta5, Ta8, Ri5]; dielectric properties [De9, Hu11, Si17, Fr17, We1a]. Transport properties [Ue1, Ue2, Ta9, Sc15, Ry1, Mu10, Ma32, Ma3, Ko9, Ka21, Ik5, Be29, An4], electronic properties [Mo12]. Lattice vibration [Lx1, Ha14, Ka3, Dr3], shock-wave compression [Do4], elastic properties [Fw5], grain size influence on Θ_0 [Rz2], relaxation time [Wz5, Bo4]. Properties with additives: Mg [J1/3, J01], Mn [Bh1], Fe [Sc25], Co, Ni [Ku1, Co23a], Zn [Si16], Nb + Ta [Gu1, Ku1], Ln [Go1, As2, Bo4, J01], Bi [Bo3, J01], Sb [Ha13, J01], Sr [He14, Al1, He6], PbNb₂O₃ [Sr1], C₂, Zr, Si, Fe, Mg [Br22a]; defect study [Co24, Mu9, Me4, Ma36, Si19c, Ra5, Bi14a, Di4]; neutron scattering [Y'a2a].

**) P & S [W016, Me4, Ma36, Si19c, Ra5, Bi14a, Di4]; effect of additives on occurrence [Ra5, Ro20a, Di4]; hex. form due to oxygen vacancies or metal substitution for Ti [Di4], magnetic properties with Ti, Cr, V, Mn, Re, Fe, Co, Ru, Ir, Pt substitution [Di4].

3.1 ABX₃ Perowskit-Struktur

Compound	Sym	$\frac{a}{\text{\AA}}$	$\frac{b}{\text{\AA}}$	$\frac{c}{\text{\AA}}$	angle	Ref.	Magnetic Data in 3.3.4, Tab.
A²⁺B⁴⁺O₃ (continued)							
CaTiO ₃	O	5.381	5.443	7.645		P _e 3	P & S [Ba18, Ze1, Ze2, Le10, Na13, Na15, Me4, Ku3]; optical properties [Si21, Pe8, Mu13]; detailed structure [Ka21a]
CdTiO ₃	C	5.348	5.417	7.615		Gr3a Ra22	Structure determined Pbn2 ₁ [Ka22], structure questioned [Ge3a], P & S [Me4], S.S. with NaNbO ₃ [Le2], electrical properties [Sh24a]; perovskite-ilmenite transformation [Li0]
PbTiO ₃	T	3.904		4.152		Sh21	Complete structure [Sh21], P & S [Me4, Sh19, Co13, Sh15, Sh24b]. optical properties [Pe8, Fu5], piezoelectric properties [Ue3, Fe2, Fe1, Is1a], slow neutron scattering [So2], S.S. with (Ba, Sr, Ca, Pb) (Ti, Zr, Sn)O ₃ [Sh19, Ta14, Ha20, Ba12, No7, On2, Th2, Ok7, Ta6, R17, On1a, Pe9, Is1, Uc2, Sh34, Fe1, Bu10, Fe3, Fe9, Fu5, He14, Iu3, St35, Di1a], radiation damage [Ha30], S.S. with PbGeO ₃ [D15b]
(CuA)TiO ₃	C	3.960				Sh21 De18	T = 535 °C, cubic T > 490 °C A = Ca (25%) a = 7.393 Å; Cd (25%) a = 7.399 Å;
	C	\approx 7.4					Sr (20%) a = 7.420 Å
EuTiO ₃	C	7.810				Ho12 Ro20	P & S [Br20, Mcb1]. Prop. [Mc2, Mc3, Mc4, Si4]
La _{0.5} K _{0.5} TiO ₃	C	3.914				Ag1	Dielectric properties [Sm8, Ag1]
La _{0.5} Na _{0.5} TiO ₃	C	3.86				Ro20	Dielectric properties [Sm8, Ag1]
Ca _{0.5} K _{0.5} TiO ₃	C	3.90				Ro20	S.S. with La
Nd _{0.5} K _{0.5} TiO ₃	C	3.874				Re2	
Y _{0.5} Na _{0.5} TiO ₃	O	5.326				Iv2	Dielectric properties [Ag1, Bu3, Sm8, Sm26]
Bi _{0.5} K _{0.5} TiO ₃	T	3.913				Iv2	Dielectric properties [Ag1, Bu3, Sm8, Sm26]
Bi _{0.5} Na _{0.5} TiO ₃	R	3.891				Ke18	S.S. with SrTiO ₃ [Ti1, Ve9, We16]
La _{0.5} TiO ₃	C	3.887				Ke18	
SrVO ₃	C	3.848				W014	P & S [Re8]
SrVO _{3.0}	C	3.838					
							6

****) Superconductivity [Am2, Ap2, Ea2, F10, Ko7, Sc19, Sc20, Sc21]; Raman scattering [Sc4, Sc3, R16, Os1, Ni1a, Fl1b]; NMR [W⁺]; Mössbauer: Co³⁺ [Bh3]. Optical properties [Ba6, Ba15, Ba16, Ca6, Co9, Dv1, Ea1, Gr1, K29, Mu11, Mu12, Mu13, Fa4a, Fe12, Va6, Z02, Am3, Si12, Va12, Vaf, R17, Pa5, Tu1]; Hall mobility [Fr10, Fr12, Pa5, Tu1]; EsR: Cr⁴⁺ [R17, Ba8, R17, Un2], Ni³⁺ [Ho17], Gd³⁺ [R17, R15, Sa2, Si1]; magnetoresistance [Fr7, Tu3, Ya3b]; piezoelectric properties [Fr7, Tu3, Ya3b]; diffusion and formation of oxygen defects [Pa3, Pa4, Wa9, Wa10]; thermal conductivity (33 < T < 110 °K) [Su7]; elastic constants from sound wave attenuation [Be6, Jo1a]; electromechanical behavior [Ru12]; pressure dependence of dielectric properties [He6a, Sa2]; photoconduction [Ya4, Ya5, Ya3b]; magnetic properties [Fr5]; vibrational modes [Ja3, Jo14]; inelastic neutron scattering [Sh16a], electrooptic effect [So3].

3.1 ABX₃ perovskite structure

Compound	Sym	$\frac{a}{\text{\AA}}$	$\frac{b}{\text{\AA}}$	$\frac{c}{\text{\AA}}$	angle	Ref.	Remarks	Magnetic Data in 3.3.4, Tab. 6
A²⁺B⁴⁺O₃ (continued)								
CaVO _{3.0}	C	3.767	5.352	7.547			W ₀₁₄ R ₀₁₆	P & S [Ru7, De2, Re8, Re9]
CaVO _{3.05}	O	5.326					W ₀₁₄	
BaCrO ₃	C	3.780					Ch _{1a}	Hex (9L), high pressure phase, semiconducting, $\Delta E = 0.09 \text{ eV}$
	H	5.62					Ch _{1a}	Hex (4L), high pressure phase, semiconducting, $\Delta E = 0.11 \text{ eV}$
	H	5.659		9.359			Ch _{1a}	Hex (6L), high pressure phase
	H	5.627		13.690			Ch _{1a}	Hex (12L), high pressure phase
	H	5.662		27.752			Ch _{1a}	Hex (14L), high pressure phase
	H	5.652		32.515			Ch _{1a}	Hex (27L), high pressure phase
	H	5.649		62.706			Ch ₁	
SrCrO ₃	C	3.818	5.316	7.486		G ₀₁₇		
CaCrO ₃	O	5.287				R ₀₁₉	P & S [De2]	
PbCrO ₃	C	4.00				Ha ₇	Hex (2L), P & S [Ha16, Sy1]	
BaMnO ₃	H	5.672		4.71		Sy ₁	Hex (9L), high pressure phase	
	H	5.667		20.948		Ha ₇	Hex (4L), high pressure phase, P & S [Ha16]	
	H	5.669		9.375		Sy ₁	Hex (4L), high temperature phase	
	H	5.645		9.264		Sy ₁	Hex (4L), S.S. with (Eu, Ba, La)MnO ₃ [Iv]	
SrMnO ₃	H	5.449		9.085		Sy ₁	Hex (6L), high pressure phase	
CaMnO ₃	H	5.431		13.396		Ma ₆	96% Mn ⁴⁺ , P & S [V012, To13, Yu1, Yu8], S. S.	
	O	5.270	5.275	7.464			with Bi [Bo6, Bo12, Si19]	
Ca _{0.05} Sr _{0.25} MnO ₃	O	5.302	5.304	7.488		Ma ₆		
BaFeO _{3-x}	R	4.099				Mo ₁₀	$\alpha = 88^\circ 47'$	
	C	3.997				Mo ₁₀	$\chi = 0.36$ P & S [De15, Er1, Mo11, Ma22, Va8]	
	T	7.956				Mo ₁₀	$\chi = 0.25$; K _β X-ray spectra [Ko6a]	
	H	5.672				Mo ₁₀	$\chi = 0.19$	
BaFeO _{2.6}	O	5.83	4.15	8.006		Mo ₁₈	Brownmillerite structure, see Fig. 21	
SrFeO _{3.0}	C	3.850		13.90		Mo ₁₁	$T = 1000^\circ \text{C}$, $T = 20^\circ \text{C}$ (triclinic)	
SrFeO _{2.84}	T	3.851		5.54		P & S [Wa17, Ya1, Ga17, Sh17], S. S. with La [Ga16, Wa17, Wa20], Bi [Ma8], Ti [Cl2, Br18]		
SrFeO _{2.50}	O	5.671	15.59	3.867		Ma ₄		
	O	5.64	14.68	5.528		Ma ₄	P & S [Ba23], S. S. with Al [Ba24, Ba25], Brown-	
CaFeO _{2.50}	O					Be40	millerite structure, see Fig. 21	
CaFe _{0.5} Al _{0.5} O _{2.6}	O	5.58	14.50	5.39			P & S [Be39, Sm4], neutron diffraction [Ta10, Fr16, Wi16, Ta10, Gr4]	
PbFeO _{2.5}	T		7.79	15.85			Prop. [Gr5, Po1, Wh4, Be40, Sm4]	
							P & S [Mo15]	

3.1 ABX₃ Perowskit-Struktur

Compound	Sym.	$\frac{a}{\text{\AA}}$	$\frac{b}{\text{\AA}}$	$\frac{c}{\text{\AA}}$	angle	Ref.	Magnetic Data in 3.3.4, Tab.
A³⁺B⁴⁺O₃ (continued)							
BaCoO _{4.72}	H	5.59		4.83			Ga7
Sr ₂ CoO _{3-x}	C	7.725		4.832			Y _{a1} 1.4% Co ₄₊ , S.S. with La [Wa7]
BaNiO _{4.8}	H	5.58					La4
CaGeO ₃	C	3.723					R _{8a}
CdGeO ₃	C	3.70					R _{8a}
BaZrO ₃	C	4.20					Ha20
SrZrO ₃	O	5.792	5.818	8.189		Fo4	High pressure phase; pseudocubic P & S [Ho2, Me4, Be2]; S.S. with BaTiO ₃ [Ve7], PbTiO ₃ [Ha20]; optical properties [Pe7, Du5]
						P ₃	T = 2000 °C P & S [Ho2, Me4, Sm3, Sc18a], D.T.A., T < 1000°C [Ca5], optical properties [Pe7, Du5], S.S. with Hf [Be2a]
CaZrO ₃	C	4.18				Fo4	T = 2000 °C, cubic T > 1300 °C
	O	5.587	5.758	8.008		T _{i3}	P & S [Si15, Me4, Ru9, Ru14], S. S. with Cr [Ni2]
	O	4.10				Fo4	T = 2000 °C, cubic T > 1600 °C
PbZrO ₃	O	5.872	11.744	8.202		Sa8	P & S [Is1, Me4, Sa7], phase transitions [Go28, Go29, Go30, Sa8, Te5, Te8, Ue1, Sh15a, Te8d], radiation damage [Ha30], optical properties [Pe7], neutron diffraction [Uo5], dielectric pro- perties [Kh4, Kh6, Kh8, Go29], piezo-electric effect [Ro1, Th2, Is14a], S.S. with Ca [Kh4, Si15], (BiNa) and (BiK) [Bu3], Pb(Ni _{1/3} Nb _{2/3})O ₃ [Bu10], BiFeO ₃ [Ce10], Hf [Go31]
						Ha2	T = 230 °C, cubic T > 230 °C
						Ho12	P & S [Mc4]
							Prep. + Prop. [Sm33, Bu3]
							Prep. + Prop. [Sm33, Bu3]
EuZrO ₃	C	4.149				Sc17	P & S [Bo19, Sc16, Ro2a], S.S. with Sr [Br15]
Bi _{0.5} K _{0.5} ZrO ₃	C	4.099				Sc17	P & S [Bo19, Sc16, Ro2a], S.S. with Ti [Ro2a, Br17], S.S. with Zr [Br17]
Bi _{0.5} Na _{0.5} ZrO ₃	C					Mc1	P & S [Sc16, Go17, Ro2a]
BaMoO ₃	C					Mu7	Hex (6L)
SrMoO ₃	C						
CaMoO ₃	O	5.45	5.58	7.77		Ke9	Slight distortion, P & S [Ke9]
BaTcO ₃	H	5.758		14.046		Mu7	Mu7
	C	8.140				Ke9	
SrTcO ₃	C	3.95				Mu7	Defect pyrochlore structure
CaTcO ₃	O	3.87				Ru6	Hex (9L), structure determination [Do2], Prop. [Ca2], S. S. with Sr [Do3, Lo1], S. S. with Zr, Mn, Ir, Ni [Do3a]
PbTcO ₃	C	10.360					
BaRuO ₃	H	5.75					
						L01	Hex (4L), high pressure phase

3.1 ABX_3 perovskite structure

Compound	Sym	$\frac{a}{\text{\AA}}$	$\frac{b}{\text{\AA}}$	$\frac{c}{\text{\AA}}$	angle \	Ref.	Remarks	Magnetic Data in 3.3.4, Tab.
$A^{2+}B^{4+}O_8$ (continued)								
BaRuO ₃	H	5.71	5.57	14.00			Hex (6L), high pressure phase	6
SrRuO ₃	O	5.53	7.85				P & S [Kh7], Prop. [Ca2, Lo3]	6
CaRuO ₃	O	5.36	5.53				Prop. [Ca2, Lo3]	
SrRu _{0.8} Ir _{0.8} O ₃	O	5.55	5.58				P & S [Ra6], Defect pyrochlore structure	
PbRuO ₃	C	10.25	5.61	7.84			High pressure phase	
BaSnO ₃	C	5.56	4.117	7.86			P & S [Wa2, Co8, Sm2], S.S. with Sr [Sm3], (Ba, Sr, Pb)TiO ₃ [Na9, Du4, My2], optical properties [Du5, Ya3], Mossbauer in S.S. with Ti [Be7, Bo9, Kr6]; S.S. with Ti, tetragonal at 91% Ti [Do1]	
SrSnO ₃	C	8.070	5.668	7.885			P & S [Ho2, Me4, Co8], optical properties [Du5, Ro12, Co8, Me4]; optical properties [Du5]; S.S. with BaTiO ₃ cubic at 13% CaSnO ₃ , [Do1]	
CaSnO ₃	O	5.519	5.457	5.577			P & S [Na13, Co8]	
CdSnO ₃	O	4.076	4.076	4.043	$\beta = 89^\circ 45'$		High pressure preparation	
PbSnO ₃	M	4.07					$T = 125^\circ \text{C}$, cubic $T > 125^\circ \text{C}$	
BaCeO ₃	C	4.397					P & S [Ho2], optical properties [Du5/a]	
SrCeO ₃	O	6.011	6.156	8.588			[Sm3], dielectric properties [Sm3/a]	
CaCeO ₃	C	7.70					P & S [Ho2], optical properties [Du5], dielectric properties [Sm3/a]	
CdCeO ₃	C	7.65					Pseudocubic	
PbCeO ₃	C	7.62					Na14	
BaPrO ₃	C	8.708					Na14	
BaHfO ₃	C	4.172					Na15	
SrHfO ₃	C	4.069					P & S [Ho2]	
CaHfO ₃	O	5.568					S.S. with CaZrO ₃ [Be24], P & S [Sc18a]	
CdHfO ₃	M	3.942					Ho2	
PbHfO ₃	T	4.136					P & S [Na15], S.S. with SrZrO ₃ [Be24a]	
PbReO ₃	C	4.134					Prep. [Ru14]	
BaIrO ₃	C	10.425					Sh16	
SrIrO ₃	H	5.76					De7	
PbIrO ₃	M	5.60					Cubic $T > 215^\circ \text{C}$, S.S. with PbZrO ₃ [Go31]	
	O	5.58					Sh16	
	C	10.271					$T = 250^\circ \text{C}$, cubic $T > 215^\circ \text{C}$	
	O	3.145					Defect pyrochlore type	
	C	4.265					S.S. with Sr [Do3], distorted Hex. (9L); structure [Ro2b]	
	O	5.864					Prep. [Ro2a], distorted Hex (6L)	
							Lo1a	
							High pressure phase (Perovskite)	
							Lo4	
							P & S [Ra6], defect pyrochlore type	
							Ro2b	
							Not perovskite	
							Wa2	
							P & S [We7, Ni3], electrical properties [Ik4]	
							We7	

Goodenough/Longo

3.1 ABX₃ Perowskit-Struktur

[Lit. S. 275]

Compound	Sym	α Å	b Å	c Å	angle	Ref.	Remarks	Magnetic Data
$A^{3+}B^{4+}O_3$ (continued)								
BaThO ₃	C	8.985						
SrThO ₃	C	8.84					P & S [H ₀ 2, Na15, Me4, Be24]	
CaThO ₃	C	8.74					Na15 Pseudocubic, S.S. with Ba [Be24]	
CdThO ₃	C	8.74					Na15 Pseudocubic	
PbThO ₃	C	8.960					Na15 Pseudocubic	
BaUO ₃	C	4.387					Na15 P & S [S ₀ 16, Ru4, Tr9], S.S. with BaTiO ₃ [Va9]	
BaNpO ₃	C	4.384					L _a ⁵ Ke4 Pseudocubic	
BaPuO ₃	C	4.357					Ke3 Pseudocubic	
SrPuO ₃	C	4.28					Ke3 Pseudocubic	
$A^{3+}B^{4+}X_3$ or $A^{3+}B^{3+}X_3$; X = S, Se								
BaTiS ₃	H	6.77					C11 Hex (2L), P & S [No9, As3b], orthorhombic and tetragonal modifications [Ha6]	
BaTiSe ₃	H	7.054					As3a Hex (2L), P & S [No9]	
SrTiS ₃	H	6.730					Ha6 Hex (2L), P & S [No9], orthorhombic and tetragonal modifications [Ha6]	
PbTiS ₃	T	4.16					St27 "Layer structure" P & S [No9]	
BaZrS ₃	O	7.037		9.983			Cl3 Distorted perovskite, P & S [Ha6, No9, As3b]	
BaZrSe ₃	H	7.188					As3a Hex (2L), P & S [No9]	
SrZrS ₃	O	13.49		9.79			Cl1 Distorted perovskite, P & S [No9]	
CaZrS ₃	O	13.07		9.58			Cl1 Distorted perovskite	
BaTaS ₃	H	6.847					As3b Hex (2L) P & S [No9]	
BaTaSe ₃	H	7.134					As3a Hex (2L) P & S [No9]	
ATaSe ₃	O	11.0		6.8			No9 A = Sr and Pb - not perovskite	
LnInS ₃	O	\approx 3.95		\approx 11.78			Ka13 Ln = La, Ce, Pr, Nd and Sm;	
LnGaSe ₃	H	\approx 10.3					$T_{\text{melt}} \approx 1100^\circ\text{C}$	
$A^{3+}B^{3+}O_3$								
LaAlO ₃	R	5.357					Ge5 P & S [Be34, Da1, Re5, De14], ESR: Gd, Cr [Ki3; St16a]. Luminescence: Eu [Ya3, Bl13, Bl14]. Pr [Ma30, De8], Cr [Bl15, Bo14]; twinning + derwining [Fa9, Fa10]; nuclear quadrupole resonance [De17]; S.S. with BaTiO ₃ [Sm15, Is2b]; space group R $\bar{3}c$ [Ra3, Ge4b], Review [Ge4b]	
							T = 650 °C; cubic $T > 522^\circ\text{C}$ [Wo15a, Ge4b, A \times 3], inelastic neutron scattering [A \times 3]	
CeAlO ₃	C	3.818					Ge5 P & S [Be34, Ro16, Sc13, Ke2]	
PrAlO ₃	R	5.327					P & S [Be34, Ma27, Yw4, Z01, Re5, Li2, Ru10, Sc13]	6
	R	5.307						

Compound	Sym	a Å	b Å	c Å	angle °	Ref.	Remarks	Magnetic Data
$A^{3+}B^{3+}O_3$ (continued)								
PrAlO ₃	T	3.74		3.76	$\alpha = 60^\circ 25'$	Ge5	Ma27	Discussion of disagreement between [Ge5] and [Ma27] given in [Ge5] and [To12a]
NdAlO ₃	R	5.286		7.473		P & S [Be34, Da2, Z01, Ke2, Ge5, Re5, Li2, Ru10, Sc13, Da1]	6	
SmAlO ₃	O	5.285	5.290	7.43	$\alpha = 60^\circ 19'$	Ge5	P & S [Be34, Ke2, Re5, Li2, Sc13, Z01]	6
EuAlO ₃	R	5.316	5.292	7.458		Ma27	Discussion of disagreement between [Ge5] and [Ma27] given in [Ge5] and [To12a]	6
GdAlO ₃	O	5.271	5.292	10.52		T = 850 °C, rhombohedral $T > 800$ °C	P & S [Bo14, Re5, Li2]	6
TbAlO ₃	H	3.760	5.304	7.447		Prep. $T < 900$ °C, see Fig. 17a	P & S [Be34, Da1, Ga28, Sc13, Li2, Ma39]; optical properties [Bi13, Bi14, Bi16, Ca8, Oh7]; NMR, Al ³⁷ [Bo24]	6
DyAlO ₃	O	5.247				Prep. < 900 °C, see Fig. 17a	Neutron diffraction [Bi2], P & S [Ga28, Sc13], optical properties [Hu6, Hu6a]	6
HoAlO ₃	H	3.73	5.308	7.415		Bi2	Prep. < 900 °C, see Fig. 17a	6
ErAlO ₃	H	3.730	5.31	10.51		Be36	Neutron diffraction [Hu6, Hu6a]	6
TmAlO ₃	O	5.23		7.40		Gi3	Prop. < 900 °C, see Fig. 17a	6
LuAlO ₃	H	3.700		10.50		P & S [Be34, Ga28, Da1, Da2, Sc13], neutron diffraction [Bi1, He12], optical properties [Hu5, Sc24, Fa5]	neutron diffraction [Bi1, He12], optical properties [Hu5, Sc24, Fa5]	6
YAlO ₃	O	5.18	5.33	7.36		Be36	Prep. < 900 °C, see Fig. 17a	6
ErAlO ₃	H	3.670	5.16	10.51		Sc13	P & S [Ga28]	6
TmAlO ₃	H	3.660	5.32	7.33		Be36	Prep. < 900 °C, see Fig. 17a	6
YbAlO ₃	O	5.15	5.33	10.50		Sc13	P & S [Ga28]	6
LuAlO ₃	O	5.128	5.332	7.29		Be36	Prep. < 900 °C, see Fig. 17a	6
YAlO ₃	O	5.179	5.329	7.317		Sc13	P & S [Ga28]	6
BiAlO ₃	H	3.68		7.370		Sc28	No perovskite [Ga28, Sc13]	6
PrAlO ₃	T	7.61				Ge6	P & S [Mi8, Be4], ESR; Fe ³⁺ and Gd ³⁺ [Wh3]; decomposition of YAG [Ma26]	6
AmAlO ₃	R	3.78				Be36	Prep. < 900 °C, see Fig. 17a	6
LaScO ₃	O	3.75				Na15	Not able to be reproduced [Bu3]	6
CeScO ₃	O	5.678				Ru13		6
PrScO ₃	O	5.615				Ke8		6
NdScO ₃	O	5.574				Ge2	P & S [Sc13, Ke2]	6
SmScO ₃	O	5.53				Ke2	No dimensions	6
						Ge2	P & S [Sc13]	6
						Sc13	P & S [Sc13, Ke2]	6

3.1 ABX₃ Perowskit-Struktur

[Lit. S. 275]

Compound	Sym	a Å	b Å	c Å	angle	Ref.	Remarks	Magnetic Data in 3.3.4, Tab.
$A^{3+}B^{3+}O_3$ (continued)								
EuScO ₃	O	5.51	5.76	7.94			<i>Sc13</i>	
GdScO ₃	O	5.487	5.756	7.925			<i>Ge2</i>	
DyScO ₃	O	5.43	5.71	7.89			<i>Sc13</i>	
HoScO ₃	O	5.42	5.71	7.87			<i>Sc13</i>	
YScO ₃	O	5.431	5.712	7.894			<i>Ge2</i>	
BaScO ₃	T _r	4.042	4.127	4.042	$\alpha = \gamma' = 90^\circ 41'$ $\beta = 91^\circ 52'$	T01b	P & S [Sc13, Ke2] High pressure preparation [To11a]	
LaTiO _{3-x}	C	3.934					W016	
La _{0.67} TiO ₃	C	3.887					K018	P & S [Si4, Be33, Ho12, Ke15, Ke16, Jo4] Ti ⁴⁺ , S.S. with SrTiO ₃ [Ti1, Ke18, ve9, We16], BaTiO ₃ [<i>J</i> 04]
CeTiO ₃	T	5.513					W016	
PrTiO ₃	T	5.508					W016	P & S [Be33, Ho12, Si4]
NdTiO ₃	O	5.482					W016	P & S [Be33, Ho12, Si4]
SmTiO ₃	O	5.398					W016	P & S [Be33, Si4, Mc1c]
GdTIO ₃	O	5.353					W016	P & S [Bo36, Ho12, Si4, Mc1c]
EuTiO ₃	C	7.810					W012	Ti ⁴⁺ , P & S [Br20, Mc1b], Prop. [Mc3, Mc4, Si4], neutron diffraction [Mc2]
TbTiO ₃	O						Mc1c	
DyTiO ₃	O						Mc1c	
HoTiO ₃	O						Mc1c	
ErTiO ₃	O						Mc1c	
TmTiO ₃	O						Mc1c	
YbTiO ₃	O						Mc1c	
LuTiO ₃	O						Mc1c	
YTiO ₃	O						Mc1c	
LaVO ₃	O						W014	P & S [Si5, Be33, Ke16, Re8, Wo4, Ke18, Ke15, Yal, Ro3], S.S. with CaVO _{2.5} [Ke18, Wo14], S.S. with SrVO _{3.5} [Wo14]
CeVO ₃	O	5.486	5.486	7.74			W014	P & S [Be33, Re8, Wo4, Vi2, Ge2]
PrVO ₃	O	5.487	5.562	7.751			W014	P & S [Be33, Re8, Wo4, Vi2, Ge2]
NdVO ₃	O	5.451	5.579	7.734			W014	P & S [Be33, Re8, Wo4, Vi2, Ge2]
SmVO ₃	O	5.393	5.588	7.672			W014	P & S [Be33, Re8, Wo4, Vi2, Ge2]
GdVO ₃	O	5.343	5.614	7.637			W014	P & S [Be33, Bo36, Re8, Ge2]
DyVO ₃	O	5.302	5.602	7.601			W014	P & S [Re8]
ErVO ₃	O	5.262	5.604	7.578			W014	P & S [Re8]
YVO ₃	O	5.284	5.605	7.587			W014	P & S [Re8]
PuVO ₃	O	5.45	5.58	7.76			Ru13	
AmVO ₃	O	5.48	5.61	7.78			Ke8	

3.1 ABX₃ perovskite structure

Compound	Sym	$\frac{a}{\text{\AA}}$	$\frac{b}{\text{\AA}}$	$\frac{c}{\text{\AA}}$	angle	Ref.	Remarks	Magnetic Data
$\text{A}^3+\text{B}^3+\text{O}_8$ (continued)								
LaCrO ₃	O	5.479	5.515	7.753		Qu1	Semiconducting 0.6 eV [Ru11], neutron diffraction [Ko1], optical properties [Ra8], P & S [Ge2, Ru11, Wo4, Ke2, Na14]. S.S. with Ni, Mn [Be33, Be21]; $T_{\text{melt}} = 2500^\circ\text{C}$ [Fo2], EPR [We4]	in 3.3.4, Tab. 6
	R	5.47				Ru11	$T = 280^\circ\text{C}$, rhombohedral $280 < T < 1030^\circ\text{C}$	6
	C	3.92				Ru11	$T = 1230^\circ\text{C}$	6
	O	5.47	5.50	7.75	$\alpha = 60^\circ 32'$	Iw1		
	C	7.754	7.740			Ya1	P & S [Ru10, Be33, Wo4, Ke2]	6
La _{0.9} Bi _{0.1} CrO ₃	O	5.475	5.475	7.718		Qu1	P & S [Ge2, Ru10, Be33, Wo4], $T_{\text{melt}} = 2420^\circ\text{C}$	6
La _{0.9} Si _{0.1} CrO _{3-x}	O	5.448	5.479			Qu1	[Fo2], dielectric properties [Ra8]	6
PrCrO ₃	O					Qu1	P & S [Ru10, Ge2, Be33, Wo4, Ke2], $T_{\text{melt}} = 2405^\circ\text{C}$ [Fo2]	6
NdCrO ₃	O	5.425	5.478	7.694		Qu1	P & S [Ru10, Ge2, Be33, Wo4, Ke2], $T_{\text{melt}} = 2405^\circ\text{C}$ [Fo2]	6
SmCrO ₃	O	5.367	5.508	7.643		Qu1	P & S [Ru10, Ge2, Be33, Wo4, Ke2], $T_{\text{melt}} = 2385^\circ\text{C}$ [Fo2]	6
EuCrO ₃	O	5.340	5.515	7.622		Qu1	P & S [Ru10, Ge2, Be33], $T_{\text{melt}} = 2370^\circ\text{C}$ [Fo2]	6
GdCrO ₃	O	5.312	5.525	7.606		Qu1	Neutron diffraction [Be42], Ma24], specific heat [De1a]	6
TbCrO ₃	O	5.291	5.518	7.576		Qu1	Neutron diffraction [Be38], $T_{\text{melt}} = 2345^\circ\text{C}$ [Fo2], dielectric hysteresis disappears at $\approx 540^\circ\text{C}$ indicating no center of symmetry [Ra8]	6
DyCrO ₃	O	5.265	5.520	7.552		Qu1	Neutron diffraction [Be32, Be47, Be50], dielectric properties [Co6], $T_{\text{melt}} = 2330^\circ\text{C}$ [Fo2], dielectric hysteresis disappears at $\approx 460^\circ\text{C}$ indicating no center of symmetry [Ra8], S.S. with HoMnO ₃ [Ap1b]	6
HoCrO ₃	O	5.243	5.519	7.538		Qu1	Dielectric properties [Co6], $T_{\text{melt}} = 2325^\circ\text{C}$ [Fo2]	6
						Qu1	$T_{\text{melt}} = 2320^\circ\text{C}$ [Fo2], dielectric hysteresis disappears at $\approx 520^\circ\text{C}$ indicating no center of symmetry [Ra8]	6
ErCrO ₃	O	5.223	5.516	7.519		Qu1	Dielectric hysteresis disappears at $\approx 480^\circ\text{C}$ indicating no center of symmetry [Ra8]	6
TmCrO ₃	O	5.209	5.508	7.500		Qu1	P & S [Ge6, Ge2, L ^{0.5} , Ka18, Pa14, Yu5], dielectric properties [Ra8], $T_{\text{melt}} = 2340^\circ\text{C}$ [Fo2]	6
YbCrO ₃	O	5.195	5.510	7.490		Sh9	High pressure preparation	6
LuCrO ₃	O	5.176	5.497	7.475				
YCrO ₃	O	5.241	5.521	7.532				
InCrO ₃	O	5.170	5.355	7.543				

Goodenough/Longo

3.1 ABX₃ Perowskit-Struktur

[Lit. S. 275]

Compound	Sym	a Å	b Å	c Å	angle	Ref.	Remarks	Magnetic Data in 3.3.4, Tab.
A³⁺B³⁺O₃ (continued)								
TlCrO ₃	O	5.302	5.405	7.647	$\alpha = 90^\circ 35'$	Sh9 Su10	High pressure preparation	6
BCrO ₃	Tr	3.90	3.87	3.90	$\beta = 89^\circ 10'$	Ru13 [T ₀ 11a]	High pressure preparation; S.S. with BiMnO ₃	6
PuCrO ₃	O'	5.46	5.51	7.76		P & S [Na1/4]		
LaMnO ₃	O'	5.533	5.722	7.694		P & S [W ₀ 12, J ₄ , J ₀ 8, J ₀ 12, Ha22, J ₀ 7, J ₀ 9, Ya1, Ro11], S.S. with Cr, Fe, Co, Ni [Be33, Ba21, G ₄ , J ₀ 7, J ₀ 8, J ₀ 9, W ₀ 2, W ₀ 6, Fu2, B ₁ 7], S.S. with (Ba, Sr, Ca, Pb)TiO ₃ [Ha31, Ha32, T ₀ 3, To6, To12], S.S. with GdCoO ₃ [De23], 24% Mn ⁴⁺		
CeMnO ₃	R	3.892	5.537	7.818	$\alpha = 90^\circ 36'$	W ₀ 2 Ve12		
PrMnO ₃	O'	5.445	5.557	7.575		Ve12	P & S [Be33, V ₁ 1, complete structure [Qu2]	6
NdMnO ₃	O'	5.380	5.787	7.557		Ve12	P & S [Be33, V ₁ 1, Sz1], complete structure [Qu2]	6
SmMnO ₃	O'	5.359	5.854	7.482		Ve12	P & S [Be33]	6
EuMnO ₃	O'	5.338	5.843	7.453		Ve12	P & S [Sz1]	6
GdMnO ₃	O'	5.313	5.842	7.432		Ve12	P & S [Be33, Sz1], S.S. with LaCoO ₃ [De23]	6
TbMnO ₃	O'	5.297	5.831	7.403		Ve12	Complete structure determination [Qu2]	6
DyMnO ₃	O'	5.275	5.828	7.375		Ve12	P & S [Sz1]	6
HoMnO ₃	H	6.177	6.177	11.43		Sz1	Preparation temperature 1600 °C, see Fig. 17a	
	H	6.136	6.136	11.42		Y ₂ 2	Magnetic properties [Ve12, Be32], dielectric properties [Be35, Co7], P & S [Sz1], see Fig. 17a	6
ErMnO ₃	O'	5.26	5.84	7.35		Wa4 Ya2	High pressure phase, P & S [Wa5, V ₁ 1, Sz1]	
	H	6.115	6.062	11.41		Wa4 Ya2	Magnetic properties [Ve12, Be32], dielectric properties [Be35, Co7], see Fig. 17a	
TmMnO ₃	O'	5.24	5.82	7.335		Wa4 Ya2	High pressure phase	
YbMnO ₃	H	6.062	5.23	11.40		Wa4 Ya2	Magnetic properties [Ve12, Be32, Ro8, Bo11], dielectric properties [Be35, Ro8, Bo11, Co7, Is11], P & S [Sz1], see Fig. 17a	
	H	6.062	5.81	7.32		Wa4 Ya2	High pressure phase	
LuMnO ₃	O'	5.22	5.80	7.30		Wa4 Ya2	Magnetic properties [Ve12, Be32], dielectric properties [Be35, Co7], see Fig. 17a	
YMnO ₃	H	6.042	6.025	11.37		Wa4 Ya2	High pressure phase	
	H	6.125	5.79	7.31		Wa4 Ya2	Dielectric or magnetic properties [Ta13, Ro8, Be35, Co5, Co7, Co3, Bo11, Is11, Pe17, Pe16, Be32, Be29, Be43, Be44, Be449, Ko3, Ki8], see Fig. 17a	

Berichtigungen zu Band III/4a

S. 177, letzte Zeile: statt $\text{Ba}_2\text{TdPaO}_6$ lies $\text{Ba}_2\text{TbPaO}_6$

S. 219, Zeile 16 von unten: statt $\text{KMg}_{1-x}\text{Ni}_x\text{Fe}_3$ lies $\text{KMg}_{1-x}\text{Ni}_x\text{F}_3$

S. 252, Zeile 26 von oben (Überschrift): statt $\text{Sr}_3\text{Fe}_3\text{UO}_9$ lies $\text{Sr}_3\text{Fe}_2\text{UO}_9$

Errata in Vol. III/4a

p. 177, bottom line: instead of $\text{Ba}_2\text{TdPaO}_6$ read $\text{Ba}_2\text{TbPaO}_6$

p. 219, line 16 from the bottom: instead of $\text{KMg}_{1-x}\text{Ni}_x\text{Fe}_3$ read $\text{KMg}_{1-x}\text{Ni}_x\text{F}_3$

p. 252, line 26 from above (headline): instead of $\text{Sr}_3\text{Fe}_3\text{UO}_9$ read $\text{Sr}_3\text{Fe}_2\text{UO}_9$

3.1 ABX₃ perovskite structure

Compound	Sym	<i>a</i> Å	<i>b</i> Å	<i>c</i> Å	angle	Ref.	Remarks	Magnetic Data
<i>A</i> ³⁺ <i>B</i> ³⁺ <i>O</i> ₃ (continued)								
YMnO ₃	O	5.26	5.84	7.35		Wa3	High pressure phase; S.S. with: Fe, perovskite at 15% Fe [Ch6]	
BiMnO ₃	M	10.93	11.31	7.98	$\beta = 92^\circ 24'$	Bo12	P & S [Su10]; S.S. with Ca [Bo6, Bo12, St19], PbTiO ₃ [Bo6, Bo7], Sr [IV], La [IV], BiCrO ₃ [To11a]; crystallographic transformation	6
PuMnO ₃ LaFeO ₃	C O	3.86 5.556	5.565	7.862		Ru13 Ge6	Pseudocubic P & S [Be33, Fo5, Re5, Wo3, Ke2, Da2, Na14, Ya1], S.S. with Ni, Mn [Be33], S.S. with Al, Co, Cr, Sc [Ka17, Wo2], rhombohedral $T > 980^\circ\text{C}$ [Da1], S.S. with: PbNb ₂ O ₆ [Fr11], Pb [Re5a], Bi [Ri5b]	6
CeFeO ₃ PrFeO ₃	O O	5.441 5.495	5.577 5.578	7.809 7.810		Ro1a Ge6	P & S [Ke2, Be33] P & S [Be33, Fo5, Re5], S.S. with Al, Co, Cr, Sc [Ka17]	6
NdFeO ₃	O	5.441	5.573	7.753		Ge6	P & S [Be33, Fo5, Re5, Wo3], S.S. with Pb [Re5a], Bi [Re5b]	6
SnFeO ₃	O	5.394	5.592	7.711		Ge6	P & S [Be33, Fo5, Re5, Wo3], S.S. with Pb [Re5a], Bi [Re5b]	6
EuFeO ₃ GdFeO ₃	O O	5.371 5.346	5.611 5.616	7.686 7.668		Ge6 Ge6	P & S [Re5], S.S. with Pb [Re5a], Bi [Re5b] P & S [Be33, Re5], crystal structure [Co2I], S.S. with Pb [Re5a], Bi [Re5b]	6
TbFeO ₃ DyFeO ₃ HoFeO ₃	O O O	5.326 5.302 5.278	5.602 5.598 5.591	7.635 7.623 7.602		Ei1 Ei1 Ei1	P & S [Ko6], S.S. with: Pb [Re5a], Bi [Re5b] P & S [Da2], S.S. with: Pb [Re5a], Bi [Re5b] P & S [Ko6], S.S. with: Pb [Re5a], Bi [Re5b], HoMnO ₃ [Ap1a]	6
ErFeO ₃	O	5.263	5.582	7.591		Ei1	P & S [Fo5], crystal structure [Wi7], S.S. with: Pb [Re5a], Bi [Re5b]	6
TmFeO ₃	O	5.251	5.576	7.584		Ei1	Crystal structure [Wi8], S.S. with: Pb [Re5a], Bi [Re5b]	6
YbFeO ₃	O	5.233	5.557	7.570		Ei1	P & S [Ko6, Be1, Ha27], S.S. with: Pb [Re5a], Bi [Re5b]	6
LuFeO ₃ YFeO ₃	O O	5.213 5.283	5.547 5.592	7.565 7.603		Ei1 Ei1	P & S [Sa6], S.S. with: Pb [Re5a], Bi [Re5b] P & S [Fo5, Ru11, Ko6, Wo3, Ge4, Ma26, Va7, Sh12a], crystal structure [Co2I], S.S. with: Pb [Re5a], Bi [Re5b]	6
TlFeO ₃	O	5.319	5.448	7.796		Sh9		

Goodenough/Longo

3.1 ABX₃ Perowskit-Struktur

Compound	Sym	<i>a</i> Å	<i>b</i> Å	<i>c</i> Å	angle	Ref.	Magnetic Data
$A^3+B^3+O_8$ (continued)							
BiFeO ₃	R	5.62			$\alpha = 59^\circ 41'$	<i>Mi0</i>	P & S [F112, I10, K05, K14, T07, T09, T012, Yu3, Yu1, Za2, Sm34, T010, Ge10a, R022], neutron diffraction [P11, K14, K15, K16, Bh2]. S. S. with: LaAlO ₃ [Fe5], LaFeO ₃ [K15, Kb5, Ro7, Ro9, I10b, R010, K16], PbTi, ZrTiO ₃ [La6, Fe8, Ge10, Fe2, Sm7], BaTiO ₃ [Ve5, K15], SrTiO ₃ [Fe6], LaCrO ₃ [R05], SrSnO ₃ [H11], Bi ₄ Ti ₃ O ₁₂ [Is12], SrFeO ₃ [Ma8], Pb ₂ FeNbO ₆ [R010, Yu1, Yu2, Sm12, Sm13, Is10a, Zh1, Is8, Kr3, Kr5], Sr(Sn _{1/3} Mn _{2/3})O ₃ [Ni6, Vi4], Sr _{0.7} La _{0.3} MnO ₃ [Ro10], PbNb ₂ O ₆ [Fr11]; BiMnO ₃ [Ma37], Pb(Fe _{1/3} W _{1/3})O ₃ [Sm26], PrFeO ₃ [Vi4a], complete structure S.G. R3c [Mi0]
LaCoO ₃	R	5.436			$\alpha = 60^\circ 48'$	<i>W09</i>	R3c, $T < 375^\circ\text{C}$; R3, $T > 375^\circ\text{C}$ [<i>Ra3</i>]; P & S [As3, W04, He7, Sc23], Prop. [Me17, Ko1, Ra3, Ge12, Ra3, J09, Go16, Na1, Bi6, He7, Mu4, Me18], S. S. with Sr [Me18, Ra4, J013], S. S. with Sr and Th [Sc23]
PrCoO ₃	R	5.52			$\alpha = 60^\circ 0'$	<i>Ra3</i>	$T = 937^\circ\text{C}$: atomic positions demand R3 symmetry
NdCoO ₃	O	5.331	5.373	7.587		<i>Be33</i>	P & S [W04]
SmCoO ₃	O	5.336	5.336	7.547		<i>Be33</i>	P & S [W04], thermal conductivity [Ge12]
GdCoO ₃	O	5.289	5.354	7.541		<i>Be33</i>	P & S [W04]
TbCoO ₃	O	5.228	5.404	7.436		<i>Be33</i>	P & S [A55]
BiCoO ₃	C	4.228					Studied in review of TbBO ₃ compounds [Ma24]. No cell dimension
LaNiO ₃	R	5.461					T_{011b} High pressure preparation [T011a]
BiNiO ₃	C	4.173					<i>W08</i> P & S [W06], neutron diffraction [Ko1]
LaGaO ₃	O	5.496					T_{011b} High pressure preparation [T011a]
	R	5.544					<i>Ge2</i> P & S [Ke2, Da2, Be34, Br25, Da1, Ma25a]
CeGaO ₃	C	3.87					$T = 900^\circ\text{C}$, rhombohedral $T > 875^\circ\text{C}$ (by DTA)
PrGaO ₃	O	5.465					<i>Ge2</i> Distorted P & S [Be34, Br25, Ma25a]
NdGaO ₃	O	5.426					<i>Ge2</i> P & S [D1, B34, B25, Ke2, Ma25a], complete structure [Br26], S. S. with LaGaO ₃ [Br25]
SmGaO ₃	O	5.369					<i>Ma25a</i> High pressure preparation
EuGaO ₃	O	5.351					<i>Ma25a</i> High pressure preparation
GdGaO ₃	O	5.322					<i>Ma25a</i> High pressure preparation
TbGaO ₃	O	5.307					<i>Ma25a</i> High pressure preparation

3.1 ABX₃ perovskite structure

Compound	Sym	<i>a</i> Å	<i>b</i> Å	<i>c</i> Å	angle	Ref.	Remarks	Magnetic Data in 3.3.4, Tab.
<i>A³⁺B³⁺O₈</i> (continued)								
DyGaO ₃	O	5.282	5.534	7.556			<i>Ma25a</i>	High pressure preparation
HoGaO ₃	O	5.251	5.531	7.536			<i>Ma25a</i>	High pressure preparation
ErGaO ₃	O	5.239	5.527	7.522			<i>Ma25a</i>	High pressure preparation
TmGaO ₃	O	5.224	5.515	7.505			<i>Ma25a</i>	High pressure preparation
YbGaO ₃	O	5.208	5.510	7.490			<i>Ma25a</i>	High pressure preparation [Ma25]
LuGaO ₃	O	5.188	5.505	7.484			<i>Ma25a</i>	High pressure preparation
YGaO ₃	O	5.257	5.536	7.533			<i>Ma25</i>	High pressure preparation [Ma26]
LaYO ₃	O	5.868	6.071	8.438			<i>Ge3</i>	P & S [Pa2, Mo6], optical properties (Eu ³⁺) [Bl13]
BiYO ₃	C	4.92					<i>To11b</i>	High pressure preparation [To11a]
LaNbO ₃	C	5.524	5.679	7.900			<i>Si5</i>	Pseudocubic
LaRhO ₃	O	5.4143	5.7473	7.8026			<i>W05</i>	P & S [Ch11, Wo9, Kh1]
PrRhO ₃	O	5.3778	5.7551	7.7745			<i>Sh8a</i>	P & S [Ch11]
NdRhO ₃	O	5.3211	5.7613	7.7083			<i>Sh8a</i>	P & S [W05]
SmRhO ₃	O	5.2985	5.7607	7.6802			<i>Sh8a</i>	P & S [Ch11]
EuRhO ₃	O	5.2774	5.7605	7.6584			<i>Sh8a</i>	P & S [Ch11]
GdRhO ₃	O	5.2541	5.7492	7.6226			<i>Sh8a</i>	P & S [Ch11]
TbRhO ₃	O	5.2449	5.7314	7.6002			<i>Sh8a</i>	P & S [Ch11]
DyRhO ₃	O	5.2299	5.7227	7.5823			<i>Sh8a</i>	P & S [Ch11]
HoRhO ₃	O	5.2160	5.7117	7.5610			<i>Sh8a</i>	P & S [Ch11]
ErRhO ₃	O	5.2028	5.6974	7.5428			<i>Sh8a</i>	P & S [Ch11]
TmRhO ₃	O	5.1861	5.6700	7.5125			<i>Sh8a</i>	P & S [Ch11]
LuRhO ₃	O	5.301	5.435	7.586			<i>Sh9</i>	P & S [Ge3, Pa2]
InRhO ₃	O	5.723	5.914	8.207			<i>Ro16</i>	
LaInO ₃	O	5.627	5.891	8.121			<i>Ro16</i>	
NdInO ₃	O	5.589	5.886	8.082			<i>Sh9</i>	High pressure preparation
SmInO ₃	O	5.567	5.835	8.078			<i>Sh9</i>	High pressure preparation
EuInO ₃	O	5.548	5.842	8.071			<i>Sh9</i>	High pressure preparation
GdInO ₃	O	5.519	5.751	8.041			<i>Sh9</i>	High pressure preparation
DyInO ₃	O	5.500	5.787	8.053			<i>Sh9</i>	High pressure preparation
YInO ₃	O	5.888	6.092	8.480			<i>Mo6</i>	
LaHoO ₃	O	5.85	6.07	8.43			<i>Sc12</i>	P & S [Sc13, Mo6]
LaErO ₃	O	5.85	6.06	8.42			<i>Sc12</i>	P & S [Sc13, Mo6]
LaTmO ₃	O	5.85	6.02	8.41			<i>Sc12</i>	P & S [Sc13, Mo6], complete structure determined, S.G. Pbn2 ₁ , [Mu8], T _{mett} = 2120 °C [Tr0]
LaYbO ₃	O	4.325					<i>T^{r0}</i>	T = 2080 °C
LaLuO ₃	C	5.82	6.02	8.37			<i>Sc12</i>	P & S [Sc13, Mo6]
PrLuO ₃	O	5.751	5.977	8.320			<i>Mo6</i>	

3.1 ABX₃ Perowskit-Struktur

[Lit. S. 275]

Tab. 2b. A₂B'BX₆ compounds

Compound	Sym	a Å	b Å	c Å	angle	Ref.	Remarks	Magnetic Data
$A_2^+B^{3+}X_6; X = F^{-1}, Cl^{-1}$								
Cs ₂ NaAlF ₆	H	6.168		29.76			<i>Ba5a</i>	Hex (12 L)
Rb ₂ NaAlF ₆	C	8.29		28.02			<i>Ba5a</i>	Hex (12 L)
Rb ₂ LiAlF ₆	H	5.802		13.648			<i>Ba5a</i>	R. Perovskite
K ₂ LiAlF ₆	H	5.574		13.754			<i>Wi1b</i>	Hex (6L), Prep. $T > 470$ °C
K ₂ NaAlF ₆	C	5.614					<i>Wi1b</i>	
K ₂ KAIF ₆	C	8.105					<i>Me21</i>	
N ₂ NaAlF ₆	M	8.65					<i>St33</i>	P & S [St33, Me19, Cr5a], S.S. with Fe [Cr5a]
(NH ₄) ₂ (NH ₄)AlF ₆	M	5.46	5.61	7.80	$\beta = 90^\circ 11'$		<i>Na17</i>	
Cs ₂ CsScF ₆	C	8.90					<i>Pa9</i>	Prep. [Ba0]
Cs ₂ KScF ₆	C	9.32					<i>Ho16a</i>	Prep. [Ba0]
Rb ₂ RbScF ₆	C						<i>Bo2</i>	Prep. [Ba0]
K ₂ KScF ₆	C						<i>Bo2</i>	$T < 680$ °C
N ₂ _a Na _a ScF ₆	M	5.60	5.81	8.12	$\beta = 90^\circ 45'$		<i>Th1</i>	
(NH ₄) ₂ (NH ₄)ScF ₆	M	6.49		9.45			<i>Bo2</i>	
K ₂ KTiF ₆	C	17.46	9.26	8.75			<i>Br7</i>	High temperature form
K ₂ NaTiF ₆	C	8.56					<i>Br7</i>	P & S [Ba5], magnetic properties, $n_{eff} = 1.70$,
Na _a NaTiF ₆	M	6.49					<i>Br7</i>	$\Theta_p = 0$ K [Eh1]
Cs ₂ KVF ₆	C	9.26					<i>Ba5a</i>	Structure determined [Bu4a]
Cs ₂ NaVF ₆	C	8.367					<i>Ba5a</i>	P & S [Ba5]
Rb ₂ KVF ₆	C	5.53	5.83	7.99	$\beta \approx 90^\circ$		<i>Ba5a</i>	Hex (12L)
Rb ₂ NaVF ₆	C	9.04		30.40			<i>Ba5a</i>	
Rb ₂ LiVF ₆	H	6.267					<i>Ba5a</i>	
K ₂ KVF ₆	C	8.88					<i>Ba5a</i>	
K ₂ NaVF ₆	H	8.47					<i>Ba5a</i>	
K ₂ NaVF ₆	C	5.891		28.77			<i>Ba5a</i>	
(NH ₄) ₂ (NH ₄)VF ₆	C	8.315					<i>Ba5</i>	Magnetic properties, 80 $< T < 300$ °K,
Cs ₂ RbCrF ₆	C	9.04					<i>PaBa</i>	$n_{eff} = 2.79$, $\Theta_p = -14$ °K [Fi4]
Cs ₂ KCrF ₆	C	9.15					<i>Ba5a</i>	
Cs ₂ NaCrF ₆	H	8.99					<i>Ba5a</i>	
Rb ₂ KCrF ₆	C	6.231					<i>Ba5a</i>	
Rb ₂ NaCrF ₆	C	8.81					<i>Ba5a</i>	
Rb ₂ LiCrF ₆	H	8.42					<i>Ba5a</i>	
K ₂ KCrF ₆	H	5.865					<i>K16</i>	Hex (12 L)
K ₂ NaCrF ₆	T	8.56					<i>P & S [Pe2]</i>	
K ₂ KCrF ₆	C	8.54					<i>Bo2</i>	High temperature form

3.1 ABX₃ perovskite structure

Compound	Sym	<i>a</i> Å	<i>b</i> Å	<i>c</i> Å	angle °	Ref.	Remarks	Magnetic Data
<i>A</i> ⁺ <i>B</i> ³⁺ <i>X</i> ₆ ; X = F ⁻¹ , Cl ⁻¹ (continued)								
K ₂ NaCrF ₆	C	8.266	5.679	7.878	$\beta \approx 90^\circ$	<i>Kn5</i> <i>V01</i>	Prop. [Sh28]	in 3.3.4, Tab.
Na ₂ NaCrF ₆	M	5.468	9.01	16.60		<i>Pa6a</i> <i>Pe2</i>	Magnetic properties, $\rho^* = 4.95 \mu_B$ [Pe2]	
(NH ₄) ₂ (NH ₄)CrF ₆	C	17.50	8.171	8.577		<i>Kn4</i> <i>Mi2</i>		
K ₂ KMnF ₆	T	10.46	9.05	30.40		<i>Ba5a</i> <i>Fex</i> (12L)		
K ₂ NaMnF ₆	C	6.260	H			<i>Ba5a</i> <i>Bo2</i>		
Cs ₂ CsFeF ₆	C	8.88				<i>Ba5a</i>		
Cs ₂ KFeF ₆	C	8.87				<i>Ba5a</i>		
Cs ₂ NaFeF ₆	C	8.47				<i>Ba5a</i>		
Rb ₂ RbFeF ₆	C	8.891				<i>Hex</i> (12L)		
Rb ₂ KFeF ₆	C	8.58				<i>Bo2</i>		
Rb ₂ NaFeF ₆	C	8.323				<i>Kn5</i>		
Na ₂ NaFeF ₆	M	5.506				<i>Cr5a</i>	P & S [Mi5], magnetic properties, 92 < T < 296 °K,	
Li ₂ LiFeF ₆	C	8.88				<i>Mi2</i>	P & S [Mi5], $\eta_{eff} = 5.85$, $\Theta_p = -2^\circ K$ [Fi1]	
(NH ₄) ₂ (NH ₄)FeF ₆	T	6.39				<i>Si33</i> <i>Pa9</i>	Magnetic properties, 93 < T < 293 °K, $\eta_{eff} = 6.00$, $\Theta_p = 0^\circ K$ [Fi1]	
Cs ₂ CsCoF ₆	C	9.10				<i>K16</i>	Low temperature form P & S [Si33, K16]; magnetic properties, 92 < T < 294 °K, $\eta_{eff} = 5.86$, $\Theta_p = -2^\circ K$ [Fi1]	
Rb ₂ RbCoF ₆	C	9.23				<i>K16</i>	Magnetic properties, 90 < T < 290 °K, $\eta_{eff} = 5.28$, $\Theta_p = +2^\circ K$ [K16]	
K ₂ KCoF ₆	C	8.90				<i>K16</i>	P & S [Ho13], magnetic properties, 90 < T < 290 °K, $\eta_{eff} = 5.48$, $\Theta_p = -2^\circ K$ [K16]	
K ₂ NaCoF ₆	C	8.57				<i>K16</i>	P & S [Me27, Ho13], magnetic properties, 73 < T < 300 °K, $\eta_{eff} = 5.53$, $\Theta_p = -10^\circ K$ [Co23, K16]	
Na ₂ NaCoF ₆	C	8.22				<i>Me27</i>	Pseudocubic, P & S [Ho13], magnetic properties, 90 < T < 290 °K, $\eta_{eff} = 5.39$, $\Theta_p = -5^\circ K$, [K16]	
K ₂ KNiF ₆	C	7.91				<i>Bo2</i>	P & S [K16], magnetic properties, 90 < T < 295 °K, does not obey Curie-Weiss law [K12, K13, We20]	
K ₂ KCuF ₆	C	8.44				<i>K16</i>	Magnetic properties, $\eta_{eff} = 2.8$ [K12]	
Cs ₂ KGaF ₆	C	8.50				<i>Kn5</i>		
K ₂ NaGaF ₆	C	8.975				<i>Sc26</i>		
(NH ₄) ₂ (NH ₄)GaF ₆	C	8.246				<i>Ho16</i>		
Cs ₂ KAgF ₆	C	9.041						
		9.175						

3.1 ABX₃ Perowskit-Struktur

[Lit. S. 275]

Compound	Sym.	$\frac{a}{\text{\AA}}$	$\frac{b}{\text{\AA}}$	$\frac{c}{\text{\AA}}$	angle	Ref.	Remarks	Magnetic Data
$A_3^{+}B^{3+}X_6$; X = F ⁻¹ , Cl ⁻¹ (continued)								
Cs ₂ CsInF ₆	C	9.50						B ₀₂
Cs ₂ KInF ₆	C	9.219						H _{016a}
Rb ₂ RbInF ₆	C	9.20						B ₀₂
K ₂ KInF ₆	C	17.71						B ₀₂
(NH ₄) ₂ (NH ₄) ₂ MoO ₃ F ₃	C	9.10						P _{a9}
Cs ₂ NaCeF ₆	C	9.26						B _{e52a}
Cs ₂ KCeF ₆	C	9.61						B _{e52a}
Cs ₂ RbCeF ₆	C	9.75						B _{e52a}
Cs ₂ CsCeF ₆	C	9.84						B _{e52a}
CsKKCeF ₆	C	9.36						B _{e52a}
CsRbRbCeF ₆	C	9.60						B _{e52a}
Rb ₂ KCeF ₆	C	9.40						B _{e52a}
Rb ₂ RbCeF ₆	C	9.49						P & S [B ₀₂]
RbKCKCeF ₆	C	9.20						B _{e52a}
K ₂ KCeF ₆	C	9.07						B _{e52a}
Rb ₂ RbPrF ₆	C	9.48						B ₀₂
Rb ₂ NaSmF ₆	C	9.163						A ₁₄
Cs ₂ NaSmF ₆	C	8.988						A ₁₄
Cs ₂ NaTbF ₆	C	9.107						A ₁₄
Rb ₂ NaTbF ₆	C	9.9208						A ₁₄
Rb ₂ NaHoF ₆	C	8.881						A ₁₄
Cs ₂ NaErF ₆	C	9.061						A ₁₄
Rb ₂ NaErF ₆	C	8.867						A ₁₄
Cs ₂ NaYbF ₆	C	9.022						A ₁₄
Rb ₂ NaYbF ₆	C	8.824						A ₁₄
Cs ₂ NaYF ₆	C	9.056						A ₁₄
Rb ₂ NaYF ₆	C	8.8693						A ₁₄
Cs ₂ AgAuCl ₆	T	7.38						E ₁₃
Cs ₂ AgAuCl ₆	C	5.28						E ₁₃
Cs ₂ AuAuCl ₆	T	7.49						E ₁₃
Cs ₂ KTiF ₆	C	9.36						H _{016a}
K ₂ KTiF ₆	C	11.86						B ₀₂
(A ³⁺ A ³⁺) (B ³⁺ +B ⁴⁺)O ₆								
BaLaMnTiO ₆	C	3.960						
SrLaMnTiO ₆	R	3.912						
CaLaMnTiO ₆	R	3.872						
CaYMnTiO ₆	O	5.32						
PbLaMnTiO ₆	R	3.993						

in 3.3.4,
Tab.

PbLaMnTiO₆ | R | 3.933 | | | $\alpha = 90^\circ 12'$ | Ha32 | S.S. with $x = \text{Pb}_x\text{NbMnO}_6$; cubic $\geq 50\%$

Ref. p. 275]

3.1 ABX₃ perovskite structure

Compound	Sym	a Å	b Å	c Å	angle	Ref.	Remarks	Magnetic Data in 3.3.4, Tab.
(A ²⁺ +A ³⁺) (B ³⁺ +B ⁴⁺)O ₆ (continued)								
SrLaFeTiO ₆	C	3.92				B18		
SrLaMnIrO ₆	C	3.93				B18		
SrLaFeIrO ₆	C	3.94				B18		
A ³⁺ +BB'O ₆								
La ₂ MgTiO ₆	C	3.96						
Nd ₂ MgTiO ₆	C	3.90						
LaCeMgTiO ₆	C	3.929						
Bi ₂ MgTiO ₆	C	3.98						
Y ₂ Ni _{0.4} Mg _{0.6} TiO ₆	C	3.83						
La ₂ MgMnO ₆								
La ₂ CoMnO ₆								
La ₂ NiMnO ₆								
La ₂ CuMnO ₆	C	3.90						
La ₂ MgGeO ₆	C	3.88						
Y ₂ MgGeO ₆	C	4.06						
La ₂ MgZrO ₆	C	4.174						
La ₂ CaZrO ₆	C	5.59						
La ₂ LiNbO ₆	O	7.91						
La ₂ MgRuO ₆	C	7.84						
La ₂ MnRuO ₆	C	7.90						
La ₂ NiRuO ₆	C	7.97						
La ₂ ZnRuO ₆	C	4.02						
La ₂ Ni _{0.4} Mg _{0.6} SnO ₆	C	7.926						
La ₂ MgReO ₆	C	7.908						
La ₂ NiReO ₆	T	5.611						
La ₂ CoReO ₆								
La ₂ FeReO ₆								
La ₂ MgIrO ₆	C	7.92						
La ₂ MnIrO ₆	C	7.86						
La ₂ CoIrO ₆	O	5.60						
La ₂ NiIrO ₆	C	7.90						
La ₂ CuIrO ₆	M	5.80						
A ³⁺ +BV ⁵⁺ O ₆								
Ba ₂ BiVO ₆	O	6.123	6.180	8.622		V _{e2}	P & S [V _{e3} , V _{e3}], dielectric properties [V _{e2}]	
	C	4.372				V _{e2}	Cubic $> 320^\circ \text{C}$	

Goodenough/Longo

3.1 ABX₃ Perowskit-Struktur

[Lit. S. 275]

Compound	Sym	a Å	b Å	c Å	angle	Ref.	Remarks	Magnetic Data
in 3.3.4, Tab.								
Ba ₂ ScNbO ₆	C	8.220				P & S [Ag1, Br16]		
Ba ₂ VNbO ₆	C	4.051				Ch10		
Ba ₂ MnNbO ₆	C	4.090				Ha32	P & S [Ag1]	
Ba ₂ FeNbO ₆	C	4.057				Ga1	P & S [Ga13, Fi10, Ag1]	
Ba ₂ CoNbO ₆	C	4.06				Bl8		
Ba ₃ NiNbO ₆	C	4.1				Bl8		
Ba ₂ SrNbO _{6,5}	C	8.54				Ga1		
Ba ₂ YNbO ₆	C	4.180				Br16	P & S [Fi10]	
Ba ₂ RhNbO ₆	C	8.17				Bl8		
Ba ₁ InNbO ₆	C	8.279				Br16	P & S [Ga1]	
Ba ₂ BaNbO _{6,5}	C	8.68				Ga1	P & S [B ^r 16], cubic $T > 300$ °C [Fi10]	
Ba ₂ LaNbO ₆	T	8.607				Ga1	Probably ordered	
Ba ₂ CeNbO ₆	C	4.293				Br16	Probably ordered, cubic $T > 300$ °C [Fi10]	
Ba ₂ PrNbO ₆	C	4.285				Ga1	P & S [B ^r 16], cubic $T > 300$ °C [Fi10]	
Ba ₂ NdNbO ₆	C	8.540				Ga1	P & S [B ^r 16], cubic $T > 300$ °C [Fi10]	
Ba ₂ SmNbO ₆	C	8.518				Ga1	P & S [B ^r 16], cubic $T > 300$ °C [Fi10]	
Ba ₂ EuNbO ₆	C	8.507				Ga1	P & S [B ^r 16]	
Ba ₂ GdNbO ₆	C	8.496				Ga1	P & S [B ^r 16], fluorescences [Bl11, Ni1, Bu14]	
Ba ₂ TbNbO ₆	C	4.229				Br16	Probably ordered	
Ba ₂ DyNbO ₆	C	8.437				Ga1	P & S [B ^r 16]	
Ba ₃ ErNbO ₆	C	8.427				Ga1	P & S [B ^r 16]	
Ba ₃ TmNbO ₆	C	8.408				Ga1	P & S [B ^r 16]	
Ba ₃ YbNbO ₆	C	8.374				Ga1	P & S [B ^r 16], dielectric properties [Ag1]	
Ba ₃ LuNbO ₆	C	8.364				Ga1	P & S [B ^r 16]	
Ba ₂ TiNbO ₆	C	8.42				Si6		
Ba ₂ BiNbO ₆	R	6.086				V ^e 2	P & S [Vi3, Ve3], dielectric properties [Vi2b]	
Sr ₂ AlNbO ₆	C	7.784				Fi10	P & S [Si1]	
Sr ₂ CaNbO _{6,5}	C	8.20				Ga13		
Sr ₂ YNbO ₆	C	3.965				Ch10		
Sr ₂ CrNbO ₆	R	7.87				Bl8	P & S [Br14]	
Sr ₂ MnNbO ₆	T	3.97				Ha32	P & S [Ku12], cubic $T > 200$ °C [Ku12]	
Sr ₂ FeNbO ₆	C	3.960				Ku6	P & S [Ga13, Ku12]	
Sr ₂ CoNbO ₆	C	3.968				Bl8	$T = 250$ °C, cubic $T \geq 250$ °C	
Sr ₂ GaNbO ₆	C	3.93				Br14		
Sr ₂ SrNbO _{6,5}	C	3.9477				Ga13	Cubic $T > 630$ °C	
Sr ₂ YNbO ₆	R	8.34				Ku12		
Sr ₂ InNbO ₆	C	5.184				Fi10	P & S [Br14]	
		8.106						

3.1 ABX₃ perovskite structure

Compound	Sym	<i>a</i> Å	<i>b</i> Å	<i>c</i> Å	angle °	Ref.	Remarks	Magnetic Data in 3.3.4, Tab.
<i>A</i> ₃ ⁺ BNb ₆ ⁺ O ₆ (continued)								
Sr ₃ P ₂ NbO ₆	T	5.822		8.431		Ku12		
Sr ₃ NdNbO ₆	T	5.780	5.94	8.367		Ku12		
Sr ₃ SmNbO ₆	M	5.85	5.91	8.30	$\beta = 90^\circ 12'$	Fi10		
Sr ₃ EuNbO ₆	M	5.84	5.90	8.30	$\beta = 90^\circ 12'$	Fi10		
Sr ₃ GdNbO ₆	M	5.83	5.90	8.28	$\beta = 90^\circ 15'$	Fi10		
Sr ₃ TbNbO ₆	M	5.82	5.88	8.27	$\beta = 90^\circ 8'$	Fi10		
Sr ₃ DyNbO ₆	M	5.81	5.87	8.26	$\beta = 90^\circ 9'$	Fi10		
Sr ₃ HoNbO ₆	M	5.81	5.86	8.23	$\beta = 90^\circ 6'$	Fi10		
Sr ₃ ErNbO ₆	M	5.80	5.84	8.23	$\beta = 90^\circ 4'$	Fi10		
Sr ₃ TmNbO ₆	C	8.20				Fi10	Slight distortion	
Sr ₃ YbNbO ₆	C	8.196				Ku12	Cubic $T > 540^\circ \text{C}$	
Sr ₃ LuNbO ₆	C	8.19				Ku12	Cubic $T > 540^\circ \text{C}$	
Sr ₃ LaCoNbO ₆	C	7.99				Bi8		
Sr ₃ LaNiNbO ₆	C	7.95				Bi8		
La ₃ LiNbO ₆	T	7.80		8.28		Bi8		
Ca ₃ AlNbO ₆	O	5.382	5.408	7.614		Fi8		
Ca ₃ VNbO ₆	O	5.44	5.51	7.77		Ch9		
Ca ₃ CrNbO ₆	O	5.418	5.494	3.858		Fi8		
Ca ₃ MnNbO ₆	O	5.44	5.55	7.74		Ha32		
Ca ₃ FeNbO ₆	O	5.451	5.551	3.881		Fi8		
Ca ₃ YNbO ₆	O	5.580	5.819	8.046		Fi8		
Ca ₃ InNbO ₆	O	5.532	5.715	7.913		Fi8		
Ca ₃ LaNbO ₆	O	5.652	5.866	8.140		Fi8		
Ca ₃ PrNbO ₆	O	5.623	5.866	8.116		Fi8		
Ca ₃ NdNbO ₆	O	5.612	5.858	8.104		Fi8		
Ca ₃ SmNbO ₆	M	5.590	5.860	8.090		Fi8		
Ca ₃ GdNbO ₆	M	5.572	5.841	8.080	$\beta = 90^\circ 10'$	Fi8		
Ca ₃ TbNbO ₆	O	5.571	5.830	8.072		Fi8		
Ca ₃ DyNbO ₆	O	5.580	5.819	8.062		Fi8		
Ca ₃ HoNbO ₆	O	5.580	5.812	8.050		Fi8		
Ca ₃ ErNbO ₆	O	5.575	5.794	8.020		Fi8		
Ca ₃ YbNbO ₆	O	5.571	5.769	8.000		Fi8		
Pb ₃ AlNbO ₆	C	10.53				Is2	Defect pyrochlore type P & S [Ag1, Ve4]	
Pb ₃ Sc _{0.5} Cr _{0.5} NbO ₆	T	4.074				T01	Dielectric properties [J03, Sm18, Te8v], S.S. with Pb(Ti, Zr, Hf)O ₃ [J03], crystal growth [Ga5]	
Pb ₃ CrNbO ₆	C	10.54				F111	Possible rhombohedral distortion	
Pb ₂ MnNbO ₆	C	4.023				F111	Defect pyrochlore type P & S [Ha32], S.S. with Fe and PbTiO ₃ [Ha31]	

Compound	Sym	a Å	b Å	c Å	angle °	Ref.	Remarks	Magnetic Data
A₂⁺BNb₆⁺O₆ (continued)								
Pb ₂ FeNbO ₆	R	4.014			$\alpha = 89^\circ 55'$	Ku10	P & S [Ro8], S.S. with BiFeO ₃ [Sm12, Is8, Yw2], complete structure [Pl3], crystal growth [Ga5], dielectric properties [Kh8, Sm25, Sm16, Bo8, Sh32, Sk1, Sh33], optical spectra [Pi5], B site ordering [Yw9], S.S. with Ta [Sh33]	6
Pb ₂ CoNbO ₆	C	8.084				Ro8	Dielectric properties [Ku10, Ag1, Ve4]	6
Pb ₂ NiNbO ₆	C	4.030				Ku10	Dielectric properties [Ku10] with 5% Ba [Sh32]	6
Pb ₂ GaNbO ₆	C	10.65				Fi11	High pressure preparation, no dimension [To11a]	6
Pb ₂ YNbO ₆	C	4.110				Ku9	Pyrochlore type	
Pb ₂ InNbO ₆	C	5.86				Ku10	Dielectric properties [Ku10]	
Pb ₂ HoNbO ₆	O	5.858				Fi11	Cubic $T > 280$ °C, dielectric properties [Sm25, Ku9, Ku10, Ag1, Is17], S.S. with PbFe _{1/3} W _{1/3} O ₃ [To5, To11, Ro17]	
Pb ₂ TmNbO ₆	O	5.848				Ku9	Cubic $T > 280$ °C, dielectric properties [Ku9, Ku10, Is17]	
Pb ₂ YbNbO ₆	O	5.850				Vi3	Defect pyrochlore type	
Pb ₂ LuNbO ₆	O	5.902				Vi5	Dielectric properties [Ve4, Vi5]	
Pb ₂ BiNbO ₆	M	10.777				Vi5	Dielectric properties [Ve4, Vi5]	
Pb ₂ Mg _{0.5} Mn _{0.5} NbO ₆	C	4.018				Vi5	Dielectric properties [Ve4, Vi5]	
Pb ₂ Co _{0.5} Mn _{0.5} NbO ₆	C	4.020				Vi5	Dielectric properties [Ve4, Vi5]	
Pb ₂ Ni _{0.5} Mn _{0.5} NbO ₆	C	4.018				Vi5	Dielectric properties [Ve4, Vi5]	
Pb ₂ Zn _{0.5} Mn _{0.5} NbO ₆	C	4.028				Vi5	Dielectric properties [Ve4, Vi5]	
Pb ₂ Cd _{0.5} Mn _{0.5} NbO ₆	C	4.060				Ro8	Dielectric properties [Ve4, Vi5, Ro8, Ve4]	6
A ₃ ⁺ BSb ₆ ⁺ O ₆								
Ba ₂ ScSbO ₆	C	8.197				Si6	Not perovskite [Bl8]	
Ba ₂ CsSbO ₆						Bl8	Not perovskite [Bl8]	
Ba ₂ MnSbO ₆						Bl8	Hex (6L), P & S [Si6, Bl8]	6
Ba ₂ FeSbO ₆						Bl8	Hex (6L)	
Ba ₂ CoSbO ₆						Bl8	Not perovskite [Bl8]	
Ba ₂ NiSbO ₆						Bl8	Hex (6L)	
Ba ₂ RhSbO ₆						Bl8	P & S [Bl3, Bl8]	
Ba ₂ InSbO ₆						Bl8	P & S [Bl3, Bl8]	
Ba ₂ GdSbO ₆						Bl8	P & S [Si6, Bl8]	
Sr ₂ CrSbO ₆						Bl8	P & S [Si6, Bl8]	6
Sr ₂ MnSbO ₆						Bl8	P & S [Si6, Bl8]	6
Sr ₂ FeSbO ₆						Bl8	P & S [Si6, Bl8]	6
Sr ₂ CoSbO ₆						Bl8	Not single phase (no dimensions)	6
Sr ₂ NiSbO ₆						Bl8		

3.1 ABX₃ Perowskit-Struktur

[Lit. S. 275]

Sr₂NiSbO₆

T

B18

Not single phase (no dimensions)

Compound	Sym	α Å	b Å	c Å	angle °	Ref.	Remarks	Magnetic Data
$A_3^2 + B Sb^3 + O_6$ (continued)								
Sr ₂ GaSbO ₆	T	7.84	7.91			Si16		
Sr ₂ RhSbO ₆	O	5.55	7.99			B18		
Ca ₂ PesbO ₆	O	5.47	7.74			B14/4		
SrLaMgSbO ₆	C	7.99				B18		
SrLaCoSbO ₆	C	7.93				B18		
SrLaNiSbO ₆	C	7.80				B18		
SrLaCuSbO ₆	T			8.35				
$A_3^2 + B Ta^5 + O_6$								
Ba ₂ AlTaO ₆	C	8.220				Fi10	No compound [Ag1, Sm8] Dielectric properties [Ag1, Br13, Br14], P & S	
Ba ₂ ScTaO ₆	C	8.104				Si15	[Ga15]	
Ba ₂ VTaO ₆	H					Si1	P & S [Ch10]	
Ba ₂ CrTaO ₆	C	4.076				Fi15	Hex (6L) no dimensions	
Ba ₂ MnTaO ₆	C	4.048				Fi15	P & S [Si1]	
Ba ₂ FeTaO ₆	C					Fi15	P & S [Ga12], dielectric properties [Ag1], S.S. with BaTiO ₃ [Na9]	
Ba ₂ NiTaO ₆	C	8.152				Si1		
Ba ₂ YTaO ₆	C	8.424				Fi10	P & S [Ag1, Br13, Br14, Fi5, La9], doped with Nd, Sm, Yb [Ga15]	
Ba ₂ InTaO ₆	C	8.282				Si1	P & S [Ag1, Ga15] doped with Nd, Sm, Yb [Ga15]	
Ba ₂ BaTaO ₆ ^a	C	8.70				Fi10	P & S [Br13], doped with Nd [Ga15], cubic > 300 °C	
Ba ₂ LaTaO ₆	R	6.07				Fi13	P & S [Br13], doped with Nd [Ga15], cubic > 300 °C	
Ba ₂ PrTaO ₆	R	6.05				Fi15	[Fi15]	
Ba ₂ NdTaO ₆	R	6.04				Fi10	P & S [Br13, Fi5] cubic $T > 300$ °C [Fi5]	
Ba ₂ SmTaO ₆	R	6.01				Fi10	P & S [Br13, Fi5] cubic $T > 300$ °C [Fi5]	
Ba ₂ EuTaO ₆	C	8.486				Fi10	P & S [Ga15]	
Ba ₂ GdTaO ₆	C	8.470				Fi10	Doped with Nd [Ga15]	
Ba ₂ TbTaO ₆	C	8.440				Fi10		
Ba ₂ DyTaO ₆	C	8.420				Fi10	P & S [Ga15]	
Ba ₂ HoTaO ₆	C	8.416				Fi10	P & S [Ga15]	
Ba ₂ ErTaO ₆	C	8.398				Fi10	P & S [Ga15]	
Ba ₂ TmTaO ₆	C	8.388				Fi10	P & S [Ga15]	
Ba ₂ YbTaO ₆	C	8.378				Fi10	P & S [Ga15], dielectric properties [Ag1]	
Ba ₂ LuTaO ₆	C	8.354				Si1	P & S [Ga15], doped with Nd [Ga15]	
Ba ₂ TiTaO ₆	C	8.42				Ve2	Dielectric properties [Vz3, Ve3]	
Ba ₂ BTaO ₆	R	6.047				Fi10	P & S [Si1], B-B' ordering [Si1]	
Sr ₂ AlTaO ₆	C	7.786						

3.1 ABX₃ Perowskit-Struktur

[Lit. S. 275]

Compound	Sym	α Å	b Å	c Å	angle	Ref.	Remarks	Magnetic Data
A ²⁺ -BTa ₃ O ₆ (continued)								
Sr ₂ VTaO ₆	C	3.967				Ch10 Na7	P & S [Ro20], S.S. with Fe [Na7]	
Sr ₂ CrTaO ₆	C	3.94				Ku12 Ku7	P & S [Ku12, Si1, Na5, Na7], B-B' ordering [Si1, Be5], S.S. with SrTiO ₃ and Ba ₂ FeTaO ₆ [Na5, Be5], S.S. with BaTiO ₃ [Na5]	6
Sr ₂ MnTaO ₆	C	3.994						
Sr ₂ FeTaO ₆	T	3.960						
Sr ₂ GaTaO ₆	C	3.973				Ku7 Si1	Cubic at 250 °C [Ku7, Na5, Na6]	
Sr ₂ SrTaO ₆ s	C C	7.892 8.34			$\alpha = 59^\circ 46'$	Ga13 Ru12	P & S [Br13]	
Sr ₂ YTaO ₆	R	5.837				Si1	P & S [Si1]	
Sr ₂ RhTaO ₆	C	7.936				Fi10	P & S [Br13]	
Sr ₂ InTaO ₆	C	8.110				Ku12	P & S [Ku12]	
Sr ₂ LaTaO ₆	T	5.953				Fi10	P & S [Ku12]	
Sr ₂ PrTaO ₆	M	5.87	5.98	8.357	$\beta = 90^\circ 9'$	Fi10	P & S [Ku12]	
Sr ₂ NdTaO ₆	M	5.86	5.96	8.34	$\beta = 90^\circ 9'$	Fi10	P & S [Ku12]	
Sr ₂ SmTaO ₆	M	5.85	5.93	8.31	$\beta = 90^\circ 11'$	Fi10	P & S [Ku12]	
Sr ₂ EuTaO ₆	M	5.84	5.91	8.30	$\beta = 90^\circ 12'$	Fi10	P & S [Ku12]	
Sr ₂ GdTaO ₆	M	5.83	5.90	8.29	$\beta = 90^\circ 13'$	Fi10	P & S [Ku12]	
Sr ₂ TbTaO ₆	M	5.82	5.88	8.28	$\beta = 90^\circ 9'$	Fi10	P & S [Ku12]	
Sr ₂ DyTaO ₆	M	5.82	5.87	8.26	$\beta = 90^\circ 8'$	Fi10	P & S [Ku12]	
Sr ₂ HoTaO ₆	M	5.81	5.85	8.23	$\beta = 90^\circ 8'$	Fi10	P & S [Ku12]	
Sr ₂ ErTaO ₆	M	5.80	5.84	8.23	$\beta = 90^\circ 4'$	Fi10	P & S [Ku12]	
Sr ₂ TmTaO ₆	C	8.20				Fi10	Slight distortion	
Sr ₂ YbTaO ₆	C	8.196				Ku12	P & S [Si1]	
Sr ₂ LuTaO ₆	C	8.18				Fi10	Slight distortion	
Sr ₂ LaCoTaO ₆	C C	7.99				Bl8	P & S [Si1]	
Sr ₂ LaNiTaO ₆	T	7.95				Bl8	P & S [Si1]	
Sr ₂ LaCuTaO ₆	T	7.80				Fi8	P & S [Si1]	
Ca ₂ AlTaO ₆	O O O O O O	5.381	5.407	8.28		Ch9	P & S [Si1]	
Ca ₂ YTaO ₆	O O O O O O	5.45	5.49	7.612		Fi8	P & S [Si1]	
Ca ₂ CrTaO ₆	O O O O O O	5.418	5.491	7.76		Fi8	P & S [Si1]	
Ca ₂ MnTaO ₆	O O O O O O	5.462	5.571	3.857		Fi8	P & S [Si1]	
Ca ₂ FeTaO ₆	O O O O O O	5.451	5.560	3.873		Fi8	P & S [Si1]	
Ca ₂ YTaO ₆	O O O O O O	5.580	5.819	3.880		Fi8	P & S [Si1]	
Ca ₂ InTaO ₆	O O O O O O	5.531	5.714	3.880		Fi8	P & S [Si1]	
Ca ₂ LaTaO ₆	O O O O O O	5.654	5.890	3.880		Fi8	P & S [Si1]	
Ca ₂ PrTaO ₆	O O O O O O	5.629	5.867	3.880		Fi8	P & S [Si1]	
Ca ₂ NdTaO ₆	O O O O O O	5.616	5.857	3.880		Fi8	P & S [Si1]	
Ca ₂ SmTaO ₆	O O O O O O	5.606	5.853	3.880		Fi8	P & S [Si1]	

3.1 ABX_3 perovskite structure

$\text{Ca}_2\text{SmTaO}_6$	O	5.606	5.853	8.096	F_{i8}^{+}	Possibly lower symmetry
-----------------------------	---	-------	-------	-------	--------------	-------------------------

$\text{Al}^{3+}\text{BTa}^{5+}\text{O}_6$ (continued)						
---	--	--	--	--	--	--

Compound	Sym	a Å	b Å	c Å	angle	Ref.	Remarks	Magnetic Data
$\text{Ca}_2\text{GdTaO}_6$	M	5.572	5.841	8.080	$\beta = 90^\circ 12'$	F_{i8}^{+}		in 3.3.4, Tab.
$\text{Ca}_2\text{TbTaO}_6$	M	5.574	5.833	8.076	$\beta = 90^\circ 12'$	F_{i8}^{+}		
$\text{Ca}_2\text{DyTaO}_6$	O	5.582	5.820	8.064		F_{i8}^{+}		
$\text{Ca}_2\text{HoTaO}_6$	O	5.586	5.811	8.054		F_{i8}^{+}		
$\text{Ca}_2\text{ErTaO}_6$	O	5.582	5.796	8.033		F_{i8}^{+}		
$\text{Ca}_2\text{YbTaO}_6$	O	5.570	5.772	8.002		F_{i8}^{+}		
$\text{Pb}_2\text{AlTaO}_6$	C	10.51				F_{i11}^{+}		
$\text{Pb}_2\text{ScTaO}_6$	C	4.080				G_{i5}^{+}		
$\text{Pb}_2\text{MnTaO}_6$	C	10.73				F_{i11}^{+}	Defect pyrochlore type, 5% Sr for Pb gives perovskite [Sh32]	6
$\text{Pb}_2\text{FeTaO}_6$	C	4.011				G_{i5}^{+}	P & S [Ag1], crystal growth [Ga5], Prop. [Sh32]	6
$\text{Pb}_2\text{CoTaO}_{6.5}$	C	4.038				K_{i11}^{+}	Dielectric Properties [Ru11, Sh32]	6
Pb_2YTaO_6	C	10.70				F_{i11}^{+}	Defect pyrochlore type	6
$\text{Pb}_2\text{PrTaO}_6$	C	10.75				F_{i11}^{+}	Defect pyrochlore type	6
$\text{Pb}_2\text{NdTaO}_6$	C	10.68				F_{i11}^{+}	Defect pyrochlore type	6
$\text{Pb}_2\text{SmTaO}_6$	C	10.70				F_{i11}^{+}	Defect pyrochlore type	6
$\text{Pb}_2\text{YbTaO}_6$	O	5.85	5.90	8.22		K_{i9}^{+}	Dielectric Properties [Ag1, Is17, Fi11]	6
$\text{Pb}_2\text{LuTaO}_6$	O	5.848	5.899	8.214		K_{i9}^{+}	Cubic $T > 280^\circ\text{C}$; dielectric properties [Is17]	6
$\text{Pb}_2\text{BiTaO}_6$	T	10.686		10.816		V_{i3}^{+}	Distorted defect pyrochlore type	6
$\text{Pb}_2\text{Mg}_{0.5}\text{Mn}_{0.5}\text{TaO}_6$	C	4.015				V_{i5}^{+}	Dielectric properties [V_{i5}^{+}, V_{e4}^{+}]	6
$\text{Pb}_2\text{Ni}_{0.5}\text{Mn}_{0.5}\text{TaO}_6$	C	4.009				V_{i5}^{+}	Dielectric properties [V_{i5}^{+}, V_{e4}^{+}]	6
$\text{Al}^{3+}\text{BB}'\text{O}_6$; $\text{B}' = \text{Bi}^{3+}$, Pa^{5+} , Pu^{6+}								
$\text{Ba}_2\text{LaBiO}_6$	C	8.759				Sc_{i8b}^{+}		
$\text{Ba}_2\text{BiBiO}_6$	C	8.549				Sc_{i8b}^{+}		
$\text{Ba}_2\text{ScPaO}_6$	C	8.860				$Ke5^{+}$		
$\text{Ba}_2\text{SrPaO}_{6.5}$	C	8.718				$Ke5^{+}$		
Ba_2YPaO_6	C	8.596				$Ke5^{+}$		
$\text{Ba}_2\text{InPaO}_6$	C	8.932				$Ke5^{+}$		
$\text{Ba}_2\text{BaPaO}_{6.5}$	C	8.885				$Ke5^{+}$		
$\text{Ba}_2\text{LaPaO}_6$	C	8.800				$Ke5^{+}$		
$\text{Ba}_2\text{CePaO}_6$	C	8.862				$Ke5^{+}$		
$\text{Ba}_2\text{PrPaO}_6$	C	8.840				$Ke5^{+}$		
$\text{Ba}_2\text{NdPaO}_6$	C	8.792				$Ke5^{+}$		
$\text{Ba}_2\text{SmPaO}_6$	C	8.783				$Ke5^{+}$		
$\text{Ba}_2\text{EuPaO}_6$	C	8.770				$Ke5^{+}$		
$\text{Ba}_2\text{GdPaO}_6$	C	8.753				$Ke5^{+}$		
$\text{Ba}_2\text{TdPaO}_6$	C							

3.1 ABX₃ Perowskit-Struktur

[Lit. S. 275]

Compound	Sym	α Å	b Å	c Å	angle	Ref.	Remarks	Magnetic Data
$A^{2+}BB'O_6; B' = Bi^{5+}, Pa^{5+}, Pu^{6+}$ (continued)								
Ba ₂ DyPaO ₆	C	8.740				Kes		
Ba ₂ HoPaO ₆	C	8.730				Kes		
Ba ₂ ErPaO ₆	C	8.716				Kes		
Ba ₂ TmPaO ₆	C	8.692				Kes		
Ba ₂ YbPaO ₆	C	8.678				Kes		
Ba ₂ LuPaO ₆	C	8.666				Kes		
Ba ₂ PuPaO ₆	C	8.748				Kes		
Ba ₂ AmPaO ₆	C	8.793				Kes		
Sr ₂ LuPaO ₆	C	8.462				Kes		
BaSrSrPaO _{6,5}	C	8.784				Kes		
Ba ₂ MnPuO ₆	C	8.32				Aw2		
Ba ₂ InPuO ₆	C	8.50				Aw2		
Ba ₂ LaPuO ₆	C	8.63				Aw2		
Ba ₂ CePuO ₆	C	8.72				Aw2		
Ba ₂ NdPuO ₆	C	8.66				Aw2		
Ba ₂ TiPuO ₆	C	8.06				Aw2		
Ba ₂ ZnPuO ₆	C	8.38				Aw2		
Ba ₂ PbPuO ₆	C	8.58				Aw2		
$A_2^{2+}BMo^{6+}O_6$								
Ba ₂ CaMoO ₆	C	8.355				St32		
Ba ₂ C ₂ MoO ₆	C	8.08				No compound [Pa7]		
Ba ₂ FeMoO ₆	C	4.043				Pa7		
Ba ₂ CoMoO ₆	C	4.022				S.S. with Sr [Ga12]		
Ba ₂ NiMoO ₆	C	3.91				Probably ordered		
Sr ₂ CrMoO ₆	C	7.98				Probably ordered		
Sr ₂ MnMoO ₆	T	7.888				Br14		
Sr ₂ FeMoO ₆	T	7.909				Br14		
Sr ₂ CoMoO ₆	T	5.581				Ga12		
Sr ₂ NiMoO ₆	T	7.918				P & S [Pa7], Prop. [Ga12, Na4], S.S. with Ba and Ca [Ga12], neutron diffraction [Na11]		
Sr ₂ CrMoO ₆	T	5.560				P & S [Br14]		
Sr ₂ ZnMoO ₆	C	7.878				Ku8		
Sr ₂ FeMoO ₆	T	5.561				Ku8		
Sr ₂ CoMoO ₆	C	7.954				Ku8		
Sr ₂ ZnMoO ₆	T	7.966				Ku8		
						Cubic at 420 °C; no dielectric anomaly		
						[Ku8]		
						Cubic at 230 °C [Ku8, No3], no dielectric anomaly		
						[Ku8]		
						Cubic at 230 °C [Ku8, No3], no dielectric anomaly		
						[Ku8]		
						Cubic at 420 °C; no dielectric anomaly		
						[Ku8]		

3.1 ABX₃ perovskite structure

Compound	Sym	<i>a</i> Å	<i>b</i> Å	<i>c</i> Å	angle °	Ref.	Remarks	Magnetic Data
<i>A</i> ₂ ⁺ BMo ₆ ⁶⁻ O ₆ (continued)								
Ca ₂ CrMoO ₆	0	5.36	5.49	7.70	7.73	Pa7 Pa7		in 3.3.4, Tab. 6
Ca ₂ FeMoO ₆	0	5.42	5.53					6
<i>A</i> ₂ ⁺ BTe ₆ ⁶⁻ O ₆								
Ba ₂ MgTeO ₆	C	8.13						
Ba ₂ CaTeO ₆	C	8.393						
BaPbMgTeO ₆	C	8.08						
Sr ₂ MgTeO ₆	C	7.94						
SrPbMgTeO ₆	C	7.955						
Sr ₂ NiT ₂ O ₆	C	3.95						
Sr ₂ CuTeO ₆	T	7.680						
Ca ₂ CaTeO ₆	O	5.55						
Pb ₂ MgTeO ₆	C	7.99						
<i>A</i> ₂ ⁺ BW ₆ ⁶⁻ O ₆								
Ba ₂ MgWO ₆	C	8.099						
Ba ₂ CaWO ₆	C	8.390						
Ba ₂ CrWO ₆	C							
Ba ₂ FeWO ₆	C	8.133						
Ba ₂ CoWO ₆	C	8.098						
Ba ₂ NiWO ₆	C	8.066						
Ba ₂ CuWO ₆	T	7.88						
Ba ₂ ZnWO ₆	C	8.116						
Ba ₂ Sr ₂ WO ₆	C	8.53						
Ba ₂ CdWO ₆	C	8.383						
Ba ₂ BaWO ₆	C	8.62						
BaSrMgWO ₆	C	8.02						
Ba _{1.5} Ca _{0.5} Ca ₂ WO ₆	C	8.387						
BaSrCaWO ₆	C	8.29						
BaCaCa ₂ WO ₆	C	8.363						
BaSrZnWO ₆	C	8.07						
BaCaZnWO ₆	C	8.38						
Sr ₂ MgWO ₆	C	7.8						
Sr ₂ CaWO ₆	C	8.2						
Sr ₂ CrWO ₆	C	7.82						
Sr ₂ MnWO ₆	C	8.01						
Sr ₂ FeWO ₆	C	7.96						

Goodenough/Longo

179

3.1 ABX₃ Perowskit-Struktur

[Lit. S. 275]

Compound	Sym	a Å	b Å	c Å	angle °	Ref.	Remarks	Magnetic Data
<i>A₂⁺BW₆⁺O₆</i> (continued)								
Sr ₂ CoWO ₆	T	7.89		7.98		F _r 14	P & S [Br'4], Prop. [No1, Ku8, Bl2, B14] Ku8 $T \approx 400$ °C, cubic $T > 400$ °C; no dielectric anomaly	in 3.3.4, Tab. 6
Sr ₂ NiWO ₆	T	7.904 7.86		7.91		F _r 14	P & S [Br'4], Prop. [No1, Bl2, Bl4, No2, V _e 1, No2, Refa], S.S. with LaFeO ₃ [Sm23], S.S. with Ba [No2], ESR [No4], S.S. with Ca [Re4] $T \approx 300$ °C [Ku8, No4]	6
Sr ₂ CuWO ₆	C	7.908		8.40		Ku8	P & S [Ka12], dielectric properties [V _e 2]	6
Sr ₂ ZnWO ₆	T	7.66 7.92		8.01		Bl8	P & S [Ku8, Be18], S.S. with Ba, cubic $> 40\%$ Ba	
Sr ₂ SrWO ₆	C	7.956				F _r 14	$T \approx 430$ °C, cubic $T > 430$ °C [Ku8, Fr14], no dielectric anomaly [Ku8]	
SrCaMgWO ₆	C	8.3				Be18	Distorted, P & S [Si32]; cubic $T > 1100$ °C, S.S. with Ca [Ch3]	
SrCaCaWO ₆	C	7.87				Be18	Distorted, P & S [Si32]	
Ca ₂ MgWO ₆	C	8.1				St32	Distorted, P & S [Be18]	
Ca ₂ CaWO ₆	C	7.75				St32	Distorted, P & S [Be18]; not cubic $T < 1500$ °K, S.S. with Sr [Ch3, Ch4]	
Ca ₂ CrWO ₆	O	8.02				Pa7	Prop. [Bl2, Ki7]	
Ca ₂ CoWO ₆	O	5.35		5.47	7.70	Bl8	Optical properties [Re4a]	
Ca ₂ NiWO ₆	O	5.43		5.60	7.73	Bl8	Not perovskite [Bl8]	
Ca ₂ CuWO ₆	O	5.40		5.55	7.70	Be8	Dielectric properties [Sm8, Ag1, Sm13, Kh5, Mi1a, Kh6, St42], piezoelectric properties, S.S. with Ti, Zr [Si34], S.S. with Cd [Is15], S.S. with PbFe _{0.5} W _{1.5} O ₆ [Sm10], S.S. with PbTiO ₃ , Ca ₂ MgWO ₆ , Pb ₂ MgNb ₂ O ₉ [Sm20, Si35]	6
Pb ₂ MgWO ₆	C	8.0				Be8	Distorted, dielectric properties [Ag1]	
Pb ₂ CaWO ₆	C	4.2				Ve3	Prop. [Ve2, Ve4, Ro8]	
Pb ₂ MnWO ₆	O	5.736		5.756	8.066	Bo10	Prop., no cell dimensions [Ve4]	6
Pb ₂ FeWO ₆	O	5.661		5.676	9.976	Bo10	P & S [Fi11, Be18], Prop. [Te13, Bo10, K17, Fi16], B site ordering [Yu9], S.S. with BaTiO ₃ [T _{o2}]	6
Pb ₂ NiWO ₆	C	8.017				Fi6	$T \approx 20$ °C, cubic $T > 20$ °C	
Pb ₂ NiWO ₆	C	7.997				No6	Dielectric properties, P & S [T _{o11a} , T _{o11b}]	6
Pb ₂ CdWO ₆	C	8.006				No6	$T = 173$ °K – tetragonal below 290 °K	
Pb ₂ CdWO ₆	C	4.1				Be18	Distorted, dielectric properties [Ro6], S.S. with Mg [Is15]	
Pb ₂ (Li _{1/2} Nb _{1/2} W _{1/2})O ₃ [Di5]	C	4.15				Fi7	Cubic at 400 °C, transformations [Po8], S.S. with Pb (Li _{1/2} Nb _{1/2} W _{1/2})O ₃ [Di5]	

3.1 ABX₃ perovskite structure

Compound	Sym	<i>a</i> Å	<i>b</i> Å	<i>c</i> Å	angle	Ref.	Remarks	Magnetic Data
<i>A</i> ³⁺ BW ⁶⁺ O ₆ (continued)								
Pb ₂ Na _{0.5} Sc _{0.5} WO ₆	T	8.104				V _{e4}	Dielectric properties, no cell dimensions	in 3.3.4, Tab.
Pb ₂ Na _{0.5} Fe _{0.5} WO ₆	T	8.202				V _{e4}	Dielectric properties, no cell dimensions	
Pb ₂ Na _{0.5} YD _{0.5} WO ₆	T	8.082				V _{e4}	Dielectric properties, no cell dimensions	
Pb ₂ Mg _{0.5} Mn _{0.5} WO ₆	T	8.018				V _{i5}	Dielectric properties [V _{i5} , V _{e4}]	6
Pb ₂ Co _{0.5} Mn _{0.5} WO ₆	T					V _{i5}	Dielectric properties [V _{i5} , V _{e4}]	6
Pb ₂ Ni _{0.5} Mn _{0.5} WO ₆	C					No cell dimensions, Prop. [V _{i5} , V _{e2} , V _{e3} , V _{e4}]		
Pb ₂ Li _{0.5} Fe _{0.5} WO ₆	C	8.008				V _{e3}	Dielectric properties [V _{i5} , V _{e2} , V _{e3} , V _{e4}]	6
Pb ₂ Li _{0.5} Co _{0.5} WO ₆	C	4.013				V _{e3}	Dielectric properties [V _{i5} , V _{e2} , V _{e3} , V _{e4}]	6
Pb ₂ Li _{0.5} La _{0.5} WO ₆	C	8.04				V _{i5}	Dielectric properties [V _{i5} , V _{e2} , V _{e3} , V _{e4}]	6
Pb ₂ Li _{0.5} YD _{0.5} WO ₆	C	4.100				V _{e3}	Dielectric properties [V _{i5} , V _{e2} , V _{e3} , V _{e4}]	6
Pb ₂ Li _{0.5} YD _{0.5} WO ₆	C					V _{e4}	Dielectric properties, no cell dimensions	
Pb ₂ Li _{0.55} Mn _{0.45} WO ₆	C					V _{e4}	Dielectric properties, no cell dimensions	
Pb ₂ Li _{0.55} Zr _{0.45} WO ₆	C					V _{e4}	Dielectric properties, no cell dimensions	
Pb ₂ Li _{0.55} Hf _{0.45} WO ₆	C					V _{e3}	Dielectric properties, no cell dimensions	
Pb ₂ YD _{0.5} WO ₆	C	4.124				R ₀₈	Dielectric properties [V _{e2} , V _{e3} , V _{e4}]	6
Pb ₂ FeMn _{0.5} WO ₆	C	4.037						
<i>A</i> ³⁺ BReO ₆ , Re ³⁺ and Re ⁶⁺								
Ba ₂ MgReO ₆	C	8.082				S ₁₈	P & S [L _{o2} , Sc ₁₈], single crystal [S ₁₇]	
Ba ₂ CaReO ₆	C	8.356				S ₁₈	P & S [L _{o2} , Sc ₁₈]	
Ba ₂ ScReO ₆	C	8.163				S ₁₈	P & S [Sc ₁₈]	
Ba ₂ MnReO ₆	C	8.118				S ₁₈	P & S [L _{o2} , Wa ₁₅], single crystal + Prop. [S ₁₇]	6
Ba ₂ FeReO ₆	C	8.05				S ₁₈	P & S [L _{o2} , Wa ₁₅], single crystal + Prop. [S ₁₇]	6
Ba ₂ CoReO ₆	C	8.086				S ₁₈	[Ba ₂] _a suggests Ba ₂ Fe _{1+x} Re _{1-x} O ₆	6
Ba ₂ NiReO ₆	C	8.04				S ₁₈	P & S [L _{o2} , Wa ₁₅], single crystal + Prop. [S ₁₇]	6
Ba ₂ ZnReO ₆	C	8.106				S ₁₈	P & S [L _{o2}]	6
Ba ₂ SrReO ₆	T	8.60				S ₁₈	P & S [L _{o2}]	6
Ba ₂ YReO ₆	C	8.372				S ₁₈	P & S [L _{o2}]	
Ba ₂ CdReO ₆	C	8.322				S ₁₈	P & S [Sc ₁₈]	
Ba ₂ InReO ₆	C	8.258				S ₁₈	P & S [Sc ₁₈]	
Ba ₂ BaReO ₆	T	8.65				Ba ₂₅₄	Prep. 900 °C, α_0 increases with prep. temperature	6
Ba ₂ LaReO ₆	C	8.547					suggesting Ba ₂ Re _{1-x} Re _x ⁶⁺ La _{1-x} Ba _x O ₆ ;	
Ba ₂ NdReO ₆	C	8.51				S ₁₈	P & S [S ₁₈]	
Ba ₂ SmReO ₆	C	8.458				Ba ₂₅₄		
Ba ₂ EuReO ₆	C	8.438				S ₁₈	Prop. [L _{o2}], P & S [Sc ₁₈]	
Ba ₂ GdReO ₆	C	8.431				Ba ₂₅₄		
Ba ₂ TbReO ₆	C	8.399						

3.1 ABX₃ Perowskit-Struktur

[Lit. S. 275]

Compound	Sym	a Å	b Å	c Å	angle °	Ref.	Remarks	Magnetic Data
$A_2^{3+}BReO_6$, Re^{5+} and Re^{6+} (continued)								
Ba ₂ DyReO ₆	C	8.391						Ba25a
Ba ₂ HoReO ₆	C	8.375						Ba25a
Ba ₂ ErReO ₆	C	8.354						Sl8
Ba ₂ TmReO ₆	C	8.342						Ba25a
Ba ₂ YbReO ₆	C	8.329						Ba25a
Ba _{2-x} Sr _x YbReO ₆	C	8.230						Ba25a
BaSrFeReO ₆								
Ba ₂ YReO ₆	T	7.88	5.85		7.94			Sl8
Sr ₂ MgReO ₆	O	5.76			8.21			Sl8
Sr ₂ CaReO ₆	C	8.02						Sl8
Sr ₂ ScReO ₆	C	7.82						distorted
Sr ₂ CrReO ₆	C	8.01						6
Sr ₂ MnReO ₆	C	7.86						6
Sr ₂ FeReO ₆	T	7.86						distorted
Sr ₂ CoReO ₆	T	7.88						P & S [L _o 2, Wa15]
Sr ₂ NiReO ₆	T	7.85						Sl8
Sr ₂ ZnReO ₆	T	7.89						Sl8
Sr ₂ GaReO ₆	C	7.843						Sl8
Sr ₂ SiReO ₆	T	8.41						Sl8
Sr ₂ YReO ₆	C	8.197						P & S [Sc18]
Sr ₂ CdReO ₆	O	5.73	5.81		8.13			Ba25b
Sr ₂ InReO ₆	C	8.071						Sl8
Sr ₂ GdReO ₆	C	8.239						Ba25b
Sr ₂ TbReO ₆	C	8.223						Ba25b
Sr ₂ DyReO ₆	C	8.210						Ba25b
Sr ₂ HoReO ₆	C	8.200						Ba25b
Sr ₂ ErReO ₆	C	8.181						Ba25b
Sr ₂ TmReO ₆	C	8.167						Ba25b
Sr ₂ YbReO ₆	C	8.155						Ba25b
Ca ₂ MgReO ₆	O	5.48	5.56		7.77			Sl8
Ca ₂ CaReO ₆	O	5.67	5.78		8.05			Sl8
Ca ₂ ScReO ₆	O	5.49	5.63		7.86			P & S [Sc18]
Ca ₂ CrReO ₆	O	5.38	5.47		7.67			Sl8
Ca ₂ MnReO ₆	O	5.52	5.55		7.82			Sl8
Ca ₂ FeReO ₆	O	5.41	5.53		7.69			Sl8
Ca ₂ CoReO ₆	O	5.46	5.58		7.71			Sl8

3.1 ABX₃ perovskite structure

Compound	Sym	<i>a</i> Å	<i>b</i> Å	<i>c</i> Å	angle	Ref.	Remarks	Magnetic Data
<i>A</i> ²⁺ BReO ₆ , Re ⁵⁺ and Re ⁶⁺ (continued)								
Ca ₂ NiReO ₆	O	5.45	5.55	7.67			S18	
Ca ₂ CdReO ₆	O	5.64	5.77	7.99			S18	
Pb ₂ MnReO ₆	O	5.69	5.74	8.024			Ro8	
Pb ₂ MnReO ₆	O	5.67	5.75	8.008			Ro8	
<i>A</i> ²⁺ BOsO ₆								
Ba ₂ MgOsO ₆	C	8.08					S18	
Ba ₂ CaOsO ₆	C	8.362					S18	
Ba ₂ ScOsO ₆	C	8.152					S18	
Ba ₂ MnOsO ₆	H						Hex (6L)	
Ba ₂ FeOsO ₆	H	5.82					Hex (6L)	
Ba ₂ ZnOsO ₆	C	5.76					S18	
Ba ₂ SrOsO ₆	T	8.095					S18	
Ba ₂ CdOsO ₆	T	8.43					S18	
Goodenough/Longo								
Ba ₂ InOsO ₆	C	8.325					S18	
Ba ₂ BaOsO ₆	T	8.224					S18	
Sr ₂ MgOsO ₆	T	8.66					S18	
Sr ₂ CaOsO ₆	C	7.86					S18	
Sr ₂ ScOsO ₆	C	8.21					S18	
Sr ₂ CrOsO ₆	C	8.02					S18	
Sr ₂ FeOsO ₆	C	7.84					S18	
Sr ₂ CoOsO ₆	T	7.85					S18	
Sr ₂ GaOsO ₆	C	7.86					S18	
Sr ₂ SiOsO ₆	T	7.82					S18	
Sr ₂ InOsO ₆	C	8.32					S18	
Ca ₂ CaOsO ₆	OO	8.06					S18	
Ca ₂ CrOsO ₆	OO	5.73					S18	
Ca ₂ CoOsO ₆	O	5.38					S18	
A ²⁺ BUO ₆	O	5.47					S18	
Ba ₂ BeUO ₆	C	8.82					Aw1	Doubtful
Ba ₂ MgUO ₆	C	8.381					S15	
Ba ₂ CaUO ₆	C	8.67					S15	
Ba ₂ ScUO ₆	C	8.49					S15	
Ba ₂ TiUO ₆	C	8.05					Aw1	
Ba ₂ CrUO ₆	C	8.297					S15	Ti ⁴⁺
Ba ₂ MnUO ₆	C	8.52					S15	Also prepared as Hex (6L)
Ba ₂ FeUO ₆	C	8.312					S15	P & S [Aw1]
Ba ₂ CoUO ₆	C	8.372					S15	Prop. [D15]

3.1 ABX₃ Perowskit-Struktur

[Lit. S. 275]

Compound	Sym	a Å	b Å	c Å	angle	Ref.	Remarks	Magnetic Data
$A_{\frac{3}{2}+}BUO6$ (continued)								
Ba ₂ NiUO ₆	C	8.336			8.84			Si5
Ba ₂ CuUO ₆	T	8.18						Si5
Ba ₂ ZnUO ₆	C	8.397						Si5
Ba ₂ GeUO ₆	C	8.56						Aw1
Ba ₂ SrUO ₆	C	8.84						Doubtful
Ba ₂ YUO ₆	C	8.69						Distorted, P & S [Ru4#]
Ba ₂ ZrUO ₆	C	8.35						Distorted
Ba ₂ RhUO ₆	H	5.84						Aw1
Ba ₂ CdUO ₆	O	6.07						Si5
Ba ₂ InUO ₆	O	8.521						Si5
Ba ₂ InUO _{6.5}	C	8.551						Si5
Ba ₂ BaUO ₆	T	6.285						Ri4
Ba ₂ LaUO ₆	C	8.73						Complete structure determined, P & S [Si5, Ru4]
Ba ₂ CeUO ₆	C	8.87						Distorted
Ba ₂ NdUO ₆	C	8.76						Ce ⁴⁺
Ba ₂ SmUO ₆	C	8.76						Aw1
Ba ₂ EuUO ₆	C	8.68						Aw1
Ba ₂ GdUO ₆	C	8.66						Aw1
Ba ₂ DyUO ₆	C	8.65						Aw1
Ba ₂ HoUO ₆	C	8.65						Aw1
Ba ₂ ErUO ₆	C	8.67						Aw1
Ba ₂ YbUO ₆	C	8.60						Distorted
Ba ₂ LuUO ₆	C	8.57						Aw1
Ba ₂ HfUO ₆	C	8.31						Aw1
Ba ₂ HgUO ₆	C	8.83						Aw1
Ba ₂ PbUO ₆	C	8.85						Doubtful
Ba ₂ SrSrUO ₆	C	8.66						Doubtful
Sr ₂ MgUO ₆	O	8.19						Ru4
Sr ₂ CaUO ₆	O	5.93						Si5
Sr ₂ CrUO ₆	O	8.09						Si5
Sr ₂ MnUO ₆	C	8.28						Distorted
Sr ₂ FeUO ₆	C	8.11						Si5
Sr ₂ CoUO ₆	C	8.19						Distorted
Sr ₂ NiUO ₆	C	8.15						Distorted, optical properties [Re4a]
Sr ₂ SnUO ₆	M	5.959						Complete structure; P & S [Si5, Ru4, Be25, Ip1]
Sr ₂ CdUO ₆	O	5.91	6.03	8.553	β = 90° 11'	Ri4	6	
Sr ₂ InUO ₆	C	8.33	6.01	8.42		Si5	6	
Sr ₂ CaCaUO ₆	O	5.83	6.01	8.36		Si5		

Ref.

Magnetic
Tab.

Remarks

Remarks

Ref.

3.1 ABX₃ perovskite structure

Compound	Sym	<i>a</i> Å	<i>b</i> Å	<i>c</i> Å	angle °	Ref.	Remarks	Magnetic Data
<i>A</i> ³⁺ B ₂ UO ₆ (continued)								
Ca ₂ CaUO ₆	M	5.728	5.958	8.301	$\beta = 90^\circ 33'$	Si4	Complete structure determined, P & S [SI5, Ru4,	in 3.3.4, Tab.
Pb ₂ PbUO ₆	O	13.71	12.36	8.21		Si26	<i>B</i> e25, <i>I</i> p1]	Not perovskite
<i>A</i> ³⁺ B ₂ 'B'O ₆ ; B' = Np ⁶⁺ , Pu ⁶⁺								
Ba ₂ SrNpO ₆	C	8.799						
Ba ₂ BaNpO ₆	C	8.860						
Ba ₂ SrSrNpO ₆	C	8.735						
Ba ₂ SrPuO ₆	C	8.780						
Ba ₂ BaPuO ₆	C	8.840						
Ba ₂ SrSrPuO ₆	C	8.717						
Sr ₂ SrPuO ₆								Not perovskite
<i>A</i> ³⁺ B ₂ 'B'O ₆ ; B' = Tc ⁷⁺ , Re ⁷⁺ , Os ⁷⁺ , Ir ⁺								
Ba ₂ LiTcO ₆	C	8.092						
Ba ₂ NaTcO ₆	C	8.292						
Sr ₂ LiTcO ₆	C	7.84						
Sr ₂ NaTcO ₆	T	8.09						
Ca ₂ Li _{1.5} Co _{0.5}	C							
Ba ₂ LiReO ₆	C	8.118				Si4		
Ba ₂ NaReO ₆	C	8.296				Si4		
Sr ₂ LiReO ₆	C	8.296				Si8		
Sr ₂ NaReO ₆	C	7.87				Si8		
Ca ₂ LiReO ₆	C	8.13				Si8		
Ba ₂ LiOsO ₆	C	7.83				Si8		
Ba ₂ NaOsO ₆	C	8.100				Si8		
Sr ₂ LiOsO ₆	C	8.282				Si8		
Sr ₂ NaOsO ₆	C	7.86				Si8		
Ca ₂ LiOsO ₆	C	8.13				Si8		
Ba ₂ LiAlO ₆	C	7.83				Si8		
Ba ₂ NaAlO ₆	C	8.33				Si6		
Ba ₂ AgIO ₆	C	8.46				Si6		

3.1 ABX₃ Perowskit-StrukturTab. 2c. A₃BB₂O₈ (for H symmetry see Fig. 1c)

Compound	Sym	$\frac{a}{\text{\AA}}$	$\frac{b}{\text{\AA}}$	$\frac{c}{\text{\AA}}$	angle	Ref.	Remarks	Magnetic Data in 3.3.4, Tab.
A ₃ BB ₂ O ₈								
Ba ₃ MgNb ₂ O ₉	H	5.77		7.08		Ga9	P & S [Ga13, Bu8], see Fig. 1(c)	
Ba ₃ CaNb ₂ O ₉	H	5.92		7.25		Ga9	See Fig. 1(c)	
Ba ₃ FeNb ₂ O ₉	C	4.085				Ga9		
Ba ₃ CoNb ₂ O ₉	C	4.09				Ga9	P & S [Ro20, Ag1], dielectric properties [Sm8], optical properties [Re4a]	
Ba ₃ NiNb ₂ O ₉	C	4.074				Ga9	Dielectric properties [Ka12, Ve3]	
Ba ₃ CuNb ₂ O ₉	T	8.04		8.40		Ga9	Cubic > 653 K	
Ba ₃ ZnNb ₂ O ₉	C	8.166				Ga9	P & S [Ga13, Ag1]	
Ba ₃ CdNb ₂ O ₉	C	4.094				Ga9		
Ba ₃ BaNb ₂ O ₉	C	4.168				Ga9		
Ba ₃ CaNb ₂ O ₉	H	6.01		8.0		Ga9	P & S [Bu8], see Fig. 1(c)	
Ba ₃ PbNb ₂ O ₉	C	4.26				Ga9		
Ba ₃ FeNb ₂ O ₉	H	5.66		6.98		Ga9	See Fig. 1(c)	
Sr ₃ MgNb ₂ O ₉	H	5.76		7.16		Ga9	See Fig. 1(c)	
Sr ₃ CaNb ₂ O ₉	T	3.997		4.018		Ga9		
Sr ₃ CoNb ₂ O ₉	C	8.01		6.90		Ga9	P & S [Ag1], optical properties of S.S. with Ba and Ca [Re4a], see Fig. 1(c)	
Sr ₃ NiNb ₂ O ₉	H	5.64				Ka12	Prop. [Ve2]	
Sr ₃ CuNb ₂ O ₉	T	7.888		8.148		Ga9	P & S [Ga13], see Fig. 1(c)	
Sr ₃ ZnNb ₂ O ₉	H	5.66		6.95		Ga9		
Sr ₃ CdNb ₂ O ₉	C	4.089				Bi8	Distorted perovskite	
Ca ₃ CaNb ₂ O ₉	C	3.88				Ag1		
Ca ₃ NiNb ₂ O ₉	C	4.04				Ag1	Dielectric properties [Sm27, Ag1, Ou1, Ou1a, Ou2, Bo5, Is4, Bo16, Be23, Kh5, Kh4, Kh8, Sm14, Sm20, Sm29, Sm8, Cr6b], crystal growth [Ba ₅ , My3], electrooptic effect [Sm29]	
Pb ₃ MgNb ₂ O ₉						Ag1	No cell dimensions	
Pb ₃ MnNb ₂ O ₉	C	4.05				Bo5	Dielectric properties [Bo5, Ag1]	
Pb ₃ CoNb ₂ O ₉	C	4.02				Ag1	Dielectric properties [Ag1, Sm8, Bo5, Is4], crystal growth [Bo5, My3], S.S. with Mg [Sm20, Sm27, Sm14, Is4, Cr6b], S.S. with Pb(Ti, Zr)O ₃ [Bu10], electric effect [Sm29a]	
Pb ₃ ZnNb ₂ O ₉	C	4.05				Bo5	Dielectric properties [Bo5, Kh7, Be23a]	
Pb ₃ Sc _{1/3} W _{1/3} Nb ₂ O ₉	C	4.074				To1	Dielectric properties [Ve4]	
Pb ₃ CdNb ₂ O ₉	C	8.246				To1	Dielectric properties [Ve2, Ve3, Ve4]	

3.1 ABX₃ perovskite structure

Compound	Sym	α Å	b Å	c Å	angle °	Ref.	Remarks	Magnetic Data
A ₃ BB' ₂ O ₉ (continued)								in 3.3.4, Tab.
Ba ₃ MgRu ₂ O ₉	H							
Ba ₃ MgSb ₂ O ₉	H	5.83		14.26		Ca2	Hex (6L), magnetic properties 84 < T < 948 °K, $\Theta_N = 390$ °K [Ca2]	
Ba ₃ CaSb ₂ O ₉	H	5.99		14.84		Bl8	Hex (6L)	
Ba ₃ CoSb ₂ O ₉	H	5.84		14.35		Bl8	Hex (6L)	
Ba ₃ NiSb ₂ O ₉	H	5.82		14.25		Bl8	Hex (6L), optical properties of S.S. with Sr and Nb [Re4a]	
Ba ₃ CuSb ₂ O ₉	H	5.82		14.22		Bl8	Hex (6L)	
Ba ₃ SrSb ₂ O ₉	H	6.15		15.6		Bl8	Hex (6L)	
Ba ₃ BaSb ₂ O ₉	H	6.09		15.9		Bl8	Hex (6L)	
Sr ₂ MgSb ₂ O ₉	C	7.96				Bl8		
Sr ₂ CaSb ₂ O ₉	C	8.17				Bl8		
Sr ₂ CoSb ₂ O ₉	C	7.99				Bl8		
Sr ₂ NiSb ₂ O ₉	C	3.98				Re4a	Cell probably doubled, optical properties [Re4a]	
Sr ₂ CuSb ₂ O ₉	T	7.84		8.19		Bl8	Optical properties [Re4b]	
Sr ₂ SrSb ₂ O ₉	O	5.78		8.34		Bl8		
Sr ₂ La _{0.5} Li _{0.5} Sb ₂ O ₉	O	5.62		8.00		Bl8	Crystal growth [Ga7], see Fig. 1(c)	
Ba ₃ MgTa ₂ O ₉	H	5.782		7.067		Ga10	P & S [Ga8], crystal growth [Ga7], see Fig. 1(c)	
Ba ₃ CaTa ₂ O ₉	H	5.895		7.127		Ga10	See Fig. 1(c)	
Ba ₃ MnTa ₂ O ₉	H	5.819				Ga10	P & S [Ro20], crystal growth [Ga7], optical properties [Re4a], see Fig. 1(c)	
Ba ₃ FeTa ₂ O ₉	C	4.10				Ga10	P & S + Prop. [Ve2, Ve3]	
Ba ₃ CoTa ₂ O ₉	H	5.776				Ga10	P & S [Ga13], crystal growth [Ga7], see Fig. 1(c)	
Ba ₃ NiT ₂ O ₉	H	5.758				Ga10	P & S [Ga13], see Fig. 1(c)	
Ba ₃ CuTa ₂ O ₉	T	8.132		8.432		Ka12	See Fig. 1(c)	
Ba ₃ ZnTa ₂ O ₉	H	5.782		7.097		Ga10	P & S [Ro20], crystal growth [Ga7], see Fig. 1(c)	
Ba ₃ SrTa ₂ O ₉	H	5.95		7.47		Ga11	P & S [Ga13], see Fig. 1(c)	
Ba ₃ CdTa ₂ O ₉	C	4.167				Ga10	See Fig. 1(c)	
Ba ₃ BaTa ₂ O ₉	H	6.10				Ga10		
Ba ₃ PbTa ₂ O ₉	C	4.250				Ga10		
Ba ₃ Zn _{0.5} Ni _{0.5} Ta ₂ O ₉	C	4.08				Ga10		
Sr ₃ MgTa ₂ O ₉	H	5.652		6.951		Ga10	P & S [Ro20], see Fig. 1(c)	
Sr ₃ CaTa ₂ O ₉	H	5.764		7.096		Ga10	See Fig. 1(c)	
Sr ₃ CoTa ₂ O ₉	H	5.630		6.937		Ga10	P & S [Ga13], see Fig. 1(c)	
Sr ₃ NiT ₂ O ₉	H	5.607		6.923		Ga10	P & S [Ga13], see Fig. 1(c)	
Sr ₃ CuTa ₂ O ₉	T	7.860		8.248		Ka12	P & S + Prop. [Ve2, Ve3]	
Sr ₃ ZnTa ₂ O ₉	H	5.664		6.951		Ga10	P & S [Ga13], see Fig. 1(c)	
Pb ₃ MgTa ₂ O ₉	C	4.03		B05		Ga10	Prep. [Ag7], electrooptic effect [Sm29a]	
Pb ₃ CoTa ₂ O ₉	C	4.02		B05		Ga10		
Pb ₃ NiT ₂ O ₉	C	4.02		B05		Ga10	Prep. [Ag1]	

3.1 ABX₃ Perowskit-Struktur

[Lit. S. 275]

Compound	Sym	α Å	b Å	c Å	angle	Ref.	Remarks	Magnetic Data in 3.3.4, Tab.
La ₃ Co ₂ B ³⁺ O ₉	O	5.58	5.58	7.89				
La ₃ Co ₂ NbO ₉	O	5.57	5.57	7.87				
La ₃ Co ₂ SbO ₉								
A ₃ B ₂ B ³⁺ O ₉	H	5.72		14.02				
Ba ₃ Cr ₂ MoO ₉	H	5.74		14.08				
Ba ₃ Fe ₂ MoO ₉	C	4.168						
Ba ₃ In ₂ MoO ₉	C	6.148	6.184	8.642				
Ba ₃ Bi ₂ MoO ₉	O	4.37						
Ba ₃ LiNbMoO ₉	R	4.091						
Ba ₃ LiTaMoO ₉	C	4.090						
Pb ₃ Bi ₂ MoO ₉	T	11.262		11.452				
Ba ₃ Sc ₂ WO ₉	C	8.24						
Ba ₃ Cr ₂ WO ₉	H	5.75						
Ba ₃ Fe ₂ WO ₉	H	5.74						
Ba ₃ Co ₂ WO ₉	H	5.74						
Ba ₃ Y ₂ WO ₉	C	8.374						
Ba ₃ Rh ₂ WO ₉	H	5.74		14.15				
Ba ₃ In ₂ WO ₉	C	8.321						
Ba ₃ L ₂ a ₂ WO ₉	C	8.58						
Ba ₃ Nd ₂ WO ₉	C	8.513						
Ba ₃ Eu ₂ WO ₉	C	8.605						
Ba ₃ Gd ₂ WO ₉	C	8.411						
Ba ₃ Dy ₂ WO ₉	C	8.386						
Ba ₃ Ho ₂ WO ₉	C	4.252						
Ba ₃ Er ₂ WO ₉	C	8.386						
Ba ₃ Yb ₂ WO ₉								
Ba ₃ Lu ₂ WO ₉	R	6.131						
Ba ₃ Bi ₂ WO ₉	R	4.098						
Ba ₃ LiNbWO ₉	R	4.095						
Si ₂ Fe ₂ WO ₉	T	3.945						
Si ₂ La ₂ Mg ₂ WO ₉	C	7.91						
Si ₂ La ₂ Co ₂ WO ₉	C	7.90						
Pb ₃ Sc ₂ WO ₉	C	8.134						
Pb ₃ Mn ₂ WO ₉								
Pb ₃ Fe ₂ WO ₉	C	4.02						
Pb ₃ Bi ₂ WO ₉	T	10.637		10.79				

3.1 ABX₃ perovskite structure

Compound	Sym	a Å	b Å	c Å	angle °	Ref.	Remarks	Magnetic Data
$A_3B_2B''_4O_9$ (continued)								
Pb ₃ ScMnWO ₉	O	5.80	5.90	8.138		Ve4	No cell dimensions	in 3.3.4, Tab.
Pb ₃ CrMnWO ₉	O	5.80	5.90	8.178		Ve4	No cell dimensions	6
Pb ₃ FeMnWO ₉	O	5.80	5.90	8.178		Ve4	No cell dimensions	6
Pb ₃ CdMnWO ₉	O	5.80	5.90	8.178		Ve4	No cell dimensions	6
Pb ₃ CoFeWO ₉	C	8.090	5.813	5.877	13.8	Prop. [Ve4, Ro8]	Prop. [Ve4, Ro8]	6
Pb ₃ LiNbWO ₉	C	8.015	5.70	5.81	14.10	Ve4	Dielectric properties [Ve2, Ve4, Vi5]	6
Pb ₃ Cd _{1/3} Nb _{2/3} WO ₉	H	5.81				Ve4	Dielectric properties [Ve2, Ve4]	6
Ba ₃ Cr ₂ ReO ₉	H	5.81				T ₀₁	Hex (6L)	6
Ba ₃ Fe ₂ ReO ₉	H	5.81				Si8	Hex (6L)	6
Sr ₃ Cr ₂ ReO ₉	C	8.015				Si8	Hex (6L)	6
Sr ₃ Fe ₂ ReO ₉	C	7.890				Si8	Hex (6L)	6
Sr ₃ In ₂ ReO ₉	C	8.297				Si8	Hex (6L)	6
Ba ₃ Sc ₂ UO ₉	C	8.49				Si5	Hex (6L)	6
Ba ₃ Cr ₂ UO ₉	H	5.82				Si5	Hex (6L)	6
Ba ₃ Fe ₂ UO ₉	C	8.232				Si5	P & S [Ro14]	6
Ba ₃ Y ₂ UO ₉	C	8.70				Si5	Slight distortion	6
Ba ₃ In ₂ UO ₉	C	8.512				Si5		6
Sr ₃ Cr ₂ UO ₉	C	8.00				Si5		6
Sr ₃ Fe ₂ UO ₉	C	8.066				Ro14	Prop. [Be5], S.S. with Sr ₃ Fe ₂ WO ₉ [Se6a]	6

Tab. 2d. A²⁺(B_xB'_yB''_z)O₉

Compound	Sym	a Å	b Å	c Å	angle °	Ref.	Remarks	Magnetic Data
Ba[Zn _{0.2} Fe _{0.2} Nb _{0.4}]O ₉								
Ba[Zn _{0.2} Fe _{0.2} Ta _{0.4}]O ₉	C	4.08						Ga13
Sr[Zn _{0.2} Fe _{0.2} Ta _{0.4}]O ₉	C	4.08						Ga13
Ba[Li _{0.25} Nb _{0.55}]O ₉	C	4.01						Ga13
Ba[Na _{0.25} Nb _{0.75}]O ₉	C	4.095						Ka12
Ba[Na _{0.35} Ta _{0.65}]O ₉	C	4.107						Ka12
Ba[Na _{0.35} Ta _{0.75}]O ₉	C	4.137						Ga6
Sr[Na _{0.35} Ta _{0.75}]O ₉	C	4.055						Ga6
Ba[Fe _{0.18} Nb _{0.82}]O ₉	C	4.07						Ga13
Ba[Fe _{0.18} Ta _{0.82}]O ₉	C	4.07						Ga13
Sr[Fe _{0.18} Nb _{0.82}]O ₉	C	3.96						Ga13
Ba[Fe _{1/3} Fe _{2/3} Ta _{4/3}]O ₉	C	4.08						Ga13
Ba[Co _{1/3} Co _{2/3} Ta _{4/3}]O ₉	C	4.09						Ga13
Sr[Co _{1/3} Co _{2/3} Ta _{4/3}]O ₉	C	4.00						Ga13
Ba[Na _{0.4} W _{0.6}]O ₉	C	4.158						Ka12

3.2 Descriptions of perovskite-related structures

3.2.1 A-cation vacancies

3.2.1.1 No A cations

Because a skeleton of shared-corner octahedra is stable, it is possible to remove all the A cations from the perovskite structure without collapsing the $\square BX_3$ subarray. In the case of $\square \text{ReO}_3$, for example, the structure remains cubic. However, a partial or a complete collapse of the skeleton is found in many $\square BX_3$ compounds. The completely collapsed structure has hexagonal-close-packed X layers with one-third of the octahedral sites occupied by B atoms, as indicated in Fig. 19. This results in a simple-cubic array of B cations with corner-shared octahedra having a B-X-B angle of 132° . For comparison, Fig. 19 also shows the corner-shared octahedra across a close-packed $\square X_3$ plane of the cubic $\square \text{ReO}_3$ structure, where the B-X-B angle is 180° . It is possible to go from one structure to the other by a simple increase of the B-X-B angle, the B cations forming a simple-cubic array in all structures. In the partially collapsed structure, represented by CrF_3 , and B-X-B angle is intermediate, $\approx 150^\circ$. Trifluorides of the first-row transition metals have the partially collapsed structure, those of the second- and third-row transition metals have the ReO_3 structure where the number of outer d electrons per cation is ≤ 3 , but the completely collapsed structure where it is ≥ 6 . The B cations of the latter group either have no atomic moment (Rh^{III} and Ir^{III} have $t_{2g}^0 e_g^0$) or disproportionate into magnetic and nonmagnetic ions ($\text{Pd}^{2+}, t_{2g}^6 e_g^2$ and $\text{Pd}^{\text{IV}}, t_{2g}^6 e_g^0$), so that there are no magnetic interactions between neighboring cations. The other trifluorides, on the other hand, are all antiferromagnetic, and coupling between like atoms of the second and third long periods is stronger than that between like atoms of the first long period. Since the B-X-B superexchange interaction is enhanced by a larger B-X-B angle, it is reasonable to assume that the interactions between neighboring B cations stabilizes the ReO_3 structure. These interactions may be either weaker interactions between localized electrons, as in the magnetic fluorides, or stronger interactions, as in metallic ReO_3 . In this connection, stabilization of the cubic structure in the tungsten bronzes $A_x^{\pm m} \text{WO}_3$ for $m > 0.3$ is significant. The conduction electrons introduce cation-anion-cation interactions while simultaneously reducing the energy gained by a ferroelectric distortion.

Electron-ordering distortions may be superposed on the array of corner-shared octahedra. MnF_3 , for example, exhibits the Jahn-Teller distortions shown in Fig. 10(a) superposed on the partially collapsed structure. WO_3 , on the other hand, exhibits several low-temperature phases characteristic of an interplay of antiferroelectric distortions and different degrees of the collapse of the B-X-B angle.

3.2.1.2 The bronze structures

Although $\square BX_3$ compounds with the ReO_3 structure and cubic ABX_3 compounds have the same BX_3 array, complete solid solutions $\square_x A_{1-x} BX_3$, $0 \leq x \leq 1$, are not possible. Although there is no ordering of the vacancies for larger x , except for $\text{Na}_{0.75} \text{WO}_3$ [A1], for smaller x there is ordering accompanied by a collapse of the BX_3 array within basal planes perpendicular to a unique axis. Such a collapse creates the tetragonal and hexagonal tunnel structures of Fig. 20. The tetragonal structure contains three types of tunnels, one containing cubic, twelve-coordinated A' sites, one containing pentagonal-prism, fifteen-coordinated A'' sites, and one small tunnel containing nine-coordinated A''' sites, which are only occupied by Li^+ ions. Without Li^+ ions, all these sites are filled at $A_{0.2}^{\prime\prime} A_{0.4}^{\prime\prime\prime} BX_3$. This phase, which may occur for a

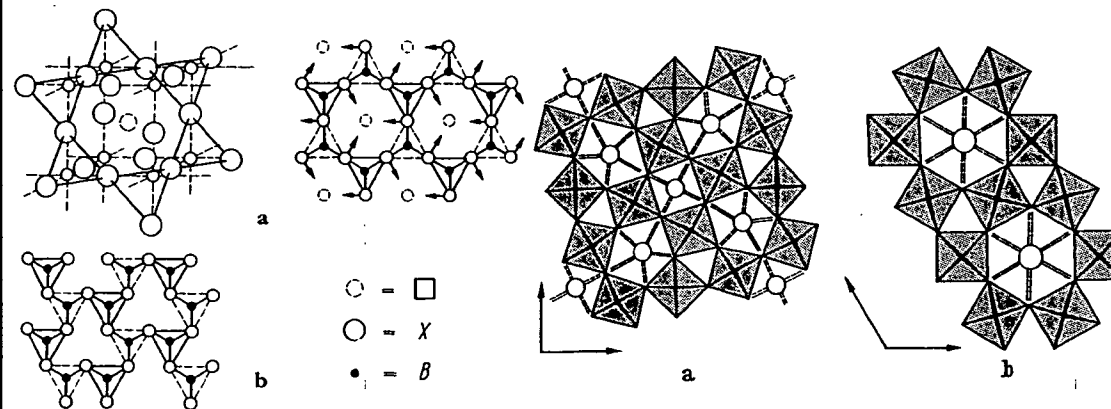


Fig. 19. Projections on B-cation planes of two $\square BX_3$ structures. Triangles in full and dotted lines represent faces of octahedra below or above the B-cation plane. a) Cubic $\square \text{ReO}_3$ structure DO_3 . Arrows indicate cooperative atomic motions that collapse the structure. b) Completely collapsed $\square \text{RhF}_3$ structure.

Fig. 20. Bronze structures found in $A_x \square_{1-x} BX_3$ systems. a) Tetragonal (II) structure occurring for $x \leq 0.6$. b) Hexagonal structure occurring for $x \leq 0.33$ [Wa1].

range of $x \leq 0.6$, is labelled tetragonal (II) in Tab. 3 to distinguish it from the antiferroelectric tetragonal (I) phase of WO_3 . The hexagonal structure contains hexagonal-prism, eighteen-coordinated A sites and is restricted to the range of composition $x \leq 0.33$. An orthorhombic tunnel structure has also been identified for AB_2O_6 compounds [Ga15a].

Tab. 3. Color vs. x for Na_xWO_3 and compositional ranges for the bronze structures in the A^{1+}WO_3 perovskites. Adapted from [Di3]

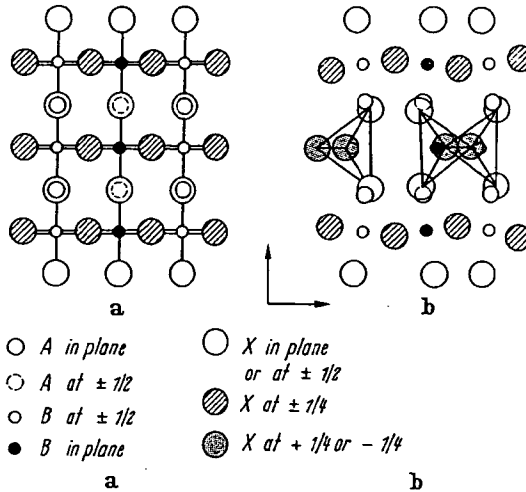
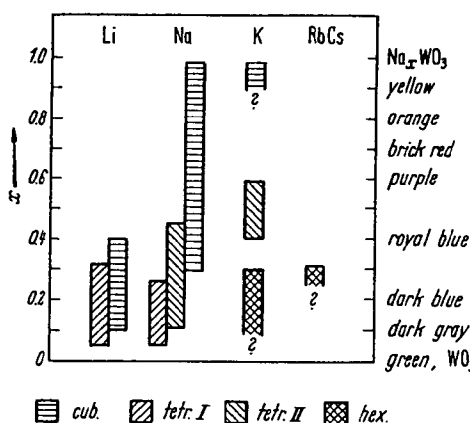


Fig. 21. Projections onto (110) planes of a) cubic perovskite and b) brownmillerite structures. Brownmillerite structure is formed by removing alternate [110] strings of oxygen from central row of a) and regrouping remaining oxygen into the tetrahedra shown in b) [Wa1].

3.2.2 Anion-deficient compounds

3.2.2.1 Compounds ABX_{3-x}

Several systems ABX_{3-x} , where $0 \leq x \leq 0.5$, have been reported as anion-deficient perovskites. $\text{SrTiO}_{2.5}$ and $\text{SrVO}_{2.5}$, for example, both give simple x-ray powder patterns in qualitative agreement with the assumption of a perovskite structure having one-sixth of the anions missing at random. Further, the homogeneity range of SrTiO_{3-x} is reported [Wa1] to extend over $0 \leq x \leq 0.5$ without any change of lattice parameter. However, if an anion is removed from a close packed structure, the metal atoms to which it was formerly bonded will have highly unsymmetrical coordination, and some local rearrangement of the anion can be expected. The nature of this local rearrangement depends upon the character of the B cation. In order to learn what rearrangements may occur locally, it is necessary to examine those special cases where long-range order occurs, since local changes of cation coordination are difficult to detect by x-ray diffraction and have not been investigated by other methods.

In the system $\text{SrFe}^{3+}_{2x}\text{Fe}^{4+}_{1-2x}\text{O}_{3-x}$, $0 \leq x \leq 0.5$, it is known that the Fe^{3+} ions are stable in either tetrahedral or octahedral coordination. Therefore, it is reasonable to anticipate the creation of fourfold coordination about half of the Fe^{3+} ions in the system. This is possible because the d electrons of Fe^{3+} ions are localized, so that Fe^{3+} and Fe^{4+} ions are distinguishable, even though the d electrons of the end member $\text{SrFe}^{4+}\text{O}_3$ appear to be collective. Support for the creation of tetrahedral sites, as well as a suggestion of how the tetrahedra might be arranged, is given by $\text{Ca}_2\text{Fe}_2\text{O}_5$, which has the brownmillerite structure [Be41] of Fig. 21. Within every other (001) BX_2 plane of the cubic perovskite, alternate [110] rows of anions are removed. The remaining anions in these planes are displaced alternately along [110] and [−110] directions toward the anion vacancies, the B cations shifting slightly also to maintain equal B-X distances with all four near-neighbor anions. The result is fourfold coordination for all B cations in these (001) BX_2 planes, sixfold coordination for all B cations in the alternate (001) BX_2 planes.

The x-ray pattern of $\text{K}_2\text{Ti}_2\text{O}_5$ has a strong resemblance to that of perovskite. However, $\text{KTiO}_{2.5}$ is not an anion-deficient perovskite, but is completely ordered, each Ti^{4+} ion having five oxygen near neighbors forming a trigonal bipyramidal [An3]. It has little similarity to perovskite.

The oxygen-deficient, tetragonal compounds $(\text{Ba}_{2x}\text{Bi}_{1-2x})\text{BiO}_{3-x}$, $0.22 < x < 0.5$, retain an octahedral grouping for Bi in the B sites, but the A positions have only six oxygen near neighbors, two each at 2.7, 3.1 and 3.6 Å [An1].

These examples indicate that a variety of orderings must occur in anion-deficient perovskites. Further structural work needs to be done.

3.2.2.2 Alloys $M^cX_{1-x}M^f_s$

Since the alloys $M^cX_{1-x}M^f_s$ are generally considered to represent interstitial X atoms in an ordered, face-centered-cubic $M^cM^f_s$ alloy, it is not surprising that the phase is stable over a considerable range of anion deficiency. Since these alloys are metallic, it is probable that the X-atom vacancies are randomly distributed.

3.2.2.3 Shear structures $\square BO_{3-x}$

Ranges of composition have been reported for BO_{3-x} , where B = Mo or W. MAGNÉLI [Ma14] has shown that these compositional ranges consist of a series of discrete phases having an x-ray diffraction pattern dominated by a cubic $\square ReO_3$ -type (DO_9) subcell, but exhibiting superlattice lines. The superlattice of any discrete phase is not due to an ordering of anion vacancies within this basic structure, but to a regular interruption of the DO_9 structure by planes of discontinuity across which octahedra share edges rather than corners. In these structures the oxygen vacancies condense into regularly spaced planes and are then eliminated by a shear displacement of the type shown schematically in Fig. 22. These "shear" planes may be constituted in different ways: For the series of phases B_nO_{3n-2} , six octahedra in a group share edges, and for the phases B_nO_{3n-1} groups of four octahedra share edges. In both cases the discontinuities continue in two dimensions throughout the structure where they separate DO_9 blocks n octahedra thick. The β - WO_{3-x} phases, $0.10 \leq x \leq 0.17$, belong to the series B_nO_{3n-2} with $12 < n \leq 20$. The observed compositional range (W, Mo)- O_{3-x} , $0.07 \leq x \leq 0.12$, contains six discrete B_nO_{3n-1} phases corresponding to $n = 8, 9, 10, 11, 12$, and 14 [Ma17a]. The origin of the shear planes appears to be an interplay between electrostatic and elastic forces: Electrostatic repulsive energies between B cations sharing common octahedral-site edges is minimized by cationic displacements (of ferroelectric type) away from the center of symmetry of the interstice and the shared octahedral edge. These displacements can be cooperative, costing a minimum of elastic energy, if the shared edges are coplanar. The origin of the regular spacing between planes is not established. Presumably it is primarily due to elastic energy, although collective-electron effects [Go11] probably play a contributing role.

3.2.3 Structures deficient in B cations

3.2.3.1 Bismuth compounds

Bismuth compounds with chemical formula $(Bi_2A_{m-2})B_{m-1}O_{3m}$ have the structural formula $(Bi_2O_2)^{2+}(A_{n-1}B_nO_{3n+1})^{2-}$, $n = m - 1$. These compounds consist of a regular intergrowth of the perovskite structure with Bi_2O_2 sheets consisting of BiO_4 square pyramids sharing edges [Au2], as indicated in Fig. 23. Between the Bi_2O_2 sheets are n layers of corner-shared octahedra and $(n - 1)$ layers of perovskite-type A cations in the twelve-coordinated interstices. Where $n = 1$, the pyramidal sheets alternate with

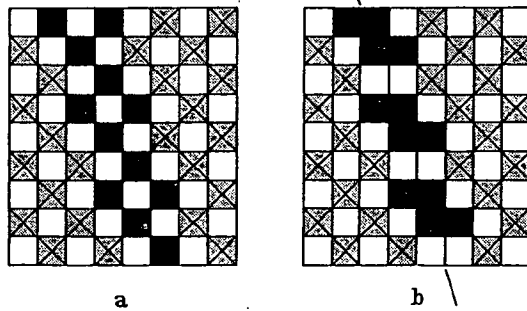


Fig. 22. Projection onto (001) planes of a) cubic $\square ReO_3$ structure and b) B_nO_{3n-1} shear plane. Anions are removed from black octahedra, which then move to adjacent positions to form configuration b) [Wa1].

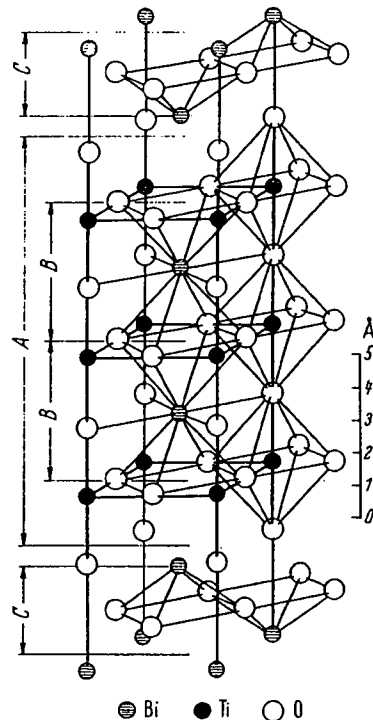


Fig. 23. One half of the pseudo-tetragonal unit cell of $Bi_4Ti_3O_{12}$ (from $x \approx 0.25$ to $x \approx 0.75$). A denotes the perovskite layer $(Bi_4Ti_3O_{12})^{2+}$, C the $(Bi_4O_5)^{2+}$ layers, and B the unit cells of the hypothetical perovskite structure $BiTiO_3$ [Au2].

single octahedral layers, and no sites are available for A cations. This particular phase has been prepared in a large number of oxides and oxyfluorides, where B = Ti, Nb, Ta and the O/F ratio depends upon the valencies of the A and B cations (see Tab. 4).

Many of these compounds are reported to exhibit ferroelectric distortions within the perovskite layers, and they will certainly be important for technical applications in the future.

3.2.3.2 Hexagonal $A_nB_{n-1}X_{3n}$ structures

As shown in Fig. 1(c), the cubic perovskite may be indexed on an hexagonal basis. It consists of cubic stacking of close-packed AX_3 layers with B cations in the all-anion octahedral interstices. Within a (110) plane, B-cation octahedra share common corners as shown schematically in Fig. 3(a). In the $Ba_2Ta_4O_{15}$ structure [Ga5a], the stacking sequence of the AX_3 layers is $a-b-c-b-c-a$, as shown in Fig. 24, and the B-cation vacancies are where the stacking is hexagonal. Thus the structure consists of perovskite blocks n AX_3 layers and $(n - 1)$ B layers thick, separated by a stacking fault at a layer of B-cation vacancies. These hexagonal structures appear to be stabilized where the tolerance factor is $t > 1$.

3.2.3.3 $AX \cdot (ABX_3)_n$ structures

Materials having compositions intermediate between ABX_3 and A_2BX_4 may have similar diffraction patterns. However, this compositional region contains several phases having the structural formula $AX \cdot (ABX_3)_n$. Each phase contains perovskite sheets n units thick separated by AX (NaCl-type) sheets. The limiting composition A_2BX_4 , corresponding to $n = 1$, is shown in Fig. 25. It is important for the theory of magnetism because, if A is nonmagnetic, then by symmetry there is no net molecular field within an antiferromagnetic layer from cations in adjacent antiferromagnetic layers. This permits the study of two-dimensional antiferromagnetism. The A_2BX_4 structure also permits the study of B^{2+} cations in oxides with a smaller B-X-B separation (hence stronger interaction) than is found in the BO compounds with rocksalt structure. The possible significance of this is illustrated by La_2NiO_4 . The Ni^{2+} electrons of ϵ_g symmetry appear to be collective in La_2NiO_4 , localized in NiO.

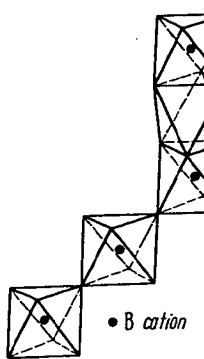


Fig. 24. Schematic (110) projection of the $Ba_2Ta_4O_{15}$ structure. Horizontal lines refer to BaO_3 close-packed layers with stacking a , b , or c .

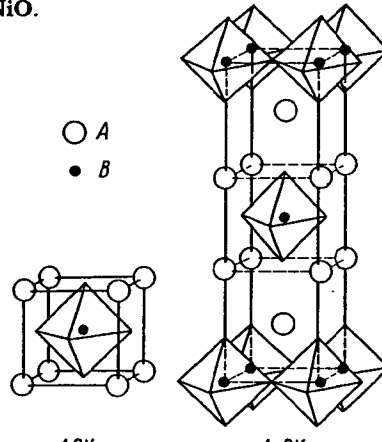


Fig. 25. Comparison of ABX_3 and A_2BX_4 structures [Tr1].

3.2.4 Data: Crystallographic properties of non- ABX_3 compounds of composition A_xBX_3 , $\square BX_3$, $(AX)_n(ABX_3)_m$ and $Bi_2O_2(A_{n-1}B_nO_{3n+1})$ with perovskite-related structure (Tab. 4)

Tab. 4.

See Fig. 20(a) for the tetragonal II bronze structure with $a \approx 12.5 \text{ \AA}$, $c \approx 4 \text{ \AA}$ and Fig. 20(b) for the hexagonal bronze structure with $a \approx 7.4 \text{ \AA}$, $c \approx 7.5 \text{ \AA}$.

Within any section, the compounds are ordered by B-cation atomic number, and the order of the sections is as follows:

Tab. 4a — A_xBX_3
 A_xBO_3 ; B = Nb, Mo, Ta, W, Re
 A_xFeF_3

Tab. 4b — $\square BX_3$

Tab. 4c — $\square BB'X_6$

Tab. 4d — $(AX)_n(ABX_3)_m$

X = F⁻¹, Cl⁻¹; B²⁺ = Mg, Cr, Mn, Fe, Co, Ni, Cu, Zn, Cd

X = O⁻²; B = Al, Ti, Cr, Mn, Fe, Co, Ni, Cu, Ga, Ge, Zr, Nb, Mo, Tc, Ru, Rh, Sn, Hf, Ir, Pb, U

Tab. 4e — $Bi_2O_2(A_{n-1}B_nO_{3n+1})$

$n = 1$; B = Mo, W $n = 2$; B = Nb, Ta $n = 3$; B = Nb, Ti $n = 4, 5$ and 8 ; B = Ti

3.2 Perowskit-ähnliche Strukturen

[Lit. S. 275]

For abbreviations, see p. 131.
Tab. 4a. A_xBX_3 compounds

Compound	Sym	a Å	b Å	c Å	angle	Ref.	Remarks	Magnetic Data
A_xNbO_3								in 3.3.4, Tab.
$Ba_{0.5}NbO_3$	O	12.17	20.5	7.87		F_{r1b}	Structure and review [<i>Ga15a</i>], S. S. with (Pb, Ca, Sr) _{0.5} NbO ₃ [<i>Su4c</i> , <i>F71b</i> , <i>Is3a</i>], dielectric properties [<i>Gr10</i>]	
$Ba_{0.5}NbO_3$	T	12.60		3.95		<i>Ga14</i>		
$Sr_{0.5}NbO_3$	C	4.016				<i>Ri3</i>		
$Sr_{0.5}NbO_3$	C	3.981				<i>Ri3</i>		
$Sr_{0.5}NbO_3$	O	11.021	7.33	5.604		<i>He12a</i>		
$Sr_{0.5}NbO_3$	O	5.764	15.09	5.232		<i>Fr2a</i>		
$Ca_{0.5}NbO_3$	O	17.51	17.81	7.72			Dielectric properties [<i>Go20</i> , <i>Su4g</i>], S. S. with (Ba, Sr)Nb ₂ O ₆ [<i>Ba25c</i> , <i>F71b</i> , <i>Is2a</i> , <i>Kr7</i> , <i>Sm16a</i> , <i>Su4c</i>], P & S [<i>Ro16a</i>], S. S. with Ti, Zr, Sn [<i>Su1a</i> , <i>Su4b</i> , <i>Su4c</i>], S. S. with Li, Na, K, Rb, Cs, Y, La, Sm [<i>Su4b</i> , <i>Su4c</i>]	
$Pb_{0.5}NbO_3$	O						Prep. $T < 1250$ °C	
							$T = 570$ °C	
							P & S [<i>Ke8</i> , <i>Ro13</i> , <i>Sa6a</i>]; dielectric properties, S. S. with K ₂ Si ₂ Nb ₆ O ₁₆ [<i>Bu5</i>]	
							<i>Iy1</i>	
							<i>Ko10</i>	
							<i>Iy1</i>	P & S [<i>Ke8</i> , <i>Ro13</i>]
							<i>Iy1</i>	P & S [<i>Ke8</i> , <i>Ro13</i>]
							<i>Ro13</i>	(Ln = Sm ... Lu) not able to be prepared
							<i>Ke6</i>	P & S [<i>Ke8</i> , <i>Ro13</i>], detailed structure [<i>Tr7</i>]
							<i>Ke6</i>	
							<i>Ke6</i>	P & S [<i>Ko10</i>]
							<i>Ke6</i>	
							<i>Ke6</i>	
							<i>Ke6</i>	
							<i>Ke6</i>	
							<i>Ke6</i>	
							<i>Bu5a</i>	$T_{melt} = 1395$ °C
							<i>Va13</i>	Dielectric and optical properties [<i>Va13</i> , <i>Ge14</i> , <i>Sm6a</i> , <i>Bu5a</i> , <i>Va11a</i>], Raman effect [<i>Bu4b</i>]; S. S. with K [<i>Bu5a</i>], Sr [<i>Va11a</i>]; elastic proper- ties [<i>Sp10</i>], piezoelectric properties [<i>Wa15a</i>]
								Dielectric + optical properties [<i>Gr1a</i> , <i>Bu5</i>]
$Sr_2KNb_6O_{16}$	T	13.47				<i>Gi1a</i>		

3.2 Perovskite-related structures

Compound	Sym	a Å	b Å	c Å	angle °	Ref.	Remarks	Magnetic Data
A_xNbO_3 (continued)								in 3.3.4, Tab.
$Sr_3NaNb_6O_{16}$	O	17.4	17.4	3.90				
$Na_3LaNb_6O_{16}$	C	3.918						
$Na_3BiNb_6O_{16}$	C	3.925						
$K_3Li_2Nb_6O_{16}$	T	12.47						
$K_2LaNb_6O_{16}$	T	12.580						
$K_2CeNb_6O_{16}$	T	12.545						
$K_2PrNb_6O_{16}$	T	12.530						
$K_2NdNb_6O_{16}$	T	12.497						
$K_2SmNb_6O_{16}$	T	12.474						
$K_2EuNb_6O_{16}$	T	12.457						
$K_2GdNb_6O_{16}$	T	12.450						
$K_2TbNb_6O_{16}$	T	12.440						
$K_2DyNb_6O_{16}$	T	12.431						
$K_2HoNb_6O_{16}$	T	12.426						
$K_2YNb_6O_{16}$	T	12.424						
$K_2BiNb_6O_{16}$	O	17.75						
$Rb_2LaNb_6O_{16}$	T	12.633						
$Ba_6(Ti_2Nb_6)O_{30}$	T	12.54						
$Ba_6(Zr_2Nb_6)O_{30}$	T							
$Ba_6(FeNb_6)O_{30}$	O	17.95	17.95	7.98				
$Si_6(FeNb_6)O_{30}$	O	17.50	17.50	7.72				
$A_6(B_xNb_{10-x})O_{30}$	T	≈ 12.5		≈ 3.9				
$Ba_xMgNb_{14}O_{46}$	O	18.00	18.00	8.02				
$Sr_xMgNb_{14}O_{46}$	O	17.55	17.55	7.82				
$Ba_{0.27}Sr_{0.76}Nb_2O_{6.78}$	T	12.4032		3.9134				
$K_{0.6}NbO_{2.6}F_{0.6}$	T	12.632		3.950				
A_xMoO_3								
$Rb_{0.27}MoO_3$	H		7.321		7.683			
$K_{0.33}MoO_3$	C		3.917					
$K_{0.39}MoO_3$	C		3.920					
$K_{0.48}MoO_3$	T		12.32					
					3.859			

Goodenough/Longo

Compound	Sym	a Å	b Å	c Å	angle	Ref.	Remarks	Magnetic Data
A_xMoO_3 (continued)								
K _{0.28} MoO ₃	M	18.249	7.560	9.855	$\beta = 117^\circ 32'$	G _r 2	"Blue Mo bronze"; Prep. [Wo10], metallic conductivity [Bo20], structural discussion [St22], optical properties [Dz2a]	in 3.3.4, Tab.
K _{0.28} MoO ₃	M	14.278	7.723	6.387	$\beta = 92^\circ 34'$	S _t 24	"Red Mo bronze"; Prep. [Wo10], Semiconducting [Bo20], structural discussion [St22]	
Na _{0.37} MoO ₃	C	3.853				B _i 6	High pressure preparation, $\Theta_{\text{es}} < 1.3^\circ \text{K}$ [St22]	
Na _{0.36} MoO ₃	C	3.847				B _i 6	High pressure preparation	
Na _{0.16} MoO _{2.88}	M	9.57	5.50	12.95		S _t 25	Complete structure, random vacancies [St25]; optical properties [Dz2a]	
A_xTaO_3								
BA _{0.5} TaO _{3-x}	T	12.60		3.95		G _a 14	($x = 0 \dots 0.5$), P&S [Is2a]	
BA _{0.6} TaO ₃	H	21.14		3.917		L _a 8	Dielectric properties, P&S [Is2a, Ga14], review [Ga15a]	
Sr _{0.5} TaO _{3-x}	T	12.41		3.90		G _a 14	($x = 0 \dots 0.5$), review [Ga15a]	
Ca _{0.5} TaO ₃	C	3.886				J _a 7	Review of literature, P&S [Is2a]	
Pb _{0.5} TaO ₃	T	17.635		7.757		I _s 9	$T = 300^\circ \text{C}$, tet. $T > 270^\circ \text{C}$	
Pb _{0.7} TaO ₃	C	17.71		7.788		K _a 16	P&S [Sh12], optical properties [Ka16]	
Ca _{0.5} TaO ₃	C	7.522				I _y 1	P&S [Ke8, Ro13, T _r 8], Prep. [Sa6a]	
La _{0.33} TaO ₃	T	3.918		7.913		I _y 1	P&S [Ke8, Ro13, T _r 8], Prep. [Sa6a]	
La _{0.33} TaO ₃	T	3.915		7.878		I _y 1	P&S [Ke8, Ro13], Prep. [Sa6a]	
Ce _{0.33} TaO ₃	T	3.895		3.910		I _y 1	P&S [Ke8, Ro13], Prep. [Sa6a]	
Pr _{0.33} TaO ₃	O	3.895		7.836		I _y 1	P&S [Ke8, Ro13], Prep. [Sa6a]	
Nd _{0.33} TaO ₃	O	3.876		3.916		I _y 1	P&S [Ke8, Ro13], Prep. [Sa6a]	
Sm _{0.33} TaO ₃	O	3.882		3.896		I _y 1	P&S [Ke8, Ro13]	
Eu _{0.33} TaO ₃	O	3.871		3.885		K _e 8	P&S [Ke8, Ro13]	
Gd _{0.33} TaO ₃	T	3.874		7.792		I _y 1	P&S [Ke8, Ro13]	
Tb _{0.33} TaO ₃	T	3.851		7.795		K _e 8	P&S [Ke8, Ro13]	
Dy _{0.33} TaO ₃	T	3.847		7.780		I _y 1	P&S [Ke8, Ro13]	
Ho _{0.33} TaO ₃	M	3.841		7.769		I _y 1	P&S [Ke8, Ro13]	
Er _{0.33} TaO ₃	T	3.825		7.756		I _y 1	P&S [Ke8, Ro13]	
Yb _{0.33} TaO ₃	M	3.824		7.754		I _y 1	P&S [Ke8, T _r 8, Ro13, Ly1]	
Y _{0.33} TaO ₃	T	7.810		3.839		R _e 6	P&S [Ro10]	
Th _{0.22} TaO ₃	C	7.77		7.758		K _e 6	P&S [Ro10]	
Pa _{0.25} TaO ₃	T	7.73		7.78		K _e 6	Tetragonal tungsten bronze	
U _{0.25} TaO ₃	T	7.739		7.773		K _e 6		
NP _{0.25} TaO ₃	T	7.70		7.75		K _e 6		
Pu _{0.25} TaO ₃	T	7.654		7.731		K _e 6		
Am _{0.25} TaO ₃	T	3.889		7.820		K _e 6		
K _{0.5} TaO _{2.5} F _{0.5}	T	12.569		3.961		M _a 19a		

3.2 Perovskite-related structures

Compound	Sym	<i>a</i> Å	<i>b</i> Å	<i>c</i> Å	angle	Ref.	Remarks	Magnetic Data
$\text{A}_x \text{WO}_3$	H	7.42		7.63				in 3.3.4, Tab.
$\text{Cs}_{0.32} \text{WO}_3$	H	7.38		7.59				
$\text{Cs}_{0.30} \text{WO}_3$	H	7.386		7.54				
$\text{Rb}_{0.32} \text{WO}_3$	H	7.394		7.516				
$\text{Rb}_{0.27} \text{WO}_3$	H							
$(\text{NH}_4)_{0.38} \text{WO}_3$	H	7.395		7.525				
$(\text{NH}_4)_{0.38} \text{WO}_3$	T	7.60		6.36				
$\text{K}_{0.9} \text{WO}_3$	C	3.926						
$\text{K}_{0.46} \text{WO}_3$	T	12.326		3.845				
$\text{K}_{0.3} \text{WO}_3$	H							
$\text{K}_{0.13} \text{WO}_3$	H	7.385		7.513				
$\text{Na}_x \text{WO}_3$	C	3.8		7.370				
$\text{Na}_x \text{WO}_3$	T			7.515				
$\text{Li}_{0.30} \text{WO}_3$	H							
$\text{Li}_{0.30} \text{WO}_3$	T	12.094		3.748				
$\text{Li}_{0.30} \text{WO}_3$	T	5.248		3.895				
$\text{Li}_{0.30} \text{WO}_3$	H	7.405		7.554				
$\text{Li}_{0.30} \text{WO}_3$	C	3.715						
$\text{Li}_{0.30} \text{WO}_3$	C	3.718						

3.2 Perowskit-ähnliche Strukturen

Compound	Sym	a Å	b Å	c Å	angle	Ref.	Remarks	Magnetic Data in 3.3.4, Tab.
A_xWO_3 (continued)								
$Li_{0.05}WO_3$	C	3.723						Co^{17}
$H_{0.4}WO_3$	C	3.755						Gl^1
$H_{0.23}WO_3$	T	5.22						Di^{12}
$H_{0.1}WO_3$	O	7.247	7.502	3.84				Gl^1
$Ba_{0.12}WO_3$	T	12.16		3.843				Co^{19}
$Ba_{0.10}Na_{0.88}WO_3$	T	12.12		3.834				Co^{19}
Ca_xWO_3	O	7.340	7.420	3.840				Va^{21}
	T	5.240			3.854			$x = 0.02, 0 < x < 0.01$ (monoclinic); $0.01 < x < 0.03$ (orthorhombic), studied as function of T
	T	5.292			3.832			$[Va^2, Va^4]$
$Sn_{0.34}WO_3$	H	7.430		7.581				$x = 0.035, 0.03 \leq x < 0.40$ (tetragonal); $0.04 < x < 0.095$ (two phase)
$Sn_{0.18}WO_3$	T	12.241		3.774				$x = 0.10, 0.095 \leq x < 0.105$ (tetragonal); $0.105 \leq x < 0.125$ (cubic $a = 3.790$ Å); $x > 0.125$ (two phase)
$Pb_{0.17}WO_3$	T	12.163		3.767				Gl^1
$Pb_{0.35}WO_3$	T	12.207		3.782				Be^{30}
$La_{0.08}WO_3$	C			3.829				Br^{20}
$La_{0.03}WO_3$	T			7.52				Br^{23}
$Ce_{0.1}WO_3$	C			3.828				Br^{23}
$Pr_{0.1}WO_3$	C			3.827				Os^{21}
$Nd_{0.1}WO_3$	C			3.822				$n_{eff} = 3.6$
$Sm_{0.1}WO_3$	C			3.817				$n_{eff} = 3.8$
$Eu_{0.18}WO_3$	C			3.828				$n_{eff} = 3.4$ (temperature dependent), P & S [Sh6]
$Eu_{0.10}WO_3$	C			3.815				Os^{21}
$Eu_{0.088}WO_3$	C			3.808				Os^{21}
$Cd_{0.1}WO_3$	C			3.810				Os^{21}
$Tb_{0.1}WO_3$	C			3.808				$n_{eff} = 9.6$
$Dy_{0.1}WO_3$	C			3.805				Os^{21}
$Ho_{0.1}WO_3$	C			3.801				$n_{eff} = 10.6$
$Er_{0.1}WO_3$	C			3.797				Os^{21}
$Tm_{0.1}WO_3$	C			3.794				$n_{eff} = 9.5$
								Os^{21}
								$n_{eff} = 7.5$, crystal growth [Co14]

3.2 Perovskite-related structures

Compound	Sym	a Å	b Å	c Å	angle °	Ref.	Remarks	Magnetic Data in 3.3.4, Tab.
A_xWO_3 (continued)								
$Y_{b,1}WO_3$	C	3.791				Os2	$n_{eff} = 4.5$	
$Lu_{0,1}WO_3$	C	3.788				Os2	$n_{eff} = 0$	
$Y_{0,08}WO_3$	C	3.800				B23	Tetr. $x < 0.09$, metallic conductivity [Sh6]	
Al_xWO_3	O	7.368	7.476	3.850		Po10	$x = 0.015$, 0.010 $< x < 0.030$ orthorhombic; $0.030 < x < 0.105$, two phase; studied as function of T [Va4]	
$Cu_{0,77}WO_3$	O	5.387	5.440	3.784		Po10	$0.105 < x \leq 0.135$; $x > 0.135$, two phase	
$Cu_{0,28}WO_3$	O	3.73	3.88	7.74		Co18	Semiconducting ≈ 0.15 eV	
	Tr	5.85	6.65	4.88				
$Ag_{0,91}WO_3$	O	3.73	3.85	7.35		Si8	Magnetic susceptibility $\chi_m = 34 \cdot 10^{-6}$ emu/mole	
Cd_xWO_3	O	7.316	7.532	3.848		Va3	Metallic conductivity, P & S [Po2]	
$In_{0,08}WO_3$	T	5.244		3.867		Va3	$x = 0.005$, 0.005 $\leq x < 0.02$ orthorhombic	
$In_{0,30}WO_3$	T	5.233		3.863		Bo21	$x = 0.020$, 0.02 $\leq x < 0.04$ tetragonal	
$In_{0,08}SSWO_3$	H	7.384		7.508		Bo21	$x = 0.01 \dots 0.05$, P & S ($x = 0.11$) [Bi3]	
$Tl_{0,38}WO_3$	H	7.50		7.56			$x = 0.2 \dots 0.3$, metallic conductivity, weak dia-	
	T	7.31		12.80			magnetism	
$U_{0,08}WO_3$	C	3.812				Sw1	$x = 0.26 \dots 0.33$; metallic conductivity	
$U_{0,12}WO_3$	C	3.821				Si6	Metallization, $x = 0.19 \dots 0.36$; novel preparation [Co16]	
$Cs_{0,1}(Ta_{0,3}W_{0,7})O_3$	H	7.450				Ko10	relationship of a vs. x [We2]	
$Rb_{0,3}(Ta_{0,3}W_{0,7})O_3$	H	7.342				Ko10	P & S [Si9]	
$K_{0,3}(Ta_{0,3}W_{0,7})O_3$	H	7.333				Ga4	Thermal expansion and resistivity ($10^8 \Omega \text{cm}$)	
$K_{0,5}(Ta_{0,3}W_{0,5})O_3$	T	12.36				Ga4	Thermal expansion and resistivity ($10^8 \Omega \text{cm}$)	
A_xReO_3						Ga4	Thermal expansion and resistivity ($10^7 \Omega \text{cm}$)	
$K_{\sim 0,6}ReO_3$	C	3.895				Ga14	Entire range of S. S. with Ta and Nb [De19a]	
$K_{\sim 0,3}ReO_3$	H	7.318						
$Na_{\sim 0,6}ReO_3$	T	3.825						
A_xFeF_3								
$Rb_{0,38}FeF_3$	H	7.36				Si2	Metallic conductivity	
$K_{0,98}FeF_3$	C	4.113				Ch/b	High pressure preparation, $\Theta_{ea} = 3.6^\circ \text{K}$ [Si7a]	
$K_{0,98}FeF_3$	T	12.60				Si7a	Metallic, $\Theta_{ea} < 1.3^\circ \text{K}$, P & S [Si2]	
$K_{0,28}FeF_3$	H	7.385						
$Na_{0,11}FeF_3$	R	5.37						
$Tl_{0,30}FeF_3$	H	7.35						

Goodenough/Longo

3.2 Perowskit-ähnliche Strukturen

[Lit. S. 275]

Tab. 4b. □ BX₃ compounds

Compound	Sym	a Å	b Å	c Å	angle	Ref.	Remarks	Magnetic Data
in 3.3.4, Tab.								
AlF ₃	R	5.029			$\alpha = 58^\circ 31'$	K _{e20}		
ScF ₃	R	5.708			$\alpha = 59^\circ 32'$	N _{a10}	P & S [Eh2]	
TiF ₃	R	5.519			$\alpha = 58^\circ 53'$	Si ₂	6	
TOF ₂	C	3.798			$\alpha = 58^\circ$	V _{o3}	6	
VF ₃	R	5.373			$\alpha = 57^\circ 31'$	J _{a2a}	Neutron diffraction [W _{o13}]	
CrF ₃	R	5.2643			$\alpha = 56^\circ 37'$	K _{n2}	Prop. [Bi7, Ha11, Ha12, Bo33, Ra9], structure [Ja3], neutron diffraction [W _{o13}]	
MnF ₃	R	5.332			$\alpha = 56^\circ 37'$	K _{n2}	300 °C	
MnF ₃	M	8.904	5.037	13.448	$\beta = 92^\circ 44'$	H _{e9}	Neutron diffraction [W _{o13}], Prop. [Bo33, Bo34, Ny1, K ₁₅ , He10, Sm1]	
FeF ₃	R	5.362			$\alpha = 58^\circ 0'$	H _{e11}	Neutron diffraction [W _{o13}], Prop. [Bi7, Sh5, We17, Bu1], crystal transformation [Cr5]	
CoF ₃	R	5.279			$\alpha = 57^\circ 0'$	H _{e11}	Neutron diffraction [W _{o13}], Prop. [He8, Ny1]	
GaF ₃	R	5.20			$\alpha = 57^\circ 30'$	B _{r6}	P & S [Mu1]	
ZrF ₃	C	3.96				E _{h3}		
NbF ₃	C	3.903				F _{r15}	P & S [Se2], "doubtful"	
NbO ₂ F	C	3.902				Gu ₈	6	
MoF ₃	C	3.8985				He ₁₁	Neutron diffraction [Wi6], P & S [La7]	
RuF ₃	R	5.408				He ₁₁	Neutron diffraction [Wi6]	
RhF ₃	R	5.330				He ₁₁	Neutron diffraction [Wi6], Prop. [Ba19, Ba20, Ny1, Fi3]	
PdF ₃	R	5.5234				He ₁₁		
InF ₃	R	5.722			$\alpha = 56^\circ 15'$	Mu ₁		
TeO ₃	R	5.180			$\alpha = 56^\circ 25'$	Du ₂	Prep. [Lo6], Prop. [Ny1], "doubtful"	
TaF ₃	C	3.9012				Gu ₈		
TaO ₂ F	C	3.896				F _{r15}		
WO ₃	M	7.297			$\beta = 90^\circ 55'$	Lo ₆	Structure [Br1, Ta15], neutron diffraction [Lo6], Prop. [Cr7, Cr8, Ta15, Co16, Ba22, Iw2, De16, Re10], optical properties [D, 3a], phase transformations [Pe1a]	
Re _{0.33} W _{0.67} O ₃	C	3.7574				Si ₂	P & S, [Me11, Bi4, Bi5], crystal growth [Fe21], Prop. [Si2, Fe21, Fe10, Gu6a], structure vs. oxygen content [Si2], DeHaas-Van Alphen effect [Ma27a], NMR [Na11a]	
ReO ₃	C	3.7477				Si ₂	P & S [Ro2], P & S [Em2]	
IrF ₃	R	5.418			$\alpha = 54^\circ 8'$	H _{e11}		
UO ₃	C	4.156				Wa ₆		

Tab. 4c. □ BB'X₆ compounds

Compound	Sym.	<i>a</i> Å	<i>b</i> Å	<i>c</i> Å	angle	Ref.	Remarks	Magnetic Data
BB'X ₆								
NaVF ₆	R	5.63						
LiVF ₆	R	5.30						
CaMnF ₆	R	5.59						
MgMnF ₆	R	5.26						
NaNbF ₆	C	8.26						
LiNbF ₆	R	5.47						
NaMoF ₆	C	8.194						
LiMoF ₆	R	5.43						
NaTcF ₆	R	5.77						
NaRuF ₆	R	5.80						
LiRuF ₆	R	5.39						
GePdF ₆	R	5.53						
PtPdF ₆	R	5.52						
SnPdF ₆	R	5.70						
PtPdF ₆	R	5.55						
NaSbF ₆	C	8.184						
LiSbF ₆	R	5.44						
CaHfF ₆	C	8.462						
NaTaF ₆	C	8.28						
LiTaF ₆	R	5.48						
NaWF ₆	C	8.18						
LiWF ₆	R	5.45						
NaReF ₆	C	8.18						
NaOSF ₆	R	5.80						
LiOsF ₆	R	5.43						
NaIrF ₆	R	5.80						
LiHF ₆	R	5.41						
PdPtF ₆	R	5.55						
CaPbF ₆	C	8.476						

Goodenough/Longo

in 3.3.4,
Tab.

Structural review [Gi2, Ke11, Co29]

Ke11
Ke11
Ho14
Ho14
Ke11
P & S [Co29]

α = 56° 30'
α = 56° 18'
α = 55° 36'
α = 56° 54'
α = 58° 6'
n_{eff} = 1.66, Θ_p = -218 °K [Ha18]

Ke11
Ed3
Bo18
Ed4
Bo18
Bo18
Ba21
P & S [Ha7]

Magnetic properties 80 < T < 300 °K,
n_{eff} = 1.66, Θ_p = 31 °K
P & S [Ha18]

Magnetic properties 80 < T < 300 °K,
n_{eff} = 2.82, Θ_p = 31 °K
P & S [Ha18]

[Ba21]
P & S [He11], see PdF₃
[Ba21]
Magnetic properties, n_{eff} = 2.98, Θ_p = 28 °K
[Ba21]
Magnetic properties, n_{eff} = 2.72, Θ_p = 1.2 °K
[Ba21]
P & S [Sc22]

Complete structure; P & S [Ke11]

Ba21

Tab. 4d. $(AX)_n(ABX_3)_m$ compounds

Compound	Sym	a Å	b Å	c Å	angle	Ref.	Remarks	Magnetic Data in 3.3.4, Tab.
Halides								
Cs_2MgF_4	T	4.055		13.79		<i>Ba1</i>		
Rb_2MgF_4	T	3.955		13.706		<i>Re6</i>		
K_2MgF_4	T	4.07		13.88		<i>Ch8a</i>		
$(NH_4)_2MgF_4$	T	4.007		14.43		<i>V01</i>		
Tl_2MgF_4	M	3.344	9.533	5.657	$\beta = 87^\circ 12'$	<i>V01</i>	Not K_2NiF_4 type	
Na_2CrCl_4	T	5.215		16.46		<i>Se2</i>		
Cs_2CrCl_4	T	5.143		15.73		<i>Se2</i>	Possibly distorted K_2NiF_4 [$Se2$]	
Rb_2CrCl_4	T	4.31		14.63		<i>Co25</i>		
K_2CrCl_4	T					<i>Le7</i>	K_2NiF_4 type	6
Cs_2MnCl_4	T					<i>Co25</i>	P & S [$V01$], Prop. [D_{e20} , B_{r7}]	6
Rb_2MnF_4	T	4.228		13.89		<i>B_{r5}</i>	P & S [$V01$, G_{o25}], Prop. [D_{e20} , C_{o15}]	6
K_2MnF_4	T	4.20		13.14		<i>T_{r1}</i>		6
Rb_2FeF_4	T	4.20		13.38		<i>De12</i>		
K_2FeF_4	T	4.140		12.98		<i>Ru6</i>	P & S [$Ru3$, $Ru8$]	6
$K_2Fe_3F_7$	T	4.130		21.15		<i>Ru6</i>	Prop. [$Ru8$, $Sr2$, $Sr2$, $Va1$, $Le8$], dielectric properties [$La1a$]	6
Tl_2FeF_4	T	4.194		13.91		<i>P & S [Ru3, Ru8]</i>		
Rb_2CoF_4	T	4.135		13.67		<i>Ru8</i>	Prop. [$Ru3$, $Ru5$]	6
K_2CoF_4	T	4.07		13.08		<i>Ba10</i>	Prop. [$Sr2$, G_{o26} , D_{e20} , $Ru5$, T_{i5} , W_{e20}], dielectric properties [$La1b$], neutron diffraction [P_{I4} , P_{I5} , P_{I6} , P_{I7} , $Le6$, $Le7$]	6
Tl_2CoF_4	T	4.11		14.05		<i>Ru8</i>		
Rb_2NiF_4	T	4.087		13.71		<i>Ru8</i>		
K_2NiF_4	T	4.006		13.076		<i>Ba10</i>		
$(NH_4)_2NiF_4$	T	4.08		13.78		<i>Ru8</i>		
Tl_2NiF_4	T	4.051		14.22		<i>Ru8</i>		
Rb_2CuF_4	T	4.238		13.28		<i>Ru6</i>	P & S [$Ru3$], optical properties [$Sc10a$]	6
K_2CuF_4	T	4.145		12.72		<i>Ru6</i>	Prop. [$Ru6$, $Va1$], P & S [K_{n1} , G_{u1a}]	6
Na_2CuF_4	M	3.261	9.354	5.601	$\beta = 87^\circ 30'$	<i>Ba3</i>	P & S [$Ru3$] – not K_2NiF_4 type	6
Tl_2CuF_4	T	4.199		13.66		<i>Ru6</i>	P & S [$Ru3$]	6
$(NH_4)_2CuCl_4$	O	7.20	7.20	15.46		<i>Wi9</i>		
$(CH_3NH_3)_2CuCl_4$	O	7.30	7.54	18.55		<i>Gr7</i>	Prop. [D_{e20} , B_{o15} , K_{o8}], Prop. [$Re7$]	6
$(C_2H_5NH_3)_2CuCl_4$	O	7.35	7.47	21.18		<i>Wi9</i>	Prop. [D_{e20} , B_{o15} , K_{o8}], Prop. [$Re7$]	6
Rb_2ZnF_4	T	4.125		13.67		<i>Ba1</i>	P & S [$Sc10$]	
K_2ZnF_4	T	4.02		13.05		<i>Sc10</i>		
$K_3Zn_2F_7$	T	4.063		21.22		<i>B_{r12}</i>		

3.2 Perovskite-related structures

Compound	Sym	a Å	b Å	c Å	angle	Ref	Remarks	Magnetic Data
Halides (continued)								
(NH ₄) ₂ ZnF ₄	T	4.14			13.97			
Tl ₂ ZnF ₄	T	4.105			14.10			
Rb ₂ CdF ₄	T	4.414			13.98			
Rb ₂ Cd ₃ F ₇	T	4.403			22.71			
K ₂ CdF ₄	T							
K ₂ Cd ₂ F ₇	T							
Cs ₂ CdCl ₄	T							
Oxides								
SrLaAlO ₄	T	3.75			12.5			
Sr ₂ TiO ₄	T	3.88			12.58			
Sr ₃ Ti ₂ O ₇	T	3.90			20.38			
Sr ₂ Ti ₃ O ₁₀	T	3.90			28.1			
Ca ₃ Ti ₂ O ₇	O	5.412			19.50			
Ca ₄ Ti ₃ O ₁₀	O	5.404			27.14			
NaLaTiO ₄	T	3.76			12.95			
NaNdTiO ₄	T	3.76			12.79			
NaSmTiO ₄	T	3.77			12.59			
NaGdTIO ₄	T	3.77			12.46			
NaDyTiO ₄	T	3.77			12.22			
NaTmTiO ₄	T	3.78			12.05			
NaLuTiO ₄	T	3.78			11.92			
NaYTIO ₄	T	3.786			12.209			
Na ₃ Y ₂ Ti ₃ O ₁₄	T	3.79			20.2			
Na ₂ Y ₂ Ti ₃ O ₁₀	T	3.79			28.2			
Eu ₂ TiO ₄	T	3.89			12.53			
Eu ₃ Ti ₂ O ₇	T	3.899			20.295			
Sr ₂ CrO ₄	T	3.82			12.4			
Sr ₃ Cr ₂ O ₇	T	3.82			20.1			
SrLaCrO ₄	T	3.84			12.52			
Sr ₂ MnO ₄	T	3.79			12.43			
Ca ₂ MnO ₄	T	3.667			12.063			
Ca ₂ Mn ₂ O ₇	T	3.709			19.44			
Ca ₂ Mn ₃ O ₁₀	T	3.724			26.90			
Sr _{1.5} La _{0.5} MnO ₄	T	3.88			12.5			
Sr ₂ FeO _{4-x}	T	3.864			12.390			
Sr ₂ Fe ₂ O _{7-x}	T	3.853			20.149			
								x = 0.3
								x = 0.1, P & S [Br10], Prop. [Ma7]
								6
								6
Goodenough/Longo								
in 3.3, 4, Tab.								
Ru ¹ Ba10	P & S [Ru1, Br11, Lu2, Po9, Ha19a], Eu ³⁺ fluores-							
Ru ² Pe3 P & S [Lu2]	P & S [Ru17] Pe3 P & S [Ro17]							
Bl ¹² Bl ¹²	(Na and Ln ordered). Fluorescence: Eu [Bl12a]							
Bl ¹² Bl ¹²	Fluorescence: Eu [Bl12a]							
Bl ¹² Re2 Re2	Bl ¹² P & S [Bl12], fluorescence: Eu [Bl12a]							
Bl ¹² Re2	Bl ¹² P & S [Mc1b]							
Bl ¹² Re2	Bl ¹² P & S [Mc1b]							
Lo ^{1a} Lo ^{1a}	Cr ⁴⁺ , high pressure preparation Cr ⁴⁺ , high pressure preparation							
Bl ⁹	Substitution of La [Sr2] P & S [Ru1, Br11] 97% Mn ⁴⁺ ; P & S [Ru1, Br11] 97% Mn ⁴⁺ ; P & S [Ru1, Br11]							
Bl ⁹ Ga19 Ga19	La ⁷ Ga19 Ga19							

3.2 Perowskit-ähnliche Strukturen

[Lit. S. 275]

Compound	Sym	a Å	b Å	c Å	angle	Ref.	Remarks	Magnetic Data in 3.3.4, Tab.
Oxides (continued)								
$\text{Sr}_3\text{Fe}_2\text{O}_{7-\alpha}$ cont.	T	3.892		20.054			$\alpha = 1$, Prop. [Ma7]	
$\text{Sr}_2\text{FeO}_3\text{F}$	T	3.84	12.98				$\text{Ga}3$	
SrLaFeO_3	T	3.86	12.69				$\text{B}19$	
SrLaCoO_4	O	3.80	12.50				$\text{B}19$	6
La_2CoO_4	T	5.482	5.539	12.66			$\text{Ra}2$	
$\text{La}_2\text{Co}_0.8\text{Li}_{0.8}\text{O}_4$	T	3.77		12.58			$\text{B}19$	
$\text{La}_{1.6}\text{Sr}_{0.6}\text{Co}_{0.4}\text{Mg}_{0.4}\text{O}_4$	T	3.82	12.58				Prop. [Sr2, Go26]	
$\text{La}_{1.5}\text{Sr}_{0.5}\text{Co}_{0.5}\text{Ti}_{0.5}\text{O}_4$	T	3.85	12.62				$\text{B}19$	
La_2NiO_4	T	3.855	12.652				$\text{Ra}2$	
Pr_2NiO_4	T						P & S [F01, Fo3], Prop. [Sm34, Sm24]	
Nd_2NiO_4	T	3.81	12.31				Prop. [Sm34], Prop. [Sm24]	
SrLaNiO_4	T	3.80	12.51				Prop. [Sm34, Sm24]	
$\text{La}_2\text{Ni}_{0.8}\text{Li}_{0.8}\text{O}_4$	O	3.75	12.89				$\text{F}01$	
La_2CuO_4	T	5.36	5.41	13.17			$\text{B}19$	
Pr_2CuO_4	T	3.81	13.24				$\text{B}19$	
Nd_2CuO_4	T	3.96	12.23				$\text{Lo}1c$	
Sm_2CuO_4	T	3.94	12.15				$\text{Lo}1c$	
Eu_2CuO_4	T	3.91	11.93				$\text{Fr}25$	
Cd_2CuO_4	T	3.91	11.92				$\text{F}01$	
SrLaGaO_4	T	3.89	11.85				$\text{P} \& \text{S} [\text{Fr}25]$	
Ca_3GeO_4	T	3.84	12.71				$\text{Fr}25$	
Ba_2ZrO_4	T	3.70	11.88				$\text{F}01$	
Sr_2ZrO_4	T	4.187	13.48				$\text{P} \& \text{S} [\text{Fr}25]$	
$\text{Sr}_3\text{Zr}_2\text{O}_7$	O O O	5.801	12.445				$\text{B}19$	
$\text{Sr}_4\text{Zr}_3\text{O}_{10}$	O O O	5.798	20.94				$\text{Re}2$	
$\text{K}_2\text{NbO}_3\text{F}$	T	5.795	5.814				100 kbars, 900 °C required, P & S [Ri88]	
Sr_2MoO_4	T	3.96	29.34				$\text{Sc}18a$	
Ba_2TcO_4	T T	3.92	12.67				$\text{Pe}3$	
Sr_2TcO_4	T T	4.011	12.84				$\text{Pe}3$	
Sr_3RuO_4	T	3.902	13.40				$\text{Ga}2$	
Sr_2RhO_4	T	3.870	12.72				$\text{Ba}10$	
SrLaRhO_4	T	3.85	12.74				$\text{Ke}9$	
Ba_2SnO_4	T	3.92	12.90				$\text{Ra}6$	
Sr_2SnO_4	T	4.130	12.78				$\text{Ra}6$	
Ca_2SnO_4	T	4.037	13.27				$\text{B}19$	
Ba_2HfO_4	T	4.161	12.53				$\text{We}8$	
Sr_2HfO_4	T	4.089	13.45				$\text{P} \& \text{S} [\text{Wa}2]$	
			12.52				$\text{We}8$	
							Not K_2NiF_4 type, [We8]	
							$\text{Sc}18a$	
							$\text{Sc}18a$	

Compound	Sym	<i>a</i> Å	<i>b</i> Å	<i>c</i> Å	angle °	Ref.	Remarks	Magnetic Data in 3.3.4, Tab. 6
Oxides (continued)								
Sr_2IrU_4	T	3.89		12.92		Ra7	Prop. [$Ro2a$]	
Ca_2IrO_4	H	9.423		3.195		Ba5a	Not K_2NiF_4 type	
Ba_2PbO_4	T	4.296		13.30		We8	P & S [$W\alpha 2$]	
A_2PbO_4	T	4.38		14.79		We8	A = Sr + Ca, not K_2NiF_4 type	
Cs_2UO_4	T	4.345		13.83		Ko11		
Rb_2UO_4	T	4.335		13.10		Ko11		
K_2UO_4	T	5.795	5.97	11.68		Ko11		
$\beta\text{-Na}_2\text{UO}_4$	O					Ko11		

Tab. 4e: see next page

3.2 Perowskit-ähnliche Strukturen

Tab. 4e. $\text{Bi}_3\text{O}_8(\text{A}_{n-1}\text{B}_n\text{O}_{8n+1})$ compounds

Compound	Sym	α Å	b Å	c Å	angle	Ref.	Remarks	Magnetic Data
Bi_2MoO_6	O	5.49	5.50	16.24				
Bi_2WO_6	O	5.49	5.50	16.24				
$\text{BaBi}_2\text{Nb}_2\text{O}_9$	O	5.533	5.533	25.55				
$\text{SrBi}_2\text{Nb}_2\text{O}_9$	O	5.504	5.504	25.05				
$\text{CaBi}_2\text{Nb}_2\text{O}_9$	O	5.435	5.485	24.87				
$\text{PbBi}_2\text{Nb}_2\text{O}_9$	O	5.492	5.503	25.53				
$\text{K}_{0.6}\text{Bi}_{1.5}\text{Nb}_2\text{O}_9$	T	5.535	5.506	25.72				
$\text{Na}_{0.6}\text{Bi}_{1.5}\text{Nb}_2\text{O}_9$	O	5.506	5.506	25.26				
$\text{BaBi}_2\text{Ta}_2\text{O}_9$	O	5.47	5.47	26.94				
$\text{SrBi}_2\text{Ta}_2\text{O}_9$	O	5.556	5.556	25.60				
$\text{CaBi}_2\text{Ta}_2\text{O}_9$	O	5.435	5.468	24.97				
$\text{PbBi}_2\text{Ta}_2\text{O}_9$	T	5.479		25.085				
$\text{Bi}_2\text{NbTiO}_9$	O	5.496	5.496	25.40				
$\text{Bi}_2\text{TaTiO}_9$	O	5.405	5.442	25.11				
$\text{BaBi}_2\text{Ti}_2\text{Nb}_2\text{O}_{12}$	O	5.402	5.436	25.15				
$\text{PbBi}_2\text{Ti}_2\text{Nb}_2\text{O}_{12}$	T	3.874		33.70				
$\text{Bi}_4\text{Ti}_3\text{Nb}_2\text{O}_{12}$	O	3.867		33.55				
	O	5.410	5.448	32.84				
$\text{BaBi}_4\text{Ti}_4\text{O}_{18}$	T			41.85				
$\text{SrBi}_4\text{Ti}_4\text{O}_{18}$	T	5.461		40.95				
$\text{CaBi}_4\text{Ti}_4\text{O}_{18}$	T	5.428		40.75				
$\text{PbBi}_4\text{Ti}_4\text{O}_{18}$	T	5.418		41.35				
$\text{Bi}_5\text{Ti}_3\text{GaO}_{18}$	T	5.437		41.05				
$\text{Bi}_5\text{Ti}_3\text{FeO}_{18}$	O	5.408	5.455	41.31				
$\text{K}_{0.6}\text{Bi}_{4.6}\text{Ti}_4\text{O}_{18}$	T	5.445		41.15				
$\text{Na}_{0.8}\text{Bi}_{4.6}\text{Ti}_6\text{O}_{18}$	T	5.440		40.65				
$\text{Ba}_2\text{Bi}_4\text{Ti}_6\text{O}_{18}$	O	5.427		50.37				
$\text{Ba}_2\text{Bi}_4\text{Ti}_3\text{Fe}_2\text{O}_{18}$	O	5.514	5.526	50.37				
$\text{Sr}_2\text{Bi}_4\text{Ti}_6\text{O}_{18}$	T	5.490	5.500	50.185				
$\text{Pb}_2\text{Bi}_4\text{Ti}_6\text{O}_{18}$	T	5.461		48.80				
$\text{Ba}_3\text{Bi}_4\text{Ti}_3\text{Fe}_2\text{O}_{27}$	O	5.491	5.502	49.70				
				76.20				

III Figuren 871...877

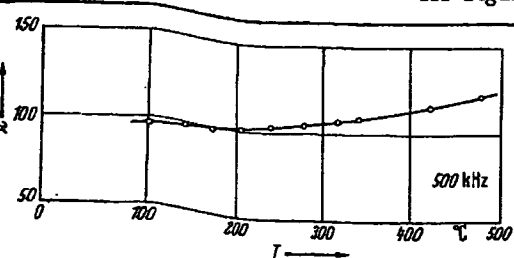


Fig. 871. $\text{CaBi}_2\text{Nb}_2\text{O}_9$ (ceramics). κ vs. T [61S11].

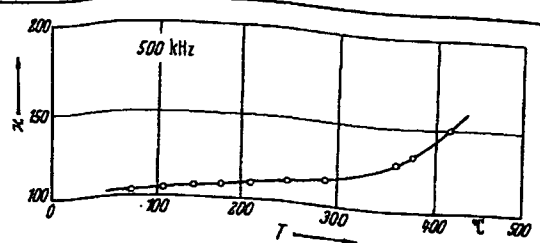


Fig. 872. $\text{CaBi}_2\text{Ta}_2\text{O}_9$ (ceramics). κ vs. T [61S11].

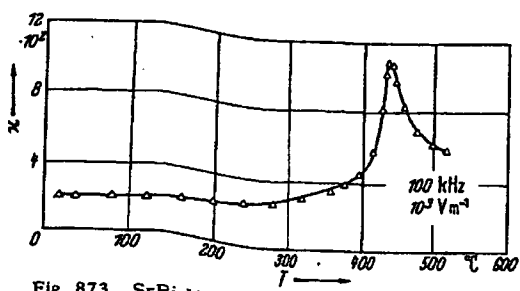


Fig. 873. $\text{SrBi}_2\text{Nb}_2\text{O}_9$ (ceramics). κ vs. T [62S17].

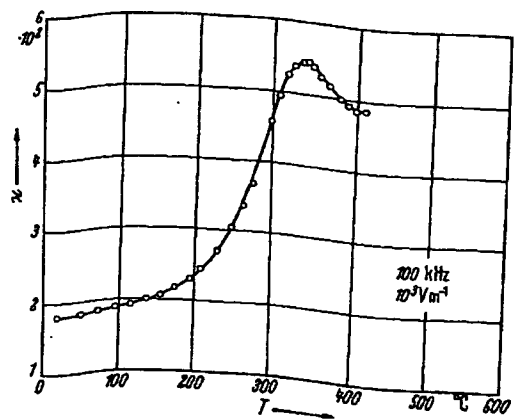


Fig. 874. $\text{SrBi}_2\text{Ta}_2\text{O}_9$ (ceramics). κ vs. T [62S17].

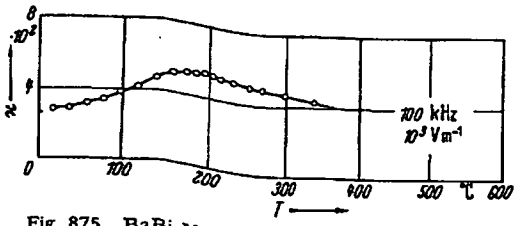


Fig. 875. $\text{BaBi}_2\text{Nb}_2\text{O}_9$ (ceramics). κ vs. T [62S17].

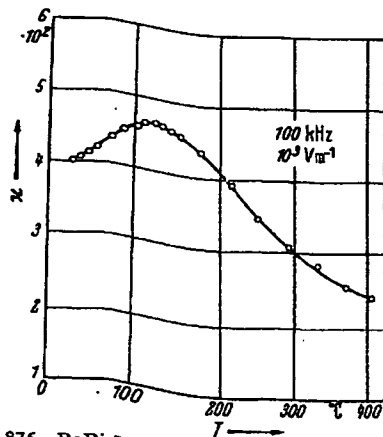


Fig. 876. $\text{BaBi}_2\text{Ta}_2\text{O}_9$ (ceramics). κ vs. T [62S17].

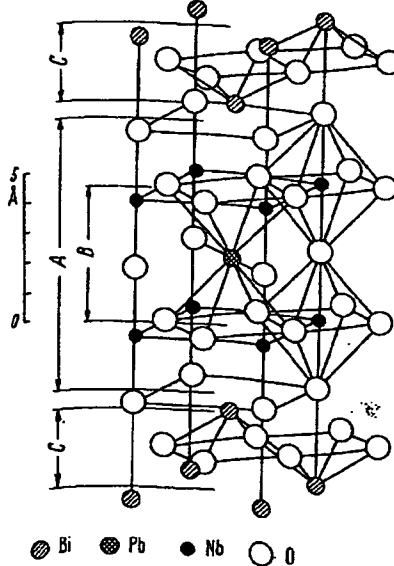
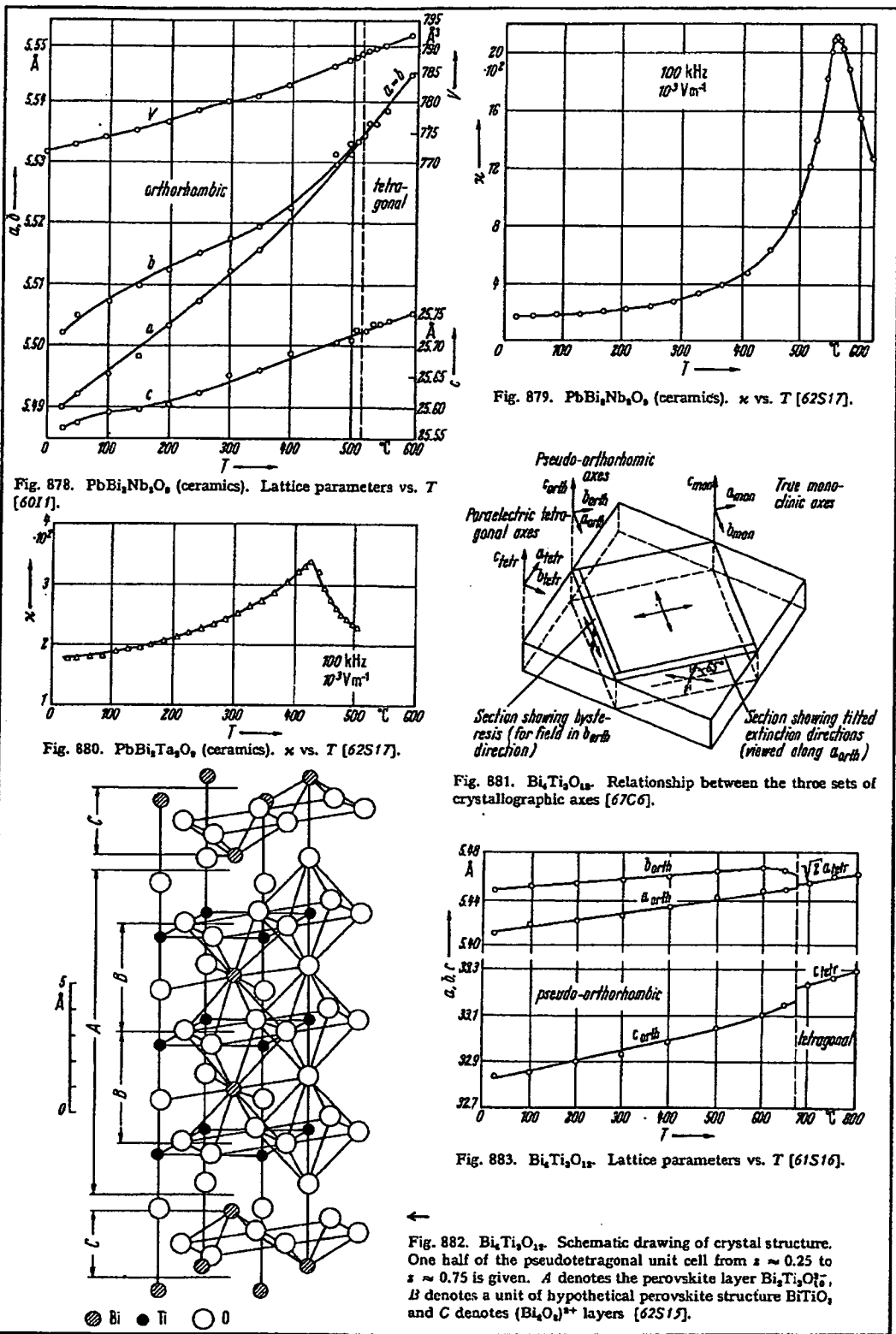


Fig. 877. $\text{PbBi}_2\text{Nb}_2\text{O}_9$. Schematic drawing of crystal structure. One half of the pseudotetragonal unit cell from $s \approx 0.25$ to $s \approx 0.75$ is given. A denotes the perovskite layer $\text{PbNb}_2\text{O}_7^{2-}$, B denotes a unit of hypothetical perovskite structure PbNbO_3 , and C denotes $[\text{Bi}_2\text{O}_6]^{3+}$ layers [62S17].

III Figures 878...883



III Figures 890...895

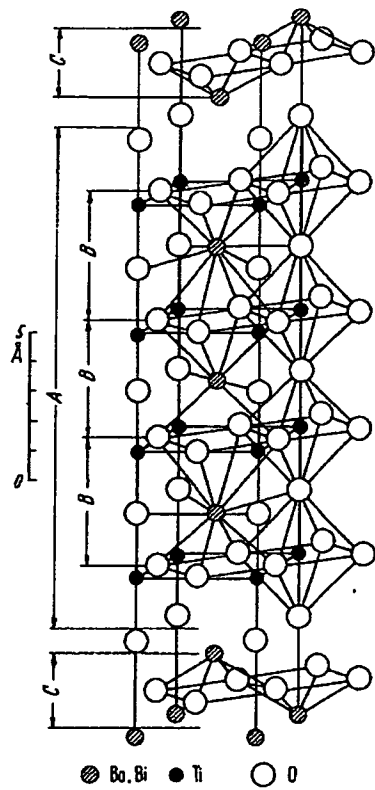


Fig. 890. $\text{BaBi}_4\text{Ti}_4\text{O}_{15}$. Schematic drawing of crystal structure. One half of the pseudotetragonal unit cell from $z \approx 0.25$ to $z \approx 0.75$ is given. A denotes the perovskite layer $\text{BaBi}_4\text{Ti}_4\text{O}_{15}$, B denotes a unit of hypothetical perovskite structure ($\text{Ba}, \text{Bi}\text{TiO}_3$, C denotes $(\text{Bi}_4\text{O}_5)^{2+}$ layers [62S15].

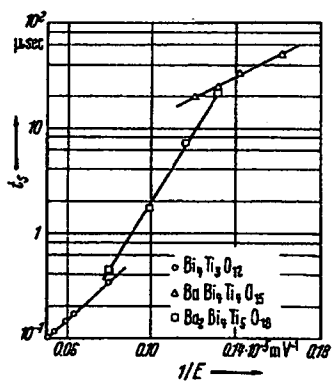


Fig. 892. $\text{BaBi}_4\text{Ti}_4\text{O}_{15}$, $\text{Ba}_2\text{Bi}_4\text{Ti}_4\text{O}_{15}$, $\text{Bi}_4\text{Ti}_3\text{O}_{12}$. t_s vs. $1/E$. [62F1]. t_s : switching time.

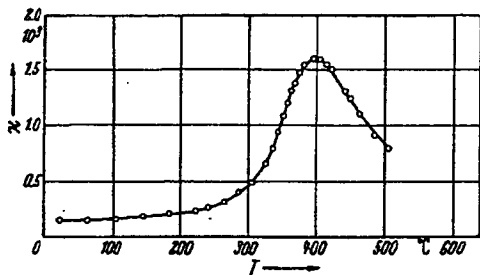


Fig. 891. $\text{BaBi}_4\text{Ti}_4\text{O}_{15}$ (ceramics). \times vs. T [61S15].

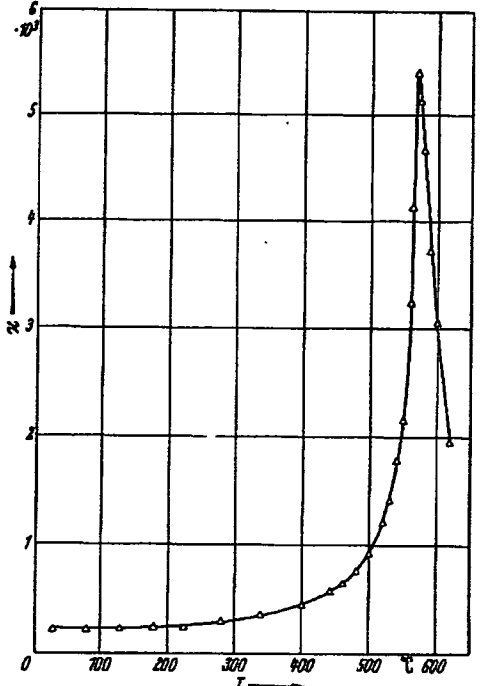


Fig. 893. $\text{PbBi}_4\text{Ti}_4\text{O}_{15}$ (ceramics). \times vs. T [61S15].

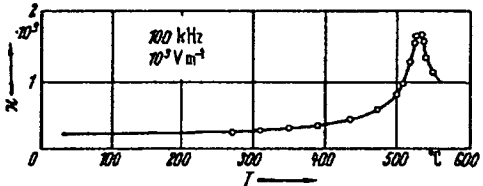


Fig. 894. $\text{SrBi}_4\text{Ti}_4\text{O}_{15}$ (ceramics). \times vs. T [62S17].

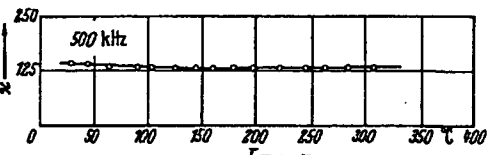


Fig. 895. $\text{CaBi}_4\text{Ti}_4\text{O}_{15}$ (ceramics). \times vs. T [61S11].

III Figuren 896...901

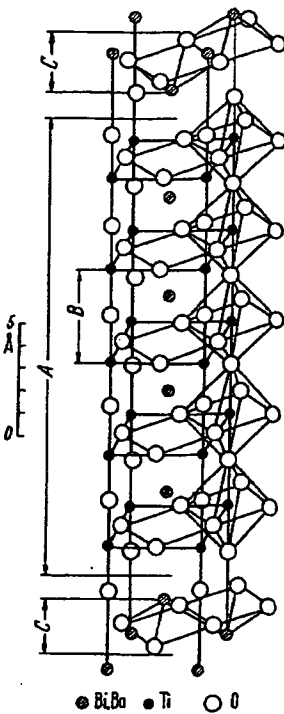


Fig. 896. $\text{Ba}_2\text{Bi}_4\text{Ti}_4\text{O}_{15}$. Schematic drawing of the crystal structure. One half of the tetragonal unit cell from $z = 0.25$ to $z = 0.75$ is given. A denotes the perovskitic layer of $\text{Ba}_2\text{Bi}_4\text{Ti}_4\text{O}_{15}$, B denotes a unit cell of the hypothetical perovskite structure $(\text{Ba}, \text{Bi})\text{TiO}_3$, and C denotes the layers of $(\text{Bi}_4\text{O}_5)^{8+}$ [62A5].

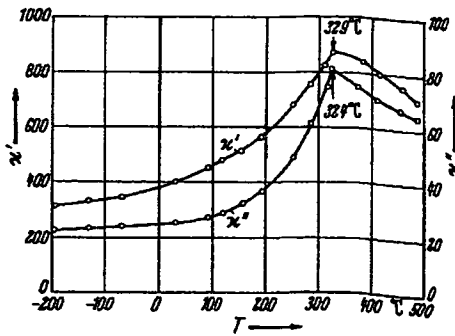


Fig. 898. $\text{Ba}_2\text{Bi}_4\text{Ti}_4\text{O}_{15}$. x' and x'' vs. T [62A5].

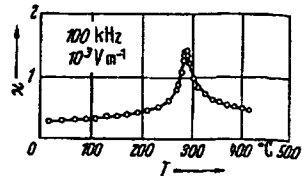


Fig. 900. $\text{Sr}_2\text{Bi}_4\text{Ti}_4\text{O}_{15}$ (ceramics). x vs. T [62S17].

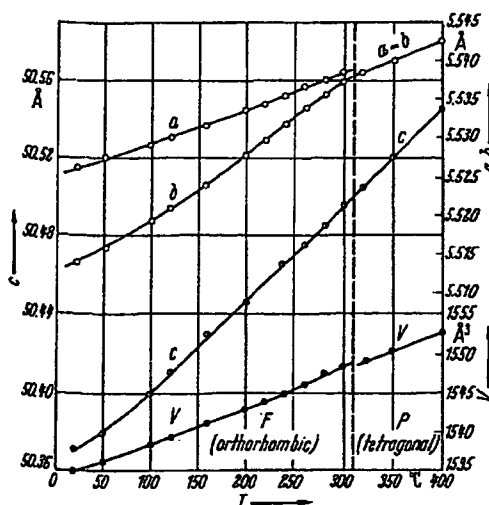


Fig. 897. $\text{Ba}_2\text{Bi}_4\text{Ti}_4\text{O}_{15}$. Lattice parameters vs. T [63I5].

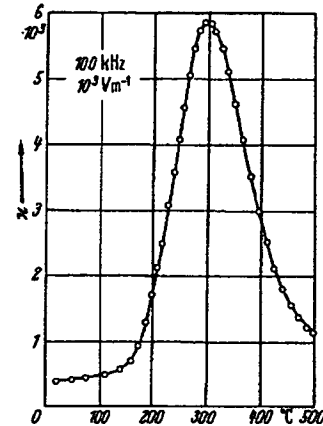


Fig. 899. $\text{Pb}_2\text{Bi}_4\text{Ti}_4\text{O}_{15}$ (ceramics). x vs. T [62S17].

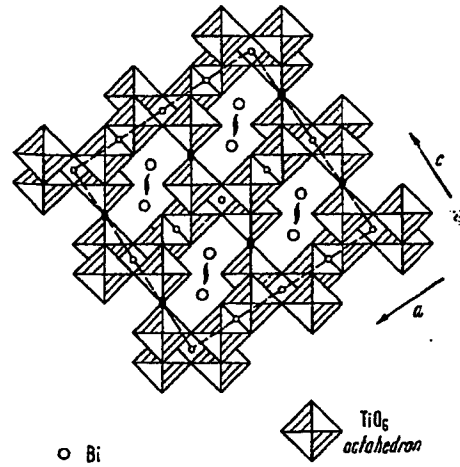


Fig. 901. $\text{Bi}_2\text{Ti}_4\text{O}_{15}$. Schematic projection of structure on $(010)_z$ [65J4].

BRIEF ATTACHMENT O

IN THE UNITED STATES PATENT AND TRADEMARK OFFICE

In re Patent Application of
Applicants: Bednorz et al.
Serial No.: 08/479,810
Filed: June 7, 1995

Date: March 1, 2005
Docket: YO987-074BZ
Group Art Unit: 1751
Examiner: M. Kopec

For: NEW SUPERCONDUCTIVE COMPOUNDS HAVING HIGH TRANSITION
TEMPERATURE, METHODS FOR THEIR USE AND PREPARATION

Commissioner for Patents
P.O. Box 1450
Alexandria, VA 22313-1450

FIRST SUPPLEMENTAL AMENDMENT

Sir:

In response to the Office Action dated July 28, 2004, please consider the
following:

ATTACHMENT O

LANGENSCHEIDT'S

German-English
English-German
DICTIONARY

OVER 40,000 ENTRIES

TWO VOLUMES IN ONE • 592 PAGES

LANGENSCHEIDT'S

German-English
English-German
DICTIONARY

For over 100
have been an
several decades
aries have been

However, Ian
To bring you a
compiled this e
which have ente
last few years I
Mondfahre, M
lunar probe, hea

Langenscheidt
another new and
ing user: it prov
sion and conjuga
entries (see pp. 7

The phonetic
headwords follow
national Phonetic

In addition to
special quick-refe
date with names
abbreviations and w

Designed for
Dictionary, with
of great value to
in home and offic

LANGENSCHEIDT'S GERMAN-ENGLISH ENGLISH-GERMAN DICTIONARY

A Washington Square Press edition

1st printing.....January, 1953
37th printing.....August, 1969

New Revised and Enlarged Edition

1st printing.....January, 1970

This WASHINGTON SQUARE PRESS edition is published by
arrangement with Langenscheidt KG, Publishers, Berlin
and Munich, Germany, and is printed from brand-new
plates made from newly set, clear, easy-to-read type.



Published by Washington Square Press,
a division of Simon & Schuster, Inc., 630 Fifth Avenue, New York, N.Y.

WASHINGTON SQUARE PRESS editions are distributed in the
U.S. by Simon & Schuster, Inc., 630 Fifth Avenue, New
York, N.Y. 10020 and in Canada by Simon & Schuster
of Canada, Ltd., Richmond Hill, Ontario, Canada.

Standard Book Number: 671-47825-7.

Copyright, ©, 1952, 1969, 1970, by Langenscheidt KG, Berlin and
Munich, Germany. All rights reserved. Published on the same day in
Canada by Simon & Schuster of Canada, Ltd. Printed in the U.S.A.
This WASHINGTON SQUARE PRESS edition may not be sold in Ger-
many, Switzerland, and Austria. A hard-bound edition of this book
is available in the U.S. from McGraw-Hill Book Company.

ne Fläche; (gleiche) Höhe, Niveau *n.*, Stand *m.*; fig. Maßstab *m.*; Wasserwaage *f.*; sea ~ Meeresspiegel *m.*; on the ~ F offen, aufrichtig; 3. v/t. gleichmachen, ebnen; fig. anpassen; richten, zielen mit; ~ up erhöhen; v/i. ~ at, against zielen auf (acc.); ~headed vernünftig, nüchtern. lever ['li:və] Hebel *m.*; Hebestange *f.*; -age ['.ɔ:rɪdʒ] Hebelkraft *f.*. levity ['levit̩] Leichtfertigkeit *f.*. levy ['levi] 1. Erhebung *f.* von Steuern; ✗ Aushebung *f.*; Aufgebot *n.*; 2. Steuern erheben; ✗ ausheben. lewd □ [lu:d] liederlich, unzüchtig. liability [laɪ'bilit̩] Verantwortlichkeit *f.*; § Haftpflicht *f.*; Verpflichtung *f.*; fig. Hang *m.*; liabilities *pl.* Verbindlichkeiten *f/pl.*, ↑ Passiva *pl.*. liable □ [laɪ'əbl̩] verantwortlich; haftpflichtig; verpflichtet; ausgesetzt (to dat.); be ~ zu neigen zu. liar ['laɪə] Lügner(in). libel ['laɪbəl̩] 1. Schmähschrift *f.*; Verleumdung *f.*; 2. schmähnen; verunglimpfen. liberal ['libe:rəl̩] 1. □ liberal (a. pol.); freigebig; reichlich; freisinnig; 2. Liberale(r) *m.*; -ity [lib're:l̩] Freigebigkeit *f.*; Freisinnigkeit *f.*. liberate [lɪ'boreɪt̩] befreien; freilassen; ~ion [lɪ'bɔ'reɪʃn] Befreiung *f.*; ~or [lɪ'berət̩] Befreier *m.*. libertine ['libe:t̩naɪn] Wüstling *m.*. liberty ['libe:t̩] Freiheit *f.*; take liberties sich Freiheiten erlauben; be at ~ frei sein. librari|an [lai'breeərɪən] Bibliothekar(in); ~y [lai'bri:bɪ] Bibliothek *f.*. lice [laɪs] *pl.* von louse. license [laisə] Am. ~se ['laisəns] 1. Lizenz *f.*; Erlaubnis *f.*; Konzession *f.*; Freiheit *f.*; Zügellosigkeit *f.*; driving ~ Führerschein *m.*; 2. lizenziieren, berechtigen; et. genehmigen; ~see [laisən'si:] Lizenznehmer *m.*. licentious □ [lai'sen:s̩] unzüchtig; ausschweifend. lichen ♀, ♂ [laɪkən] Flechte *f.*. lick [lik] 1. Lecken *n.*; Salzlecke *f.*; F Schlag *m.*; 2. (be)lecken; F verdreschen; übertreffen; ~ the dust im Staub kriechen; fallen; geschlagen werden; ~ into shape zurechtsutzen. licorice ['likɔ:ris] Lakritz *f.*. lid [lid] Deckel *m.*; (Augen)Lid *n.*. lie! [laɪ] 1. Lüge *f.*; give s.o. the ~ j-n Lügen strafen; 2. lügen. lie^a [~] 1. Lage *f.*; 2. [irr.] liegen; ~ by still-, brachliegen; ~ down sich niedergelegen; ~ in wait for j-m auflauern; let sleeping dogs ~ fig. daran führen wir lieber nicht; ~down [laɪ'daʊn] Nickerchen *n.*; ~in: have a ~ sich gründlich ausschlafen. lien § [li:n] Pfandrecht *n.*

lieu [lu:] in ~ of (an)statt. lieutenant [lef'tenənt]; & le'tenənt Am. lu:'tenənt] Leutnant *m.*; Stabshalter *m.*; ~commander & Korvettenkapitän *m.*. life [laɪf], pl. lives [laɪvz] Leben *n.*; Menschenleben *n.*; Lebensbeschreibung *f.*; for ~ auf Lebenszeit; for one's ~, for dear ~ uns (liebe) Leben; to the ~ naturgetreu; ~ sentence lebenslängliche Zuchthausstrafe; ~ assurance Lebensversicherung *f.*; ~belt ['laɪfbelt] Rettungsgürtel *m.*; ~boat Rettungsboot *n.*; ~guard Leibwache *f.*; Badewärter *m am Strand*; ~ insurance Lebensversicherung *f.*; ~jacket & Schwimmweste *f.*; ~less □ [laɪfl̩s] leblos; matt (a. fig.); ~like lebenswahr; ~long lebenslänglich; ~preserver Am. ['laɪfp'rezə:və] Schwimmgürtel *m.*; Totschläger *m.* (Stock mit Bleikopf); ~time Lebenszeit *f.*. lift [lɪft] 1. Heben *n.*; phys. □ Auftrieb *m.*; fig. Erhebung *f.*; Fahrstuhl *m.*; give s.o. a ~ j-m helfen; j-n (im Auto) mitnehmen; 2. v/t. (auf)heben; erheben; beseitigen; st. klauen, stehlen; v/i. sich heben. ligature ['lɪgə:tʃu:s] Binde *f.*; Verbund *m.*. light¹ [laɪt] 1. Licht *n.* (a. fig.); Fenster *n.*; Aspekt *m.*; Gesichtspunkt *m.*; Feuer *n.*; Glanz *m.*; fig. Leuchte *f.*; ~s pl. Fähigkeiten *f/pl.*; will you give me a ~ darf ich Sie um Feuer bitten; put a ~ zu anzünden; 2. licht, hell; blond; 3. [irr.] v/t. oft ~ up be-, erleuchten; anzünden; v/i. mst ~ up aufleuchten; ~ out Am. d. schnell losziehen, abhauen. light² [~] 1. adj. □ u. adv. leicht (a. fig.); ~ current & Schwachstrom *m.*; make ~ of et. leicht nehmen; 2. ~ (upon) stoßen od. fallen auf (acc.), geraten an (acc.); sich niedersetzen auf (dat.). lighten ['laɪtn] blitzen; (sich) erhellen; leichter machen; (sich) erleichtern. lighter ['laɪtə] Anzünder *m.*; (Taschen)Feuerzeug *n.*; & L(e)ichter *m.*. light⁻headed ['laɪt'he:dɪd] wirr im Kopf, irr.; ~hearted □ [l'ha:tɪd] leichtherzig; fröhlich; ~house ['laɪthaʊs] Leuchtturm *m.*. lighting ['laɪtɪŋ] Beleuchtung *f.*; Anzünden *n.*. light⁻minded ['laɪt'maindɪd] leichtsinnig; ~ness [laɪtnɪs] Leichtigkeit *f.*; Leichtsinn *m.*. lightning ['laɪtnɪŋ] Blitz *m.*; ~ bug Am. zo. Leuchtkäfer *m.*; ~conductor, ~rod & Blitzleiter *m.*. light-weight ['laɪtwei:t̩] Sport: Leichtgewicht *n.*. like [laɪk] 1. gleich; ähnlich; wie; such ~ dergleichen; feel ~ F sich